Pile-Up Suppression in the ATLAS Level 1 Calorimeter Trigger and Searches for Higgs Boson Pair Production

Andrew Christopher Daniells

Thesis submitted for the degree of Doctor of Philosophy

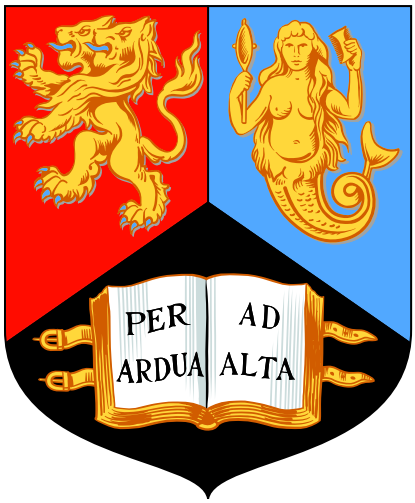

Particle Physics Group,
School of Physics and Astronomy,
University of Birmingham.

March 31, 2016

ABSTRACT

The Preprocessor system of the ATLAS Level 1 Calorimeter Trigger processes analogue signals from the 7168 trigger towers in the electromagnetic and hadronic calorimeters. Almost all of the processing takes place in the Multi-Chip Module, which has been replaced by an upgraded version of the device for operation during the second long data-taking period of the Large Hadron Collider. The development and demonstration of the signal processing and noise suppression techniques incorporated into its design to reduce the sensitivity to the effects of event pile-up is presented. With these new pile-up suppression methods it is possible to maintain sufficient performance for missing transverse energy and multijet triggers at a luminosity of approximately $2 \times 10^{34}\,\mathrm{cm}^{-2}\,\mathrm{s}^{-1}$.

A search for resonant and nonresonant Higgs boson pair production in the $hh \to b\bar{b}\tau\tau$ channel is presented for $20.3\,\mathrm{fb}^{-1}$ of $\sqrt{s} = 8\,\mathrm{TeV}$ data taken by the ATLAS experiment at the Large Hadron Collider. The results of this analysis are also combined with the corresponding results obtained in the $hh \to WW^*\gamma\gamma$, $b\bar{b}\gamma\gamma$ and $b\bar{b}b\bar{b}$ analyses. Evidence for their production is not observed and upper limits are set at the 95% confidence level on the production cross sections. For nonresonant hh production an upper limit of 0.69 (0.47) pb is observed (expected), which corresponds to 70 (48) times the Standard Model cross section for $gg \to hh$. The observed (expected) upper limits for resonant hh production from the decay of a heavy Higgs boson vary between 2.1 (1.1) pb at 260 GeV and 0.011 (0.018) pb at 1000 GeV. Interpretations of these results are made in the cases of two Minimal Supersymmetric Standard Model scenarios.

DECLARATION OF AUTHORS CONTRIBUTION

The success of the ATLAS experiment has been the result of the efforts of thousands of dedicated people who have contributed to its design, construction and operation over many years. I have been fortunate to play a part in a number of different aspects of the experiment by contributing to its early operation, physics analysis and upgrade. While at CERN I played an active part in the operation of the trigger during the 2012–2013 data-taking period. This included time spent as the online trigger shifter in the ATLAS control room and the primary Level 1 Calorimeter Trigger (L1Calo) expert on call.

I have also contributed significantly to the performance and calibration of L1Calo. This began with the introduction of noise cuts designed to suppress pile-up effects in the forward region of the calorimeter in 2012. The procedure used in obtaining these noise cuts is summarised in Reference [1]. I then went on to study methods to suppress the effects of pile-up on the Preprocessor system that included the use of the autocorrelation Finite Impulse Response filter coefficients, the development of an average pedestal correction and an alternative noise cut strategy. Much of this work is presented in Chapter 6 and Chapter 7 of this thesis and was awarded a prize within the ATLAS TDAQ community "for the best improvement of selection efficiencies over the background rate using new features for 2015" — one of the Athens workshop champagne challenges.

I assisted colleagues at Heidelberg and Rutherford Appleton Laboratory with the integration and support of these new features in the firmware of the new Multi-Chip Module and the data readout in time for the start of Run 2. Alongside this, I contributed to the implementation of these new features into the Run 2 simulation software. This included the derivation of suitable autocorrelation Finite Impulse Response filter coefficients and noise cuts, as well as assisting Daniel Narrias Villar with a parameterised version of the pedestal correction. The details of the software

implementation are not discussed in this thesis, but are covered in some detail in ATLAS internal documentation [2]. My final contribution as part of L1Calo was assisting Falk Bartels with the derivation and commissioning of autocorrelation Finite Impulse Response filter coefficients and noise cuts for operation with 25 ns and 50 ns bunch spacings in 2015.

As part of the $H \to ZZ^{(*)} \to 4\ell$ working group I have contributed to a number of ATLAS publications [3, 4, 5] and preliminary results [6] since summer 2012. I performed studies on the mass resolution performance of the analysis selection in each of the final states, with and without the use of a Z mass constraint. This work is not described in this thesis, though is explained in detail in an approved ATLAS internal document [7]. I also studied the performance of the lepton selection with the application of the additional isolation and impact parameter cuts imposed by the $H \to ZZ^{(*)} \to 4\ell$ analysis to obtain estimates of the associated systematic uncertainties. This analysis is presented in Appendix A of this thesis. Using a similar analysis, I was also able to assist with the validation of the muon corrections tools for Monte Carlo using $Z \to \mu\mu$ events.

I have participated in the analysis of $\sqrt{s} = 8\,\text{TeV}$ data collected by ATLAS in the search for Higgs boson pair production in the $hh \to b\bar{b}\tau\tau$ channel. This analysis is presented in Chapter 8 of this thesis. Chapter 9 presents the combination of this analysis with the other ATLAS Higgs boson pair production channels, where I was involved in the setting of the hh production limits using a likelihood-based technique. The results from these two chapters are part of the ATLAS paper [8], forming the final contribution to the Higgs boson pair production for Run 1 and the published material is also included in Appendix B of this thesis.

ACKNOWLEDGEMENTS

There are many people I would like to thank for their collaboration, support and encouragement during my PhD, which has resulted in the completion of this thesis. First of all, I am grateful to the Particle Physics department at the University of Birmingham for giving me the opportunity to complete this work and the Science and Technology Facilities Council for their funding of my studentship. I thank both Alan Watson and Robin Middleton for their excellent supervision over the past four and a half years and for managing to maintain regular meetings with me despite geographical displacement of one form or other.

I would like to express my gratitude to the L1Calo community as a whole for their support and appreciation of the knowledge I have accumulated on filters and noise cuts. This has been a major part of my life for many years which I have thoroughly enjoyed. In particular, I have had the pleasure of working closely at times with the likes of Bruce Barnett, Martin Wessels, Steve Hillier and Juraj Bracinik as well as sharing an office with Craig Wiglesworth. I give special thanks to Ivana Hristova for her dedicated assistance with the production and analysis of the Monte Carlo datasets required for the analysis of the autocorrelation filters and noise cuts, presented in Chapter 7 of this thesis. I will also mention those at Rutherford Appleton Laboratory (RAL), including Norman Gee, David Sankey and Weiming Qian, for sharing their technical expertise and providing good company at coffee and lunch times during the time I was based there.

There have been a number of people who have helped with my physics analyses. I am indebted to Kostas Nikolopoulos, Eleni Mountricha and Ludovica Aperio Bella for their input and support with my work on the $H \to ZZ^{(*)} \to 4\ell$ analysis. Their dedication towards this analysis and relentless work ethic was admirable and should be commended. I will also not forget the act of kindness when Kostas drove me back to my residence in Ferney-Voltaire to change after I showed up at our meeting

one morning soaked though from the rain. I shared much of the work on the $b\bar{b}\tau\tau$ analysis, as presented in Chapter 8 of this thesis, with Keita Hanawa and Ryosuke Fuchi. I also thank Xiaohu Sun and Kostas (again) for their time spent with me on the statistical treatment of the combination of the hh channels presented in Chapter 9.

This experience would have not been the same without the company of fellow PhD students at the University of Birmingham. I especially thank all the ATLAS students in Physics West 316 for making this an enjoyable and memorable time: Tim Martin, Hardeep Bansil, Tom McLaughlan, Andy Chisholm, Jodie Palmer, Benedict Allbrooke, Javier Murillo Quijada, Richard Mudd, Rhys Owen, Mark Levy, Matt Baca, Andy Foster, James Broughton and any other names that I have forgotten. I certainly wish I was able to spend more time in your company and it was always refreshing to meet you all on my occasional visits to Birmingham in the last few years.

I was fortunate enough to spend an extended period on long term attachment at CERN during what was one of the most exciting times for the LHC and is an experience I greatly appreciated. A big thanks to all those at Rosebank for being a pleasure to live with and for their many intellectually stimulating conversations while I worked from RAL. Especially Kerry, Bear dog, Tim Stanley and Indran Mathavan. Finally, I must thank my parents for their help relocating me from one place to another and for tolerating me while I finished writing this thesis.

Dedicated to my parents
and
the memory of Grandad

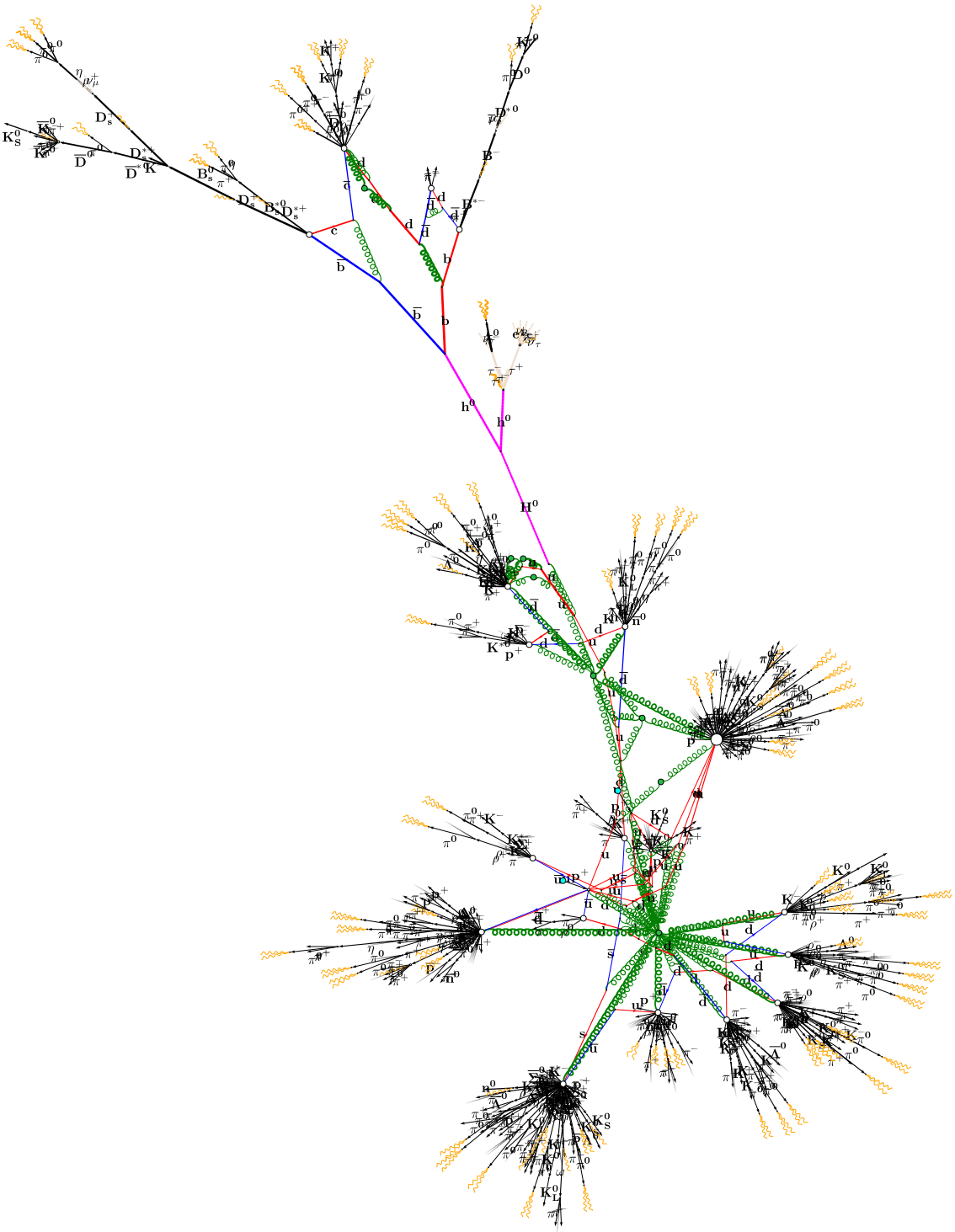

Visualisation of a $H \to hh \to b\bar{b}\tau\tau$ event at the LHC using MCViz [9].

Contents

List of Tables

List of Figures

Definitions Of Acronyms

$E_{\mathbf{T}}$ transverse energy

E_x x-component sum of all jet element E_{T} values

E_y y-component sum of all jet element E_{T} values

$E_{\mathbf{T}}^{\mathbf{miss}}$ missing transverse energy

$E_x^{\mathbf{miss}}$ x-component of the $E_{\mathrm{T}}^{\mathrm{miss}}$ vector

$E_y^{\mathbf{miss}}$ y-component of the $E_{\mathrm{T}}^{\mathrm{miss}}$ vector

$N_{\mathbf{vtx}}$ number of reconstructed primary vertices

$p_{\mathbf{T}}$ transverse momentum

$\sum E_{\mathbf{T}}$ total transverse energy

ADC Analogue-to-Digital Converter

ALICE A Large Ion Collider Experiment

AnIn Analogue Input

ATLAS A Toroidal LHC ApparatuS

ASIC Application Specific Integrated Circuit

BC Bunch Crossing

BC-mux BC-multiplexing

BCID Bunch Crossing Identification

BCM Beam Conditions Monitor

BDT Boosted Decision Tree

BSM Beyond the Standard Model

CAN Control Area Network

CDF Collider Detector at Fermilab

CERN European Organisation for Nuclear Research

CL Confidence Level

CMM Common Merger Module

CMX Common Merger module eXtended

CMS Compact Muon Solenoid

CMT Configuration Management Tool

CP Cluster Processor

CPM Cluster Processor Module

CR Control Region

CSC Cathode Strip Chamber

CTP Central Trigger Processor

DAC Digital-to-Analogue Converter

DAQ Data Acquisition

EB Extended Barrel

ECal Electromagnetic Calorimeter

EF Event Filter

EM Electromagnetic

EMB Electromagnetic Barrel

EMEC Electromagnetic Endcap

ESD Event Summary Data

EVNT Event File

EW Electroweak

EWSB Electroweak Symmetry Breaking

FCal Forward Calorimeter

FIR Finite Impulse Response

FPGA Field Programmable Gate Array

ggF gluon-gluon Fusion

GUT Grand Unified Theory

HCal Hadronic Calorimeter

HEC Hadronic Endcap Calorimeter

HL-LHC High Luminosity LHC

HLT High Level Trigger

IBL Insertable B-Layer

ID Inner Detector

IW Inner Wheel

JEM Jet/Energy-sum Module

JEP Jet/Energy-sum Processor

JES Jet Energy Scale

JVF Jet-Vertex Fraction

L1 Level 1

L1A Level 1 Accept

L1Calo Level 1 Calorimeter Trigger

L1Muon Level 1 Muon Trigger

L1Topo Level 1 Topology Processor

L2 Level 2

LAr Liquid Argon Calorimeter

LB Luminosity Block

LCD LVDS Cable Driver

LEP Large Electron-Positron collider

LH Likelihood

LHC Large Hadron Collider

LHCb LHC beauty

LHCC LHC Committee

LHCf LHC forward

LEIR Low Energy Ion Ring

LO Leading Order

LS1 Long Shutdown 1

LS2 Long Shutdown 2

LS3 Long Shutdown 3

LSB Least Significant Bit

LSP Lightest Supersymmetric Particle

LUCID LUminosity measurement using Cherenkov Integrating Detector

LVDS Low-Voltage Differential Signalling

LUT Look-Up Table

MC Monte Carlo

MCM Multi-Chip Module

MDT Monitored Drift Tube

MIP Minimum Ionising Particle

MMC Missing Mass Calculator

MoEDAL Monopole and Exotics Detector At the LHC

MS Muon Spectrometer

MSSM Minimal Supersymmetric Standard Model

MTP Mid-Term Plan

NLO Next-to-Leading Order

nMCM new Multi-Chip Module

NNLO Next-to-Next-to-Leading Order

NNLL Next-to-Next-to-Leading Logarithm

OW Outer Wheel

PDF Parton Distribution Function

PMT Photo-Multiplier Tube

PoI Parameter of Interest

PPM Preprocessor Module

PS Proton Synchrotron

PSB Proton Synchrotron Booster

QCD Quantum Chromodynamics

QED Quantum Electrodynamics

RAL Rutherford Appleton Laboratory

ReM Readout Merger

RF Radio Frequency

RDO Raw Data Object

RoI Region of Interest

RPC Resistive Plate Chamber

SCT Semi-Conductor Tracker

SF Scale Factor

SLT Single Lepton Trigger

SM Standard Model

SPS Super Proton Synchrotron

SR Signal Region

STFC Science and Technology Facilities Council

STVF Soft-Term Vertex-Fraction

SUSY Supersymmetry

TDAQ Trigger and Data AcQuisition

TDR Technical Design Report

TES Tau Energy Scale

TGC Thin Gap Chamber

TOB Trigger Object

TOTEM TOTal cross section, Elastic scattering and diffraction dissociation Measurement at the LHC

TRT Transition Radiation Tracker

TTC Trigger Timing and Control

UA1 Underground Area 1

UA2 Underground Area 2

USA15 Underground Service Area 15

VBF Vector Boson Fusion

vdM van der Meer

VME Versa Module Europa

CHAPTER 1

INTRODUCTION

It is over a century since the birth of elementary particle physics, with J. J. Thomson's discovery of the electron using cathode rays in 1897 [10]. This began the development of the early atomic model of matter, with the first accurate model for hydrogen by Niels Bohr in 1914 and the subsequent discovery of the proton and neutron. It was established that atoms are largely empty space and consist of a positively charged nucleus containing protons and neutrons, surrounded by negatively charged electrons. The electron is still considered an elementary particle of nature and at first subsequent particle discoveries were also thought of as elementary, but have since been found to have complex structure.

The realisation of the quantum nature of the Electromagnetic (EM) interaction and the development of the theories of *quantum mechanics* and *relativity* laid the foundation for the description of particles and their interactions in terms of quantum fields. In the 1960s and 1970s, the theory of fundamental particles and their interactions known as the Standard Model (SM) of particle physics was established.

Built on the theoretical framework of *quantum field theory*, it incorporated all that was known about subatomic particles at the time and predicted the existence of additional particles. It describes three of the four fundamental forces of nature, and puts *quarks* and *leptons* as the fundamental building blocks which constitute all matter. A triumph of the SM was the prediction and subsequent discovery of the massive $W^{\pm}$ and Z bosons responsible for the weak interaction at CERN in 1983 by the Underground Area 1 (UA1) [11, 12] and Underground Area 2 (UA2) experiments [13, 14], and later the top quark at the Tevatron collider by the Collider Detector at Fermilab (CDF) [15] and DØ [16] experiments in 1995. Until its discovery in 2012, the Higgs boson was the last predicted particle of the SM. The Higgs boson arises as a consequence of spontaneous Electroweak Symmetry Breaking (EWSB), which is the mechanism by which the SM particles acquire mass.

Despite the great success of the SM, it is not considered to be the final fundamental theory of particle physics. There remain many theoretical problems and cosmological observations for which it is not able to offer any explanation. One important realisation is that matter as we know it only makes up a small fraction (about 4.9%) of the mass-energy density of the observable universe. Much of the universe actually consists of *dark matter* (about 26.8%), and the remaining 68.3% is accounted for by *dark energy* [17], though we have no idea what this actually is. The SM does not include a viable dark matter candidate to explain the observed fraction of dark matter in the universe. This motivates the development of theories Beyond the Standard Model (BSM) and the search for new physics at the energy frontier. The Minimal Supersymmetric Standard Model (MSSM) is one possible extension to the SM that incorporates the minimal choice of new particle states and interactions of Supersymmetry (SUSY) that is consistent with phenomenology.

The Large Hadron Collider (LHC) was primarily conceived to explore the mechanism by which EWSB occurs and the search for signs of new physics at the energy frontier. The A Toroidal LHC ApparatuS (ATLAS) detector is one of the largest general purpose high energy particle physics experiments ever constructed. It is based at Europe's premier site for nuclear research on the Franco-Swiss border near

Geneva, called CERN. The LHC has successfully operated since the start of low energy commissioning in November 2009, where it reached a centre-of-mass energy of $\sqrt{s} = 2.36\,\text{TeV}$, beating the Tevatron's previous record of $\sqrt{s} = 1.96\,\text{TeV}$ held for eight years [18]. In March 2010, the LHC began its high-energy commissioning phase with proton-proton (pp) collisions at a centre-of-mass energy of $\sqrt{s} = 7\,\text{TeV}$ at a small instantaneous luminosity of the order $10^{27}\,\text{cm}^{-2}\,\text{s}^{-1}$.

To date the LHC has enabled a large variety of important SM measurements as well as being credited with a number of new observations and discoveries, including composite particles like the χ_b (3P) bottomonium state [19] and the rare decay $B_s^0 \to \mu\mu$ [20]. The search for the Higgs boson has taken place at many facilities, including the Large Electron-Positron collider (LEP) [21] and the Tevatron [22]. The main highlight of Run 1 was the observation of the neutral boson consistent with the SM Higgs boson by ATLAS [23] and Compact Muon Solenoid (CMS) [24] at a mass of approximately $125\,\text{GeV}$[1]. A summary of the combined search results by the ATLAS experiment is shown in Figure 1.1. This resulted in the Nobel prize in Physics 2013 being awarded to François Englert and Peter W. Higgs for their "theoretical discovery of a mechanism that contributes to our understanding of the origin of mass of subatomic particles" [25]. Since then there has been a increased effort to search for evidence of additional Higgs sectors beyond the SM at the LHC.

The bulk of the Run 1 pp physics data set was delivered during 2011 and 2012. The LHC had delivered beams of colliding protons up to a centre-of-mass energy of $\sqrt{s} = 8\,\text{TeV}$, where ATLAS recorded a maximum peak instantaneous luminosity of $7.73 \times 10^{33}\,\text{cm}^{-2}\,\text{s}^{-1}$ for stable collisions. At such a high beam intensity, the average peak number of pp interactions achieved per bunch crossing was approximately 37. The challenge for the experiment is to identify the production of vector and Higgs bosons amongst the large number of these additional soft-scale interactions known as *pile-up*.

The ATLAS Level 1 Calorimeter Trigger (L1Calo) is responsible for making the ini-

[1] Unless explicitly stated otherwise, natural units are assumed such that $c = \hbar = 1$.

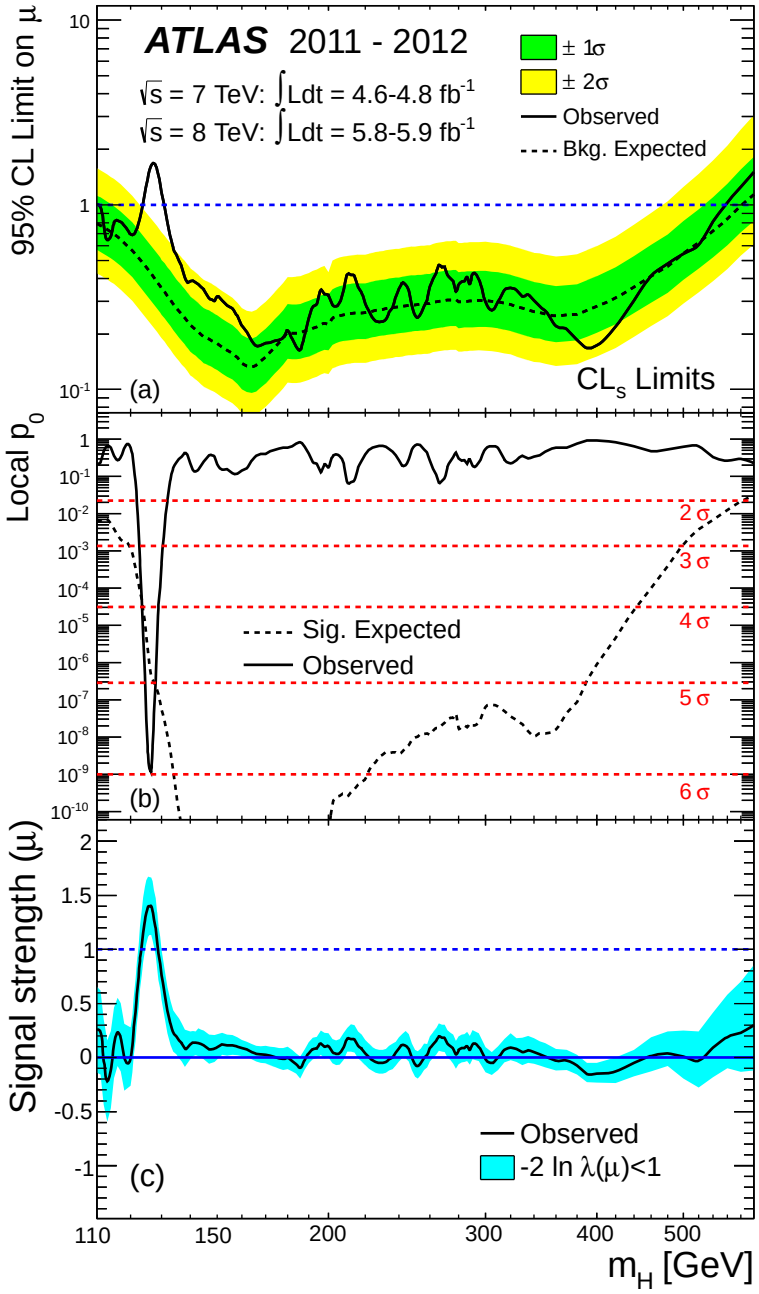

Figure 1.1: Summary of the combined search results for the observation of the Higgs boson by the ATLAS experiment [23]. Subfigure (a) shows the observed (solid black line) 95% CL upper limit on the signal strength as a function of m_H and the expectation (dashed black line) under the background-only hypothesis. The green and yellow bands show the $\pm 1\sigma$ and $\pm 2\sigma$ uncertainties on the expected limit, respectively. Subfigure (b) shows the observed (solid black line) local p_0 as a function of m_H and the expectation (dashed black line) under a SM Higgs boson signal hypothesis. Subfigure (c) shows the best-fit signal strength (solid black line) as a function of m_H and its $\pm 1\sigma$ uncertainty (blue band).

tial event selection based on low-granularity calorimeter information to reduce the event rate from the bunch crossing frequency down to around 70 kHz. The coarse granularity of trigger towers, particularly in the more forward region of the detector means the trigger is very susceptible to the effects of pile-up. Triggers which require global sums such as $E_{\mathrm{T}}^{\mathrm{miss}}$, large sums of trigger towers such as low threshold multijet triggers or triggers including a forward jet are most strongly affected. Figure 1.2 shows the Level 1 trigger rates as a function of the instantaneous luminosity for the lowest threshold unprescaled single object triggers used during 2012. The rates for most triggers depend linearly on the instantaneous luminosity, however there is a clear non-linear dependence for $E_{\mathrm{T}}^{\mathrm{miss}}$ at high luminosity, due to the increasing rate of fake triggers.

Many improvements were made to increase the overall performance of the $E_{\mathrm{T}}^{\mathrm{miss}}$ trigger for 2012 and these resulted in better $E_{\mathrm{T}}^{\mathrm{miss}}$-based triggers compared to 2011, despite the increased luminosity [26]. An important part of this improvement came from L1Calo. For 2012 the noise thresholds in the forward ($\eta > 2.5$) part of the calorimeters were raised to up to 10 GeV for certain Level 1 towers to reduce the sensitivity of $E_{\mathrm{T}}^{\mathrm{miss}}$ triggers to the significant effects of pile-up in this region [1]. This meant that the Level 1 threshold could be reduced from 50 GeV during 2011 to 40 GeV in 2012. An additional option to veto at Level 1 the first three bunches in an train, which were found to be the most sensitive to varying pile-up conditions, allowed to further lower the Level 1 $E_{\mathrm{T}}^{\mathrm{miss}}$ thresholds. The impact of these improvements on SUSY searches was significant.

During Run 2, the LHC is expected to achieve its original design centre-of-mass energy of $\sqrt{s} = 14\,\mathrm{TeV}$ and to approach twice its original design luminosity of $1 \times 10^{34}\,\mathrm{cm}^{-2}\,\mathrm{s}^{-1}$. For the L1Calo trigger to successfully operate in these demanding conditions new features are required in the processing of calorimeter signals in addition to noise cuts to suppress the pile-up effects.

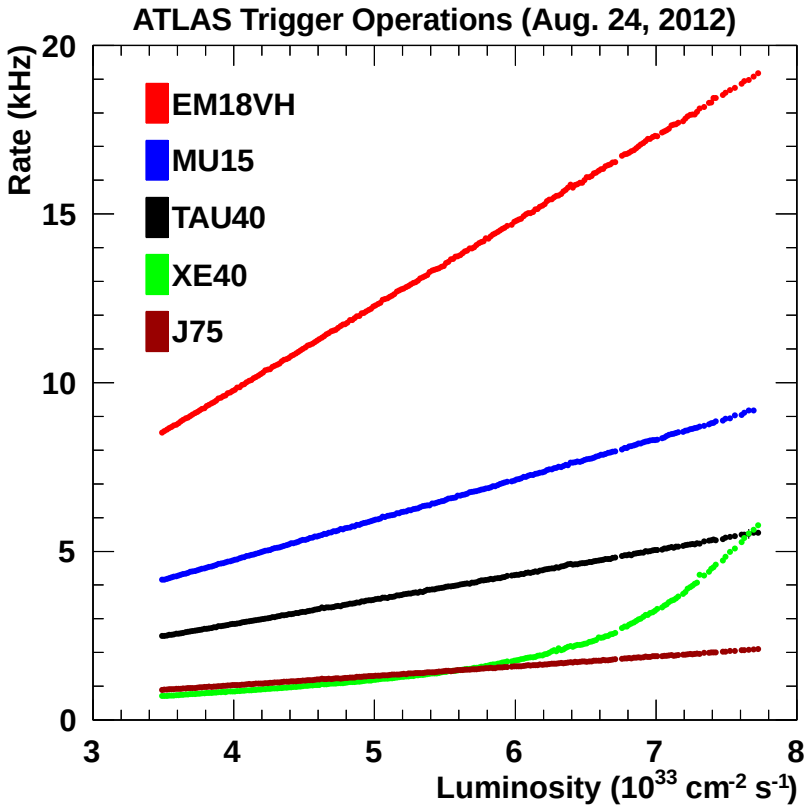

Figure 1.2: Level 1 trigger rates as a function of instantaneous luminosity for the lowest-threshold unprescaled single object triggers used during 2012: EM18VH is a trigger for an electron or photon above 18 GeV; MU15 is a trigger for a muon above 15 GeV; TAU40 is a trigger for a hadronically decaying tau lepton above 40 GeV; XE40 is a trigger for $E_{\mathrm{T}}^{\mathrm{miss}}$ above 40 GeV; and J75 is trigger for a jet above 75 GeV [27].

1.1 Document Structure

This document starts with an overview of the relevant theoretical background and the expected phenomenology of the SM Higgs sector at the LHC, as well as that of some MSSM scenarios that include different extended Higgs boson sectors. Chapter 3 gives a brief introduction to the CERN laboratory and the LHC. This is followed by an introduction to the ATLAS experiment in Chapter 4, including details about the data sample used for the analyses contained in this thesis.

The first major topic addressed in this thesis is the improvement of the signal processing performance of L1Calo and the mitigation of pile-up effects for Run 2. This

starts with an introduction of the L1Calo system and the program of upgrades during the first long shutdown of the LHC in Chapter 5. Chapter 6 covers the development of new signal processing techniques for the upgraded Multi-Chip Module (MCM), using toy simulation studies of the Preprocessor system. Chapter 7 explores the optimisation of noise cuts after the implementation of the new signal processing methods, in the context of jet and $E_{\mathrm{T}}^{\mathrm{miss}}$ trigger performance, using Monte Carlo (MC) simulated for conditions similar to those expected at the end of Run 2.

The following chapters cover the main physics analysis presented in this thesis. Chapter 8 presents the search for Higgs boson pair production in the $hh \to b\bar{b}\tau\tau$ channel and the combination of this analysis with other similar searches for Higgs boson pair production is discussed in Chapter 9. Chapter 10 then finishes this thesis with some concluding remarks.

CHAPTER 2

THE HIGGS BOSON

2.1 The Standard Model

The Standard Model (SM) of particle physics [28, 29, 30] is a theory that describes the fundamental forces acting between the elementary particles of nature with the exception of gravity. It has been used successfully to describe data from a wide range of experiments and with the LHC all of its predicted elementary particles have now been verified. The SM is a renormalisable quantum field theory whose interactions are described by a Lagrangian which is invariant under the $SU(3)_C \times SU(2)_L \times U(1)_Y$ local gauge symmetry.

The SM includes twelve elementary particles with half integer spin known as fermions. They are divided into six quarks and six leptons and grouped to form three generations of matter. The first generation of fermions do not decay and therefore form the majority of the matter in our universe. Each of the fermions has its own antiparticle

with identical properties except for having equal and opposite charge. Fermions are assumed to be point-like particles whose interactions are mediated by the strong, weak and EM forces. The quarks are defined as the only fermions that carry colour charge and thus interact via the strong force. The three neutrino flavours do not carry electric charge and therefore only interact via the weak force. This makes them very difficult to detect as they rarely interact with normal matter. However, the remaining leptons are electrically charged and will therefore interact electromagnetically. The properties of the fermions are summarised in Table 2.1, where the neutrino masses are given as upper bounds set by current experimental limits.

Table 2.1: The SM spin-$\frac{1}{2}$ fermions, composed of quarks and leptons and divided into three generations of matter. The electric charge is in units of the electron charge and the mass values are quoted from Reference [31] unless stated otherwise. The limits quoted for the neutrino masses correspond to direct measurements made from the kinematics of the tritium β-decay.

Type	Generation	Name	Symbol	Mass	Charge
Quark	I	up	u	$2.3^{+0.7}_{-0.5}\,\text{MeV}$	+2/3
		down	d	$4.8^{+0.5}_{-0.3}\,\text{MeV}$	-1/3
	II	charm	c	$1.275 \pm 0.025\,\text{GeV}$	+2/3
		strange	s	$95 \pm 5\,\text{MeV}$	-1/3
	III	top	t	$173.34 \pm 0.76\,\text{GeV}$ [32]	+2/3
		bottom	b	$4.18 \pm 0.03\,\text{GeV}$	-1/3
Lepton	I	electron	e	$0.511\,00\,\text{MeV}$	-1
		electron-neutrino	ν_e	$< 2\,\text{eV}$	0
	II	muon	μ	$105.658\,\text{MeV}$	-1
		muon-neutrino	ν_μ	$< 2\,\text{eV}$	0
	III	tau	τ	$1776.82 \pm 0.16\,\text{MeV}$	-1
		tau-neutrino	ν_τ	$< 2\,\text{eV}$	0

The fundamental forces of the SM are mediated via spin-1 vector boson particles. The EM interactions are carried by the photon and act on electrically charged particles. The weak force acts on all fermions and is carried by the massive gauge bosons $W^\pm$ and the Z. The strong force is mediated via a family of eight massless gluons that act on particles carrying colour charge. The properties of the gauge bosons

are summarised in Table 2.2. Gravity is many orders of magnitude weaker than the other three forces at the distance scales relevant to elementary particle physics and is therefore generally neglected.

Table 2.2: The SM spin-1 gauge bosons. The electric charge is in units of the electron charge and the mass values are quoted from Reference [31].

Force	Name	Symbol	Mass	Charge
EM	photon	γ	0	0
weak	W	$W^{\pm}$	$80.385 \pm 0.015\,\text{GeV}$	± 1
	Z	Z	$91.1876 \pm 0.0021\,\text{GeV}$	0
strong	gluon	g	0	0

The $\text{SU}(2)_L \times \text{U}(1)_Y$ symmetry unifies the description of the EM and weak interactions within an Electroweak (EW) theory. This combines the weak isospin $\text{SU}(2)_L$ gauge symmetry of the weak force and the hypercharge $\text{U}(1)_Y$ symmetry of Quantum Electrodynamics (QED). The $\text{SU}(3)_C$ symmetry describes the strong interaction in the non-abelian gauge theory of Quantum Chromodynamics (QCD). An important property of QCD interactions is confinement, in which the coupling strength decreases and the interaction becomes asymptotically free at high energy, and conversely leading to quarks being bound at distances of approximately 1 fm in hadrons.

The addition of the Higgs mechanism introduces a scalar field, which results in a single spin-0 particle known as the Higgs boson. The fermions and massive gauge bosons acquire mass through interactions with this Higgs field. This is discussed further in Section 2.2.

2.2 The Higgs Mechanism

In quantum field theory a symmetry is considered to be spontaneously broken if the Lagrangian remains invariant whilst the vacuum state does not [33]. The Brout–Englert–Higgs mechanism [34, 35, 36] achieves this by introducing a weak isospin

doublet of complex scalar fields to electroweak theory of:

$$\phi = \begin{pmatrix} \phi^+ \\ \phi^0 \end{pmatrix}, \tag{2.1}$$

where ϕ^+ and ϕ^0 can be defined in terms of the real scalar fields ϕ_i as:

$$\phi^+ = \frac{\phi_1 + i\phi_2}{\sqrt{2}}, \quad \phi^0 = \frac{\phi_3 + i\phi_4}{\sqrt{2}}. \tag{2.2}$$

The Lagrangian for this scalar field is given by:

$$\mathcal{L}_\phi = (D_\mu \phi)^\dagger (D_\mu \phi) - V(\phi), \tag{2.3}$$

where D_μ is the covariant derivative and the field's potential $V(\phi)$ is given by:

$$V(\phi) = \mu^2 \phi^\dagger \phi + \lambda (\phi^\dagger \phi)^2, \tag{2.4}$$

where μ and λ are constants that parametrise the masses and self-interactions of the scalar fields. The value of λ is expected to be positive and by choosing $\mu^2 < 0$ the result is a potential as shown in Figure 2.1. This is commonly referred to as the 'wine bottle' or 'Mexican hat' potential, where there is a central maximum and stable minima exist for $\phi^\dagger \phi = \mu^2/2\lambda$. This results in a non-zero vacuum expectation value υ corresponding to the minima of the potential, which are given by:

$$\langle 0|\phi|0\rangle = \sqrt{\frac{1}{2}} \begin{pmatrix} 0 \\ \upsilon \end{pmatrix}, \quad \text{with } \upsilon = \frac{|\mu|}{\sqrt{\lambda}} \simeq 246\,\text{GeV}. \tag{2.5}$$

The inclusion of the Higgs doublet provides a mechanism for generating masses for the $W^\pm$ and Z bosons while leaving the photon massless. The Higgs field potential results in the spontaneous symmetry breaking of three of the four generators of $\mathrm{SU}(2)_L \times \mathrm{U}(1)_Y$, where this gives rise to three massless Goldstone bosons. The $W^\pm$ and Z become massive by absorbing the unphysical Goldstone bosons giving rise

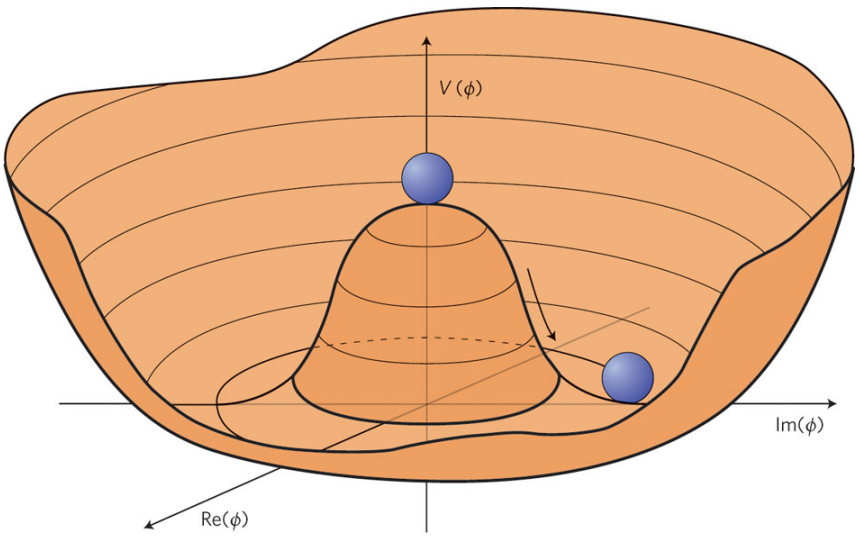

Figure 2.1: The Higgs potential, $V(\phi)$. Taken from [37].

to the longitudinal polarisation degrees of freedom of the $W^{\pm}$ and Z. The fourth unbroken generator is therefore the massless photon, corresponding to $\mathrm{U}(1)_Y$. The remaining degree of freedom introduced by the scalar doublet can be interpreted as the Higgs boson itself.

This offers an explanation for the origin of the masses of the $W^{\pm}$ and Z bosons, however does not explain the fermion masses. The fermions obtain their masses through Yukawa interactions with the Higgs field when this field acquires a non-zero vacuum expectation value. The strength of this interaction is defined by each particles coupling to the field, which is proportional to its mass.

The Higgs boson is itself a massive scalar boson associated with the Higgs field. Its mass is given by:

$$m_H = \sqrt{2\lambda}v \simeq 125\,\mathrm{GeV}. \tag{2.6}$$

The value of the Higgs self-coupling λ is a free parameter in the SM and therefore the Higgs boson mass is not predicted.

2.3 Standard Model Higgs Boson Searches

The LHC is a pp collider where the initial state particles are hadrons and the hard collisions actually occur between the proton constituents known as partons. Therefore, Parton Distribution Functions (PDFs) are required to describe the four-momentum distribution of quarks and gluons within the proton in such collisions.

Higgs boson production is a relatively rare occurrence when compared to other SM processes. Figure 2.2 shows how the production cross section evolves with the centre-of-mass energy for a number of SM processes, including the production for a SM Higgs boson with a mass of 125 GeV. The production cross section for the Higgs boson is some 10^9 times smaller than the total pp cross section, which will provide significant sources of background in many of the search channels. In order to maximise the potential of observing events with rare processes at the LHC, it is therefore necessary to collect large numbers of collisions. To this end, the LHC is designed to operate at very high beam luminosities.

The coupling strengths of the Higgs boson to fermions and bosons are proportional to their masses, therefore Higgs production generally involves heavy particles i.e. the W and Z bosons, the top quark and to a lesser extent the bottom quark. There are several mechanisms contributing to the production of the SM Higgs boson in high-energy proton collisions; the most common processes are shown in Figure 2.3. The dominant production mechanism at the LHC is from gluon-gluon Fusion (ggF), where gluons from the two colliding protons interact through a quark loop to produce the Higgs boson. The quark loop is dominated by the top quark because of its large mass, meaning that contributions from the other quarks can be ignored. In the Higgs-Strahlung production process the Higgs boson is produced in association with a W or a Z boson. In this mode, the colliding quarks produce an off-shell W or Z boson which decays back to a real W or Z boson after emitting a Higgs boson. The Vector Boson Fusion (VBF) process occurs when two quarks radiate a pair of off-shell W or Z bosons that fuse to produce the Higgs boson. This leads to a signature of

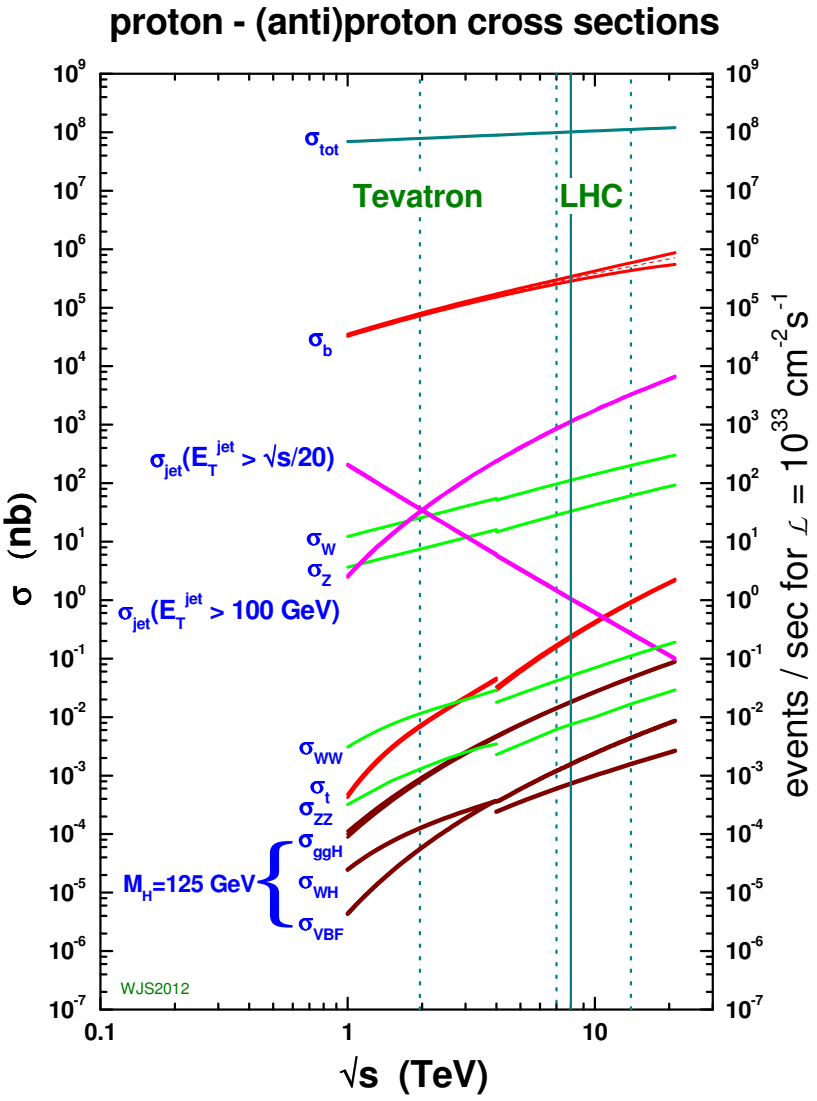

Figure 2.2: Expected cross sections for various physics processes as a function of the centre-of-mass energy. The lines highlight the operational energy of the Tevatron and LHC at different points in its history. The discontinuities arise from differences between pp and proton-antiproton collisions. Taken from [38].

the Higgs boson decay products and two well separated jets in pseudorapidity with a high invariant mass. Figure 2.4 shows the predicted cross sections for the different SM Higgs boson production processes as a function of m_H for $\sqrt{s} = 8\,\text{TeV}$ at the LHC.

The branching fractions to different decay channels are shown in Figure 2.5 as a

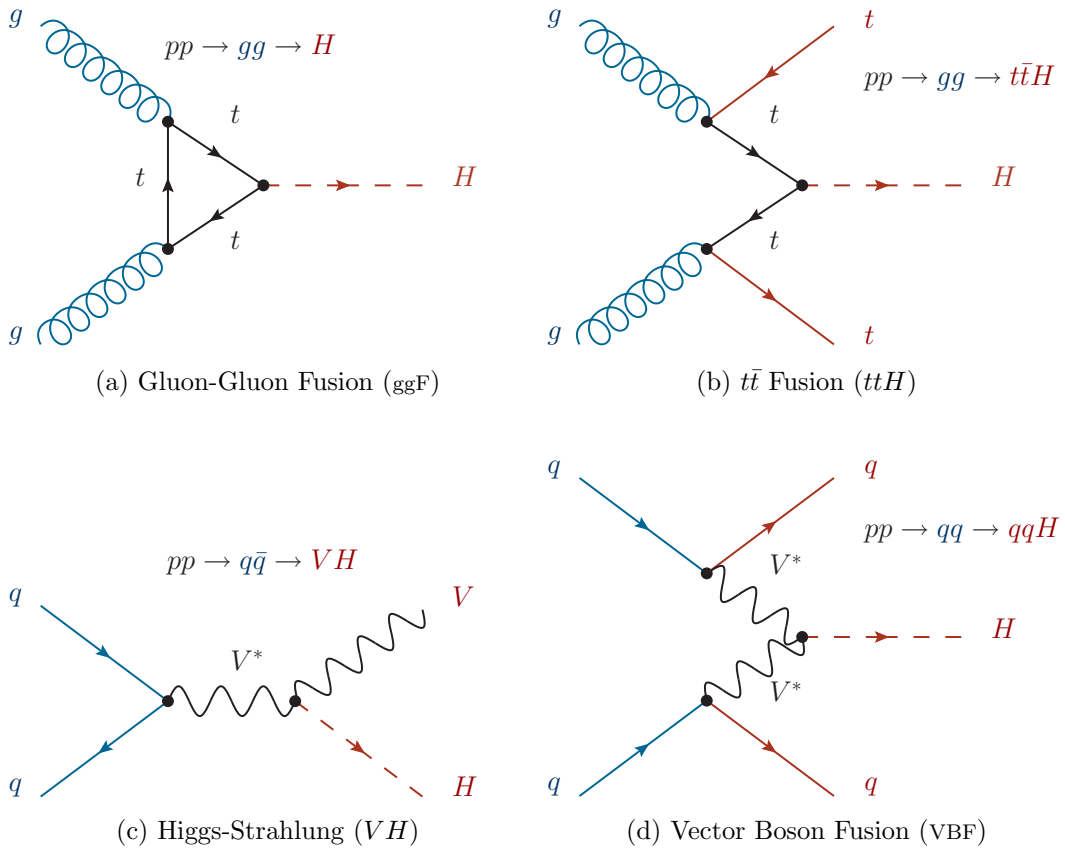

(a) Gluon-Gluon Fusion (ggF)

(b) $t\bar{t}$ Fusion (ttH)

(c) Higgs-Strahlung (VH)

(d) Vector Boson Fusion (VBF)

Figure 2.3: The main production mechanisms of the SM Higgs boson at the LHC. The colours are used to highlight the in-coming and out-going particles.

function of m_H. There are a variety of different accessible decay channels for low Higgs boson masses. These include the decays to bb, WW, $\tau\tau$, ZZ and $\gamma\gamma$ pairs. Above a mass of around 130 GeV the decays to WW and ZZ pairs become more kinematically favourable and dominate. The most sensitive channels are ZZ and $\gamma\gamma$ due to their clean signatures and excellent mass resolution.

Both the ATLAS and CMS experiments have released updated results on each of the SM Higgs boson analyses after Run 1, as well as the results of their combination. Combining the mass measurements of the ATLAS and CMS experiments using the full Run 1 data set gives a value of $m_H = 125.09 \pm 0.21$ (stat.) ± 0.11 (syst.) GeV [41]. Figure 2.6 shows a summary of the individual measurements in the high resolution $H \to \gamma\gamma$ and $H \to ZZ^{(*)} \to \ell\ell\ell\ell$ channels by each of the experiments that went into this combination.

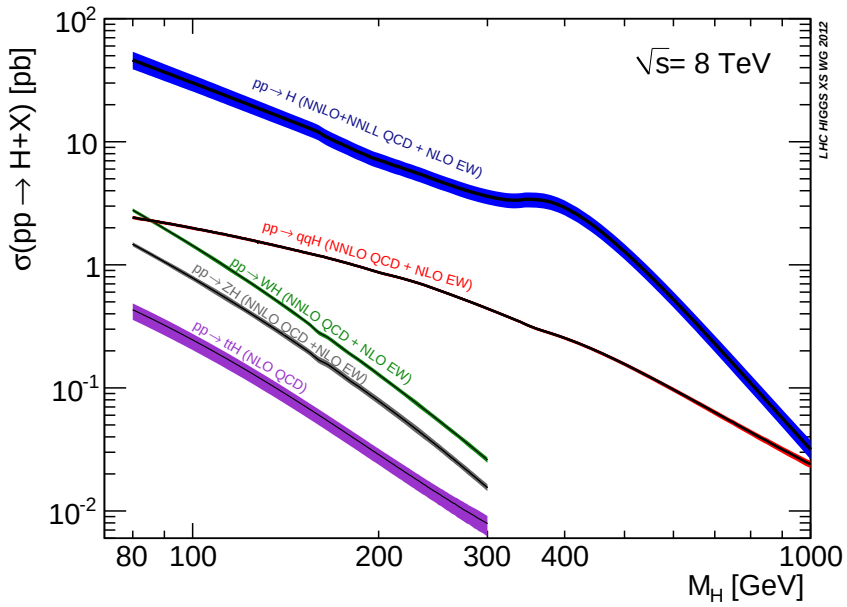

Figure 2.4: Cross sections and their uncertainties for different SM Higgs boson production processes in pp collisions at the LHC as a function of the Higgs boson mass m_H at $\sqrt{s} = 8\,\text{TeV}$ [39].

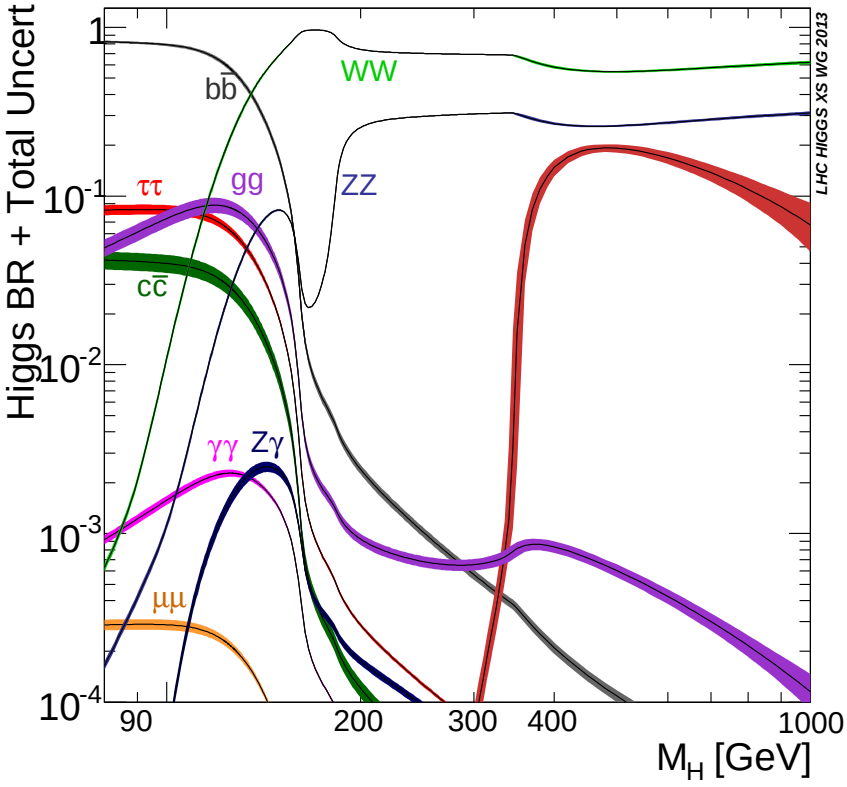

Figure 2.5: Branching ratios and their uncertainties for the SM Higgs boson into different decay channels as a function of the Higgs boson mass m_H [40].

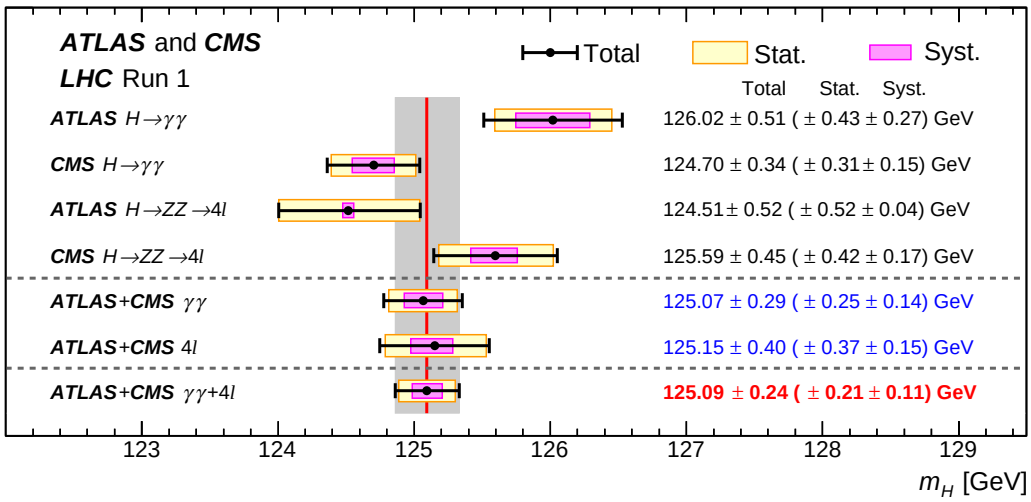

Figure 2.6: Summary of the individual ATLAS and CMS Higgs boson mass measurements and their combination for Run 1 data [41].

It is of great importance to establish that this boson is indeed the result of the mechanism responsible for EWSB and to identify whether any effects indicative of new physics are involved in the symmetry breaking mechanism. A fit to the combined ATLAS and CMS Run 1 data for the $H \to ZZ$, WW, $\gamma\gamma$, $\tau\tau$, bb and $\mu\mu$ decay modes gives a global signal yield relative to the SM expectation of 1.09 ± 0.11 [42]. Other measurements include the total decay width, spin and CP quantum numbers [43,44]. A precise measurement of its couplings to gauge bosons and fermions [45,46,47,48] is also required to verify the key prediction that their strength is proportional to the particle mass. The results from LHC Run 1 data show all these properties to be consistent with the expectation of a SM Higgs boson.

Higgs boson self-interaction is the only way to reconstruct the scalar potential of the Higgs doublet field responsible for EWSB. Rewriting this potential in terms of a physical Higgs boson leads to the trilinear Higgs boson coupling λ_{HHH} [49]:

$$\lambda_{HHH} = 6\lambda v = \frac{3m_H^2}{v}. \tag{2.7}$$

One can see here the relationship between the Higgs boson self-coupling and the trilinear Higgs boson coupling. The trilinear coupling is only accessible via Higgs

boson pair production [50,51,52]. One of the main production mechanisms at hadron colliders is $gg \to HH$ through a triangle diagram as in Figure 2.3a, where the offshell Higgs boson decays to two Higgs bosons, making this contribution sensitive to the triple Higgs coupling. This is a very challenging measurement as the cross section is relatively small and there are large backgrounds from single Higgs boson production. It has been estimated that such measurements may be possible in the $hh \to b\bar{b}\tau\tau$ channel with 600–1000 fb^{-1} of data at the LHC [53]. In extensions of the SM, such as models with an extended Higgs sector, the self-couplings of the Higgs boson may be significantly enhanced from the SM predictions [54].

2.4 Motivation for BSM Theories

Despite the great success of the SM, it is known to have many shortcomings, which suggest there may be an alternative theory that better accommodates experimental observations. It is unable to incorporate the last fundamental force of gravity. The SM does not predict a candidate particle to account for the observed dark matter in the universe. It also does not predict non-zero neutrino masses, which are inferred from the experimental observation of neutrino oscillations [55]. The SM cannot sufficiently explain the asymmetry between matter and antimatter that has resulted in the matter dominated universe we observe today. The coupling constants of the strong and electroweak interactions do not intersect at high energy scales, assuming there is a Grand Unified Theory (GUT) [56]. One final inadequacy of the SM of particular relevance to the Higgs sector is known as the *hierarchy problem*.

It is generally accepted that the SM is an effective theory up until some energy scale Λ, where the effect of new physics becomes important. The tree-level mass of the Higgs boson is given in (2.6) and radiative corrections due to the virtual effects of particles that couple to the Higgs field alter the Higgs boson squared mass as follows:

$$m_H^2 = 2\lambda v^2 - \Delta m_H^2. \tag{2.8}$$

The radiative corrections are illustrated in Figure 2.7 for both a fermion and boson loop. Taking the fermion loop diagram, which will be dominated by the top quark due to its strong coupling with the Higgs field given its large mass, the coupling to fermions of the form $-\lambda_f \bar{\psi}\phi\psi$ results in corrections to the Higgs boson squared mass of [57]:

$$\Delta m_H^2 = -\frac{|\lambda_f^2|}{8\pi^2}\Lambda^2 + ... \tag{2.9}$$

The issue here is that Λ can be as high as the Planck scale where these quantum corrections become enormously large and must be finely balanced to give cancellation that would result in a light Higgs boson. This amount of fine-tuning is considered unnatural in the SM [58].

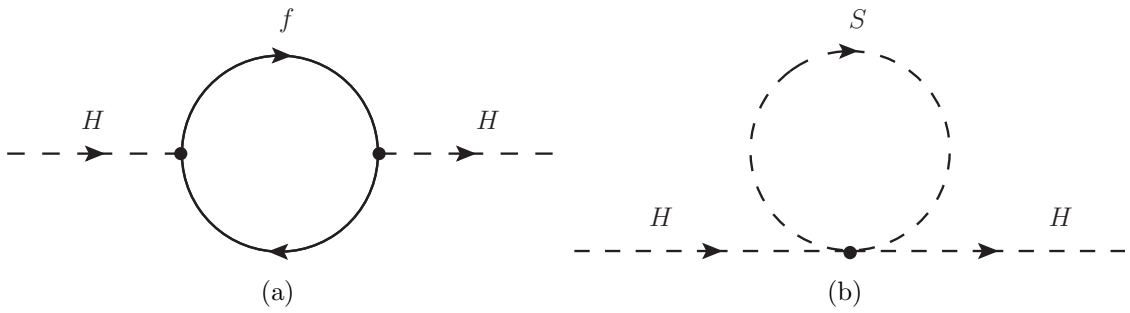

Figure 2.7: Feynman diagrams of the one-loop radiative corrections to the Higgs boson mass for (a) a fermion f and (b) a scalar boson S.

There are many BSM theories that offer a solution to this hierarchy problem. One of the favoured theories is called Supersymmetry (SUSY) in which a new symmetry between fermions and bosons is introduced giving rise to supersymmetric partner particles [31]. Each of the SM fermions receives a boson superpartner and each of the SM bosons receives a fermion superpartner, each differing by half a unit of spin. This feature can be used to cancel the divergences arising from the Δm_H^2 terms by exploiting the fact that the additional loop corrections contribute with opposite signs. If SUSY were an unbroken symmetry the masses of the superpartners would be identical to their SM partner. The fact that these superpartners have not yet been observed implies that SUSY must be a broken symmetry in which the masses of the superpartners are larger than their SM counterparts. There are motivations

to suggest that the SUSY scale should not be much larger than $\mathcal{O}(1\,\text{TeV})$ to avoid additional fine-tuning [59].

2.5 MSSM Higgs Sector

The Minimal Supersymmetric Standard Model (MSSM) is the simplest addition of SUSY to the SM [60]. A couple of the principal motivations for the MSSM as an extension of the SM are that it allows for gauge coupling unification and that providing R-parity is conserved the Lightest Supersymmetric Particle (LSP) makes a good dark matter candidate. The R-parity quantum numbers are $+1$ for SM particles and -1 for their supersymmetric partners. It is required to be conserved in order to explain the stability of the proton [31]. The MSSM introduces two complex Higgs doublets ϕ_u and ϕ_d to provide masses for up- and down-type fermions via spontaneous symmetry breaking. Assuming that the MSSM Lagrangian does not contain new sources of CP violation, this leads to the existence of five Higgs bosons: one CP-odd neutral pseudoscalar A, two CP-even neutral scalars h and H, and two charged $H^{\pm}$ particles [61]. Here, the neutral scalar h is taken to be lighter than the H boson[1].

There are only two additional parameters required to describe the MSSM Higgs sector with respect to the SM at tree-level. A common choice for these are the mass of the CP-odd Higgs boson m_A and the ratio of the vacuum expectation values of the two Higgs doublet fields:

$$\tan\beta = \frac{v_u}{v_d}, \tag{2.10}$$

where the value for $\tan\beta$ is expected to lie in the range $1 < \tan\beta < 60$ [62]. Beyond the lowest order the MSSM Higgs sector depends on further parameters, which are fixed at specific values in various MSSM benchmark scenarios.

At tree-level, the masses of the Higgs bosons and their mixing can be expressed in

[1] This convention is followed throughout the rest of this thesis

terms of the gauge boson masses m_W and m_Z plus the two additional parameters:

$$m^2_{H^\pm} = m^2_A + m^2_W, \tag{2.11}$$

$$m^2_{h,H} = \frac{1}{2}\left(m^2_A + m^2_Z \mp \sqrt{(m^2_A + m^2_Z)^2 - 4m^2_Z m^2_A \cos^2 2\beta}\right). \tag{2.12}$$

The dependence of the Higgs boson masses on the value of m_A is illustrated in Figure 2.8 for two different values of $\tan\beta$. In the decoupling limit where $m_A \gg m_Z$ the mixing angle between the CP-even states simplifies to $\alpha \approx \beta - \pi/2$. In this limit all the heavier Higgs particles decouple from the SM spectrum and only the lightest neural scalar h remains with SM-like properties. The tree-level mass of the light neutral scalar h becomes approximately constant. Figure 2.8 also demonstrates how for larger values of $\tan\beta$ the decoupling behaviour is very sudden as m_A reaches m_Z, whereas for lower values of $\tan\beta$ this onset is delayed.

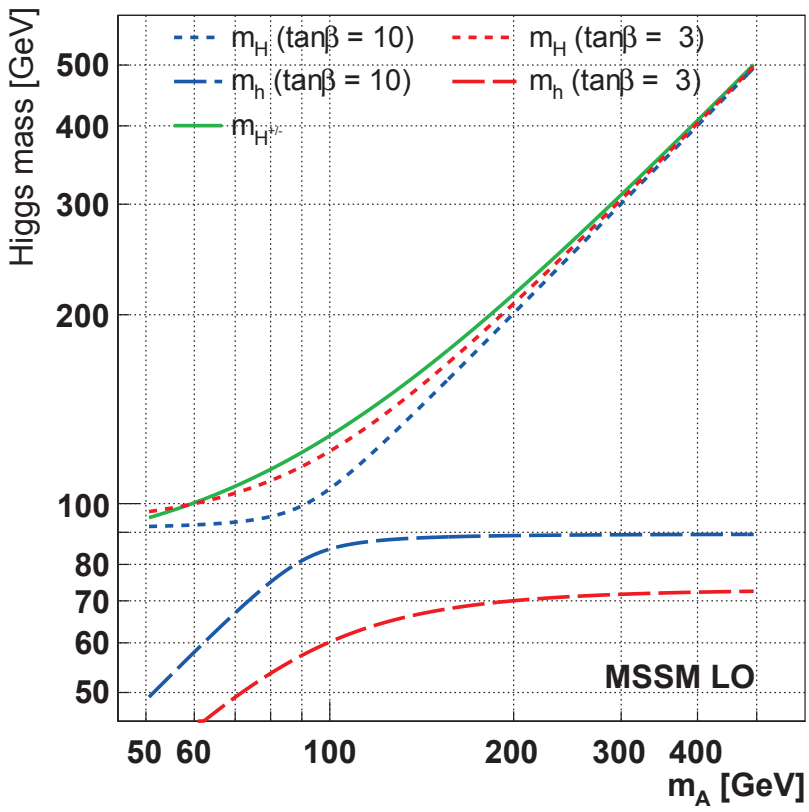

Figure 2.8: Masses of the h, H and $H^\pm$ bosons at tree-level in the MSSM as a function of the pseudoscalar mass m_A, for two different values of $\tan\beta$ [63].

The tree-level prediction for the mass of the lightest CP-even Higgs boson has a upper bound given by:

$$m_h \leq m_Z |\cos 2\beta|, \tag{2.13}$$

suggesting that m_h cannot exceed the mass of the Z boson. This appears to contradict the mass of the observed Higgs boson of 125 GeV, however the mass of the lightest Higgs is subject to large quantum corrections. The dominant contributions arise from the one-loop effects of the top quark and its scalar superpartner the top squark (stop). The incomplete cancellations of such effects can push the maximum value of m_h up to around 135 GeV [61]. The newly discovered boson is usually interpreted as the light neutral scalar h in the MSSM and is treated as a constraint on the unknown SUSY parameters, where the theoretical uncertainty on the determination of the h mass in the MSSM is approximately 3 GeV [64]

It is possible to probe the MSSM with more precise measurements of the properties of the observed Higgs boson to identify small deviations from the SM predictions. An additional approach is to pursue direct searches for the heavier A, H and $H^{\pm}$ states.

2.5.1 MSSM at Low $\tan\beta$

Common to a number of MSSM scenarios is that although the mass of the lighter neutral scalar Higgs bosons remains consistent with 125 GeV over a large region of phase space, the value of m_h generally becomes too light at very low values of $\tan\beta$ [64]. Searches at the LHC for neutral Higgs bosons in the MSSM have already excluded large regions of phase space at high values of $\tan\beta$ [65, 66]. As a result, there is increased interest in analyses capable of probing the low $\tan\beta$ region.

The low $\tan\beta$ region was originally excluded by searches performed at LEP [67], however it is possible to reopen the investigation of this region in the following discussion. The Higgs boson observation at 125 GeV suggests that the magnitude of the SUSY scale M_{SUSY} is rather high in the MSSM as this mass value is close to the

predicted upper limit for m_h [62]. This fact is also supported by the absence of any SUSY particles in direct searches performed at the LHC to date. The low $\tan\beta$ region can be reopened if the value of M_{SUSY} is allowed to be higher than 1 TeV [68]. In order to avoid significant fine tuning, the value of M_{SUSY} is typically expected to be lower than around 3 TeV in the MSSM, otherwise the h mass becomes too low to be consistent with the observed value [59]. However, given that the allowed amount of fine-tuning in a model is somewhat subjective, these types of scenarios are receiving more attention.

Figure 2.9 illustrates how the value of M_{SUSY} depends on the value of $\tan\beta$ for a range of fixed m_h values close to 126 GeV in the decoupling limit. One can see how M_{SUSY} starts to rapidly increase for particular values of m_h as low $\tan\beta$ values are approached. It is possible to accommodate acceptable values for m_h close to $\tan\beta$ as low as 1 providing that M_{SUSY} is within the range of between 100–10 000 TeV. However, for slightly larger values of $\tan\beta$ within approximately 2–5 it is possible to achieve the required mass range for M_{SUSY} values of only a few TeV.

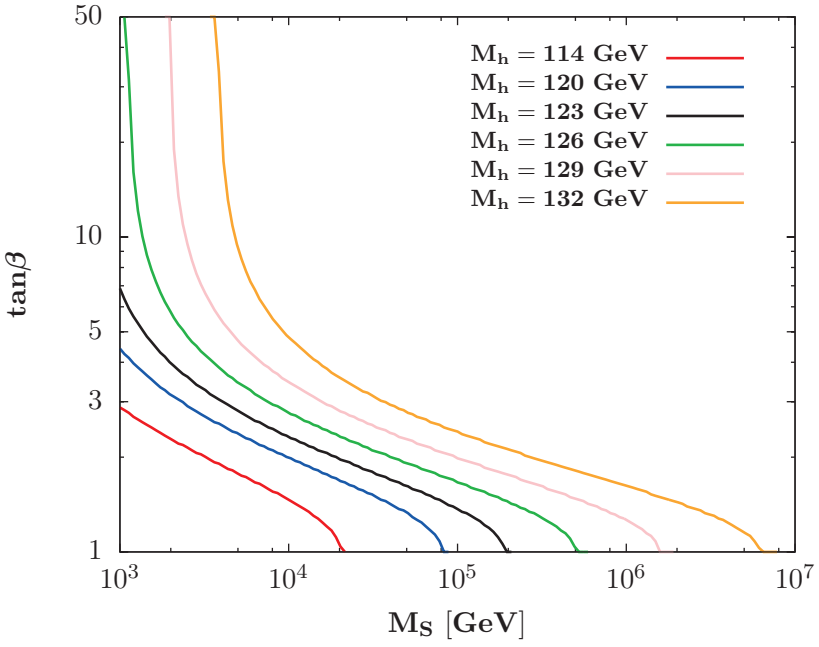

Figure 2.9: Contours for fixed values of m_h around 125 GeV in the (M_{SUSY}, $\tan\beta$) plane in the decoupling limit $M_A \gg M_Z$ [68].

In this low $\tan\beta$ scenario the production and decay of the heavier Higgs bosons has a rich phenomenology. Figure 2.10 shows the production cross sections of the heavier Higgs bosons for processes relevant at the LHC with a centre-of-mass energy of $\sqrt{s} = 8\,\text{TeV}$. In this case $\tan\beta = 2.5$ is assumed and the radiative corrections are made to give a fixed values of $m_h = 126\,\text{GeV}$. The gluon fusion process is found to dominate over the b-associated production mechanisms.

Figure 2.11 shows the branching ratios for the A, H and $H^{\pm}$ decays as functions of their masses for the same case. For the heavier CP-even H there are significant branching ratios for decays to massive gauge bosons $H \to WW/ZZ$ and Higgs bosons $H \to hh$, below the threshold for the decay to a top quark pair. In the mass region $2m_h < m_H < 2m_t$ the branching ratio for the $H \to hh$ decay is enhanced.

The decay branching ratios of the light CP-even h are shown in Figure 2.12 with respect to the SM values. The figure shows the main search channels currently pursued at the LHC that include the decays $h \to b\bar{b}$, $\tau\tau$, $\gamma\gamma$, ZZ and WW. The branching ratios can differ significantly from the SM prediction at low values of m_A, but gradually begin to approach the SM as m_A increases towards infinity.

Chapter 8 and Chapter 9 present the searches for four different channels of the $H \to hh$ decay by ATLAS and the combined search results are interpreted in the context of the two following low $\tan\beta$ scenarios.

The hMSSM Scenario

The hMSSM scenario [69, 70] assumes that the light CP-even h is the observed Higgs boson and fixes its mass to 125 GeV throughout the phase space. To some extent this scenario may be considered "model independent" as the Higgs boson properties do not depend explicitly on the details of the SUSY sector. It makes certain assumptions about the mass matrix of the CP-even Higgs boson states and their radiative corrections. It also considers that the masses of SUSY particles are sufficiently large in order to avoid detection at the LHC and so many of their effects

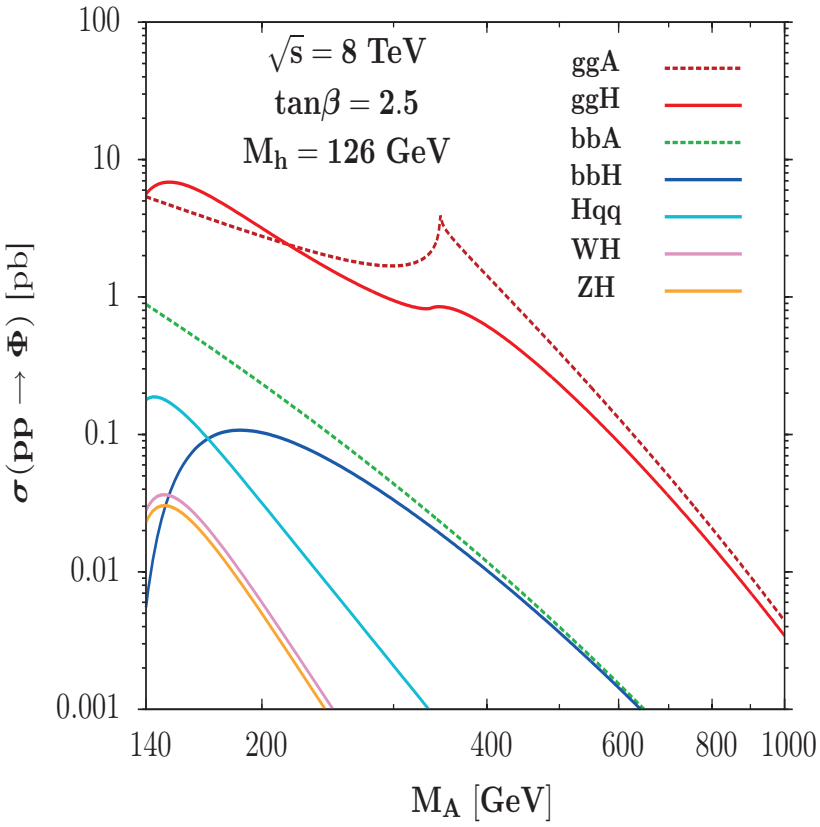

Figure 2.10: Production cross sections of the heavier MSSM Higgs bosons at $\sqrt{s} = 8\,\text{TeV}$ as a function of m_A assuming $\tan\beta = 2.5$. Radiative corrections have been made such that $m_h = 126\,\text{GeV}$. Taken from [68].

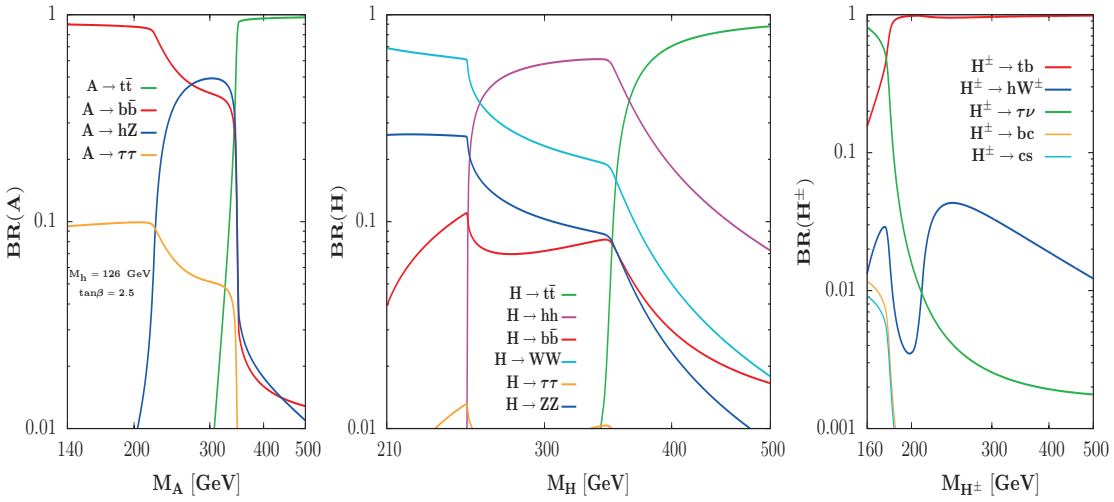

Figure 2.11: Branching ratios for the heavier MSSM Higgs bosons A (left), H (centre) and $H^\pm$ (right) assuming $\tan\beta = 2.5$ as a function of their masses. Radiative corrections have been made such that $m_h = 126\,\text{GeV}$. Taken from [68].

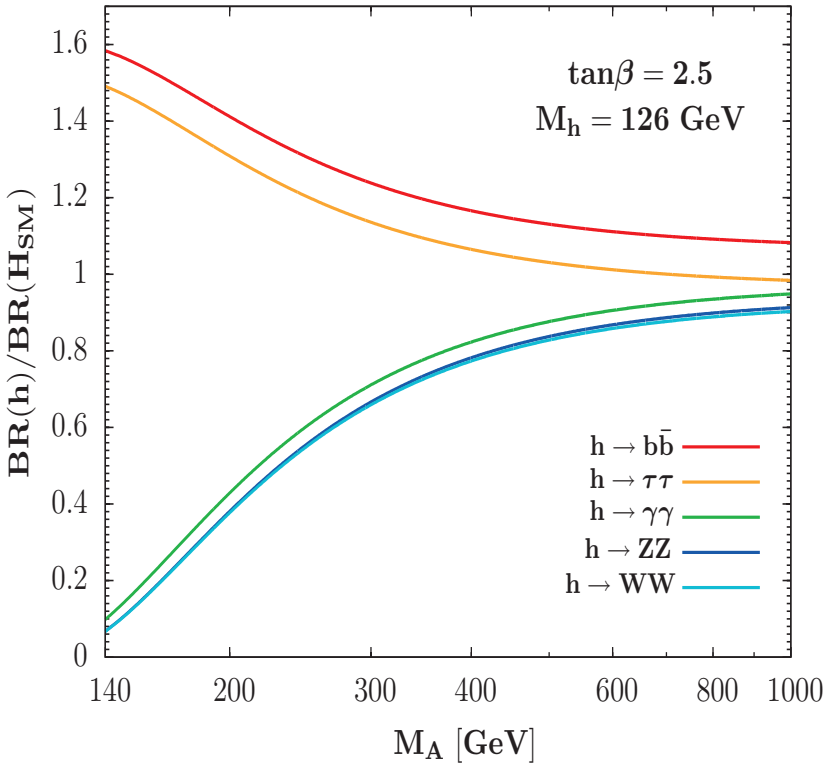

Figure 2.12: Branching ratios for the h boson in the MSSM with respect to the SM values as a function of m_A assuming $\tan\beta = 2.5$. Radiative corrections have been made such that $m_h = 126\,\text{GeV}$. Taken from [68].

on the Higgs sector can be neglected. The theory is well defined providing that the mass of the CP-odd Higgs boson is above a minimum value such that a fixed value of m_h can be maintained. However, it can be reasoned that this region where the theory breaks down is already excluded by experimental measurements [70]. Figure 2.13a shows the branching ratio for $H \to hh$ in the hMSSM scenario.

The low-$\tan\beta$-high Scenario

The approach followed in the low-$\tan\beta$-high MSSM scenario [63] differs by making explicit choices for the SUSY-breaking parameters to obtain an approximate mass of 125 GeV for the light Higgs boson in much of the phase space. The scale of M_{SUSY} varies between a few TeV at high m_A or $\tan\beta$ up to 100 TeV at low m_A or $\tan\beta$ in order to keep the value of m_h in the desired range. In the region of $\tan\beta < 3$ the

value steadily increases from approximately 122 GeV at $m_A \sim 250$ GeV to 125 GeV as m_A approaches infinity. Figure 2.13b shows the branching ratio for $H \to hh$ in the low-tan β-high scenario.

The plots show that in this low tan β regime the branching ratios for $H \to hh$ can be greater than 50% for tan $\beta < 4$ for values of m_A between the kinematic threshold for the decay to a light-scalar pair and the threshold for the decay to a top quark pair. The branching ratios for $H \to hh$ in each of the scenarios are qualitatively very similar in m_A and tan β, but with the low-tan β-high scenario reaching larger values.

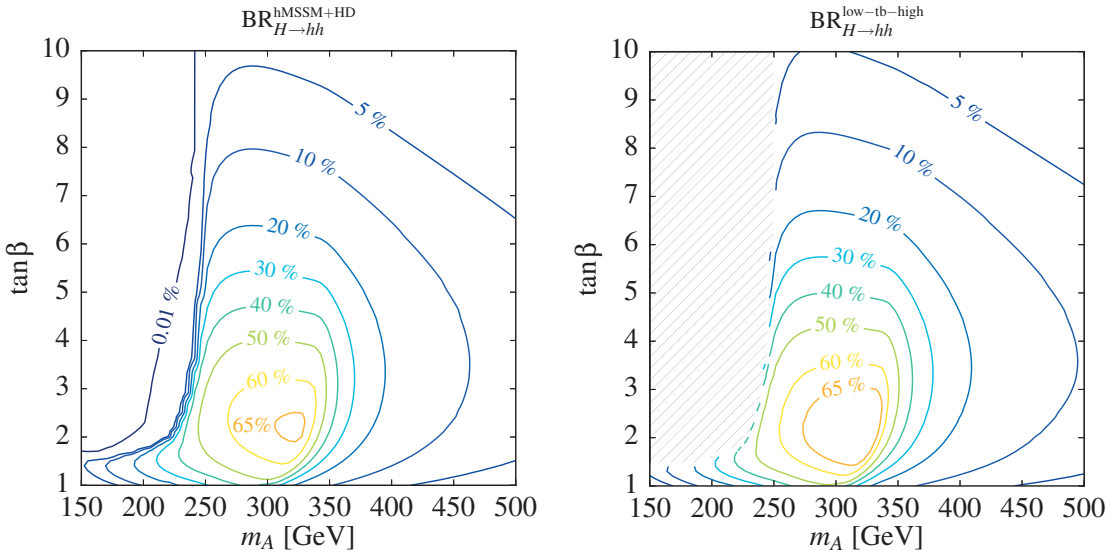

(a) (b)

Figure 2.13: Branching ratios for the decay $H \to hh$ as computed in (a) the hMSSM scenario and (b) the low-tan β-high scenario in the plane of (m_A, tan β) [63]. The hatched region in (b) is where the $H \to hh$ decay is below threshold and the small width to off-shell scalars is not computed.

CHAPTER 3

THE LARGE HADRON COLLIDER

The European Organisation for Nuclear Research (CERN) is an international organisation founded in September 1954 that operates the largest particle physics laboratory in the world. It has performed a significant part in the development of fundamental physics that includes the discovery of the W and Z bosons in 1983 [71], the determination of the number of light neutrino families in 1989 [72], and the first creation of anti-hydrogen atoms in 1995 [73]. It is also credited as the birth place of the World Wide Web.

The laboratory employs around 2500 full-time staff members and has over 10000 visiting scientists from more than 600 universities and research facilities around the world. The accelerator complex is located in the landscape between the Jura mountains and Geneva airport, as shown in the aerial photograph in Figure 3.1. It is also the site of the LHC [74], which is the world's largest and highest energy pp and heavy ion synchrotron collider.

Figure 3.1: Aerial view photograph of CERN with the paths of the accelerator rings superimposed. ©CERN.

3.1 CERN Accelerator Complex

The CERN accelerator complex is the result of the requirements of a long history of experiments and provides particle beams of various types to a number of different experimental areas, represented by the schematic in Figure 3.2. To provide the high energy particle beams for the LHC a complex chain of particle accelerators is required, where each machine in the chain further increases the energy of particle beams. This process of filling the LHC and the machines involved are described in this section.

There are two operational linear accelerators at CERN that are the starting points of protons and lead ions for the LHC. A third linear accelerator is currently under construction and will eventually replace Linac 2 as the starting point for protons in 2020. The proton source is a bottle of hydrogen gas that is ionised using an electric field before entering the accelerator. The protons are accelerated by Linac 2 through alternately charged cylindrical conductors, powered by Radio Frequency (RF) cavi-

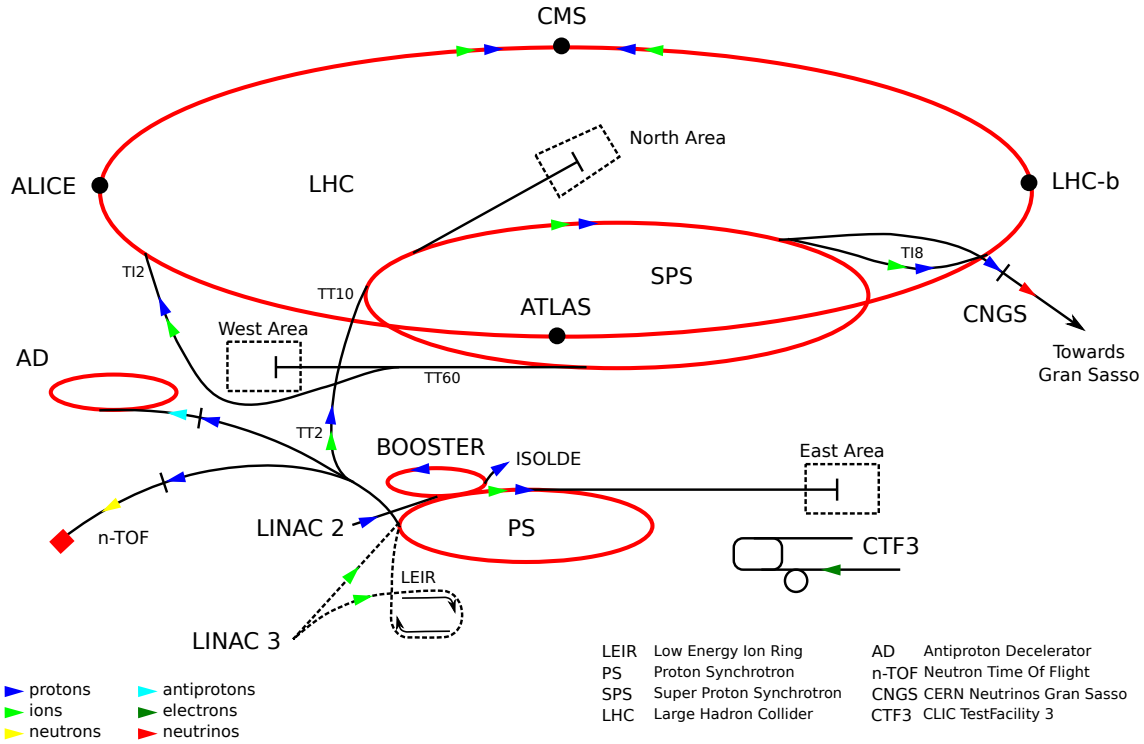

Figure 3.2: Schematic diagram of the CERN accelerator complex. Derived from [75].

ties, to an energy of 50 MeV. These protons are injected into the Proton Synchrotron Booster (PSB), where they are collated and bunched in the four vertically stacked synchrotron rings and accelerated up to 1.69 GeV for injection into the Proton Synchrotron (PS). Linac 3 has been in operation since 1994 and since 2006 it has been used to inject lead ions into the Low Energy Ion Ring (LEIR), where they are bunched and accelerated to 72 MeV before being passed to the PS.

The PS has operated since 1959 and was CERN's first synchrotron accelerator. It has a circumference of 628 m and is used to accelerate protons delivered by the PSB or heavy ions from the LEIR up to 26 GeV for injection into the Super Proton Synchrotron (SPS). The SPS started operation in 1976 and is the second-largest machine at CERN, with a circumference of 7 km. In the past it had been operated as a proton-antiproton collider and an accelerator of electrons and positrons for injection to the LEP collider. It is now predominately used to provide beams of protons and lead ions for the LHC at injection energies of 450 GeV and 177 GeV, respectively. Both of these synchrotrons use conventional electromagnets that operate at room-

temperature, including dipole magnets used to bend the beams round the rings.

The LHC occupies an underground tunnel previously constructed for the LEP collider that has a circumference of 26.7 km and lies at depth that varies between 45–170 m below the surface, on an inclined plane of 1.4% slope. It is octagonal in shape with eight straight sections and eight curved sections, as shown in Figure 3.3. To bend the beam around its eight arched sections 1232 superconducting dipole magnets are required to operate at a cryogenic liquid helium temperature of 1.9 K and can sustain a current of 11.9 kA that generates an 8.3 T magnetic field in the niobium-titanium (Nb-Ti) type II superconducting windings. Each LHC dipole is 14.3 m long and incorporates both beam pipes within a common cryostat design, due to space restrictions of the tunnel. Additionally the LHC requires 392 arc quadrupole magnets for beam focusing and the remaining magnets are primarily used for orbit correction and during beam injection and dump.

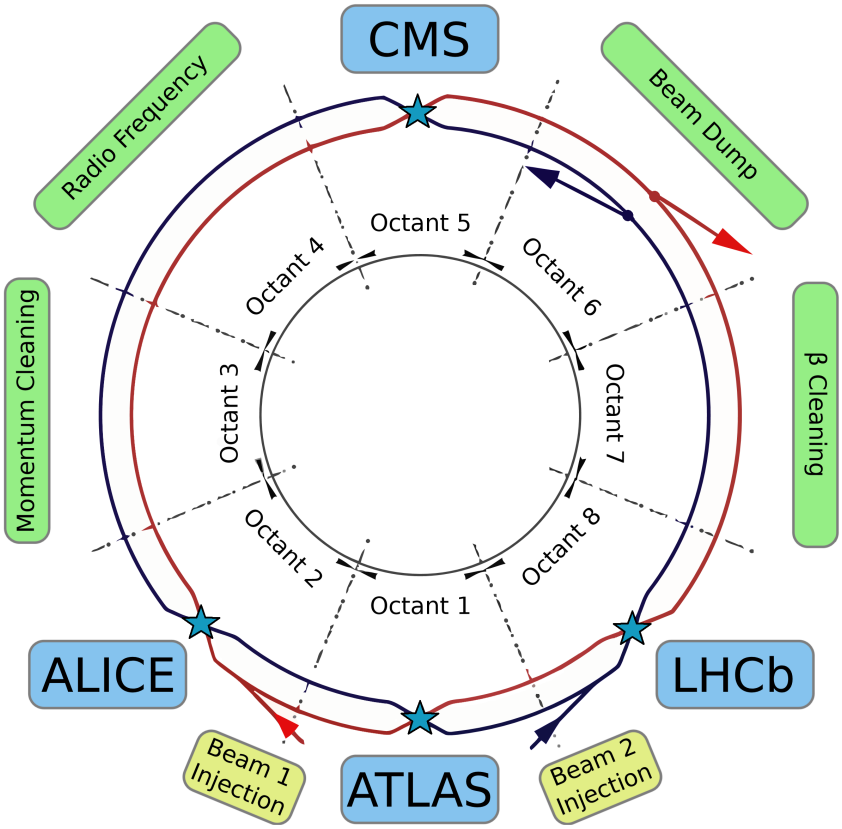

Figure 3.3: Schematic diagram of the LHC ring segments. Derived from [74].

At each of the eight straight sections in the LHC ring is either an experimental location or utility insertion. The clockwise rotating beam is injected near Point 2 and the anticlockwise rotating beam is injected near Point 8. These are also the locations of two of the experimental caverns, with the other two located at Point 1 and Point 5. The beam dumps are located at Point 6 and allow for the safe extraction of the beams at the instant of a failure in the system or at the end of the beams' useful lifetime. A system of kicker magnets must each ramp to 0.43 T m during the *abort gap* and maintain this field long enough to safely eject the beam in one full revolution. The LHC is operated at a cavity RF of just over 400 MHz that introduces a total of 35640 RF buckets spaced around the ring. The RF systems are located at Point 4 on the ring. There are a total of eight 2 MV superconducting RF cavities per beam at the LHC that provide an acceleration gradient of 485 keV/turn during the 20 minute ramping phase. There are also two regions on the LHC ring where the beam is cleaned using collimators designed to absorb the beam halo and protect the accelerator elements and experiments from beam loss. Momentum cleaning occurs at Point 3 and betatron cleaning takes place at Point 7 on the ring.

Every one in ten of the LHC RF buckets may hold a particle bunch and is assigned a Bunch Crossing Identification (BCID) number from 0 to 3563. Each of the LHC beams must be filled in a number of stages due to the smaller circumferences of the preceding accelerators. One fill of the PS defines the nominal bunch train in the LHC of 72 bunches in length, either consecutively or alternately filled in the case of 25 ns or 50 ns operation, respectively. The remaining 12 bunches in the PS are required to be empty to allow sufficient time for the kicker magnets to ramp when injecting from the PS to the SPS. The SPS can accumulate up to four of these bunch trains where each is separated by eight empty bunches (short gaps). These bunch trains are then injected into one of the LHC beams. Typically it takes 11 or 12 fills of the SPS to fill a LHC beam where 36 empty bunches are reserved (long gap) between each fill. The remaining empty bunches in the LHC form the abort gap. The exact filling scheme can depend on a number of factors that include the bunch spacing as well as performance considerations.

3.2 LHC Experiments

There are four major experiments at the LHC:

- A Toroidal LHC ApparatuS (ATLAS) [76] and Compact Muon Solenoid (CMS) [77] are both large general-purpose experiments which share many of the same physics goals and have complementary detector designs. The ATLAS experiment is described in detail in Chapter 4. The CMS detector has a compact design where tracking and calorimetry are encased within a single large solenoid magnet and surrounded by alternating layers of muon chambers and iron return yoke.

- A Large Ion Collider Experiment (ALICE) [78] is an experiment optimised to study the collisions of lead ions at the LHC to better understand the physics of strongly interacting matter and a state of matter at high temperature and densities called a quark-gluon plasma, replicating the conditions of the early universe.

- LHC beauty (LHCb) [79] is an experiment dedicated to precision measurements of the parameters of CP violation in the interactions and rare decays of b-hadrons. These studies aim to help explain the matter-antimatter asymmetry of the Universe.

The other smaller experiments at the LHC include TOTEM [80], an experiment designed to measure the total cross-section, elastic scattering and diffractive dissociation at the LHC, which has detectors installed either side of the CMS experiment at Point 5. The LHC forward (LHCf) [81] experiment is specially designed to study energetic π^0 particles generated in the forward region of the ATLAS experiment at Point 1 and aims to give insight into the origin of ultra-high-energy cosmic rays. The primary goal of the Monopole and Exotics Detector At the LHC (MoEDAL) experiment [82] is to perform a direct search for the magnetic monopole and other highly ionising stable massive particles and shares the cavern at Point 8 with LHCb.

3.3 LHC Upgrade Schedule

The planned schedule for the LHC accelerator complex upgrade program is shown in Figure 3.4 according to the Mid-Term Plan (MTP) presented at the CERN Council session in June 2015 [83]. The Run 1 *pp* data set includes data collected during 2011 and 2012 with a 50 ns bunch spacing. In this time the LHC reached approximately 75% of its nominal design luminosity and delivered an integrated luminosity of approximately $30\,\text{fb}^{-1}$. The LHC ceased operation in early 2013 after a period of lead-proton collisions for Long Shutdown 1 (LS1), to allow for major machine upgrades to take place to prepare it to run at its nominal configuration. An number of upgrades were also made to ATLAS during this time. The LHC restarted for Run 2 in 2015 at a centre-of-mass energy of $\sqrt{s} = 13\,\text{TeV}$ and initially a bunch spacing of 50 ns that was later changed to 25 ns.

The further accelerator and detector upgrades are expected to be progressively installed during the next two major shutdowns. During Long Shutdown 2 (LS2) ATLAS will commence its Phase 1 upgrade program [85]. Run 3 is expected to start in 2021 and continue until the end of 2023, by which point it is hoped an integrated luminosity of $300\,\text{fb}^{-1}$ will have been delivered. It will be followed by Long Shutdown 3 (LS3), which will see the final commissioning and integration of the Phase 2 upgrades that are currently being reviewed for Run 4 [86]. It also includes the installation of the High Luminosity LHC (HL-LHC). The intention thereafter is to run three years of operation separated by one year of shutdown during the HL-LHC program, accumulating a total of around $3000\,\text{fb}^{-1}$ and obtaining a maximum luminosity of $7.5 \times 10^{34}\,\text{cm}^{-2}\,\text{s}^{-1}$. Note that the schedule presented may be revised by the LHC Committee (LHCC) at a later date.

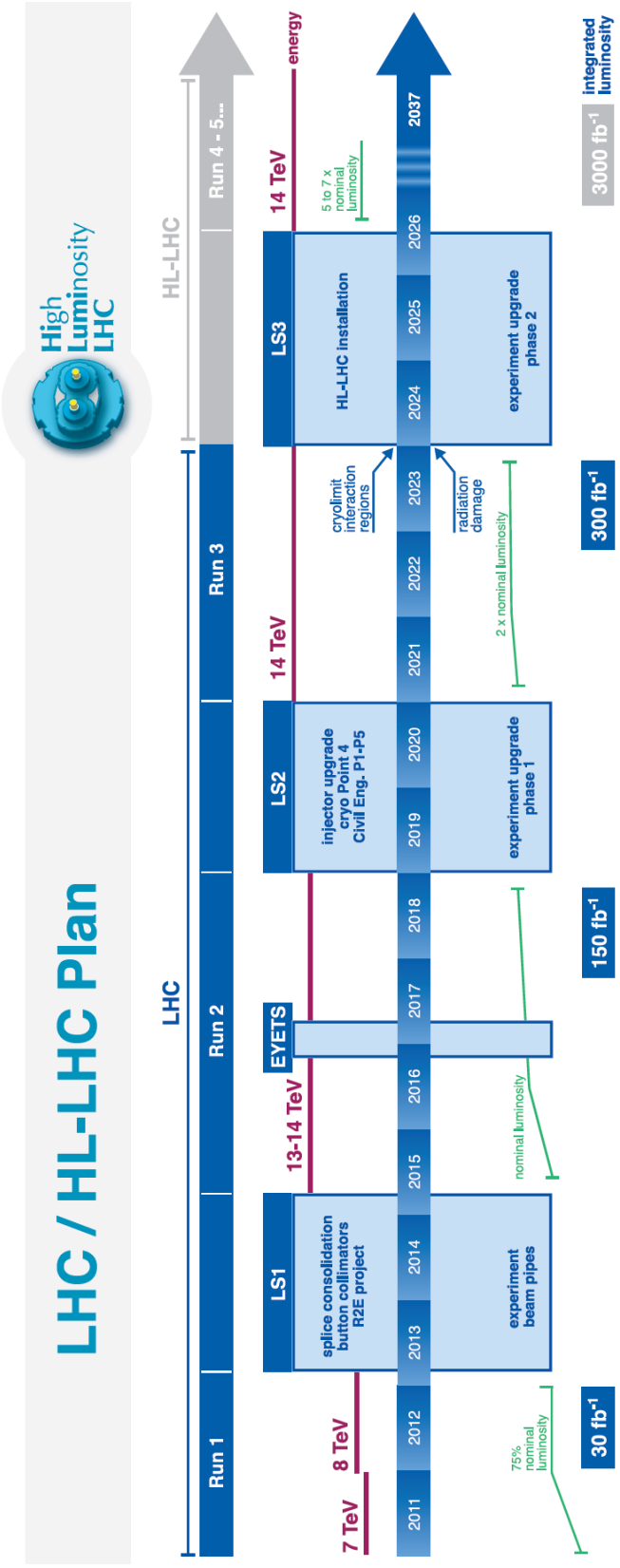

Figure 3.4: The planned LHC upgrade schedule according to the MTP that includes the proposed HL-LHC program. Taken from [84].

CHAPTER 4

THE ATLAS DETECTOR

A Toroidal LHC ApparatuS (ATLAS) (Figure 4.1) is located at Point 1 of the LHC ring and is by volume the largest detector ever installed at a collider facility. It is approximately 44 m in length, 25 m in diameter and weighs about 7000 tonnes. The detector is forward-backward symmetric with respect to the interaction point and covers almost entirely a 4π solid angle. The general layout of the detector comprises a central barrel region constructed of many sensitive concentric layers, sandwiched between two endcap regions. This highly hermetic design is essential to infer the presence of neutrinos, which pass through undetected and must be identified by measuring a momentum imbalance within a bunch crossing. The main detector subsystems include an inner detector for the precise tracking of charged particles, calorimeters to measure the energy of easily stopped particles and a muon system to make secondary measurements of highly penetrating muons. This chapter introduces many of the technical aspects of the ATLAS experiment, where much of this is described at length in the ATLAS Technical Design Report (TDR) [87].

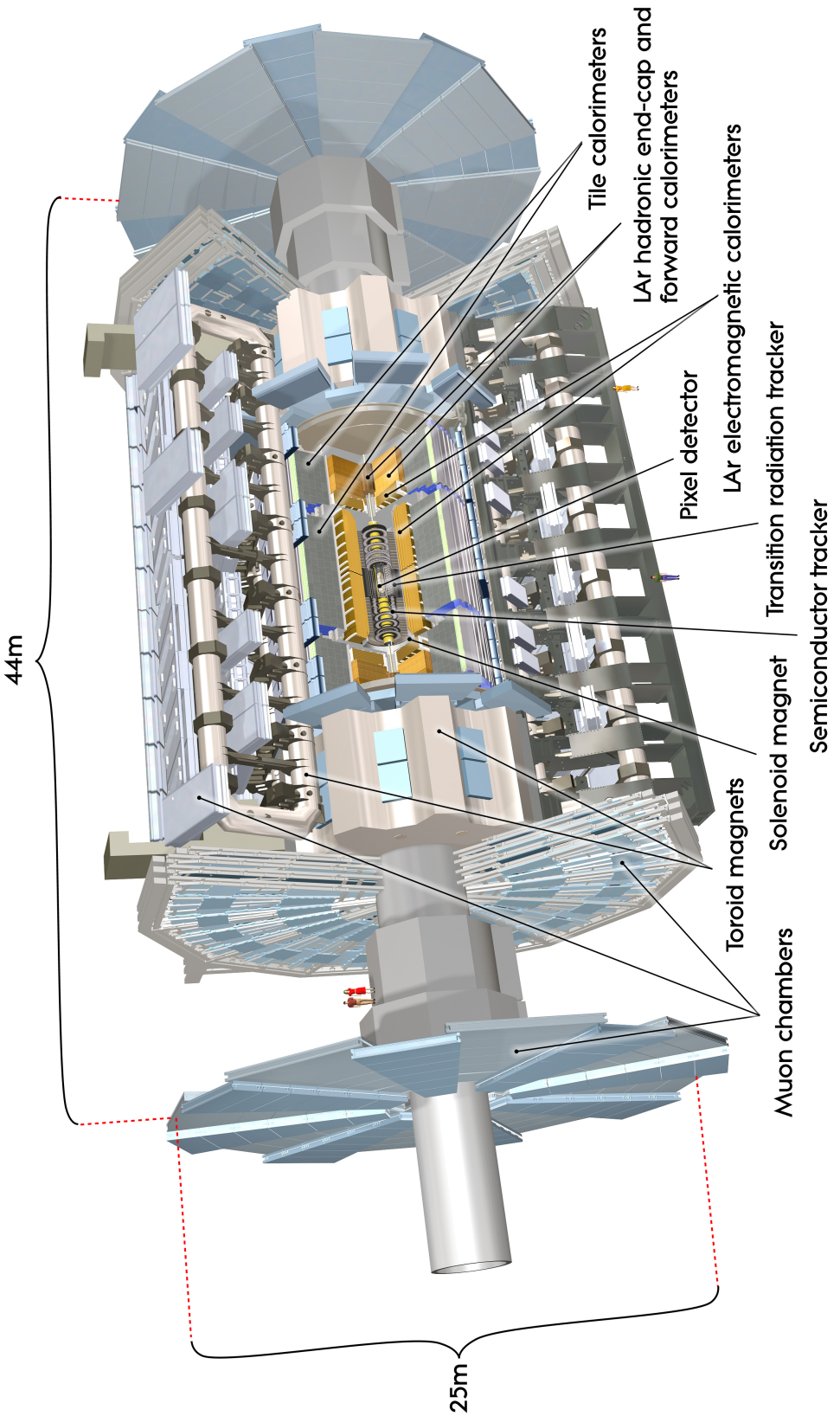

Figure 4.1: Cut-away view of the ATLAS detector. ©CERN.

4.1 Coordinate System

The spatial coordinate system of ATLAS takes the nominal interaction point at the centre of the detector as its origin. It uses a right handed Cartesian coordinate system in which the positive z-axis points in the anticlockwise beam direction and the positive x and y-axes point towards the LHC ring centre and vertically upward, respectively. It is also common to refer to the positive and negative z-sides of the detector as side-A and side-C, respectively. In terms of cylindrical polar coordinates: R is defined as $\sqrt{x^2 + y^2}$, the azimuthal angle around the beam axis is labelled ϕ and the polar angle taken relative to the beam axis is labelled θ.

It's useful to describe particle trajectories at hadron colliders in terms of rapidity:

$$y = \frac{1}{2} \ln \left| \frac{E + p_z}{E - p_z} \right|, \tag{4.1}$$

where E and p_z are the particle's energy and longitudinal momentum, respectively. For highly relativistic particles it can be assumed that a particle is massless and Equation (4.1) approximates to pseudorapidity, defined as:

$$\eta = -\ln \tan \left(\frac{\theta}{2} \right). \tag{4.2}$$

Due to the parton nature of hadrons, collisions are typically boosted in the z-direction even with symmetric beam energies. However the difference in the pseudorapidity of two particles is independent of Lorentz boost along the beam axis and so particle production is approximately constant with unit pseudorapidity. The angular separation ΔR between two objects in η-ϕ space is defined as $\Delta R = \sqrt{\Delta\eta^2 + \Delta\phi^2}$.

The fact that the momenta of incoming partons are not known in hadron colliders makes it impossible to exploit longitudinal momentum conservation, as well as the fact that too much of the momenta disappears down the beam pipe. However, the initial momentum in the transverse direction is known to be zero and therefore momentum conservation can be applied in the transverse plane. It is therefore

typical to use quantities such as transverse momentum (p_{T}), transverse energy (E_{T}), total transverse energy ($\sum E_{\mathrm{T}}$) and missing transverse energy ($E_{\mathrm{T}}^{\mathrm{miss}}$).

4.2 Magnet System

ATLAS operates a combination of two magnetic systems that provide the large magnetic flux required to bend the trajectories of charged particles so that their momenta can be measured. The Inner Detector (ID) is surrounded by a superconducting solenoid magnet that produces a 2 T axial field at a nominal current of 7.7 kA. The design has been optimised to keep the material thickness in front of the calorimeter as low as possible. This is achieved by having a thickness of only 10 cm that contributes only 0.66 radiation lengths[1] (X_0) and sharing a common vacuum vessel with the Liquid Argon Calorimeter (LAr). The magnetic flux is returned via the steel of the Tile calorimeter and its support structure.

Three large air-core toroids are used to generate a B-field for the muon chambers located in and around the toroidal structure. The barrel toroid consists of eight individual 'racetrack-shaped' vacuum vessels supported by rings of inner and outer struts, which provide much of the mechanical support structure for ATLAS. The endcap toroids are constructed from a single cold mass bolted and glued to form a rigid structure and inserted into their own cryostats. The bending power is maximised by positioning the two endcap toroids within the ends of the main barrel toroids, such that their coils are at 22.5° with respect to each other. When operational the total stored energy in the toroid system is 1.6 GJ, producing a non-uniform magnetic field which varies between 0.2 and 3.5 T.

[1] The characteristic length for electromagnetic interactions in material

4.3 Inner Detector

The ID is the closest detector system to the interaction point and features three independent tracking systems with an inner system of high-resolution detectors and an outer system of continuous tracking elements. They must provide excellent momentum resolution and measurement of the primary interaction vertex as well as secondary decay vertices associated with relatively long-lived particles such as b-hadrons. These systems must operate robustly under the high radiation environment and are capable of identifying particles with transverse momentum down to 100 MeV in the innermost layers. The ID provides tracking up to $|\eta| < 2.5$, with electron identification over $|\eta| < 2.0$ and for a wide range of energies between 0.5 and 150 GeV. A cut-away view of the ID showing the various detector components is given in Figure 4.2.

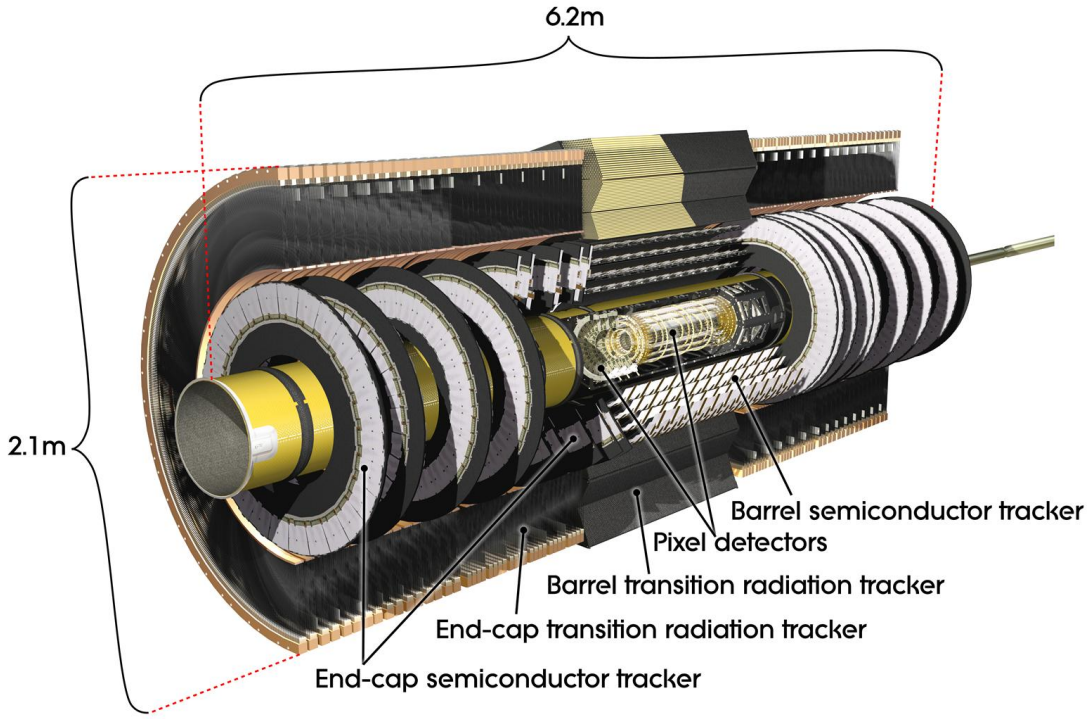

Figure 4.2: Cut-away view of the ATLAS inner detector. ©CERN.

4.3.1 Pixel Detector

The pixel detector is the innermost tracking detector. The sensors are 250 µm thick n-type silicon wafers, highly oxygenated to increase radiation tolerance, with readout pixels mounted on the n^+-implanted side. There are a total of 1744 pixel sensor boards forming the three layers of the detector, with each sensor board containing 47232 pixels. This makes the pixel detector the highest granularity detector in ATLAS with more than 80 million readout channels. The pixel cells are of nominal size 50×400 µm and segmented in R-ϕ and z.

4.3.2 Semiconductor Tracker

The Semi-Conductor Tracker (SCT) forms four cylindrical double layers of precision tracking around the pixel detector. To reduce costs and ensure operational reliability the SCT uses a more common single-sided p-in-n silicon design. The rectangular barrel modules are constructed from two 6 cm long sensors with a strip pitch of 80 µm and daisy-chained together. In the endcap region trapezoidal sensors are run radially in wheels, with strips of constant azimuth and a mean pitch of 80 µm. The SCT modules use two layers of micro-strip sensors mounted back-to-back with a stereo angle of 40 mrad between them. This arrangement allows limited knowledge of the position along the strip where the hit occurred to be gained. The intrinsic resolution of the barrel modules is 17 µm in R-ϕ and 580 µm in z. The SCT has around 6.3 million readout channels.

4.3.3 Transition Radiation Tracker

The Transition Radiation Tracker (TRT) occupies the outermost part of the ID and consists of gas filled straw tubes that provide tracking information for $|\eta| < 2.0$. It is a high volume and low density detector that produces on average around 36 hits per track. The straws in the barrel are 114 cm in length and are arranged parallel to

the beam axis, while in the endcap region 37 cm long straws are arranged radially in wheels. Each straw tube is 4 mm in diameter and is filled with a 70% Xe, 27% CO_2 and 3% O_2 gas mixture. The straw tubes act as cathodes and contain a gold plated tungsten anode wire. The straws have an intrinsic R-ϕ accuracy of 130 µm. The TRT complements the more accurate silicon components by providing a much larger number of measurements and extending the length over which tracks are measured to improve the momentum resolution.

The straw tubes are also interleaved with material to induce transition radiation to aid in electron identification. Electrons produce significant amounts of transition radiation due to their low mass. This is absorbed by the Xe gas and results in many high-threshold hits, significantly higher in energy than for Minimum Ionising Particles (MIPs). The front-end electronics of the TRT incorporates separate high-pass and low-pass filters that are used to discriminate between tracking signals and transition radiation.

4.4 Calorimetry

The ATLAS calorimeters are designed to absorb the energy of particle showers produced by electrons, photons and hadrons emerging from the interaction point. They consist of a number of sampling detectors, where layers of active sampling medium are alternated with a dense absorber material, which promotes and sustains cascading EM and hadronic showers. Liquid Argon is widely used as the active medium for its homogeneity, intrinsic linear response and radiation hardness.

Contrary to the p_{T} resolution measurement of charged particles from the curvature of their tracks, the calorimeters' energy resolution improves with increasing energy. The fractional energy resolution achieved by a sampling calorimeter can be described by the following expression for a particle of energy E:

$$\frac{\sigma_E}{E} = \frac{a}{\sqrt{E}} \oplus \frac{b}{E} \oplus c. \tag{4.3}$$

Here a is the sampling term used to quantify the statistical and sampling fluctuations in the development of showers within the layers of absorber and active medium. The noise term b includes contributions due to electronics noise and pile-up which dominates the resolution at low energies. The constant term c includes effects such as longitudinal shower leakage and therefore is dependent on total depth of the calorimeter. This sets the performance limit at high energies.

The overall calorimeter detector system is shown in Figure 4.3, which consists of LAr calorimeters surrounded by the hadronic Tile calorimeter. The calorimetry has full ϕ-symmetry and coverage around the beam axis and up to $|\eta| = 4.9$. Figure 4.4 shows schematics of the LAr accordion structure and of a single Tile module.

4.4.1 Electromagnetic Calorimetry

The Electromagnetic Calorimeters (ECals) measure precisely the energy deposited by high-energy electrons and photons. The ECal is a lead-LAr sampling calorimeter with accordion geometry, giving complete symmetry in ϕ and without any azimuthal cracks. The barrel section covers the region up to $|\eta| = 1.475$ and the endcaps between $1.375 < |\eta| < 3.2$, each contained within their own cryostat. Mechanically, the barrel calorimeter is divided into two identical half barrels at $z = 0$, while the endcaps are divided into two coaxial wheels providing an inner and outer coverage.

Figure 4.4a clearly shows the accordion geometry of the ECal and the segmentation into three active sampling depths, where the largest fraction of the shower energy is deposited in the second layer. A separate presampling layer is also used to correct for energy losses within the ID prior to reaching the main calorimetry.

4.4.2 Hadronic Calorimetry

The ATLAS Hadronic Calorimeters (HCals) comprise two different calorimetry systems: a LAr hadronic endcap calorimeter and scintillating tile barrel calorimeters. The Tile calorimeter barrel covers up to $|\eta| < 1.0$ with two extended barrels covering

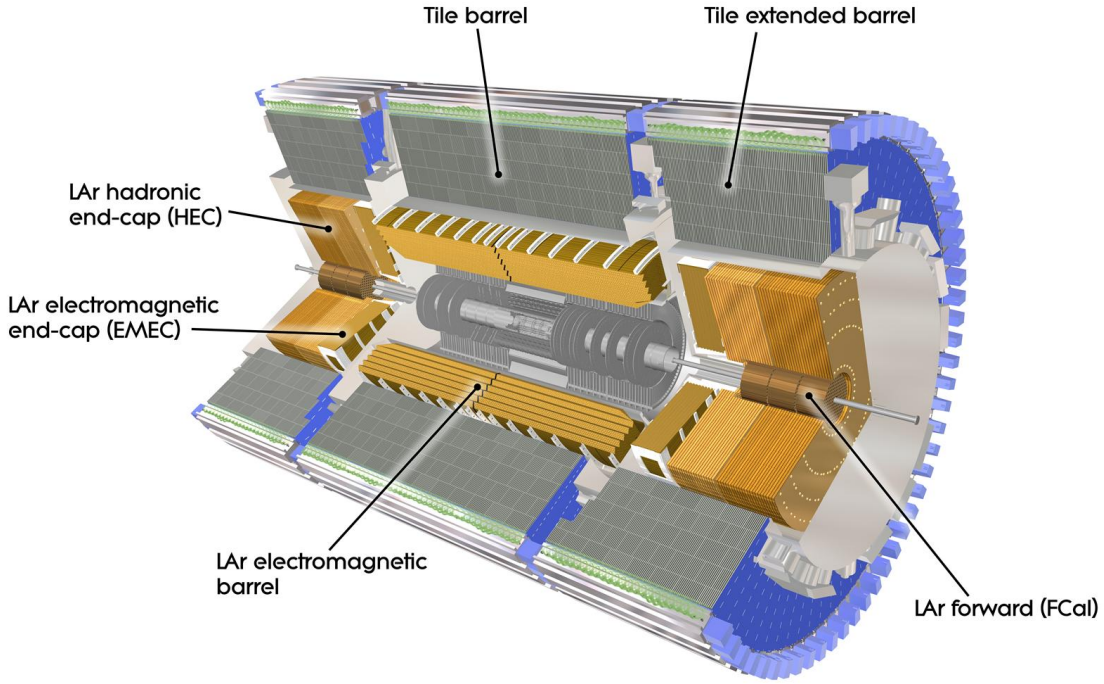

Figure 4.3: Overview of the ATLAS calorimetry systems. ©CERN.

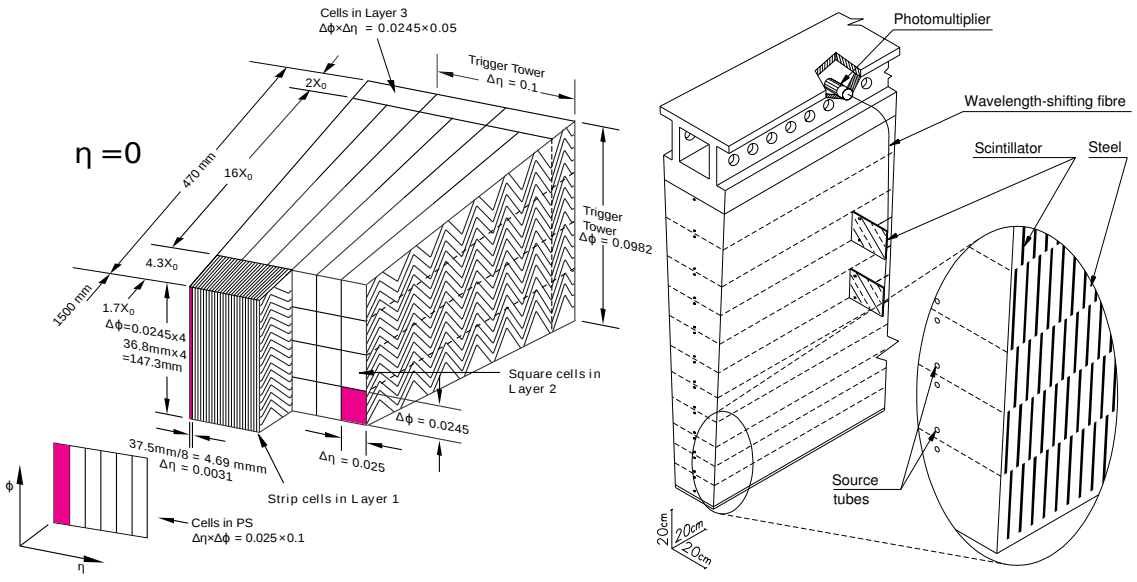

(a) (b)

Figure 4.4: Schematic view of (a) the LAr accordion structure and (b) a single Tile module or 'drawer' [27].

the regions $0.8 < |\eta| < 1.7$. The design incorporates steel absorber and active plastic scintillation tiles with a total thickness of 9.7 nuclear interaction lengths[2] (λ). The photomultiplier tubes and front-end electronics are mounted onto 1.4 m aluminium units called drawers which provide the analogue sums from groups of channels to form trigger towers. The LAr Hadronic Endcap Calorimeter (HEC) consists of a front and rear wheel in each endcap cryostat giving coverage between $1.5 < |\eta| < 3.2$ and is constructed from layers of flat copper absorber plates.

4.4.3 Forward Calorimetry

The LAr Forward Calorimeter (FCal) provides coverage in the high-η region $3.1 < |\eta| < 4.9$ and is exposed to very large particle fluxes. The FCal is integrated into the endcap cryostats providing good uniformity between the detector systems and is set back further from the interaction point than the Electromagnetic Endcap (EMEC) calorimeter to reduce the build-up of neutrons in the ID region. The restricted available depth requires a high density design approximately 10 λ deep.

The FCal consists of three modules stacked behind each other. The first module (FCal1) is optimised for EM energy measurement while two other modules (FCal2 and FCal3) provide measurement for hadronic interactions. To optimise resolution and heat removal FCal1 is constructed using a copper absorber and the hadronic modules from tungsten in order to provide good shower containment and minimise the lateral spread. To reduce the beam backgrounds entering the endcap muon system a shielding plug made from a copper alloy is mounted behind FCal3.

Each module is constructed from a metal matrix with regularly spaced channels filled by an electrode structure of small diameter rods orientated parallel to the beam axis. This design helps both to reduce the build-up of ions and provide the highest material density possible. This results in very small LAr gaps which give much shorter drift times and hence a faster signal pulse than the other calorimeters.

[2]The mean path length required to reduce the numbers of charged particles by the factor $1/e$

4.5 Muon System

The Muon Spectrometer (MS) forms the outer-most layer of the ATLAS detector and provides a measure of the muon's momentum based on the magnetic deflection from the large toroidal magnetic system. Muons are much heavier than electrons and therefore do not undergo bremsstrahlung processes very readily, leaving minimal ionisation energy in the inner detector and calorimeters. As a result they are the only particles which pass beyond the calorimeters other than neutrinos which are not detected. An overview of the various muon systems is given in Figure 4.5.

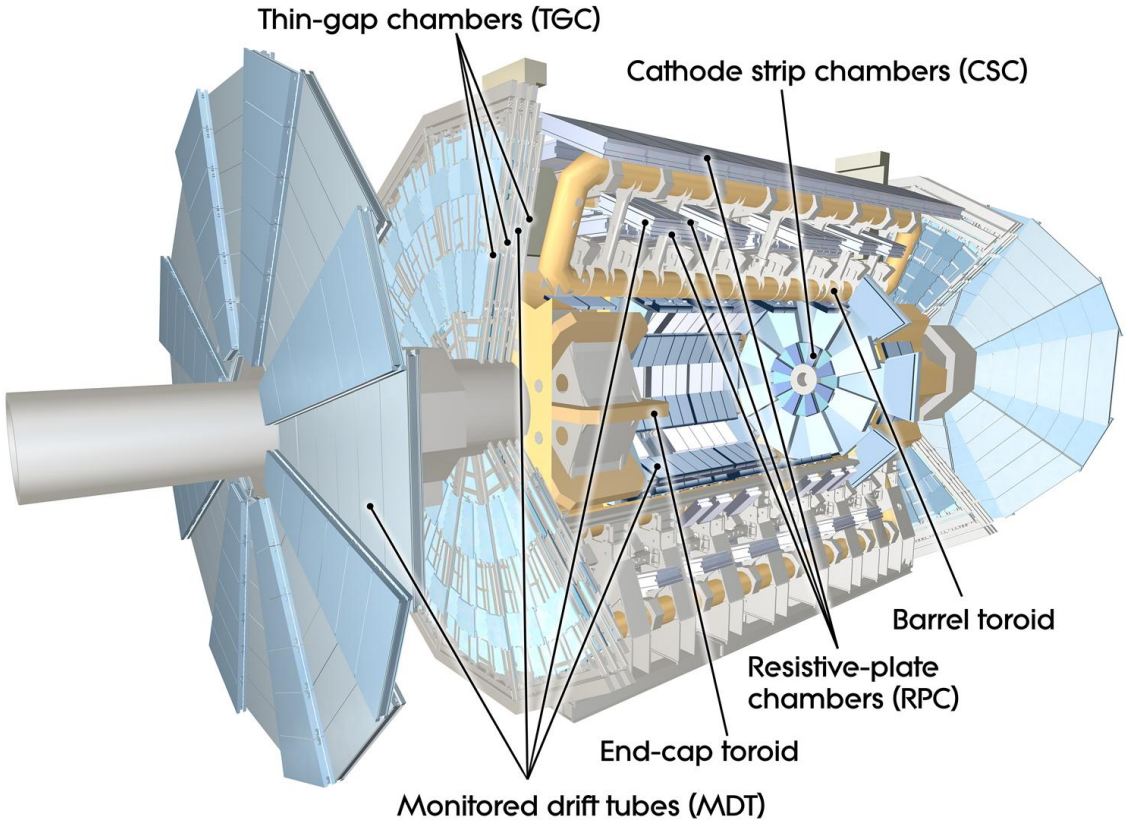

Figure 4.5: Overview of the ATLAS muon systems. ©CERN.

Three layers of chambers are arranged in cylindrical layers around the beam axis in the barrel region, while in the endcap region chambers are arranged in planes perpendicular to the beam. Precision momentum measurement is performed by the Monitored Drift Tube (MDT) chambers providing coverage up to $|\eta| < 2.7$. The MDTs

consist of layers of drift tubes 30 mm in diameter filled with an $ArCO_2$ gas mix, where each tube is capable of an average resolution of 80 µm or 35 µm per chamber. The inner-most layer of the forward region instead uses Cathode Strip Chambers (CSCs) due to the higher muon flux. The CSCs are multi-wire proportional chambers with cathode planes segmented into strips in the orthogonal direction. The resolution of a chamber is 40 µm in the bending plane and about 5 mm in the transverse plane.

The precision tracking chambers are complemented with a system of fast tracking chambers to provide the muon system with triggering capability. The barrel region uses Resistive Plate Chambers (RPCs) which consist of parallel electrode-plates in a gaseous mixture, whereas the endcaps use a type of multi-wire proportional chamber called Thin Gap Chambers (TGCs). The good time resolution of these trigger chambers means that reliable bunch crossing identification can be performed.

4.6 Trigger and Data Acquisition

The ATLAS Trigger and Data AcQuisition (TDAQ) system is responsible for online event selection and data-flow off the detector through to permanent storage. At the nominal LHC bunch crossing frequency of 40 MHz and with an approximate event size of 1.6 MB, the raw data rate would significantly exceed what can be feasibly processed and stored. To achieve the required level of rate reduction while preserving events likely to contain interesting physics processes, ATLAS operates a three-level trigger system, as shown in Figure 4.6. The first level is hardware-based and the subsequent levels, collectively known as the High Level Trigger (HLT), are based on software running on separate large-scale commercial computing farms. Each trigger level has a prescale set designed to randomly sample some proportion of events satisfying a particular trigger item. This allows much lower thresholds to be used for processes with larger production rates and can be adjusted to satisfy different luminosity conditions.

The Level 1 (L1) trigger is a fixed-latency pipelined system constructed of custom

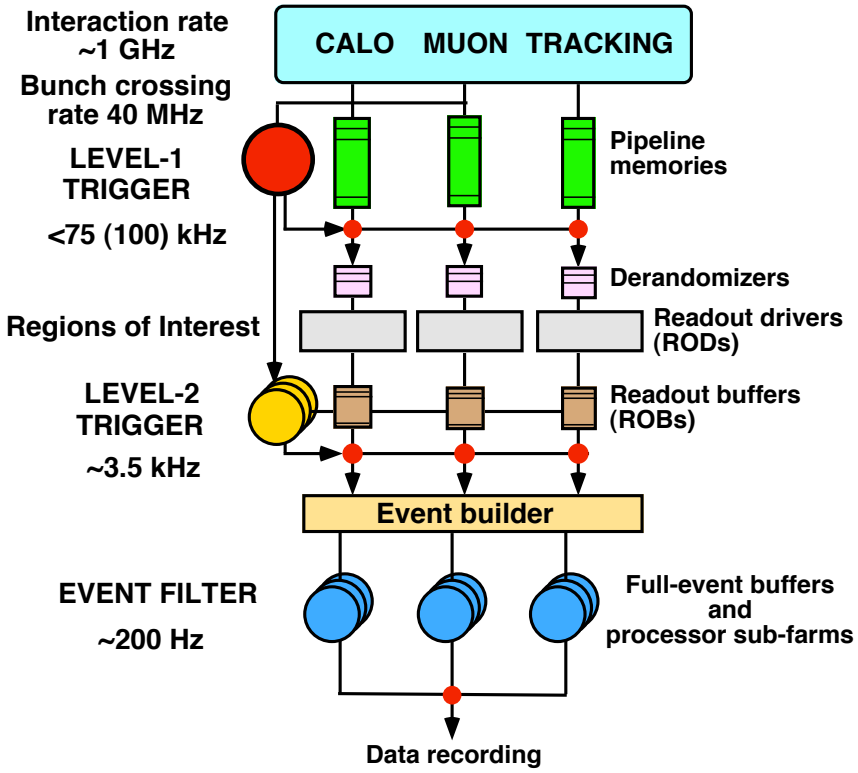

Figure 4.6: Schematic overview of the ATLAS trigger system during Run 1 [88].

electronics, which performs initial event selection based on reduced granularity information from the calorimeters and MS. It is composed of L1Calo (discussed further in Chapter 5), the Level 1 Muon Trigger (L1Muon) and the Central Trigger Processor (CTP). It searches for electrons, photons, muons, tau leptons and jets, as well as identifing events with large missing and total transverse energy. The latency budget of 2.5 µs is defined by the size of the digital pipeline memories on detector that buffer the full data from each event while the Level 1 decision is determined. If the CTP decides that an event satisfies the selection criteria, it issues a Level 1 Accept (L1A) signal that initiates the retrieval of the event data from the pipelines and the transmission of Regions of Interest (RoIs), which specify the coordinates of the Level 1 objects and indicate the thresholds passed. The maximum Level 1 accept rate that could be sustained by the detector readout systems during Run 1 was approximately 75 kHz. This limit has since been upgraded to 100 kHz for Run 2, which is relevant for the studies in Chapter 7.

The Level 2 (L2) trigger uses highly optimised algorithms to refine the identification of physics objects, based on the full granularity detector information in the regions defined by RoIs. It is required to further reduce the event rate to approximately 6.5 kHz with a mean processing time of around 40 ms per event. The Event Filter (EF) is the last stage of the trigger processing that builds the full event topology and uses more sophisticated algorithms to make a final decision on whether to record an event to permanent storage for further offline analysis. The EF must reduce the rate to around 600 Hz and has a mean processing time of 4 s per event.

Events passing the EF are assigned to one or more inclusive data streams, depending on the type of trigger menu items satisfied. This allows events containing similar signatures to be grouped together to help simplify offline analysis, at the expense of some data duplication. As well as streams designed for physics analysis, there are also streams designed for the monitoring and calibration of different detector subsystems. The Level 2 and EF have since been merged into a single processing unit running in a homogeneous HLT farm for Run 2 [85].

4.6.1 Single Lepton Triggers

The lowest threshold unprescaled Single Lepton Triggers (SLTs) are the primary triggers for many important physics analyses, including the $hh \rightarrow b\bar{b}\tau\tau$ analysis presented in Section 8. They are composed of isolated electron and muon triggers combined with higher threshold triggers without isolation. The details of the electron and muon triggers are explained in References [89] and [90], respectively.

The Level 1 trigger searches for electrons by identifying RoIs with an EM cluster E_{T} above the trigger threshold. The Level 2 algorithm builds clusters from calorimeter cells within RoIs and applies corrections based on the offline reconstruction algorithms to improve the resolution of the cluster position and energy. Tracking information confined to the RoI centre is also available at Level 2 for fast pattern recognition and track reconstruction. Finally, the EF is able to use offline-like recon-

struction algorithms with the full online cell and tracking information. The electron trigger efficiencies are shown in Figure 4.7 at each stage of the trigger chain as a function of the electron E_{T} and η for the combined single electron trigger used in the 8 TeV analyses.

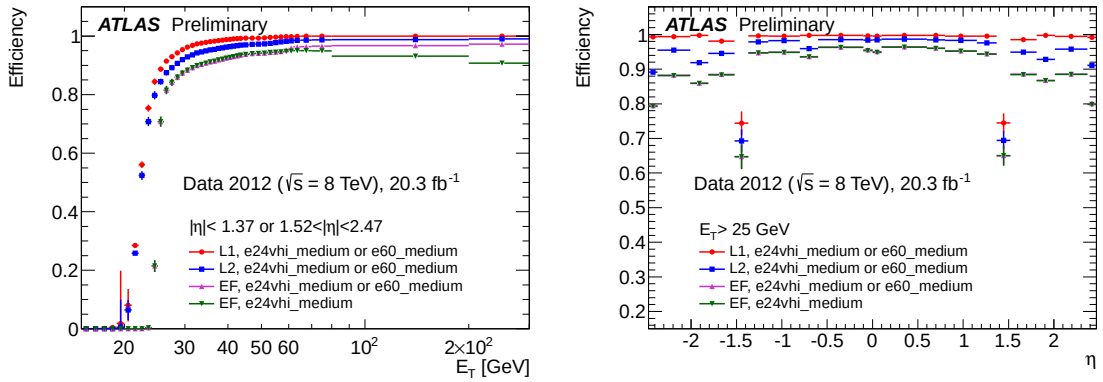

(a) (b)

Figure 4.7: Single electron trigger efficiencies after the L1, L2 and EF selections as a function of (a) the offline electron E_{T} for pseudorapidity ranges of $|\eta| < 1.37$ or $1.52 < |\eta| < 2.37$ and (b) the offline electron η for $E_{\mathrm{T}} > 25\,\mathrm{GeV}$. The efficiencies were measured with a tag-and-probe method using $Z \rightarrow ee$ decays for the `e24vhi_medium1 OR e60_medium1` trigger and are shown with combined statistical and systematic uncertainties [91].

Muons are identified at Level 1 by the spatial and temporal coincidence of hits in either the RPCs or TGCs pointing back to the interaction point. The Level 2 trigger constructs a track using data from the MDT chambers to get a more precise estimate of the track parameters. In the EF, muon candidates are first formed by using the muon detectors and then attempts are made to combine these with tracks in the ID. Figure 4.8 shows the single muon trigger efficiencies as a function of the muon p_{T} for the barrel and endcap regions.

4.7 Data Sample

The results presented later in this thesis are based on ATLAS data taken during Run 1. The cumulative luminosity for pp collisions at 7 and 8 TeV centre-of-mass

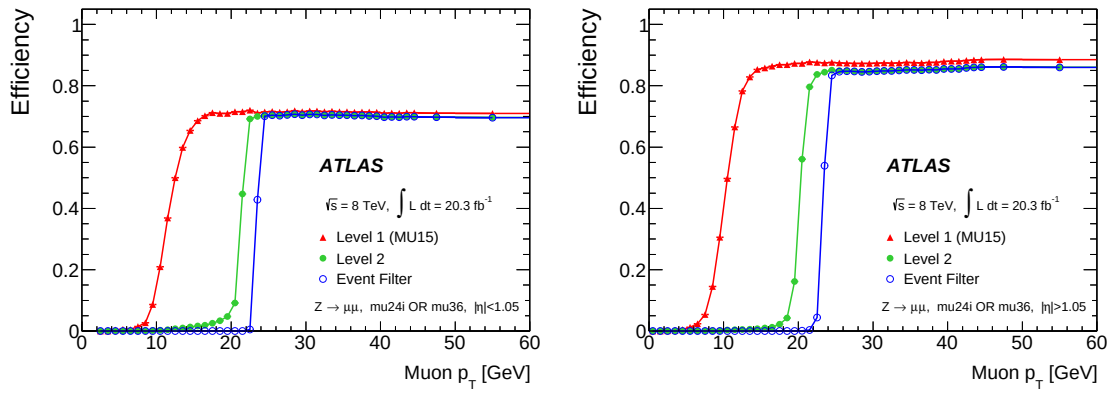

(a) (b)

Figure 4.8: Single muon trigger efficiencies after the L1, L2 and EF selections as a function of offline reconstructed muons for (a) the barrel region and (b) the endcap region. The efficiencies were measured with a tag-and-probe method using $Z \rightarrow \mu\mu$ decays for the `mu24i_tight OR mu36_tight` trigger and are shown with statistical uncertainties [90].

energy collected during 2011 and 2012 are shown in Figure 4.9. The delivered luminosity (green) is that delivered by the LHC to the ATLAS experiment during stable beams. The recorded luminosity (yellow) takes into account the inefficiency in the Data Acquisition (DAQ) system and data loss during the "warm start" phase of ATLAS. The good for physics data (blue) includes all data that satisfies the offline data quality requirements, ensuring all detector components were operating normally. High data-taking and data quality efficiencies of 96.5% and 89.9% (2011), 95.5% and 95.3% (2012) where achieved, respectively. The searches for Higgs boson pair production presented in this document only make use of the 8 TeV data sample because the larger centre-of-mass energy and greater sample size make it significantly more sensitive.

4.7.1 Luminosity Measurement

An accurate measurement of the beam luminosity delivered to ATLAS is an important component of the physics programme as it is often a major source of systematic uncertainty for cross section measurements, and is essential in evaluating

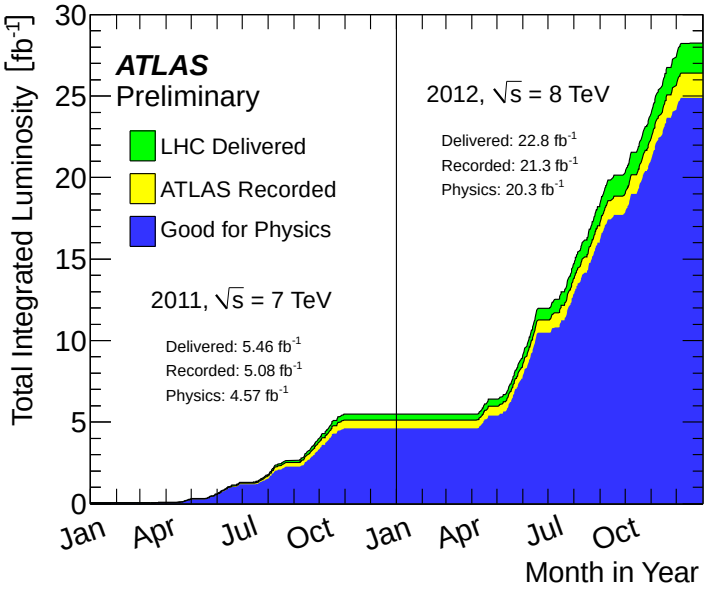

Figure 4.9: Cumulative luminosity versus time for 2011 and 2012 *pp* collisions [27].

background levels to determine the sensitivity to new physics signatures. The luminosity measurement in ATLAS is divided into time intervals referred to as Luminosity Blocks (LBs) that are one minute in duration. The total integrated luminosity is determined by the sum of the integrated luminosities in LBs that pass the data quality criteria.

The LUminosity measurement using Cherenkov Integrating Detector (LUCID) and the Beam Conditions Monitor (BCM) provide ATLAS with independent online monitoring of the instantaneous luminosity measured on a bunch-by-bunch basis. LUCID consists of sixteen 1.5 m long aluminium tubes filled with C_4F_{10} gas that surround the beam pipe at a distance of 17 m either side of the interaction point, and covers the psuedorapidity range $5.6 < |\eta| < 6.0$. The Cherenkov light is collected by Photo-Multiplier Tubes (PMTs) at the back end of each tube. The BCM consists of four diamond sensors, arranged around the beam pipe on each side of the interaction point at ± 184 cm, corresponding to $|\eta| = 4.2$. The primary function of the BCM is to monitor background levels and issue a beam-abort request in the event beam instabilities risk damage to the ID.

Each detector and algorithm is calibrated to determine its absolute luminosity scale

via dedicated van der Meer (vdM) beam scans [92]. The luminosity can be expressed in terms of the accelerator parameters as:

$$\mathcal{L} = \frac{n_b f_r n_1 n_2}{2\pi \Sigma_x \Sigma_y}, \tag{4.4}$$

where n_b is the number of colliding bunches, f_r is the revolution frequency, n_1 and n_2 are the number of protons per bunch in each beam, and Σ_x and Σ_y are the horizontal and vertical beam profile widths [93].

4.7.2 Pile-up

The consequence of the high luminosities produced at the LHC is that multiple pp interactions occur within each bunch crossing. These additional collisions contribute a background of soft energy depositions that can have adverse effects on the performance of the trigger and reconstruction of physics objects. There are two forms of pile-up experienced by ATLAS. *In-time pile-up* refers to the effects contained within the same bunch crossing and therefore scales with the number of interactions. *Out-of-time pile-up* refers to contributions from other bunch crossings that occur as a consequence of the electronic pulse durations in the calorimeters being larger than a single bunch crossing interval.

The number of pp interactions per bunch crossing follows a Poisson distribution with mean value μ and is related to the instantaneous luminosity by the following relationship:

$$\mu = \frac{\mathcal{L}\sigma_{pp}}{n_b f_r}, \tag{4.5}$$

where σ_{pp} is the inelastic pp cross section. The number of interactions averaged over all bunch crossings and averaged over the data analysed will be referred to as $\langle\mu\rangle$. The distributions of the average number of interactions per bunch crossing are shown in Figure 4.10 for the 2011 and 2012 pp data samples. The overall mean number of simultaneous interactions was 9.1 for the 2011 sample and 20.7 for the 2012 sample. The levels of in-time pile-up experienced during Run 1 were larger

than intended for the achieved luminosity, due to the LHC operating with a bunch spacing of 50 ns, instead of the design bunch spacing of 25 ns.

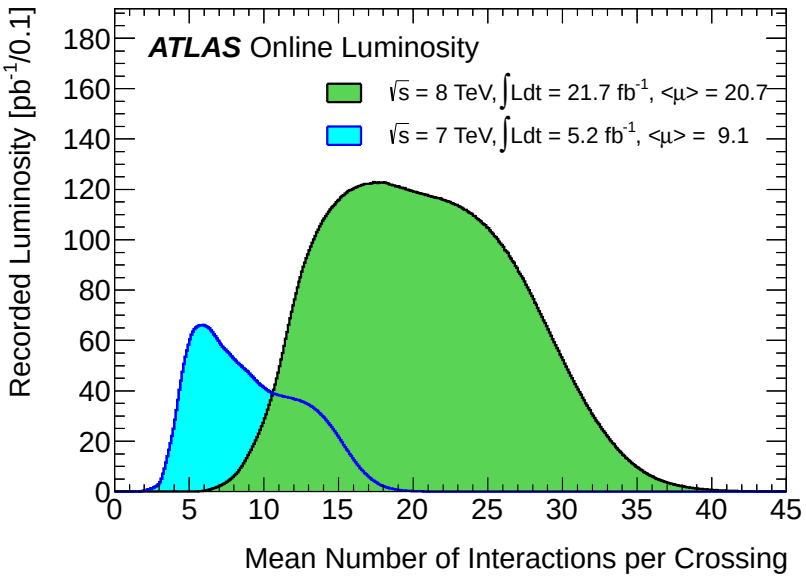

Figure 4.10: Luminosity-weighted distribution of the mean number of interactions per bunch crossing for 2011 and 2012 *pp* collisions [27].

CHAPTER 5

LEVEL 1 CALORIMETER TRIGGER

The Level 1 Calorimeter Trigger (L1Calo) is a hardware-based system located entirely off-detector in the adjacent cavern Underground Service Area 15 (USA15). Simple algorithms are implemented within fast custom logic based on Application Specific Integrated Circuits (ASICs) and Field Programmable Gate Arrays (FPGAs). L1Calo must process signals from the calorimeters to identify jets, local clusters of EM and hadronic activity, and to calculate the total and missing transverse energy of each event. These tasks must be performed at the LHC bunch crossing frequency of 40 MHz[1] and within an overall fixed latency of 2.5 µs. This chapter introduces many of the technical aspects of L1Calo as operated during Run 1, where much of this is described at length in the Level 1 Trigger TDR [88]. A brief description of the upgrades made to L1Calo for Run 2 is given in Section 5.4.

The basic Run 1 architecture of L1Calo comprises three main processing blocks, as illustrated in Figure 5.1. The ATLAS calorimeters contain over 200000 channels

[1] To be more precise, the LHC clock is in fact 40.08 MHz

which must all be processed at the bunch crossing frequency. To achieve this within the required latency, the Level 1 trigger system operates with reduced granularity. The analogue signals from calorimeter cells are summed on detector into 7168 trigger towers approximately $\eta \times \phi = 0.1 \times 0.1$ in size (with coarser granularity above $|\eta| > 2.5$) with separate signals received from the EM and hadronic calorimeters. At this point corrections for the gain, shape and timing of the different signals being added are performed and the LAr signals are converted to transverse energy using η-dependent gain factors. These signals are carried off the detector via twisted pair cables around 70 m in length and are fed into the receivers located in USA15, where the Tile signals are converted to transverse energy and gain corrections are applied to the E_{T} scale. The analogue signals are then carried via shorter cables for digital processing in the Preprocessor. The output of the Preprocessor is then used as the source for the Cluster Processor (CP) and Jet/Energy-sum Processor (JEP). Finally, the results of the algorithms implemented in the CP and JEP are collated by the Common Merger Modules (CMMs) and are sent to the CTP along with the output of the L1Muon for a trigger decision.

5.1 Preprocessor

The main purpose of the Preprocessor system is to serve as a digital signal source for the subsequent processors. The Preprocessor system also performs an important operation called Bunch Crossing Identification (BCID), which is responsible for associating a signal with a particular LHC bunch crossing, and is described in detail in Section 5.1.1. It also performs the BC-multiplexing (BC-mux) for input to the CP system and the 2×2 trigger tower E_{T} sums (jet elements) for input into the JEP system. The function and performance of this system is described at length in [94].

The Preprocessor system primarily consists of 124 Preprocessor Modules (PPMs) installed in eight standard VME crates that provide full calorimeter coverage. Figure 5.2 shows the physical layout of a PPM, where the data flow is from the front

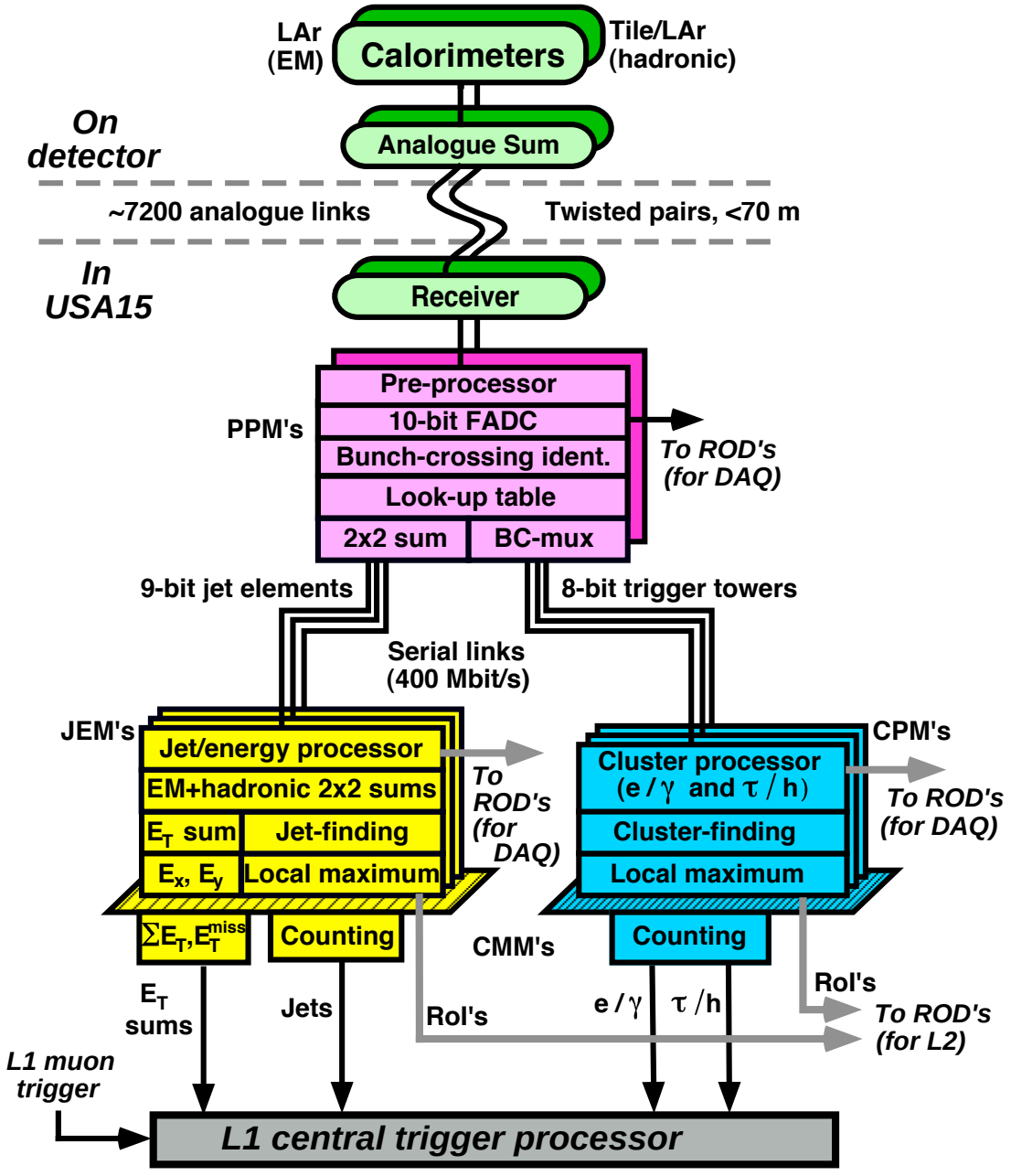

Figure 5.1: Overview of the L1Calo system architecture during Run 1. The black data paths represent the real-time data flow, while the grey data paths represent additional output to be utilised by the HLT and to be recorded by the readout systems. Taken from [76].

panel on the left to the backplane on the right. A number of important tasks are performed on daughter boards to allow for easy replacement in case of hardware failure. Each PPM handles the analogue calorimeter signals for up to 64 trigger towers that are routed to the four Analogue Input (AnIn) daughter boards. At this point a voltage offset is added to the input signals by a Digital-to-Analogue Converter (DAC) that is calibrated to ensure the correct pedestal level for the Analogue-to-Digital Converters (ADCs) located on the Multi-Chip Module (MCM) of 32 counts. The analogue signal is also rescaled by an operational amplifier to match the linear digitisation range of the ADC which has a size of about 1 V. The signals are passed on to sixteen MCMs that each process the signals for four trigger towers. The digitisation of the calorimeter signals is performed by four 10-bit ADCs located on each MCM, operating at a sample frequency of 40 MHz. The timing of the digitisation can be adjusted in 1 ns steps by PHOS4 chips to ensure sampling of the signal peak [95]. This is known as the *fine-timing* calibration. The bulk of the signal processing is performed by an ASIC on each MCM, where the BCID algorithm and E_{T} measurement are implemented. The real-time data are transmitted to the CP and JEP via a LVDS Cable Driver (LCD). The Readout Merger (ReM) FPGA controls the data readout on the arrival of a L1A signal.

5.1.1 Bunch Crossing Identification

The ability to extract timing and energy information from analogue pulses is an essential requirement for L1Calo. The function of BCID is to convert broad signal pulses into a single digitised E_{T} estimate related to the bunch crossing it originated from. The most significant challenges for the BCID system occur at small pulse heights where noise is significant and at very large pulse heights where saturation effects cause distortions to the pulse shape. The problems presented by these two regimes are sufficiently different that separate algorithms are required. Almost all signals are identified using the unsaturated BCID, as saturation is a rare occurrence by design. In total, there are three possible methods of BCID available to L1Calo.

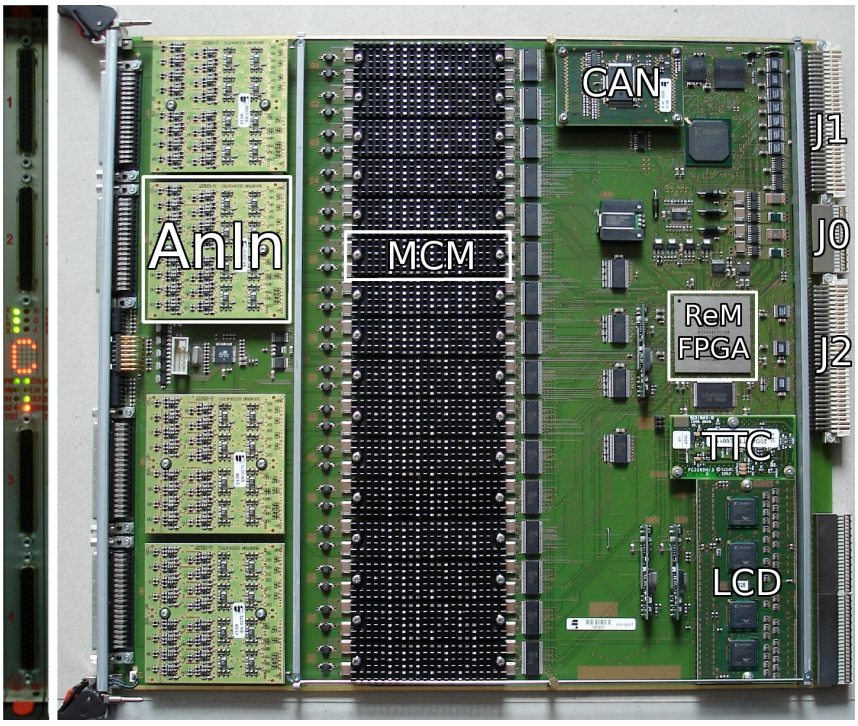

Figure 5.2: Photograph of the PPM front panel (left) and the board top view (right). The analogue signals enter the module on the left-hand side and are managed by four AnIn boards. At the centre are sixteen MCMs which digitise the signals and perform the BCID algorithms programmed into an on-board ASIC. The right-hand side of the board contains one LCD, one TTC Decoder, one CAN module, and a ReM FPGA. Taken from [94].

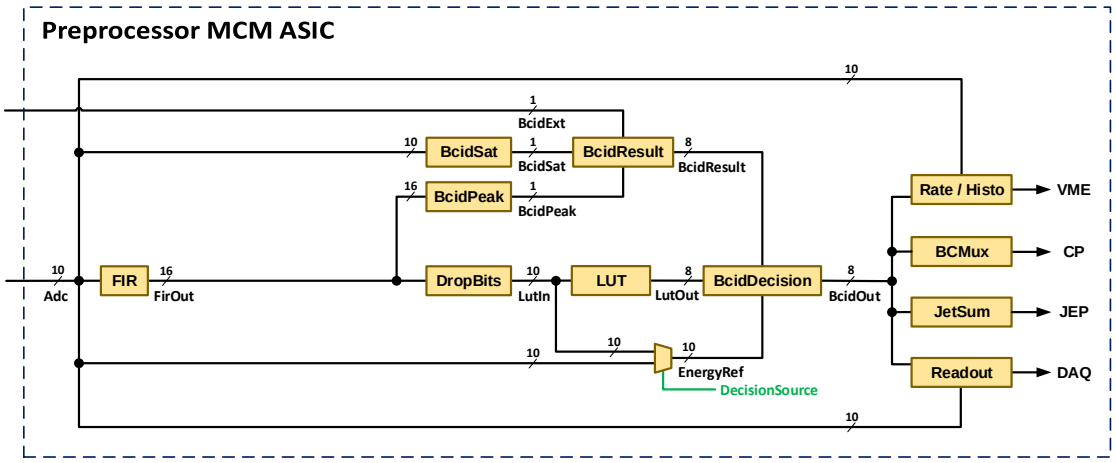

Figure 5.3: Overview of Preprocessor MCM ASIC logic for one channel. The ADC data enters the processing logic from the left-hand side and the results are sent on to the systems marked on the right-hand side.

Unsaturated BCID

The shape of the signal pulses in the unsaturated regime is required to be independent of amplitude in order to preserve the timing information and enable an accurate E_{T} estimate. At the heart of the unsaturated BCID algorithm is a Finite Impulse Response (FIR) filter that operates at the bunch crossing frequency over a window of ADC samples. Typically this window is limited to five samples, but can be extended up to fifteen for specialist studies. Five samples is sufficient to cover the entire positive amplitude of most pulse shapes, from which BCID is determined. The filter coefficients are selected in order to maximise the signal-to-noise ratio for the expected signal pulse shape, where the use of multiple samples in the filter helps to naturally suppress the effects of incoherent noise. The FIR filter output is a weighted sum of the ADC data computed using the following expression with time step t:

$$f(t) = \sum_{i=0}^{n-1} a_i \cdot d(t + i - 2), \tag{5.1}$$

where $d(i)$ are the input ADC data and a_i are the coefficients. The output of the FIR filter is operated on by a peak-finder, which compares the values for neighbouring bunch crossings to identify local energy maxima satisfying the condition $f(t-1) < f(t) \geq f(t+1)$. The final E_{T} estimate is calculated in a Look-Up Table (LUT) that requires the precision of the FIR output to be reduced to 10 bits in a so-called dropbits operation prior to this. The LUT performs a pedestal subtraction and computes an E_{T} value calibrated in GeV and encoded in 8-bits. Noise suppression by means of a threshold cut on low E_{T} values is also applied in the LUT. The peak-finder algorithm continues to identify the correct bunch crossing into the saturation region and therefore provides overlap between these two methods.

There are three parameters which require calibration for the LUT calculation, namely the `slope`, `offset` and `noisecut`. The `slope` determines the scale between the input and output of the LUT and can be finely tuned to the calorimeter EM scale through dedicated calibration studies with data. The `offset` is the equivalent of the pedestal

level in the LUT and thus is dependent on the sum of the filter coefficients as follows:

$$\texttt{offset} = \text{pedestal} \times \texttt{slope} \times \frac{\sum_{i=0}^{n-1} a_i}{2^{\texttt{dropbits}}} - \frac{\texttt{slope}}{2}. \tag{5.2}$$

To have a LUT output > 0 the product of the LUT input and `slope` must be greater than or equal to the sum of the `offset` and `noisecut`.

Saturated BCID

The dynamic range for trigger tower signals extends up until 255 GeV in transverse energy, up to which point they are required to scale linearly. At energies greater than this the precise determination of the E_{T} is not important as the event will be triggered regardless, however the identification of the correct bunch crossing remains critical. Very high energy signals will cause saturation and as a consequence the pulse shape can be significantly affected. This presents a major challenge for reliable BCID. The nature of the saturation can be either analogue or digital. Analogue saturation can occur at three different points inside the summing chain of the LAr trigger tower electronics. These are the linear mixer, including the preamplifier and shaper, the layer sum board, and the tower builder board. Figure 5.4 illustrates saturation occurring at each of these stages using simulated signals with a transverse energy of about 1 TeV. In these cases large distortions occur to the trailing edge of the signals. Digital saturation occurs when a signal exceeds the digitisation range of the 10-bit ADC (corresponding to about 2.5 V) and it simply becomes truncated at this point. Analogue saturation begins to occur at a voltage of approximately 3.4 V and therefore always occurs after digital saturation by design.

The BCID algorithm used for saturated signals operates directly on the ADC output. It relies on the leading edge of the pulse and is therefore robust against the wide variations in shape observed in the trailing edges of saturated signals. It works by comparing the two samples before saturation to different programmable thresholds, referred to as s_{low} and s_{high}. Additionally, the algorithm is only evaluated if the programmable saturation level s_{level} is reached. To maximise the available range of

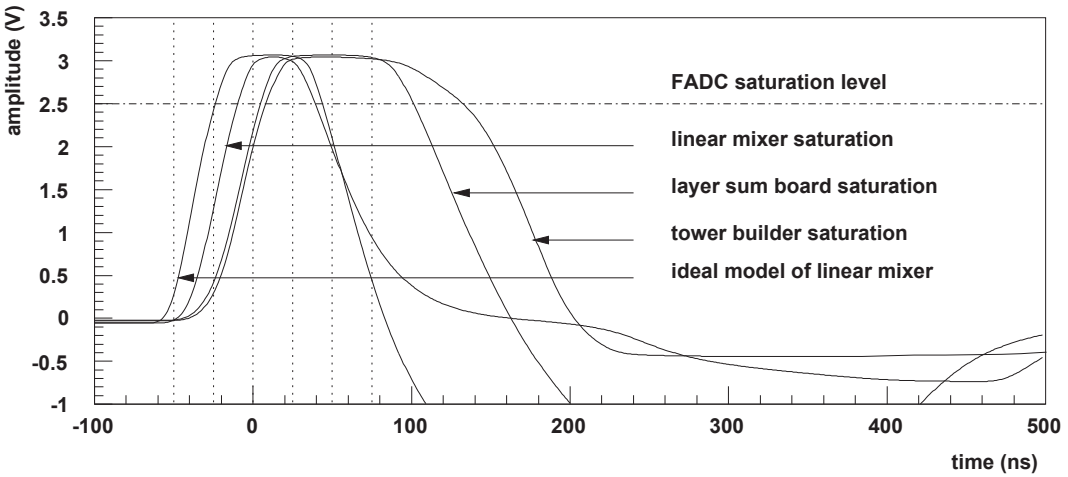

Figure 5.4: Pulse shapes for saturated trigger tower signals at different stages of the LAr summing chain. Taken from [96].

the algorithm this is set to be identical to the ADC saturation of 1023 counts. The configuration of separate thresholds means the algorithm can be tuned to work with calorimeter pulses of different shapes, where these thresholds are high enough such that the algorithm is insensitive to noise. The saturated BCID algorithm has been proved to work well up until the point where too many samples saturate, at around 3.5 TeV [97].

The algorithm is only activated on the first saturated ADC sample and is rearmed on the first sample to drop below the saturation level, to ensure the identification is only performed once per signal. The algorithm is illustrated for an example saturated signal in Figure 5.5. The Saturated BCID can assign the identification to the first or the second saturated ADC sample based on the following logic: if $d_{s-1} > s_{\text{high}}$ and $d_{s-2} > s_{\text{low}}$ then sample s is the identified bunch crossing, otherwise it is assigned to sample $s + 1$.

External BCID

The final method of BCID was foreseen as a back-up solution for saturated signals. It was intended to enable BCID to be issued externally to L1Calo using a single

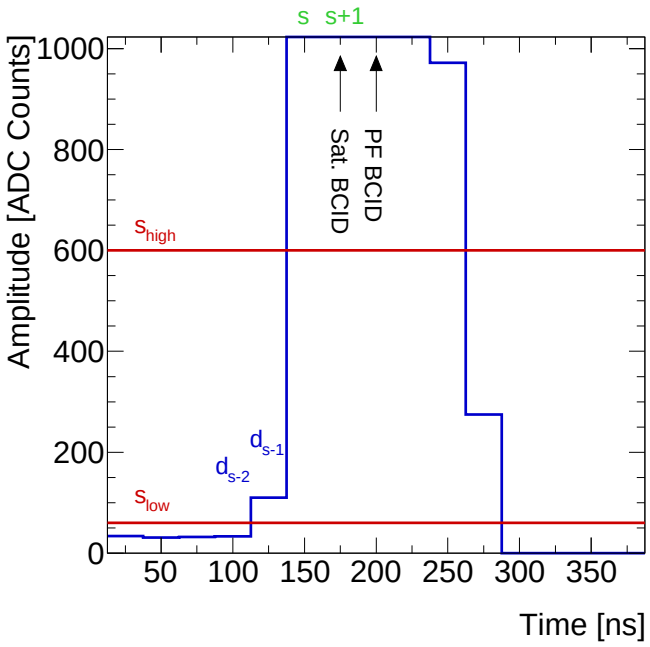

Figure 5.5: Illustration of the BCID algorithm for saturated signals. The two ADC values d_{s-2} and d_{s-1} are compared to the programmable thresholds s_{low} and s_{high} to determine if the correct bunch crossing is s or $s+1$. In this case, the peak-finder BCID fires one bunch crossing late.

comparison on the leading edge of the analogue pulse before digitisation. In practice, most of the available effort has been concentrated on the digital solution and so little work on the calibration of the discriminator threshold or timing has ever been done. As a result, this method has not been used during data-taking.

Decision Logic

A final piece of logic is required to make a decision on which of the different BCID algorithms to use depending on the energy region of the signal. The energy regions are based either on the direct ADC value or the LUT input, depending on the selection of the decision source. During Run 1 the default operation mode has been to use the latter of these. For signals in the low energy region the peak-finder is used to determine the correct bunch crossing, while signals in the high energy region make use of the saturated algorithm. It is intended that the decision logic should always select whichever of these algorithms fires earliest. If the saturated BCID is

selected, the saturated value of 255 GeV is assigned as the E_{T} estimate, and if the unsaturated BCID is selected, the LUT output is assigned. In all other cases the output will be zeroed. By the design of the system it is not possible to set the BCID on two successive bunch crossings for the same trigger tower.

5.2 Cluster Processor

The CP identifies candidate electrons, photons and hadronically decaying tau leptons using trigger tower data from both the EM and hadronic calorimeter layers within the region $|\eta| < 2.5$. This is achieved by operating a *sliding window* algorithm of 4×4 trigger towers in size as illustrated by Figure 5.6. The algorithm identifies clusters summed across both the EM and hadronic layers of 2×2 trigger towers in size, known as RoIs, that are found to be local maxima in E_{T} compared to their eight nearest neighbours. This is to ensure that candidates are not counted multiple times as a consequence of overlapping window arrangements.

For electrons and photons the most energetic of the horizontal (2×1) or vertical (1×2) cluster sums in the EM layer must be greater than a predefined threshold. This EM cluster can be required to pass certain isolation requirements, such that the EM or hadronic isolation ring and hadronic core must be less than a corresponding predefined threshold. This helps to discriminate between single objects and broader hadronic jets. For tau lepton candidates, the EM cluster sum is combined with the hadronic core of trigger towers to produce a hadronic cluster. As a consequence of this, the hadronic core isolation requirement is removed.

The processing is handled by four crates of electronics that each operate in one quadrant in ϕ of the calorimeter, with each of these crates containing 14 Cluster Processor Modules (CPMs). Each CPM scans a core region of 16×4 trigger towers and must share data across boundaries in order to provide the full coverage of trigger towers required by the sliding window. There are sixteen possible trigger thresholds which can be set within the hardware to identify cluster RoIs. Eight of

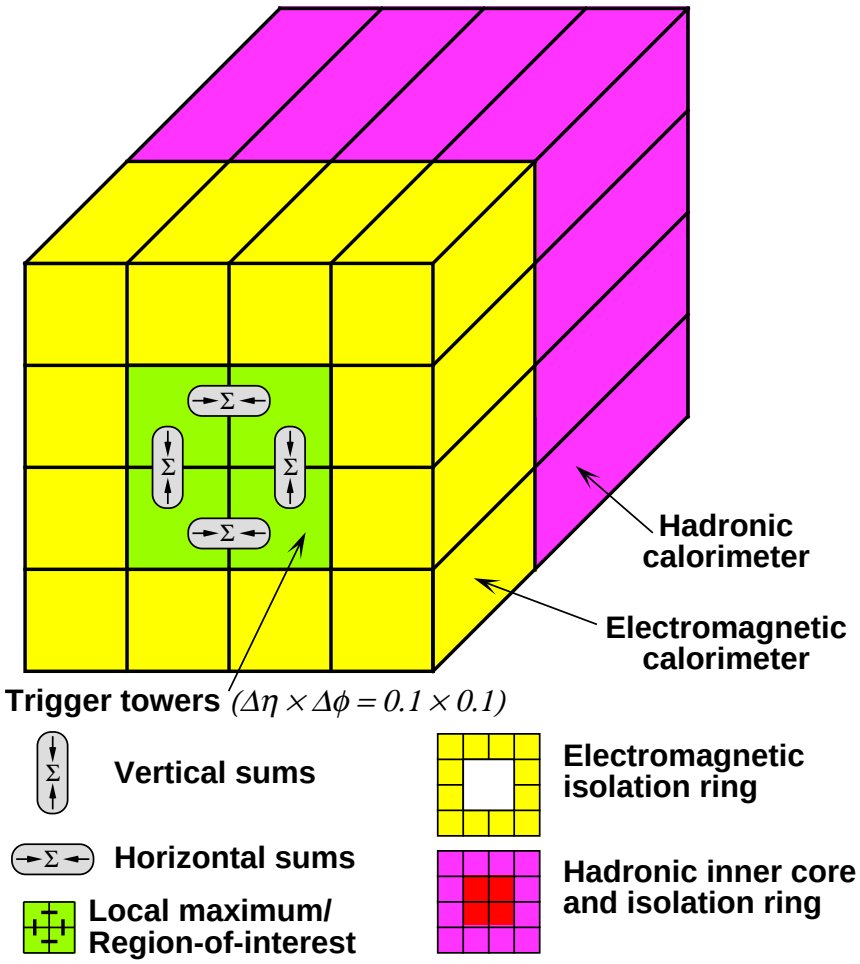

Figure 5.6: Cluster Processor sliding window electron/photon and tau/hadron algorithm that operates on the trigger towers from the EM and hadronic calorimeters. Taken from [76].

these thresholds are dedicated to EM cluster triggers and the rest are individually programmable to be either EM or hadronic cluster triggers. The numbers of objects passing each trigger item are counted in the merging logic of the CMM which presents the total multiplicities to the CTP.

5.3 Jet/Energy-Sum Processor

The JEP is designed to identify jets as well as calculate $E_{\mathrm{T}}^{\mathrm{miss}}$, total-$E_{\mathrm{T}}$ and $E_{\mathrm{T}}^{\mathrm{miss}}$-significance. These algorithms operate on jet elements that are formed by summing over 2×2 trigger towers in both the EM and hadronic calorimeter layers. The jet

algorithm is similar to the sliding window algorithm implemented in the CPM and identifies local energy maxima RoIs of 2×2 jet elements in size. The jet algorithm calculates cluster sums of 2×2, 3×3 or 4×4 jet elements in size, as shown in Figure 5.7. These sums are then compared to predefined jet E_{T} thresholds which are different for each of the cluster sizes. The jet algorithm covers the region $|\eta| < 4.9$, however special treatment of the jet elements is required in the region of the FCal $3.2 < |\eta| < 4.9$, where the granularity is much coarser in both η and ϕ. This means that triggering jets in this region is less reliable and susceptible to pile-up noise. Eight independent combinations of jet E_{T} threshold and window size are available for trigger menus.

The JEP is contained in two crates consisting of 16 Jet/Energy-sum Modules (JEMs) each that handle two opposite quadrants in ϕ. Each JEM processes a core area of 8×4 jet elements in size and calculates sums of E_{T} and also determines the E_x and E_y components of this based on the η and ϕ of jet elements for the missing energy calculation. This includes all jet elements within $|\eta| < 4.9$. The CMMs count the total jet multiplicities and perform the final system-level energy-sums for the CTP.

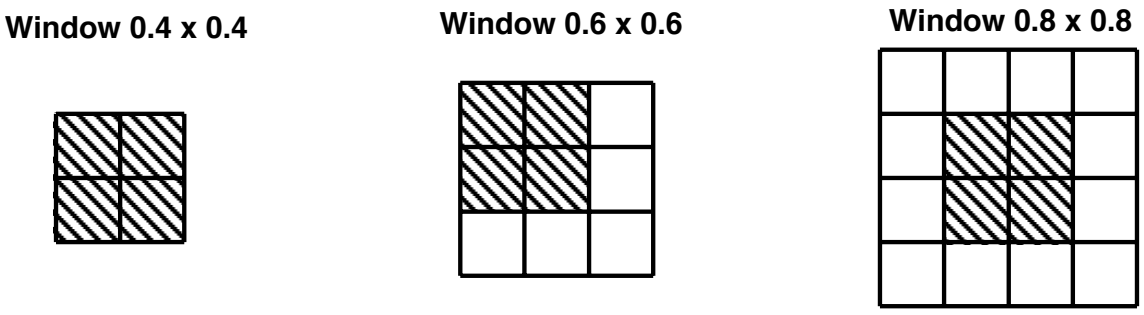

Figure 5.7: Jet trigger algorithm operates on jet elements indicated by the 0.2×0.2 grid. The three available E_{T} cluster sizes of 2×2, 3×3 and 4×4 jet elements are shown with the corresponding RoIs given by the shaded regions. Taken from [76].

5.4 Upgrades for Run 2

A number of upgrades have been made to L1Calo during LS1 and an overview of the new architecture is shown in Figure 5.8. Many of these upgrades have been made necessary due to the introduction of topological triggering at the Level 1 trigger for Run 2. To allow for such triggers the firmware of the CP and JEP modules will no longer output threshold multiplicities and will instead output Trigger Objects (TOBs) that comprise the location, E_{T} and type of object identified. The new extended merger modules (CMX) are capable of sending more trigger signals to the CTP, increasing the number of available selection and isolation thresholds for each of the EM (16), TAU (16), J (25), XE (8), TE (8) and XS (8) triggers.

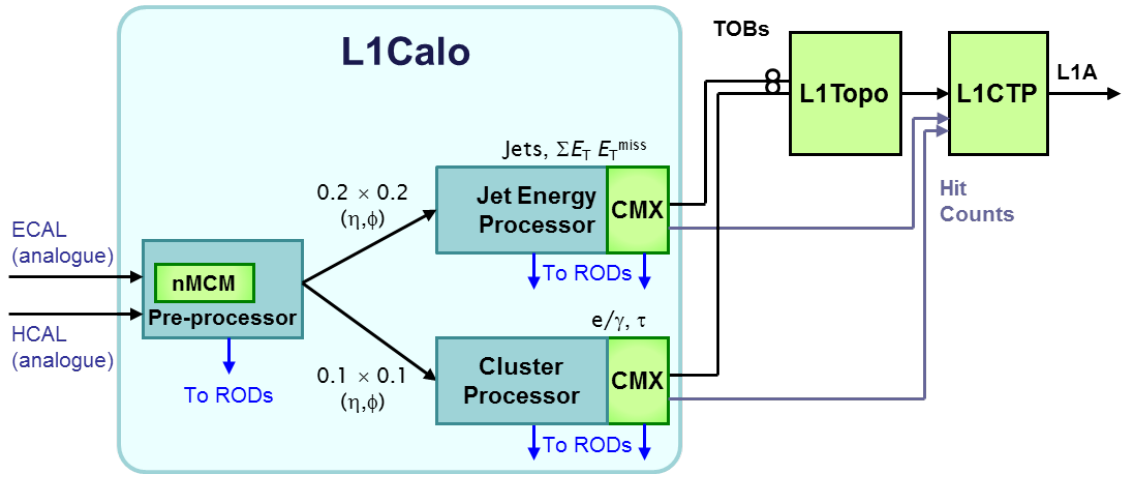

Figure 5.8: Overview of the L1Calo system architecture during Run 2. Pre-exisiting components are shown in blue and the new components are shown in green. Taken from [85].

TOBs above a certain threshold are sent to the Level 1 Topology Processor (L1Topo), which also receives data from L1Muon. L1Topo forms combined trigger objects, based on full event topology. Topological requirements enable selections which are often applied at the analysis level to be applied immediately at the Level 1 trigger, which can sometimes provide significant rate reductions. Example topological calculations performed by the L1Topo module include $\Delta\eta$ (DETA), $\Delta\phi$ (DPHI), ΔR (DR), invariant mass (INVM) and the p_{T} sum of all jets (HT). The CTP has also been upgraded

to allow for new trigger sources including L1Topo, and to provide twice as many trigger menu items.

5.4.1 New Preprocessor Multi-Chip Module

The upgraded MCM is intended to increase the resources available for processing signals and provide greater flexibility and an evolution of the features and algorithms implemented in the original design. A layout of the new Multi-Chip Module (nMCM) board design is shown in Figure 5.9. It features two dual-channel ADCs that digitise at twice the bunch crossing rate (80 MHz). Instead of the ASIC used in the previous design, the main functions for the MCM are programmed into one Xilinx Spartan-6 FPGA. It offers the possibility of improved signal processing, which is investigated in the next chapter.

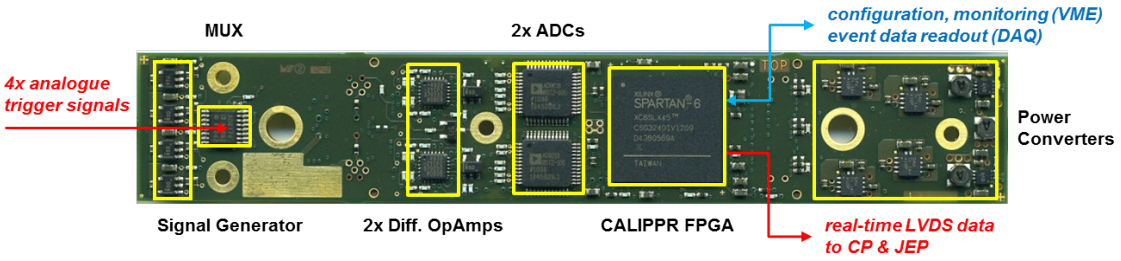

Figure 5.9: The topside view of the new Preprocessor MCM. The four analogue trigger tower signals enter the module on the left-hand side and are digitised by the dual ADCs before entering the FPGA, where the main processing occurs. Taken from [85].

CHAPTER 6

DEVELOPMENT OF THE L1CALO SIGNAL PROCESSING

6.1 Introduction

During Run 1 the processing of calorimeter signals in L1Calo was limited by the ASIC design of the MCM, where the main strategy available to suppress pile-up effects was to increase the noise cut. This approach is intended as a last resort and the fact that the thresholds cannot be configured dependent on the position within a bunch train inevitably results in overcompensation for the majority of events in order to suppress the large pedestal shift contribution for early bunch crossings in a train (described in Section 6.5). It is therefore much preferred to seek alternative signal processing techniques to minimise the use of noise cuts. The introduction of the FPGA based nMCM during LS1 provides the ideal opportunity to add additional functionality for Run 2 as well as the possibility for future firmware updates to accommodate further improvements.

To assess the performance of prospective signal processing techniques it was necessary to simulate analogue calorimeter signals representative of high pile-up conditions. This chapter assesses the performance of different FIR filter strategies to identify and reconstruct unsaturated trigger tower pulse signals. The simulated beam conditions are intended to represent the peak luminosity expected for the first year of Run 2 data-taking, corresponding to an average number of interactions per bunch crossing of 40, assuming a bunch spacing of 25 ns at a centre-of-mass energy of 13 TeV.

To adequately explore a wide range of capabilities possible with the nMCM a toy simulation called ToyMC was created to model the expected noise conditions for a trigger tower at any given $|\eta|$-bin. The ToyMC simulation models the full history of the analogue signal inputs over the circulation of the LHC with a sampling frequency of any given multiple of the bunch crossing frequency. It is also capable of producing the expected bunch filling schemes and bunch luminosity profiles to accurately simulate the effects of in-time and out-of-time pile-up on the performance of the nMCM. It also provides a true emulation of a possible hardware implementation of the signal processing functionality.

6.2 Calorimeter Noise

Noise is an important consideration for the performance of L1Calo and affects the system in the following ways. Firstly it reduces the efficiency of the BCID algorithm for identifying small signals of less than about 3 GeV in transverse energy[1] as well as degrading the resolution achieved for identified signals. These factors will affect the performance of all trigger types. Significant noise levels will also reduce the effectiveness of the isolation cuts applied to EM and hadronic τ objects. Finally the noise sets the limit on the minimum E_{T} threshold in order to avoid a high rate of fake jets, due to the large number of trigger towers which are summed together.

[1] This is true for trigger towers where pile-up noise is not the main contributor

There are two principal sources contributing to incoherent noise, which are *thermal noise* and *pile-up noise*. Thermal noise has a white spectrum and depends on the detector characteristics and signal processing electronics such as amplifiers and cables. Pile-up noise is the result of the constant bombardment of calorimeter cells from physics processes with high cross sections, due to the multiple interactions occurring at each bunch crossing.

Another noise source arises from the quantisation of the analogue calorimeter signals, which introduces an error due to the truncation performed by the ADCs. This quantisation noise has a uniform E_{T} distribution and for counts with a Least Significant Bit (LSB) of 0.25 GeV is computed to be approximately 75 MeV, given by the rule $\mathrm{LSB}/\sqrt{12}$ [98].

Each of these noise sources is taken into account, where their standard deviations in the ToyMC are shown as a function of $|\eta|$ in Figure 6.1 for trigger towers in the EM and hadronic calorimeters. Note that other types of noise including coherent noise and crosstalk are of secondary importance to the purposes of this investigation and therefore are not considered as their magnitudes are small by design.

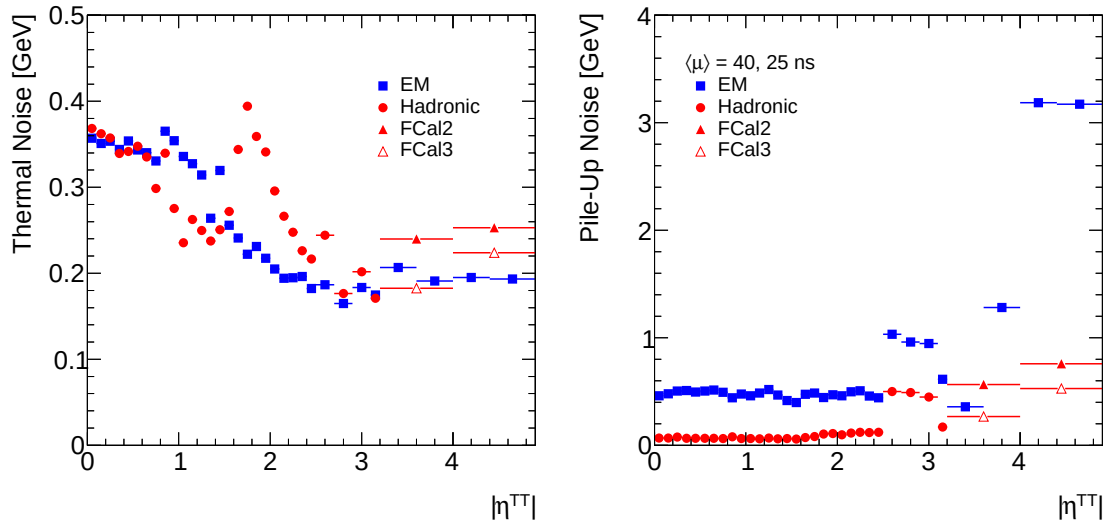

(a) (b)

Figure 6.1: Calorimeter noise as transverse energy determined by the standard deviation of ADC distributions as a function of the trigger tower $|\eta|$ for (a) thermal noise and (b) pile-up noise. See Sections 6.2.1 and 6.2.2 for more detail.

6.2.1 Thermal Noise

The thermal noise experienced by trigger towers depends on their rapidity. This is due to the fact that the transverse component of a given noise energy scales with $\sin\theta$, leading to a relatively smaller contributions in E_{T} at higher rapidity. There are also variations due to the different calorimeter detector types, changes within the structure of the different subdetectors which result in relatively smaller or larger noise contributions at given boundaries. No significant alterations are expected to the processing of the analogue signals received by the Preprocessor during LS1 and other than increases in noise due to the ageing of electronics and exposure to radiation it is reasonable to assume that contributions from the calorimeter electronics will remain very similar to Run 1. Early tests indicate that the noise handling of the nMCM is expected to be improved over the old design, with an approximate channel noise of 50 MeV [99]. However, the ToyMC adopts the worst case scenario by assuming an equivalent performance to the old MCM.

The thermal noise was measured using real experimental data by considering a bunch crossing containing no particle bunches which was sufficiently displaced in time from any other colliding bunches to avoid out-of-time contributions. This provides the most accurate representation of the thermal noise present while the detector is in full operation without any contributions from collisions.

The average noise distribution for a trigger tower at a given pseudorapidity was determined by binning the ADC data obtained in $|\eta|$ and subtracting the mean pedestal per trigger tower. The noise was estimated by taking the standard deviation obtained from a Gaussian fit to each of the distributions. To obtain a final estimate of the thermal noise, the expected quantisation noise must then be subtracted in quadrature. The results are shown in Figure 6.1a as a function of $|\eta|$ for trigger towers in the EM and hadronic calorimeters. The trigger tower noise at the centre of the detector is approximately 350 MeV, reducing to around 200 MeV for $|\eta| = 3$. There is a significant peak in the hadronic layer noise at $|\eta| = 1.8$ which corresponds to the transition point between the Tile Extended Barrel (EB) and the HEC.

The ToyMC models uncorrelated thermal noise by sampling random numbers from a Gaussian probability density function with a mean of zero and a standard deviation equal to that given in Figure 6.1a. This contribution is added to the pedestal level of the analogue input signal at the sampling frequency for all samples.

6.2.2 Pile-up Noise

Pile-up noise depends on the machine luminosity and therefore will vary with time as the bunch currents decay during a fill. It also depends on sampling depth, as deeper sections of the calorimeter are shielded from low energy particles. The pile-up noise is non-Gaussian and correlated between samples due to the calorimeter pulse shapes, which result in contributions both in-time and out-of-time.

Figure 6.2 shows example distributions of in-time pile-up experienced by trigger towers in different calorimeter regions. The distributions are obtained from MC simulation of minimum-bias data for an isolated bunch crossing, with a centre-of-mass energy of 13 TeV and $\langle\mu\rangle = 40$. The data sample was generated with the ATLAS Run 2 detector geometry, which includes the Insertable B-Layer (IBL) [100]. The shapes were acquired for each $|\eta|$-bin by subtracting the pedestal from the central ADC sample, where each ADC count corresponds to approximately 250MeV. The large size of the FCal trigger towers in η-ϕ space mean they are exposed to significant levels of pile-up, causing a large shift in the peak of the distribution to around 5 GeV.

The ToyMC generates an in-time pile-up contribution for every filled bunch crossing with an amplitude randomly chosen by sampling distributions based on the luminosity of the bunch, which scales linearly with $\langle\mu\rangle$. The calorimeter pulse shape for that trigger tower is multiplied by this amplitude and the result is added to the pedestal, where the pulse peak is centred on the current bunch crossing. The process is repeated to build up the analogue input signal for the full LHC circulation for processing by the nMCM emulation.

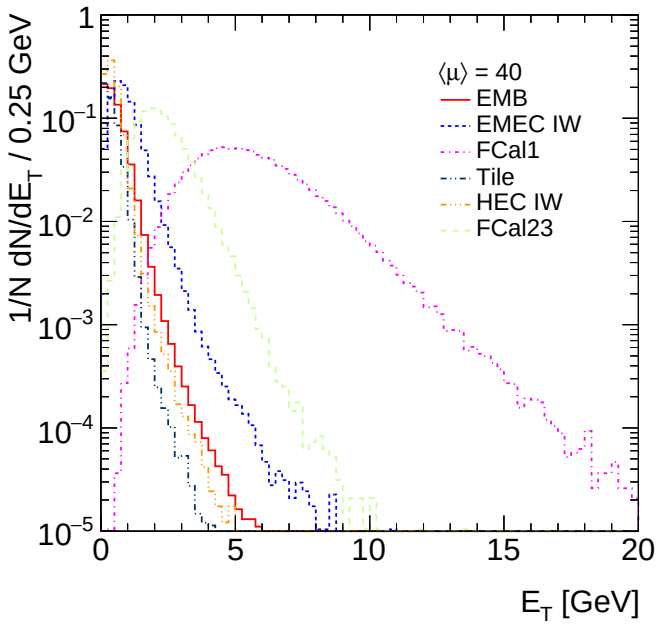

Figure 6.2: Example in-time pile-up distributions shown as a function of E_{T} obtained from minimum-bias MC data with $\langle\mu\rangle = 40$ at $\sqrt{s} = 13\,\mathrm{TeV}$ obtained for trigger towers in different calorimeter regions.

When expressed in units of transverse energy, the pile-up noise amplitude is a slowly varying function of rapidity for $|\eta| < 3$ [101]. However the considerably coarser granularity of the trigger towers in the inner-wheel region of the calorimeter endcaps and FCal results in a significant increase in the pile-up noise experienced. The noise for simulated pile-up with a 25 ns bunch spacing has been measured in the ToyMC from the standard deviation of the analogue input signal sampled for filled bunch crossings, where the effects of the average baseline shift have been accounted for.

The results are shown in Figure 6.1b where the typical noise observed in the EM and hadronic layers for $|\eta| < 2.5$ is approximately 500 MeV and 100 MeV, respectively. This means that for the Tile calorimeter thermal noise is by far the dominant source, while for the Electromagnetic Barrel (EMB) the pile-up noise is the more significant contributor. Excluding trigger towers in the transition region between the endcap calorimeter and FCal, the pile-up noise completely dominates. The total incoherent noise for a trigger tower at the centre of the detector in the EM layer is therefore 600 MeV and for a hadronic layer is 400 MeV.

6.3 Calorimeter Pulse Shapes

The general pulse shape characteristics depend on the calorimeter technology and shaping used. The analogue pulses from the LAr calorimeters extend over hundreds of nanoseconds, due to the relatively slow charge collection time. The Tile calorimeter produces narrower pulses from the rapid decay of the scintillation light. These signals then receive shaping which has been optimised to give a peaking time of about 45 ns, to minimise the total noise for a bunch spacing of 25 ns at the nominal LHC luminosity of $10^{34}\,\mathrm{cm}^{-2}\,\mathrm{s}^{-1}$ [102]. In the case of the LAr calorimeters the pulses have bipolar shaping, designed to give a net area close to zero to minimise the average baseline shift within a bunch train[2]. The Tile signals are instead able to use unipolar shaping.

The pulse shapes from physics collisions have been measured using an oscilloscope in many different regions of the EM and hadronic calorimeters, where typical signals from different calorimeter regions are shown in Figure 6.3. There is significant variation in the LAr pulse shapes as a function of $|\eta|$, as a result of changing argon gap sizes and discontinuities occurring at a number of transition regions. The drift time depends on the size of the LAr gaps, where a typical gap size for the EMB is around 2.1 mm, however to reduce space charge effects the FCal1 gap size is only 0.25 mm and results in a much smaller pulse length of around 350 ns.

The oscilloscope pulse shapes are used by the ToyMC to correctly model the out-of-time effects expected in data and are sampled according to the operational frequency. The signals are recorded with a 1 ns precision which enables detailed modelling of *timing jitter* and systematic shifts in timing. The ToyMC makes the assumption that the pulse amplitudes will scale linearly with energy for the range of unsaturated signals.

[2]In practise the pulse shapes generally have a slightly larger negative area, which results in a negative baseline shift.

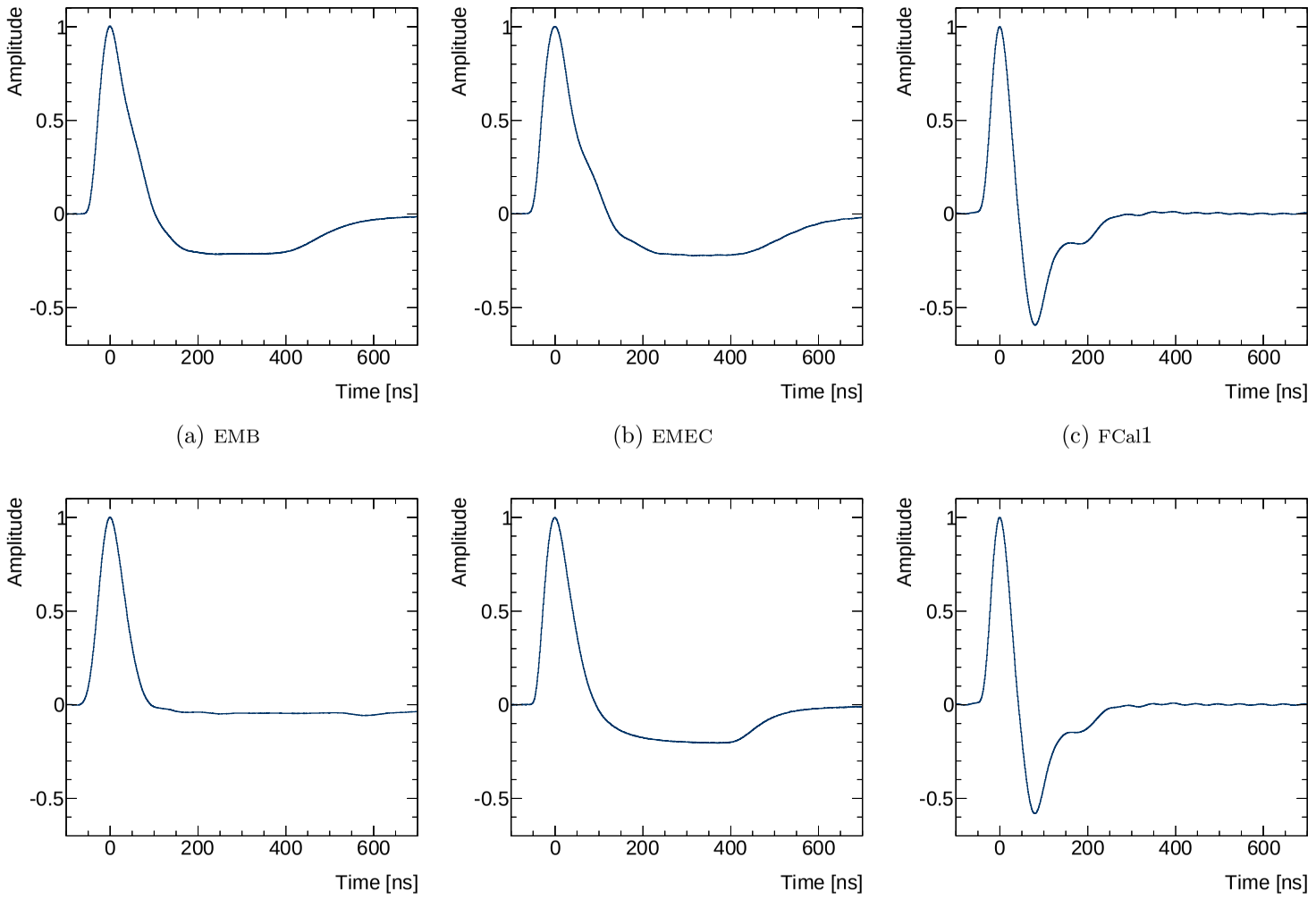

(a) EMB (b) EMEC (c) FCal1

(d) Tile (e) HEC (f) FCal23

Figure 6.3: Example trigger tower pulse shapes for different calorimeter regions and normalised to a peak height of unity.

6.4 Bunch Luminosity Filling Scheme

It is an important requirement that a representative LHC filling scheme is used in the simulation in order to properly model the out-of-time effects as a result of the finite bunch train lengths and the spacing between them. Figure 6.4a shows the filling scheme chosen for study in the ToyMC, which is based on the general train structure used during 2012. Trains of 72 bunches are grouped together in batches of either four or two and separated by a small gap of 8 bunches. Each batch is separated by a long gap of 36 bunches without beam in the pattern 4–4–2 of the number of bunch trains, until the abort gap is reached.

The individual bunch luminosities achieved by the LHC are not uniform and tend to fluctuate with a similar pattern that depends on the position within a train. A model of these bunch-to-bunch luminosity variations from 2012 data was used to produce a profile for a 25 ns bunch separation, with an overall average number of interactions per bunch crossing of 40. The distribution of the number of pile-up interactions for the individual bunches of this profile are shown in Figure 6.4b, where the variations are of the level of 10%.

6.5 Pedestal Shifts

The combination of the calorimeter pulse shapes and the filling scheme results in shifts in the average baseline within a bunch train with respect to the nominal pedestal value. These shifts are proportional to the average number of interactions per bunch crossing. The average pedestal shifts for trigger towers in different calorimeter regions are shown in Figure 6.5 for uniform and realistic bunch luminosities corresponding to $\langle\mu\rangle = 40$, for a bunch train following after a long bunch gap and a second train following after a short bunch gap. In the ToyMC the nominal pedestal measures at an average of 31.5 ADC counts without the presence of beam.

The spacing between bunch trains means that pulses of the Tile and FCal calorime-

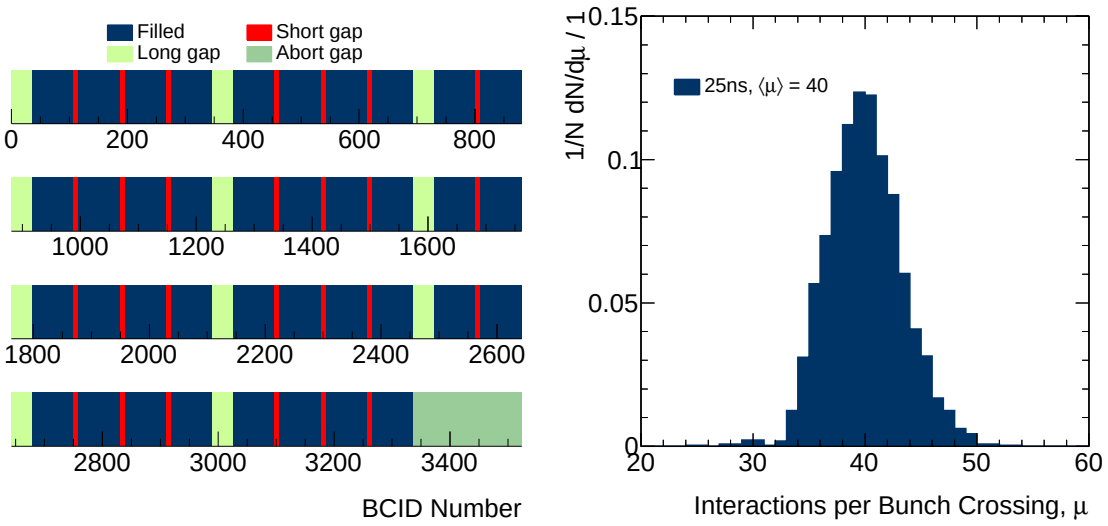

(a) (b)

Figure 6.4: Simulated luminosity scheme for 25 ns bunch spacing and $\langle\mu\rangle = 40$ where (a) shows the nominal 4–4–2 filling scheme pattern and (b) shows the distribution of the number of interactions represented by the simulation for all filled bunch crossings.

ters will have had sufficient time to return to the nominal pedestal level before encountering the next bunch train. However for the longer pulses of the other LAr calorimeters, the average response at the start of each bunch train will depend on whether they are preceded by a short or long gap.

In the LAr calorimeters the bipolar shaping is unable to fully compensate for the positive areas of the pulses in the early bunches of a bunch train, resulting in a large positive shift lasting for the first 10 bunch crossings in FCal and more than 25 bunch crossings elsewhere. In FCal the peak of the shift occurs at the second bunch in a train, however in other regions the peaks occur after the fifth and eighth crossing for bunch trains following a short and long beam gap respectively[3]. The magnitude of the shift is particularly extreme in those regions which experience the largest pile-up, and in FCal1 particularly the maximum shift is approximately 45 ADC counts above pedestal (approximately 11 GeV). The shifts are larger for bunch trains after long gaps.

[3]Assuming uniform bunch luminosities

Once the baseline has stabilised there is a small overall negative shift as a result of the larger negative net area of the LAr pulse shapes. At this point the realistic bunch luminosities cause fluctuations in the baseline which can vary significantly from one bunch to the next. At the end of a bunch train the pulse undershoots dominate which has a significant negative shift on the last bunch in the train.

The Tile calorimeter unipolar shaping results in a relatively constant positive shift throughout a bunch train which is very small at about 0.18 ADC counts due to the low pile-up.

6.6 Simulation Summary

There are two main parts to the ToyMC simulation. The first part generates an analogue signal trace for a circulation of the LHC beam and the second part processes this with an emulation of the nMCM hardware, which is easily modified in software to include new functionality. The advantage over real experimental data is that it is easy to produce large statistics samples under specific conditions to accurately compare the performance of different nMCM configurations and features.

As discussed in the previous sections the ToyMC includes both thermal and pile-up noise contributions into the trigger tower simulation by taking into account both the properties of the calorimeters and the setup of the LHC. In addition the ToyMC can randomly inject well separated 'signal' pulses with a range of amplitudes. The ability of the nMCM to identify these signals and accurately reconstruct their transverse energy will be used to optimise the performance of the nMCM.

The operation of the FIR filter is illustrated in Figure 6.6 for a section of a trace from an EMB trigger tower with an injected 10 GeV signal. The baseline coloured as red includes the original pedestal level and the sum of the thermal noise and negative areas of the calorimeter pulses. The blue and yellow areas represent the sum of the positive areas of the pile-up and signal pulses respectively.

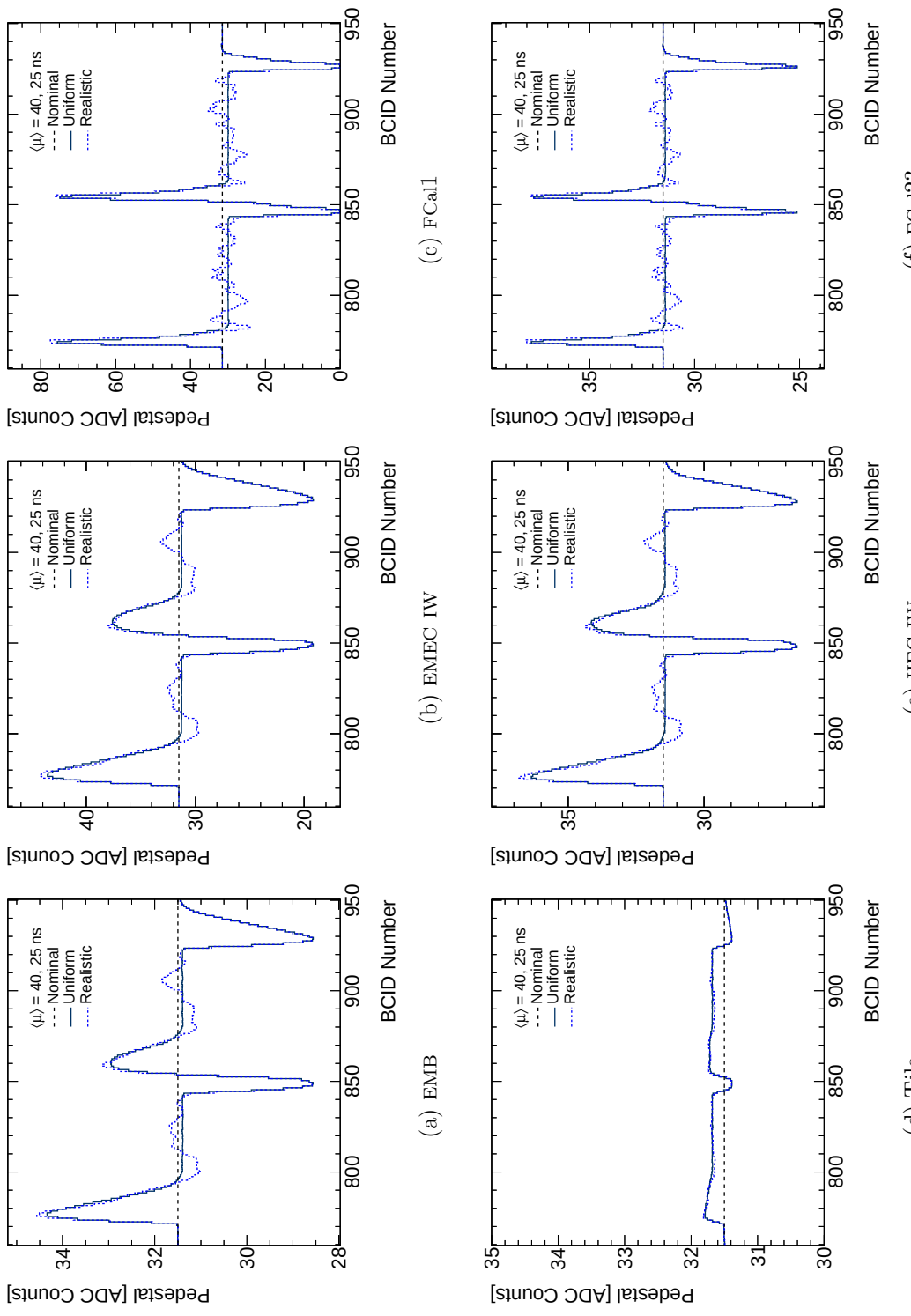

(a) EMB (b) EMEC IW (c) FCal1

(d) Tile (e) HEC IW (f) FCal23

Figure 6.5: Example pedestal shifts for uniform and realistic bunch luminosities in different calorimeter regions.

The FIR filter acts to remove distortions of the original signal due to noise, resulting in an improved signal-to-background ratio, the correct identification of the bunch crossing and accurate measurement of its transverse energy.

6.7 Measuring Filter Performance

A critical part of the filter performance is its ability to identify low E_{T} signals, commonly referred to as the BCID efficiency. The ToyMC defines this as the efficiency of the peak-finder to correctly associate an injected signal pulse with the bunch crossing it originated from. In addition the simulation categorizes those signals which failed the peak-finder identification in order to understand the relative contributions of possible inefficiencies.

One possible source of inefficiency is that the peak-finder incorrectly identifies the signal to be in another bunch crossing and is defined in the ToyMC as the case where the peak-finder fires one bunch crossing early or late. This contribution is of significant concern, as it will diminish the performance of the EM isolation and potentially cause triggers in the wrong bunch crossing. In all other cases the signal is considered to have been completely 'missed' by the peak-finder. There is also another possibility not considered here, that the very nature of the peak-finder algorithm prevents the identification of signals in consecutive bunch crossings, which would lead to one signal being effectively vetoed by the peak-finder decision. This is expected to occur infrequently and in any case the current Level 1 trigger is incapable of triggering on consecutive crossings due to simple deadtime.

Other important parts of the filter performance include the trigger tower response and resolution, which requires that a bunch crossing contains a correctly identified signal pulse. The trigger tower response is defined as

$$\mathcal{R} = \langle E_{\mathrm{T}}^{\mathrm{LUT}} / E_{\mathrm{T}}^{\mathrm{truth}} \rangle, \tag{6.1}$$

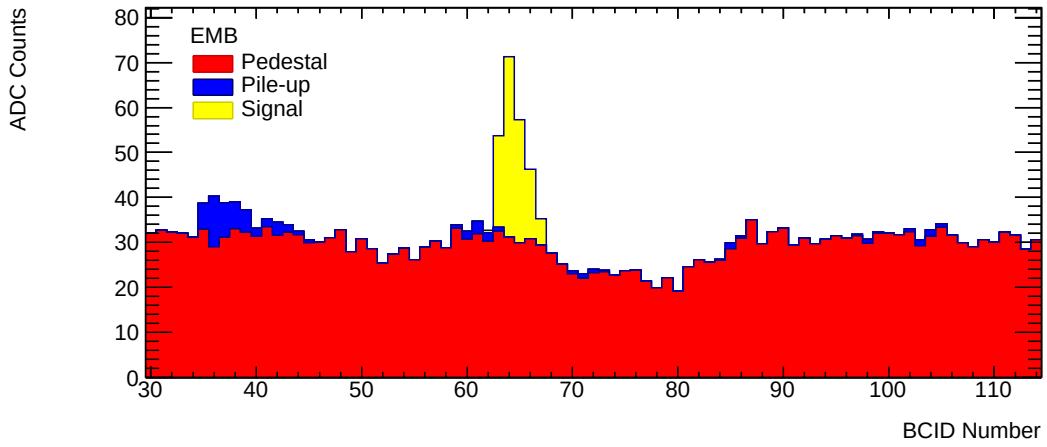

(a) ADC input into the FIR Filter

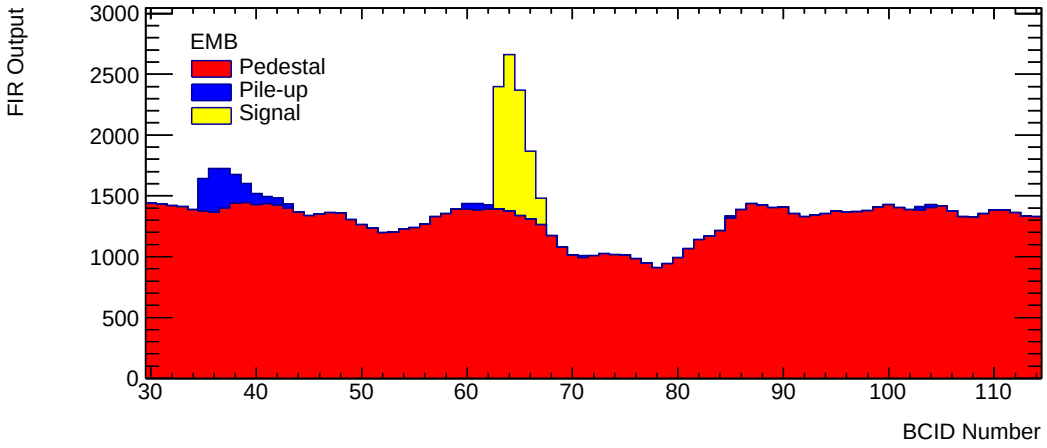

(b) Filtered output from the FIR Filter

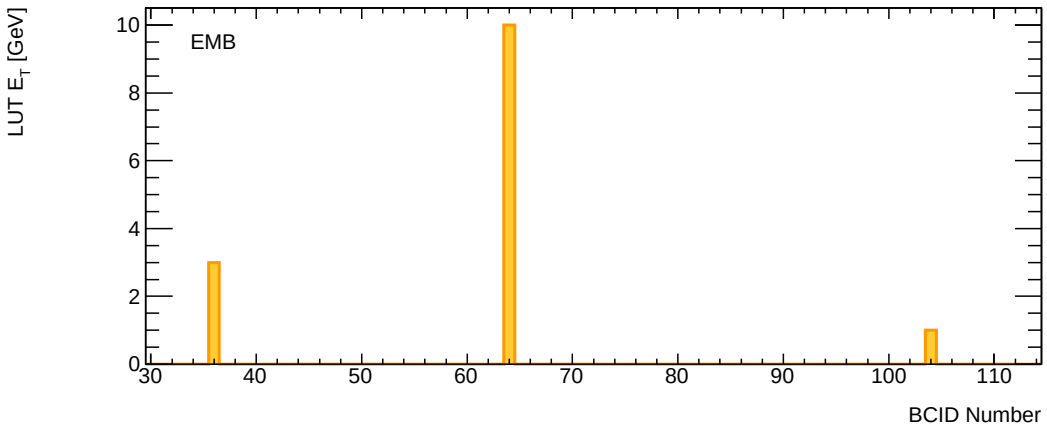

(c) LUT E_{T} output for bunch crossings identified by the peak-finder

Figure 6.6: An example of a digitised trace for an EMB trigger tower at different stages of the MCM signal processing using a matched filter. The different components going into forming the trace and the E_{T} output are shown for a single bunch train containing a ToyMC simulated 10 GeV signal event at a BCID number of 64.

where $E_{\mathrm{T}}^{\mathrm{LUT}}$ is the E_{T} as determined by the trigger tower LUT, $E_{\mathrm{T}}^{\mathrm{truth}}$ is the true E_{T} of the injected signal pulse and the mean is taken from a Gaussian fit to the $E_{\mathrm{T}}^{\mathrm{LUT}}/E_{\mathrm{T}}^{\mathrm{truth}}$ distribution. Additionally cuts are applied to clean-up the distributions at very low E_{T} by requiring the signal is well timed, with a local maximum central ADC and transverse energy cuts of LUT > 0, ADC > 40 and $E_{\mathrm{T}}^{\mathrm{truth}} > 2\,\mathrm{GeV}$ to remove tails from badly reconstructed signals.

The response of a trigger tower can depend significantly on the position within a bunch train for the LAr calorimeters as a result of the average baseline shift. The shifts also generally act in opposite directions for bunches early in a train and those later. Therefore the response is measured separately for bunches in the *start* and the *bulk* of the train, where the transition is defined by the point where the shift changes from positive to negative with respect to the nominal pedestal for uniform bunch luminosities.

The trigger tower resolution ($\sigma_{\mathcal{R}'}$) is given by the standard deviation of the Gaussian fit to the response distribution, where the distortions due to the average baseline shift have been corrected for, in order to represent the true intrinsic resolution of the filter. The corrected response is defined as

$$\mathcal{R}' = \left\langle \frac{E_{\mathrm{T}}^{\mathrm{LUT}} - \delta(\mathrm{BCID})}{E_{\mathrm{T}}^{\mathrm{truth}}} \right\rangle, \tag{6.2}$$

where the mean shift δ is determined per BCID from a simulation without signal pulses. The magnitude of the fluctuations in the trigger tower E_{T} reconstruction is determined by the fractional resolution, defined as $\sigma_{\mathcal{R}'}/\mathcal{R}'$, and is modelled as a function of the signal pulse $E_{\mathrm{T}}^{\mathrm{truth}}$. The ToyMC assumes no fluctuations in the pulse height due to the statistical processes of shower developments, as well as losses due to longitudinal shower leakage. Therefore we need only consider the noise term (N), which can be obtained from a fit to the ToyMC data using the following function:

$$\frac{\sigma_{\mathcal{R}'}}{\mathcal{R}'} = \frac{N}{E_{\mathrm{T}}^{\mathrm{truth}}}. \tag{6.3}$$

6.8 FIR Filter Strategies

The correct selection of the FIR filter coefficients is crucial for optimising the trigger tower BCID efficiency and E_{T} resolution. Three different filter strategies are considered that could be easily implemented in the nMCM.

The simplest of all is a *trivial* filter. It uses just a single multiplier to pass through the ADC data effectively unmodified. This means that only contributions in-time are included, helping to minimise pile-up contributions. However, this makes the filter susceptible to incoherent white noise that would otherwise approximately cancel over many independent samples. The *matched* filter approach was adopted during Run 1, where the coefficients are chosen to be proportional to the calorimeter pulse amplitude at each sample. This is the optimal configuration of filter coefficients for white noise [103]. *Autocorrelation* filters take advantage of the cross-correlation of a signal with itself at different samples and are effective at identifying the presence of periodic signals which are obscured by noise. The structure of the correlation will depend on the pulse shape and bunch spacing, while the strength of the correlation will depend on the pile-up conditions. It is therefore possible to produce autocorrelation coefficients optimised for a specific set of these conditions.

The ToyMC calculates the noise autocorrelation matrix of linear correlation coefficients using the sample Pearson correlation method [104]:

$$R_{ij} = \frac{n\sum S_i S_j - \sum S_i \sum S_j}{\sqrt{(n\sum S_i^2 - (\sum S_i)^2)(n\sum S_j^2 - (\sum S_j)^2)}}, \tag{6.4}$$

where S_i and S_j are the values of the ADC data samples for particular positions in the sample window and n is the number of sample windows considered. The matrix is determined by randomly selecting independent windows of ADC data centred on a filled bunch crossing, for a simulation including only thermal and pile-up noise. The set of autocorrelation coefficients $\boldsymbol{a}$ are extracted by multiplying the inverse of

the noise correlation matrix by the normalised pulse shape $\boldsymbol{g}$ [105]:

$$\boldsymbol{a} = \boldsymbol{R}^{-1} \cdot \boldsymbol{g}. \tag{6.5}$$

The correlation matrix for a FCal1 trigger tower with a sample frequency of 40 MHz and a bunch spacing of 25 ns is given in Figure 6.7a. The diagonal elements show perfect correlation between a sample and itself, while the correlation between different off-diagonal elements becomes weaker the further they are separated, and eventually show anti-correlation as a result of the pulse entering undershoot. The strength of the correlation is very similar for samples separated by the same distance, which is connected to the 25 ns bunch spacing.

The result of the autocorrelation calculation is shown in Figure 6.7b by the black points, which have been normalised to the central sample amplitude of the calibrated integer coefficients, given by the blue dashed line. The contributions to the FIR sum either side of the central sample are strongly negatively weighted by the coefficients. The filter is less dependent on the pedestal level than other filters due to the small coefficient sum, which is of significant advantage in areas that experience large pedestal shifts.

The performance of these three filter types is shown in Figure 6.8 for a FCal1 trigger tower. The autocorrelation filter demonstrated a significantly better BCID efficiency than the other filters in this high pile-up environment and reaches full efficiency at approximately 12 GeV. The trivial filter is found to perform better than the matched filter, as used during Run 1. This is because the thermal noise is insignificant in this region of the calorimeter compared to the pile-up noise and therefore the matched filter, which is optimised for white noise no longer performs well. The response of the different filters is dominated by their sensitivity to pedestal shifts and is related to the sum of the coefficients used. In the case presented, the single coefficient used for the trivial filter has a value of 15 in order to maximise the use of the LUT. The autocorrelation filter therefore has the greatest independence of the pedestal as a

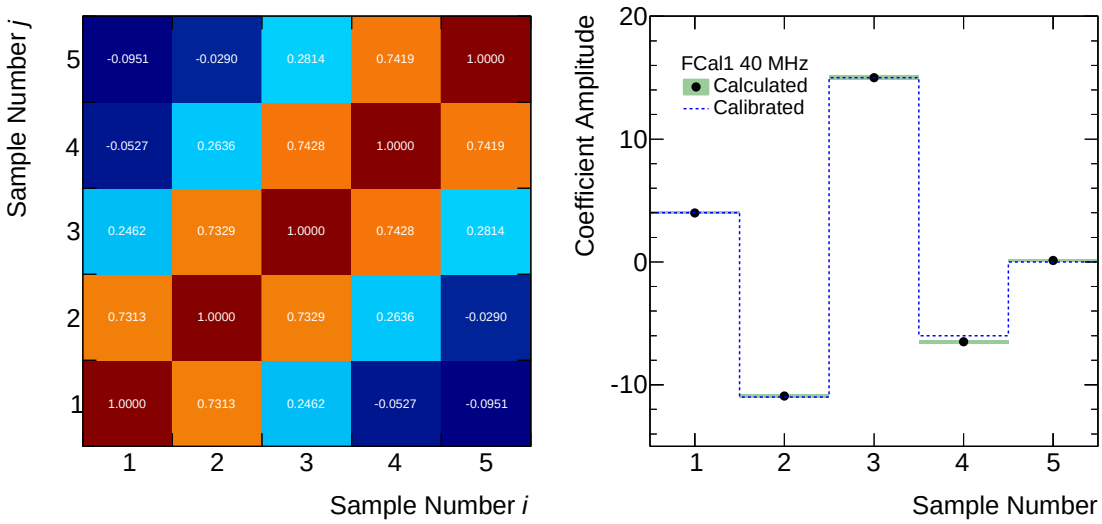

(a) (b)

Figure 6.7: Calibration of filter coefficients for a trigger tower in FCal1 with 40 MHz sampling and 25 ns bunch spacing. (a) shows the correlation matrix $\boldsymbol{R}$ between samples and (b) shows the corresponding filter coefficients $\boldsymbol{a}$ after normalisation.

result of the large negative coefficients used. Finally, the autocorrelation filter is also found to have the best resolution. The autocorrelation filter proves to have the best performance in each aspect, offering a significant improvement over the Run 1 performance in an environment dominated by pile-up noise.

6.9 Sampling Frequency

The ADCs of the nMCM digitise at a frequency of 80 MHz. One of the main motivations for choosing a higher sampling frequency is to extend the reliability of the saturated BCID algorithm to higher E_{T}. However, it is also possible to take advantage of the higher frequency samples in the FIR filter. Figure 6.9a shows the correlation matrix obtained for an EMEC Inner Wheel (IW) trigger tower with a sample frequency of 80 MHz and a bunch spacing of 25 ns. In this case, nine samples taken symmetrically about the peak sample are used so that the filter covers the same time window as that for five 40 MHz samples. The corresponding coefficients are shown in Figure 6.9b.

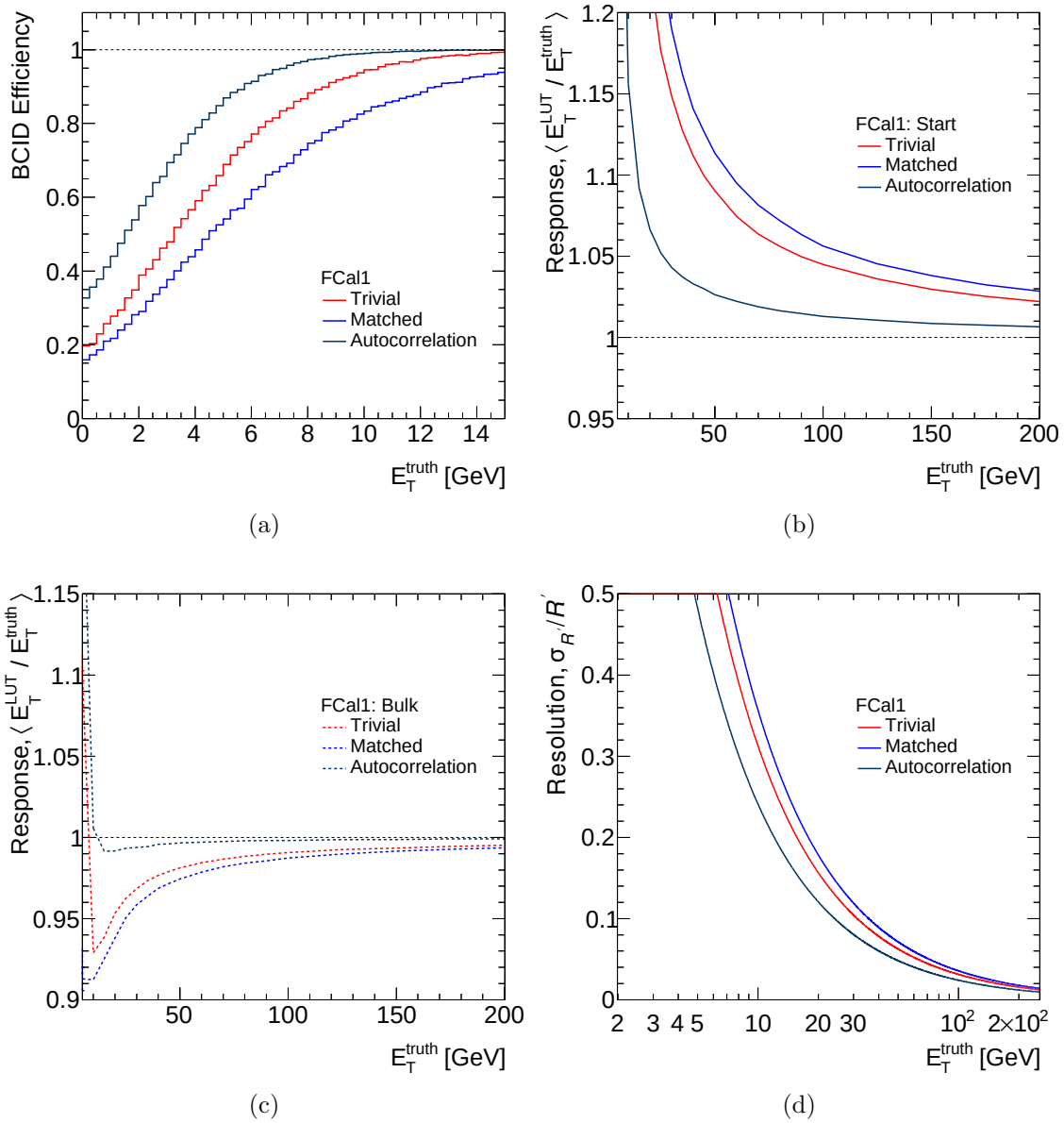

Figure 6.8: The performance of different filter strategies used in FCal1 as a function of transverse energy. Subfigure (a) shows the BCID efficiency for correctly identified signals. Subfigures (b) and (c) show the response for events at the start and bulk of the bunch train, respectively. Subfigure (d) shows the fractional resolution.

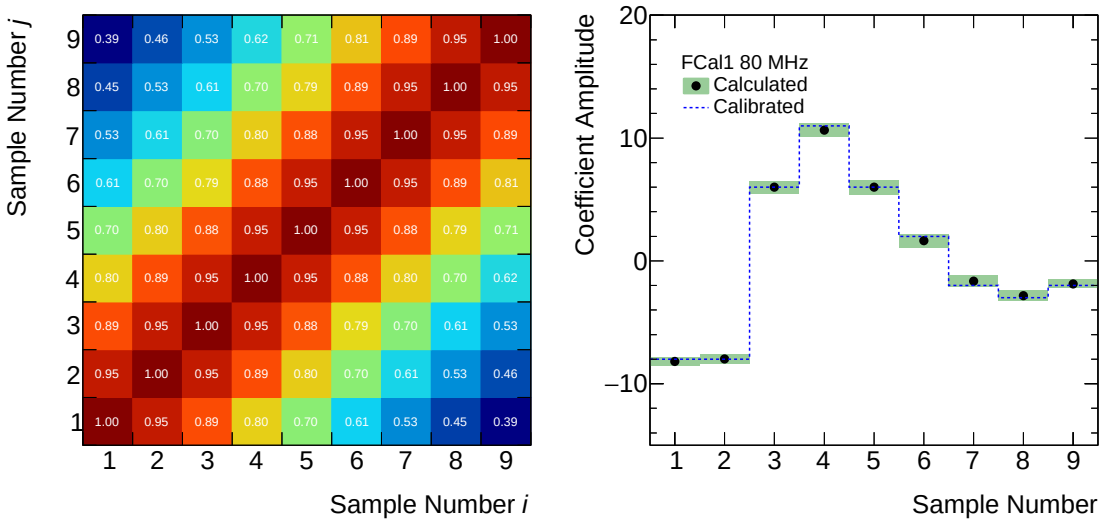

(a) (b)

Figure 6.9: Calibration of filter coefficients for a trigger tower in the EMEC IW with 80 MHz sampling and 25 ns bunch spacing. (a) shows the correlation matrix $\boldsymbol{R}$ between samples and (b) shows the corresponding filter coefficients $\boldsymbol{a}$ after normalisation.

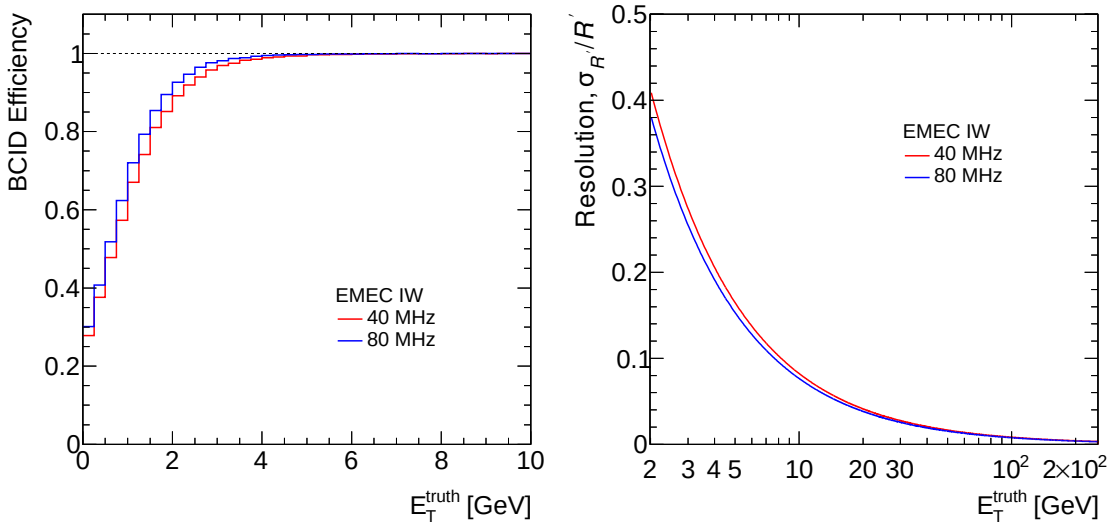

(a) (b)

Figure 6.10: Performance of a trigger tower in the EMEC IW for 40 MHz and 80 MHz sampling frequencies as a function of transverse energy. (a) shows the BCID efficiency for correctly identified signals and (b) shows the fractional resolution.

Figure 6.10 compares the performance between autocorrelation filters designed for 40 MHz and 80 MHz operation. There is an improvement observed in both the BCID efficiency and fractional resolution when operating at 80 MHz. This is also true in the other calorimeter regions except FCal1, where there is no significant difference.

The large number of channels in L1Calo places constraints on the data volume that can be readout and still achieve the maximum L1A rate. It is also a founding principle that enough data is readout such that the L1Calo trigger decision can be fully recreated offline. To this end, operating the FIR filter at 80 MHz would mean a large increase in the data volume that does not represent enough of a gain in performance when compared to the correction of the pedestal shifts. It is therefore decided to retain the FIR filter operation at 40 MHz.

6.10 Number and Precision of Coefficients

The benefit of increasing the nominal sampling window from five samples to seven was investigated, as well as increasing the nominal bit precision of the coefficients from four signed bits to five signed bits. In each of these cases there is no systematic benefit observed over the nominal configuration in the context of autocorrelation filters. Increasing the sampling window would also have the disadvantage of increasing the latency for a trigger decision.

6.11 Pedestal Correction

The pedestal shift experienced at the start of a bunch train is one of the largest factors affecting the signal processing performance. It has meant that significantly larger noise cuts than ideally necessary have been required during Run 1 to compensate for the high event rates generated by this effect alone. This effect can only be controlled up until a certain luminosity point at which the E_{T}-shift surpasses the

noise cuts. It is also possible for large noise cuts to produce large fake-$E_{\mathrm{T}}^{\mathrm{miss}}$. The shifts also cause a bias on the peak-finder algorithm to favour certain bunch crossings over others that may contribute to triggers being issued in the wrong bunch crossing. Although the autocorrelation filters are far more robust against such shifts due to the smaller coefficient sums than the matched filters, an additional solution is required.

The most favourable option is to apply an average correction to the FIR filter output, because at this point all the individual FIR sums have been combined into a single uncalibrated E_{T} estimate for the bunch crossing and the finest precision is available. Additionally, a correction at this point will not only affect the final E_{T} estimate calculated by the LUT, but will also alter the result of the peak-finder BCID decision. It is also important to compute an average for every bunch crossing independently. Represented mathematically, the corrected FIR output is given by subtracting a correction term from the original FIR output:

$$f'(t) = f(t) - (\langle f \rangle(\mathrm{BCID}) - f_{\mathrm{p}}), \text{where } f_{\mathrm{p}} = \sum_{i=0}^{n-1} a_i \times p. \tag{6.6}$$

Here the parameter f_{p} takes into account the expected pedestal level in the FIR output and is computed by the sum of the products of each filter coefficient and the measured pedestal (p) in ADC counts. The parameter $\langle f \rangle(\mathrm{BCID})$ represents the average FIR output computed for the current bunch crossing identifier number.

In the ToyMC, signal pulses are not added into the simulation until all these averages have been measured for the simulated conditions, to prevent distortions to averages measured. The average used in the ToyMC is a simple mean, calculated by accumulating the FIR output values for a given bunch crossing and dividing by the number of samples. More complex schemes such as a moving average are also possible and may prove more robust against bursts of noise during real operation, depending on the number of samples accumulated.

6.12 Firmware Implementation

Figure 6.11 shows an overview of the FPGA logic for the nMCM that is structurally similar to the ASIC design. In addition to the old MCM functionality there are blocks dedicated to the computation and correction of the average pedestal shift per bunch crossing, and separate LUTs for output to the CP and JEP systems. Note that separate monitoring and readout of each of the LUTs is required, as well as readout of the pedestal correction value. The FIR output sums are accumulated in 32-bit memories during a programmable number of LHC orbits. Once completed, the 16-bit average of each sum is computed through a bit shifted division operation. Finally the 'PedCorr' block applies the correction as shown in (6.6) by accessing the relevant average and the value of the expected pedestal level.

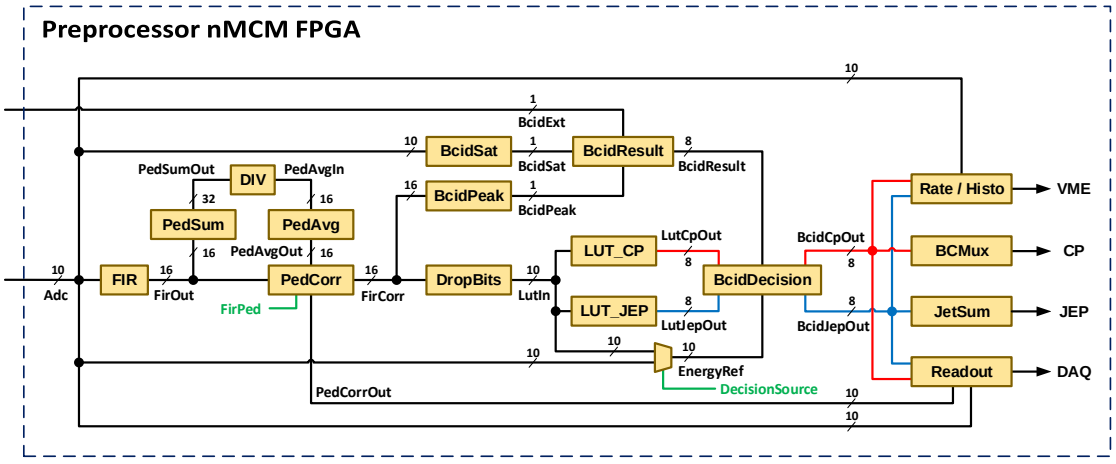

Figure 6.11: Overview of Preprocessor nMCM FPGA logic for one channel that includes both the MCM logic shown in Figure 5.3 and processing blocks for the pedestal correction and additional LUT.

6.13 Results

Considering the performance and practicality of the different options presented in the previous sections, the final setup proposed for Run 2 is to use autocorrelation filters with five 4-bit signed precision coefficients and a 40 MHz sampling frequency

in combination with the pedestal correction. The results discussed in this section compare the performance of signal processing for the Run 1 and Run 2 configurations in the ToyMC at $\langle\mu\rangle = 40$ for trigger towers in different calorimeter regions. An example of the calibration used for the matched and autocorrelation filters in these different regions is given in Table 6.1. The smaller sum of the coefficients for autocorrelation filters means that in almost all cases a lower range is used, as well as a smaller offset. In regions where pile-up is a small contribution, as in the central region of the hadronic calorimeter layer, negative autocorrelation coefficients do not appear. Typically in FCal, where the pile-up is dominant and the pulse shape narrower, the second and fourth coefficients have significant negative weights. Otherwise, the negative weights tend to appear for the first and fifth coefficients. There is a much greater variation in the calibration of the autocorrelation filters which adds complexity.

Table 6.1: Example matched (Run 1) and autocorrelation (Run 2) FIR coefficients and their corresponding LUT calibration parameters for different calorimeter regions determined in the ToyMC.

Run	Region	Coefficients	`dropbits`	`offset`	`slope`
Run 1	EMB	0 9 15 11 7	5	42994	1036
	EMEC OW	1 10 14 10 6	5	43052	1063
	EMEC IW	1 10 14 10 6	5	43052	1063
	FCal1	0 4 11 6 0	4	43243	1042
	Tile	2 10 15 11 5	5	45220	1064
	HEC OW	2 10 15 11 5	5	45220	1064
	HEC IW	0 9 15 11 6	5	43376	1071
	FCal23	0 4 11 6 0	4	43492	1048
Run 2	EMB	-8 4 12 3 -1	4	20085	1030
	EMEC OW	-5 3 6 1 -2	3	12271	1067
	EMEC IW	-14 9 13 -2 -4	4	3766	1076
	FCal1	4 -11 15 -6 0	3	8183	1091
	Tile	1 9 15 10 4	5	43428	1128
	HEC OW	0 2 4 3 1	3	42107	1066
	HEC IW	-1 5 9 5 1	4	38663	1031
	FCal23	1 -4 6 -1 0	2	16120	1040

The BCID efficiencies for the three scenarios described in Section 6.7 in the ToyMC are shown in Figure 6.12 for the Run 1 and Run 2 configurations for different

calorimeter regions. In the Run 1 configuration there is a substantial inefficiency that is most significant at very low-E_{T}, due to signals being missed altogether. This contribution is substantially reduced by the autocorrelation filters and provides much of the improvement in the efficiency of the correctly identified signals. It appears that below approximately 1 GeV many of the signals which were previously being missed are instead identified one bunch crossing early or late in the EM layer and forward hadronic regions. In some respects it is preferable to miss a signal than to identify it in an incorrect bunch crossing, but given that these signals are mostly below the typical noise cut there will be no significant effect on the behaviour of the trigger. There is also a reduction in the tail of the wrongly identified signals that is mostly responsible for the inefficiency at higher E_{T} values and will have a significant effect on the behaviour of the trigger. The calorimeter regions which benefit most greatly with the Run 2 configuration are those that have large contributions from pile-up noise. Although the contribution of missed signals is reduced for the Tile and HEC Outer Wheel (OW), there is a slight increase in the tail for signals that are identified in the wrong bunch crossing.

The linearity for signals occurring at the start of the bunch train and the fractional resolution performance for the Run 1 and Run 2 configurations are shown as a function of E_{T} in Figure 6.13 and Figure 6.14, respectively. The results for calorimeter regions with similar effects have been grouped together. The Run 1 configuration for particularly the EMEC IW and FCal1 is greatly affected by the pedestal shift at the start of the bunch train. After the application of the autocorrelation filters and pedestal correction the linearity for all the different calorimeters remains consistent over the full E_{T} range, until low E_{T}.

The fractional resolution performance is worst for trigger towers with $|\eta| > 2.5$ in the EM calorimeter layer, followed by the corresponding region in the hadronic calorimeter, with the best performance seen in the central regions. In all regions there is an improvement in the fractional resolution, except for trigger towers with $|\eta| < 2.5$ in the hadronic calorimeter layer, where there is a small degradation in the performance using the Run 2 configuration. The largest performance improvements

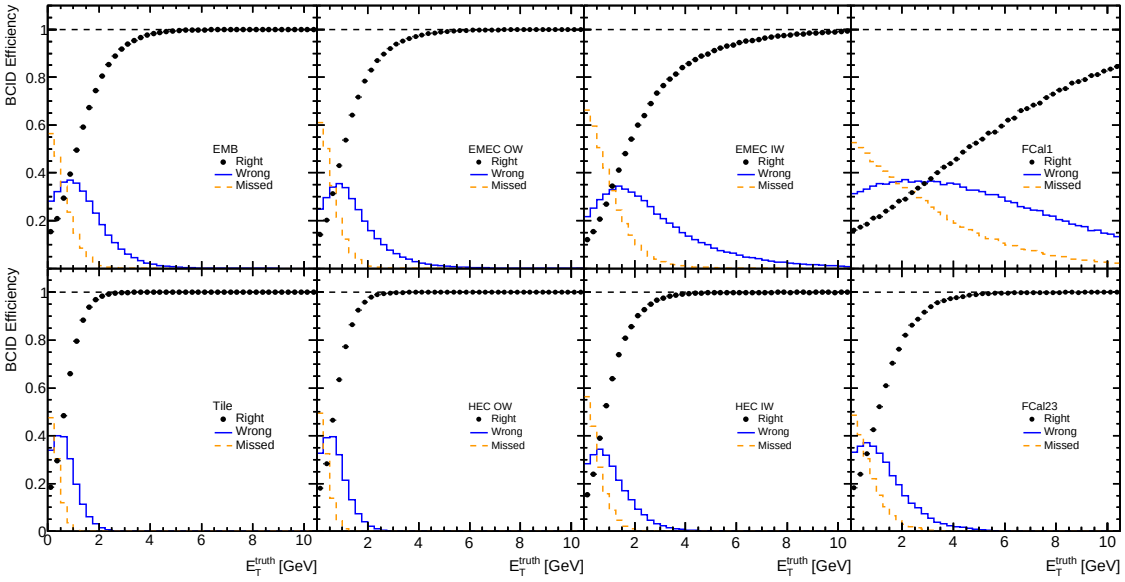

(a)

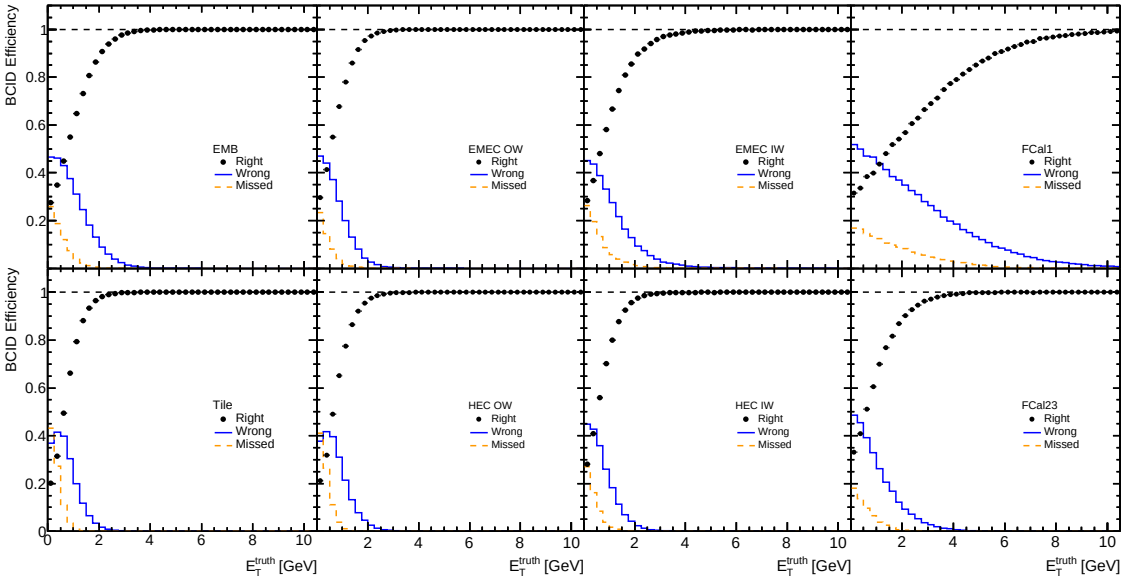

(b)

Figure 6.12: The BCID efficiency for different calorimeter regions in the ToyMC using (a) Run 1 and (b) Run 2 configurations. The black points show the BCID efficiency for correctly identified signals. The solid blue line shows where the peak-finder fires one bunch crossing early or late. The yellow dashed line shows the remaining case in which the signal is considered to have been missed by the peak-finder.

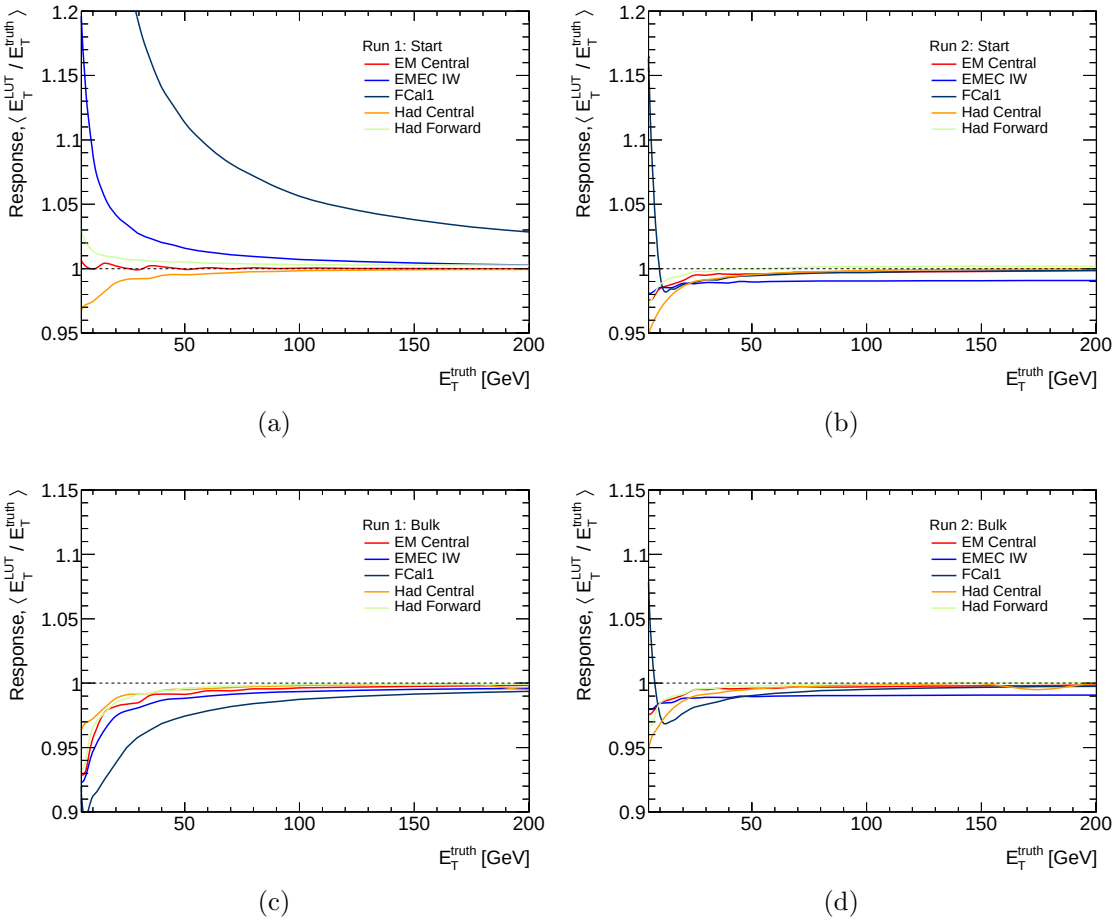

Figure 6.13: Trigger tower E_{T} response in the ToyMC as a function of the signal pulse E_{T} in different calorimeter regions. Subfigures (a) and (b) are for the Run 1 and Run 2 configurations at the start of the bunch train. Subfigures (c) and (d) are for the Run 1 and Run 2 configurations in the bulk of the bunch train.

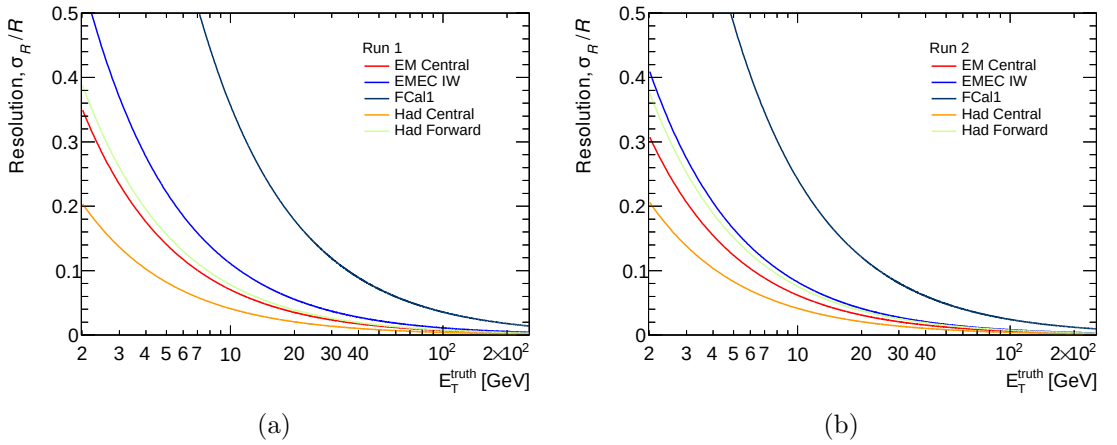

Figure 6.14: Fractional trigger tower E_{T} resolution in the ToyMC as a function of the signal pulse E_{T} for different calorimeter regions for the (a) Run 1 and (b) Run 2 configurations.

are seen in the EM layer. The results for the fitted fractional resolution curves are given in Table 6.2.

Table 6.2: The fitted fractional resolution performance in GeV for different calorimeter regions in the ToyMC for the Run 1 and Run 2 configurations, indicated by the measured noise term. The statistical uncertainties are insignificant compared to the quoted precision.

Setup	EM Central	EMEC IW	FCal1	Had. Central	Had. Forward
Run 1	0.704	1.109	3.569	0.410	0.781
Run 2	0.619	0.824	2.422	0.415	0.757

6.13.1 Timing Stability

Fluctuations in the timing of signal pulses as well as systematic shifts with respect to signals perfectly timed for the centre of the bunch crossing will degrade the performance of the signal processing. The autocorrelation filter coefficients in FCal often contain large negative coefficients neighbouring the large positive central coefficient. This is likely to make the performance of these filters more sensitive to small shifts in the timing of signals. Figure 6.15a compares the BCID efficiency for 5 GeV signals in the Run 1 and Run 2 configurations for systematic shifts in timing from −5 ns to +5 ns. Negative shifts indicate that the pulse peaks earlier than expected. Despite a significant drop in the identification efficiency at large positive shifts, causing signals to be identified in the wrong bunch crossing, the Run 2 configuration provides the best performance over the full range. A similar comparison is shown in Figure 6.15b of the response for a 30 GeV signal. In this case, positive shifts cause the response of the Run 2 configuration to rapidly diverge from unity. It is possible to achieve fine-timing calibration for signals with a total uncertainty of ±2.4 ns [106]. Therefore, it is essential that the timing of signals in FCal are kept stable and within this limit.

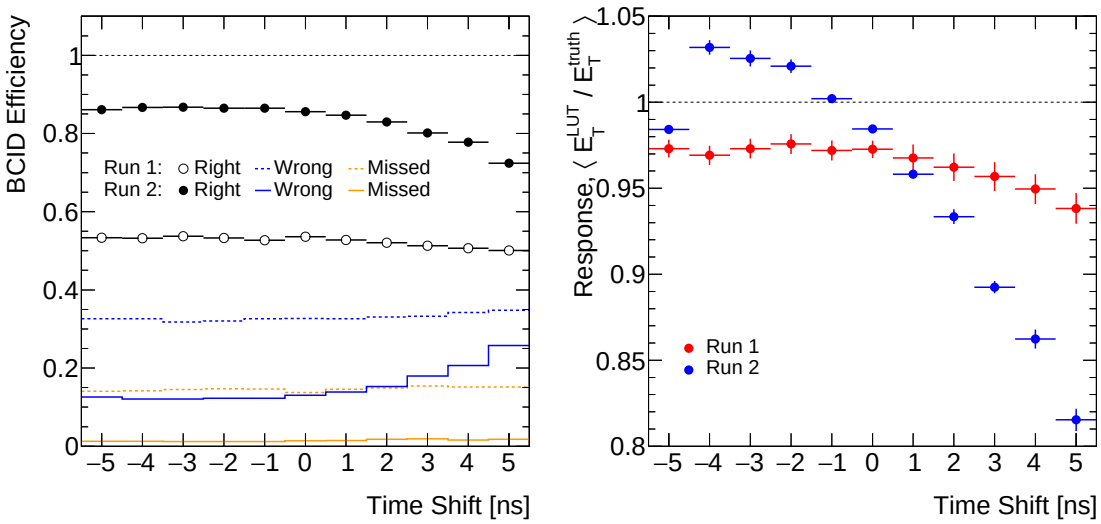

(a) (b)

Figure 6.15: FCal1 performance comparison in the ToyMC between the Run 1 and Run 2 configurations for systematic timing shifts from −5 ns to +5 ns. Subfigure (a) shows the BCID efficiency for 5 GeV signals. The black points show correctly identified signals, the blue lines show where the peak-finder fires one bunch crossing early or late, and the yellow lines show the signals missed by the peak-finder. Subfigure (b) shows the response for 30 GeV signals.

6.14 Summary

The autocorrelation FIR filter approach improves the BCID performance significantly in high pile-up environments over the matched filter, as well as offering improvements in resolution. The average pedestal correction significantly improves the response behaviour as a function of the position in a bunch train. Combing both of these strategies together offer a large improvement in performance for Run 2 and can be accommodated within the design of the nMCM.

CHAPTER 7

OPTIMISATION OF THE L1CALO TRIGGER NOISE CUTS

7.1 Introduction

The careful optimisation of the L1Calo trigger tower noise cuts is a necessary part of the pile-up suppression strategy in order to maintain the lowest feasible trigger thresholds for high luminosity collisions, and was key to the successful operation of $E_{\mathrm{T}}^{\mathrm{miss}}$ triggers during 2012. The introduction of the nMCM during LS1 has enabled the use of new signal processing techniques, better suited to the pile-up effects experienced by L1Calo, and will help to minimise the magnitude of the required noise cuts and achieve an equivalent or better trigger performance at high luminosity. The proposed mode of operation for processing trigger tower signals during Run 2 is established in Chapter 6 as the use of autocorrelation FIR filter coefficients and an average pedestal correction in combination. It is important to also develop a strategy for the optimisation of noise cuts for the average conditions expected during Run 2

with the new signal processing features.

Noise cuts are applied in the LUT of the MCMs and act to zero energies below a given threshold value. It is not possible to reconfigure the LUT without loss of data and so this value cannot be changed during collisions to meet the specific pile-up conditions at any given time. Noise cuts have a significant impact on the behaviour of L1Calo, with implications for the whole trigger system. It is therefore more practical to maintain a fixed set of noise cuts suitable for an entire run period to minimise the demands on the trigger operation and the configuration of the MC. These limitations require that noise cuts are chosen carefully to give close to optimal performance over the widest possible range of the expected luminosity.

In the following study, MC samples have been used with a simulated centre-of-mass energy of $\sqrt{s} = 14\,\text{TeV}$, an average number of interactions per beam crossing of $\langle\mu\rangle = 60$, and a bunch spacing at 25 ns intervals. This represents the conditions the LHC machine expects to achieve before the end of Run 2 and approximately corresponds to a beam luminosity of $2\times10^{34}\,\text{cm}^{-2}\,\text{s}^{-1}$. These samples use a description of the ATLAS detector geometry including the IBL, which was installed during LS1. The data sets used have been produced by reprocessing simulated events with the proposed Run 2 signal processing configuration and for five sets of noise cuts. The trigger performance is measured in each case and compared to that of the default simulation for Run 1.

Low-p_{T} jet and $E_{\text{T}}^{\text{miss}}$ triggers are extremely sensitive to pile-up, and the nMCM is critical for keeping the thresholds reasonably low during Run 2. For high-p_{T} jets, there is a significant rate increase compared to Run 1, due to the rise in the centre-of-mass energy of the LHC from 8 to 14 TeV. Apart from raising trigger thresholds, the only other way to keep the rates under control is to use combined object triggers. Therefore this study is primarily concerned with the optimisation of noise cuts for the lowest threshold unprescaled multijet and $E_{\text{T}}^{\text{miss}}$ triggers in an effort to achieve equal or better performance compared to that measured in the Run 1 simulation. The nMCM features separate LUTs for input to the cluster processors and jet/energy-

sum processors, which allows a general approach to be taken in optimising noise cuts for jets and $E_{\mathrm{T}}^{\mathrm{miss}}$ without interfering with the performance of EM and TAU triggers. Opposed to the jet and $E_{\mathrm{T}}^{\mathrm{miss}}$ triggers, the optimisation of noise cuts for EM and TAU triggers requires consideration of the interplay with isolation requirements.

Final states with multiple jets are important for the study of high-order QCD, for measurements of $t\bar{t}$ production in the fully hadronic decay channel, and for many searches for new physical phenomena. A large $E_{\mathrm{T}}^{\mathrm{miss}}$ is a key signature for searches of new physics processes such as stable weakly interacting SUSY particles.

The ATLAS integrated luminosity near $\sqrt{s} = 14\,\mathrm{TeV}$ is expected to total around $150\,\mathrm{fb}^{-1}$ by the end of Run 2. This data set will enable precise measurements of the Higgs boson production rates and properties, and search in a large phase space for physics Beyond the Standard Model (BSM). The Level 1 trigger must provide comprehensive and efficient coverage of all triggers needed for SM and Higgs physics, while serving the diverse needs of the BSM searches. Much of the trigger space is covered by the decays of electroweak particles which have masses in the range of 80 to 125 GeV. Decays of these particles are to leptons and jets, resulting in objects with an offline p_{T} greater than about 30 GeV.

7.2 Monte Carlo Samples

The ATLAS software framework is named Athena [107] and is built upon a flexible high-energy physics data processing framework called Gaudi [108]. Athena uses Python to configure and load individual software packages written in C++, where the package structure is managed by the Configuration Management Tool (CMT). Packages with similar functionality are grouped into projects, for example AtlasTrigger and AtlasReconstruction. An overview of the ATLAS data flow is shown in Figure 7.1 for both simulated events and real experimental data. Processes, which include applications and algorithms, are marked in square-cornered boxes and persistent data objects are marked in slanted boxes.

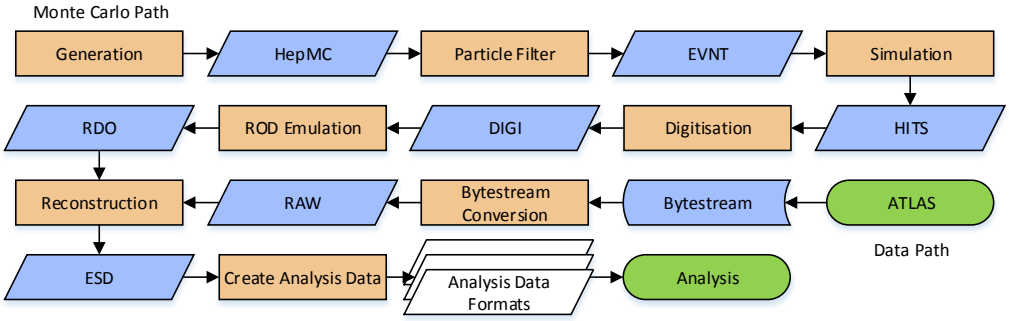

Figure 7.1: The flow of ATLAS data from event generators and through the simulation software or from the detector with both routes passing through to reconstruction and analysis.

Generators produce events in standard HepMC format [109] and can be filtered at generation time so that only events containing certain properties are stored. The generator is responsible for any prompt decays such as those of W or Z bosons, but any particles considered to be stable are stored as they are expected to propagate far enough to interact with detector material before decaying. EVNT files hold the four-vectors and production/decay vertices of particles from the different event generators, used to simulate physics processes. The generated events are processed by the ATLAS detector simulation [110] which propagates each particle through the detector within the Geant4 framework [111], recording any energy deposits in sensitive parts of the detector as hits. The digitisation software takes these hits and converts them into voltages or currents, taking into account the response of the different detectors and signal shaping. At this point detector noise is added to the event and a pile-up overlay is included. The digits of each subdetector are written out as Raw Data Objects (RDOs), which is the MC equivalent of the RAW data format produced by the bytestream conversion of real ATLAS data. The ATLAS reconstruction runs over either RAW or RDO files to produce identical output, from which point data and simulation use the same framework. Event Summary Data (ESD) files contain the full output of the ATLAS reconstruction algorithms, but also retain the detector hit information that forms the input to the reconstruction. It is therefore possible to reprocess trigger algorithms with different configurations using

this data format, without having to do the full reconstruction. This method has been used to produce the data samples used in this study. Finally, the reconstructed data are converted into data formats used for analysis.

Simulated data sets for a number of different types of physics processes are used in this study with a mixture of signatures including jets and $E_{\mathrm{T}}^{\mathrm{miss}}$. Minimum-bias events are used to represent the background event rate and are important in understanding the conditions expected for high luminosity $\sqrt{s} = 14\,\mathrm{TeV}$ collisions. Events from the $t\bar{t}$ process were produced using the Next-to-Leading Order (NLO) matrix element generator POWHEG [112,113,114,115] interfaced with PYTHIA8 [116] to perform showering and hadronization, and include all $t\bar{t}$ final states involving at least one lepton. A sample of simulated $ZH \rightarrow \nu\bar{\nu}b\bar{b}$ events was produced with the PYTHIA8 generator, and has a final state topology consisting of $E_{\mathrm{T}}^{\mathrm{miss}}$ from the $Z \rightarrow \nu\bar{\nu}$ decay and two b-jets from the decay of the Higgs boson. The final process considered is $H \rightarrow \tau\tau$, where one tau lepton decays leptonically and the other decays hadronically and was produced using POWHEG interfaced with PYTHIA8. In this sample the Higgs boson is produced via the VBF mechanism, which results in an topology containing two high-p_{T} jets with a large separation in $\Delta\eta$, as well as the tau decay signatures. The mass of the Higgs boson in each of these samples is set to 125 GeV.

7.3 nMCM Simulation

The trigger tower simulation was updated to support the important new functionality of the nMCM in order to provide a good representation of the potential Run 2 performance. Firstly, suitable autocorrelation filter coefficients were derived using the method as given in Section 6.8 for simulated ADC data and pulse shapes. The minimum-bias data set provides an excellent representation of the background physics processes the detector will experience and is therefore best suited to the derivation of the autocorrelation filter coefficients, pedestal correction values and

noise cuts. The simulation contains five different calorimeter pulse shapes corresponding to different subdetectors, the shapes of which are given in Table 7.1 for the five 40 MHz samples centred on the pulse peak. The results of the autocorrelation calculation and the calibrated coefficients are given in Table 7.2.

Table 7.1: The five 40 MHz samples of the simulation pulse shapes per calorimeter region, centred on the pulse peak and normalised to a peak height of unity.

Calorimeter	1	2	3	4	5
EMB/EMEC	0.10	0.47	1.00	0.60	0.12
HEC	0.03	0.61	1.00	0.76	0.39
FCal1	0.00	0.21	1.00	0.30	-0.45
FCal23	0.00	0.26	1.00	0.52	-0.23
Tile	0.06	0.56	1.00	0.67	0.28

Table 7.2: Example autocorrelation FIR coefficients and their corresponding LUT calibration parameters for different calorimeter regions determined from minimum-bias simulated events.

Region	Coefficients	`dropbits`	`offset`	`slope`
EMB	-1 -1 8 1 -2	3	20495	1051
EMEC OW	-2 -2 9 0 -3	3	8190	1092
EMEC IW	0 -3 6 -1 -1	2	7935	1058
FCal1	3 -7 10 -3 0	3	12340	1073
Tile	-3 4 10 5 0	4	33453	1062
HEC OW	-4 2 6 2 -2	3	16182	1044
HEC IW	-12 4 15 1 -5	4	5671	1031
FCal23	2 -8 10 -1 0	4	43492	1048

It is not feasible to produce a true emulation of the pedestal correction within the ATHENA simulation framework as it would take excessively long to accumulate the FIR output sums necessary on-the-fly. Physics samples are also not representative of typical collisions and as a result will distort such a correction. It is more practical to provide pre-computed correction values based on the location of the trigger tower, the current simulated BCID, and $\langle\mu\rangle$ conditions. For the purposes of this analysis a demonstrator method was devised to accept pre-computed correction values obtained by measuring the mean FIR output per $|\eta|$-bin and per BCID for minimum-bias data with the application of the autocorrelation filter coefficients. The limitation

of this method is that it does not provide independent trigger tower corrections, but effectively an averaged correction per $|\eta|$-bin. Figure 7.2 shows the average FIR output measured for $|\eta|$-bins in the EM and hadronic layer with minimum-bias data and for one bunch train, where the scale of the values depends on the sum of the coefficients. These values are then used in the pedestal correction as given in (6.6).

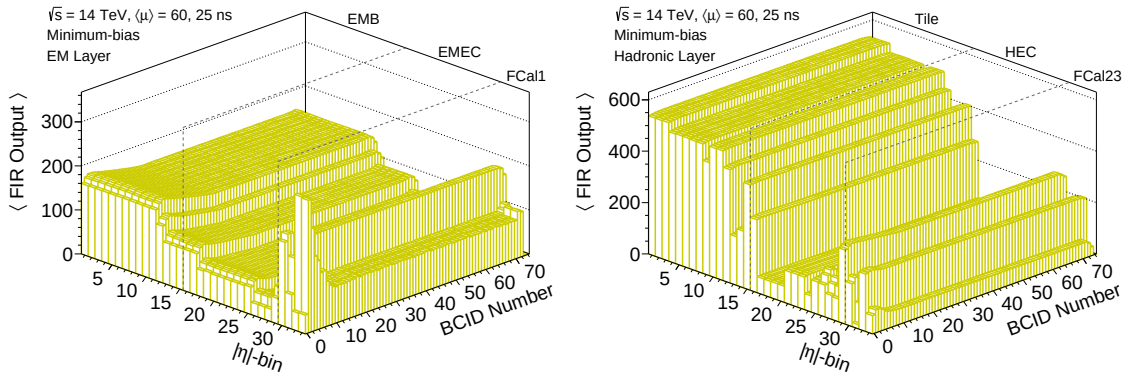

(a) (b)

Figure 7.2: Average FIR output of the autocorrelation filters in minimum-bias simulated events per $|\eta|$-bin and over one bunch train for trigger towers in (a) the EM and (b) hadronic calorimeter layers.

7.4 Derivation of Noise Cuts

The nominal noise cut applied at the trigger tower level is approximately 1 GeV and during 2012 larger noise cuts were applied to the EMEC IW and FCal in order to suppress the effects of pile-up. A more general noise cut strategy was proposed for 2015 in an effort to maintain a uniform response to physics processes over the whole detector, with the aim of maximising the physics acceptance while achieving the lowest background rates. The pile-up noise is non-Gaussian in nature and its effect on the digital processors in the Level 1 trigger system depends on the BCID efficiency of a given channel. So, instead of defining noise cuts based on some number of standard deviations of the noise, it has been decided to measure the trigger tower occupancy. This approach aims to maintain a constant value of occupancy over the

detector by treating each $|\eta|$-bin of trigger towers independently.

The trigger tower occupancy per $|\eta|$-bin is defined as the average fraction of trigger towers per event where the peak-finder has fired and is measured as a function of $\texttt{FIR}/2^{\texttt{dropbits}} \times \texttt{slope} - \texttt{offset}$. Measuring the occupancy in such a way provides a finer scale than the LUT output, which one can fit with an exponential function in order to extract the value for `noisecut` for a given occupancy working-point via interpolation. The noise cuts using this method have been obtained for five different occupancy scenarios for the Run 2 configuration (MC15): 0.25, 0.5, 1.0, 2.0, 4.0% and are shown in Figure 7.3 converted into units of GeV along with those noise cuts for the Run 1 configuration used in 2012 (MC12) for reference.

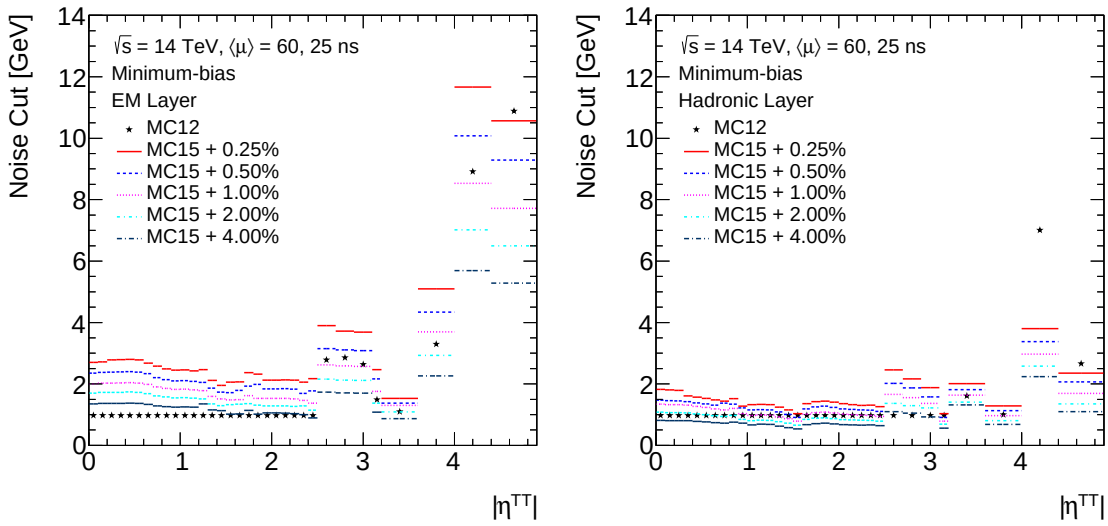

(a) (b)

Figure 7.3: Noise cut thresholds in GeV as a function of the trigger tower $|\eta|$ for (a) the EM and (b) hadronic calorimeter layers for MC12 and different occupancy values in MC15.

7.5 Trigger Optimisation

The substantial increase in the centre-of-mass energy and peak luminosity for Run 2 means that the Level 1 trigger rates are expected to be a factor of five higher using

the same Run 1 trigger menu. The main constraint on the trigger menu design is therefore the maximum L1A rate and much effort has gone into increasing this limit from 70 kHz in Run 1 to around 100 kHz for Run 2. It is therefore important to consider how the Level 1 trigger menu design must evolve to accommodate all the physics requirements of the experiment for Run 2 conditions, within this limited bandwidth and the limited number of items available.

The strategy has been to design a menu similar to that of Run 1 with slight increases to the trigger thresholds to cope with the increased rate. This is only possible with significant upgrades to the Level 1 trigger system during LS1 (as mentioned in Section 5.4), which notably include the upgraded MCM, the ability to use trigger items with restricted η ranges and topological requirements. The rates can be further controlled with the optimisation of the isolation requirements for EM and hadronic tau objects. The only other available option is to resort to heavier use of combined object triggers.

The most useful Level 1 trigger signatures for electroweak-scale particles are from isolated electrons and muons. The main goal for Run 2 is to preserve the low-p_{T} trigger thresholds at Level 1 for single electrons and muons that were used successfully in Run 1. The ability to maintain unprescaled Level 1 triggers on these objects not only maximises the data samples for Higgs studies, but also produces data samples that can be thoroughly understood and lead to high quality physics results with small systematic uncertainties. Another important goal in Run 2 is to maintain the experiment's ability to do physics with electroweak decays to hadronically-decaying tau leptons, jets and $E_{\mathrm{T}}^{\mathrm{miss}}$ from neutrinos and other non-interacting particles. Bandwidth allocations must balance the physics requirements from different working groups and are based on detailed arguments and agreed in the menu coordination group. Typically roughly equal shares are given to electrons and muons, with a large share reserved for jets, $E_{\mathrm{T}}^{\mathrm{miss}}$, tau leptons and multi-object triggers.

Table 7.3 shows a list of the proposed Level 1 trigger menu items for a luminosity of $2{\times}10^{34}\,\mathrm{cm}^{-2}\,\mathrm{s}^{-1}$ and their expected rates. The electromagnetic triggers (electrons

and photons) are denoted by the prefix 'EM'. The rates of these triggers can be controlled by adding hadronic core isolation ('H'), adding electromagnetic isolation ('I'), or by varying the thresholds with η to account for energy losses ('V'). The muon triggers are denoted by the prefix 'MU'. The tau lepton triggers are denoted by the prefix 'TAU'. Jet triggers are denoted by the prefix 'J', and $E_{\mathrm{T}}^{\mathrm{miss}}$ triggers by 'XE'. The number given before these object prefixes represent the minimum multiplicity required, while the subsequent number gives the threshold in GeV. The default $|\eta|$-region for jet triggers is assumed to be $|\eta| < 3.2$ throughout this document, with other ranges specified explicitly in the trigger name. For example, the Run 2 convention for a forward jet passing a 20 GeV threshold is J20.32ETA49, signifying the range greater than 3.2 and less than 4.9 in $|\eta|$. Topological requirements, such as the ΔR between two objects ('DR'), are followed by the objects that must satisfy the requirement. The proposal already significantly exceeds the hard limit of about 100 kHz and there is a 20% systematic uncertainty associated with the rate calculations.

The driving force behind the optimisation of the L1Calo noise cuts is the event rate of the lowest threshold unprescaled triggers. It is important that the thresholds for such triggers are as low as possible in order to maximise the potential physics coverage. This analysis considers the effect of different noise cut sets on the main single jet threshold (J100), the multijet trigger (4J20), and the main Level 1 $E_{\mathrm{T}}^{\mathrm{miss}}$ trigger (XE70) in selecting the best overall optimisation.

Figure 7.4 shows the Level 1 four-jet and $E_{\mathrm{T}}^{\mathrm{miss}}$ trigger rates as a function of the Level 1 E_{T} threshold for each of the five noise cut scenarios as well as the default 2012 configuration. It is clearly demonstrated that the event rates in the Run 2 simulation experience a much better dependence on the trigger threshold, due to the superior pile-up control of the pedestal correction and autocorrelation filters. This leads to a substantial rate reduction in the threshold ranges of interest. The noise cuts provide a further control of the rates, with the lower occupancy noise cut sets giving a consistent decrease in the expected rate for all triggers.

Table 7.3: A sample of the proposed Run 2 Level 1 trigger menu for a luminosity of $2\times10^{34}\,\mathrm{cm}^{-2}\,\mathrm{s}^{-1}$ at $\sqrt{s} = 14\,\mathrm{TeV}$. Errors given in the table are statistical uncertainties from the rate estimation tool. There is an additional 20% systematic uncertainty in the rate predictions which is not quoted. Rate numbers without errors come from a different source of estimation. Note that rate overlaps are non-trivial thus unique rates of all triggers do not add up to the total rate. [117]

Trigger	Rate (kHz)	Unique Rate (kHz)
MU20	19	18
2MU10	3.5	2.1
3MU6	1.2± 0.6	0.8
EM15VH_MU10	2.2± 0.3	0.5
2EM8VH_MU10	1.0± 0.2	0.2
EM8VH_2MU6	1.0± 0.2	0.2
EM24VHI	21.7± 1.1	16.0
EM50	8.4± 0.8	1.3
2EM15VH	6.2± 0.7	2.6
3EM7V_EM15VHI	5.0± 0.5	1.4
TAU60V	10.1± 0.9	1.7
TAU20_XE45_J20	5.5± 0.7	0.7
TAU12I_TAU20I_J25_DR28-TAU12I-TAU20I	13.3± 1.2	4.4
TAU12I_TAU20I_J20.32ETA49_DR28-TAU12I-TAU20I	1.7± 0.7	0.6
TAU12I_TAU20I_XE35	4.1± 0.7	0.9
EM15VHI_TAU12I_J25_DR28-TAU12I-EM15VHI	4.8± 0.7	0.7
EM15VHI_TAU12I_J20.32ETA49	0.7± 0.3	0.3
EM15VHI_TAU40	3.2± 0.5	0.1
EM15VHI_TAU12I_XE35	1.9± 0.5	0.1
TAU12I_MU10_J25_DR28-TAU12I-MU10	4.6± 0.5	1.4
TAU12I_MU10_J20.32ETA49	0.5± 0.2	0.5
TAU20I_MU10	3.2± 0.3	1.0
TAU12I_MU10_XE35	0.9± 0.2	1.2
J100	5.8± 0.7	0.5
J100.32ETA49	0.1± 0.1	0
3J50	1.1± 0.4	0.1
4J20	4.5± 0.7	1.4
5J15.0ETA26	3.1± 0.9	1.1
XE70	6.3± 2.6	3.5
J75_XE40	5.9± 0.8	0.2
J40_XE50_10DPHIALL-XE50-J20.0ETA25	5.0	1.4
Total	> 100	

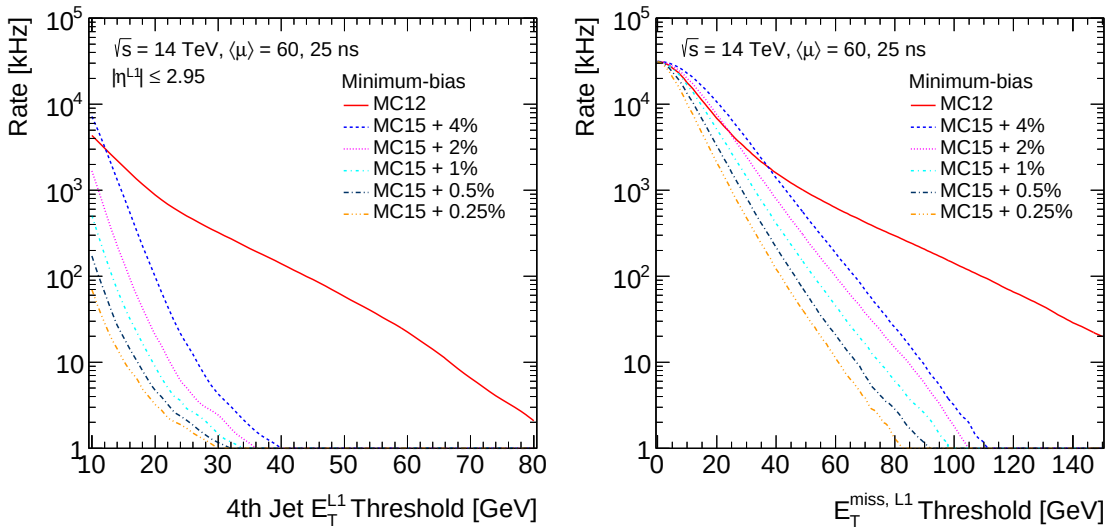

(a) (b)

Figure 7.4: Level 1 trigger rate as a function of the E_{T} threshold for (a) four-jet and (b) $E_{\mathrm{T}}^{\mathrm{miss}}$ triggers in MC12 and MC15 with different noise cut configurations.

The trigger efficiency is defined as the probability to satisfy the trigger as a function of an observable such as p_{T} or η, and is calculated as the ratio of the jet distributions in events that passed the trigger with respect to a reference distribution. The efficiency per event is defined as the probability that the jets in a given event would satisfy the trigger condition. The trigger threshold for each noise cut set is selected such that the 90% efficiency points of the turn-on curves match the same point as for the MC12 reference trigger. The trigger rates for the corresponding thresholds are then compared to determine the best performing noise cuts. Table 7.4 contains the results of the matching process. The results for a single jet trigger are also included to assess whether the noise cuts have a detrimental impact on the performance of this trigger which requires consideration when selecting an optimisation. Therefore from this point onward MC15 is assumed to represent the optimisation including the autocorrelation filters, average pedestal correction and noise cuts based on 0.5% occupancy.

Figure 7.5 compares the performance achieved by the MC12 and MC15 simulations for four-jet triggers in $t\bar{t}$ events and $E_{\mathrm{T}}^{\mathrm{miss}}$ triggers in $ZH \rightarrow \nu\bar{\nu}b\bar{b}$ events in terms of their event efficiency turn-on curves for the same trigger rate. From the shape of

Table 7.4: Trigger thresholds and rates for different MC15 noise cut configurations matched at the 90% efficiency point with MC12.

Sample	J		4J		XE	
	Threshold (GeV)	Rate (kHz)	Threshold (GeV)	Rate (kHz)	Threshold (GeV)	Rate (kHz)
MC12	100	14.4±0.7	20	882.1±5.2	70	425.2±3.6
MC15 + 0.25%	97	7.8±0.5	18	4.9±0.4	69	4.7±0.4
MC15 + 0.5%	101	7.6±0.5	20	4.7±0.4	74	4.9±0.4
MC15 + 1.0%	103	7.7±0.5	22	5.1±0.4	79	7.3±0.5
MC15 + 2.0%	107	7.4±0.5	25	5.0±0.4	83	12.5±0.6
MC15 + 4.0%	110	7.7±0.5	28	6.8±0.5	88	12.7±0.6

the signal distributions it is clear that there is a dramatic improvement in the signal acceptance with the MC15 simulation of 27.6% for the four-jet trigger and 15.6% for the $E_{\mathrm{T}}^{\mathrm{miss}}$ trigger. Multijet trigger performance depends on both the resolution for isolated jets and the resolution for separating nearby jets. The four-jet triggers are not fully efficient on the plateau, reaching approximately 93% for MC12 and 97% for MC15. This is because the coarse granularity of Level 1 jet algorithm limits the ability to resolve nearby jets. The four-jet trigger reaches its plateau efficiency 111 GeV earlier while the $E_{\mathrm{T}}^{\mathrm{miss}}$ trigger reaches full efficiency 123 GeV earlier.

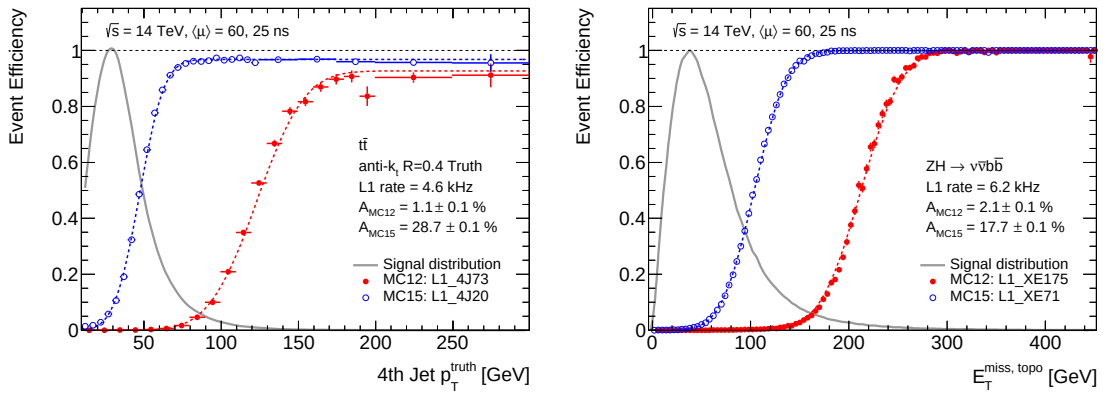

(a) (b)

Figure 7.5: Level 1 event efficiency turn-on curves for (a) four-jet triggers in $t\bar{t}$ events and (b) $E_{\mathrm{T}}^{\mathrm{miss}}$ triggers in $ZH \rightarrow \nu\bar{\nu}b\bar{b}$ events. The trigger thresholds indicated in the legends have been selected for the same trigger rate in the MC12 and MC15 simulations.

7.6 Jet Performance

Jet production is the dominant hard process at the LHC. The main requirement on the Level 1 jet trigger is to discriminate on the basis of the E_{T} and multiplicity of jets. The following sections compare the results of the MC12 and MC15 simulations for various jet performance criteria.

The Level 1 jet E_{T} estimate used in this study corresponds to the 0.8×0.8 cluster definition in $\Delta\eta \times \Delta\phi$, constructed from the sum of 4×4 jet elements. The reference jets used are reconstructed using the anti-k_t algorithm [118] with a radius parameter $R = 0.4$. The inputs to the jet algorithm are either energy deposits in the calorimeter or stable 'truth' particles from the event generator, and the jets produced are referred to as *calorimeter jets* and *truth jets*, respectively. Calorimeter jets are built from topological clusters of calorimeter cells (topoclusters) [119] with a significant energy signal above noise and reconstructed at the electromagnetic scale (EM-scale). The inputs to truth jets are simulated particles with a lifetime longer than 10 ps, excluding final-state muons and neutrinos as they leave little or no visible energy in the calorimeters.

In order to compare the Level 1 jet performance of the MC12 and MC15 simulations, the jet RoIs must be geometrically matched to jets reconstructed using the anti-k_t algorithm. The adopted method first selects all anti-k_t jets and identifies those which are isolated from other jets with $\Delta R > 1.0$. Of the remaining isolated jets only those which are marked as of good quality are accepted for matching to Level 1 jet RoIs. Bad jets include calorimeter jets which fail to satisfy the 'looser' quality criteria discussed in detail in [120], or have been faked by a truth electron or tau lepton lying within $\Delta R < 0.3$ of the jet axis. Taking each good jet, the nearest jet RoI with a cluster $E_{\mathrm{T}} > 10\,\mathrm{GeV}$ is identified, with the additional check that the jet RoI fails to better match any other anti-k_t jet in the event, including those marked as bad. The angular distance is typically measured by the ΔR between the RoI coordinate and anti-k_t jet axis, however since in the FCal there is no η granularity available to

the Level 1 jet algorithm, $|\Delta\phi|$ is used there instead. The results of the matching procedure up until this point are shown in Figure 7.7 and will be discussed later in detail. Only those jet pairs with a $\Delta R < 0.4$ for central jet RoIs, or $|\Delta\phi| < 0.4$ for forward jet RoIs are considered to be matched.

Whenever a jet cluster contains a saturated trigger tower or the cluster E_{T} is exceeded, the corresponding RoI is assigned a value of 1023. Under these circumstances the Level 1 E_{T} estimate is no longer important and an L1A will be immediately triggered. Since these jets do not properly reflect a true E_{T} estimate they are rejected from studies which require E_{T} comparison with reference jets.

7.6.1 Multiplicity

Background from thermal noise and pile-up can become a significant problem when attempting to identify multiple low E_{T} jets. It is important that an accurate count of the jet multiplicity above the required thresholds is provided even in complex multijet environments. The multiplicity depends on the jet resolution, which includes effects from BCID efficiency and noise cuts, as well as the sensitivity of the calibration to pedestal shifts.

Figure 7.6a shows the average number of Level 1 jets passing a set of low E_{T} thresholds for bunch trains following a long and a short bunch gap in the MC12 and MC15 simulations. The Level 1 jet multiplicity is dramatically affected by the pedestal shift at the start of the bunch train in MC12, however no such dependence is observed for the MC15 simulation. Figure 7.6b reflects this in showing the inclusive rate at which different Level 1 jet multiplicities are satisfied for the same thresholds.

The mean number of jets per bunch crossing with $E_{\mathrm{T}} > 10\,\mathrm{GeV}$ in MC12 reaches a maximum of approximately 60 at the start of bunch trains; the maximum in any given event is 77. The excessive number of RoIs produced has implications for the Level 1 hardware due to the limited number that can be handled by an individual JEM before an overflow occurs of four. In the event of an overflow, a L1A is issued,

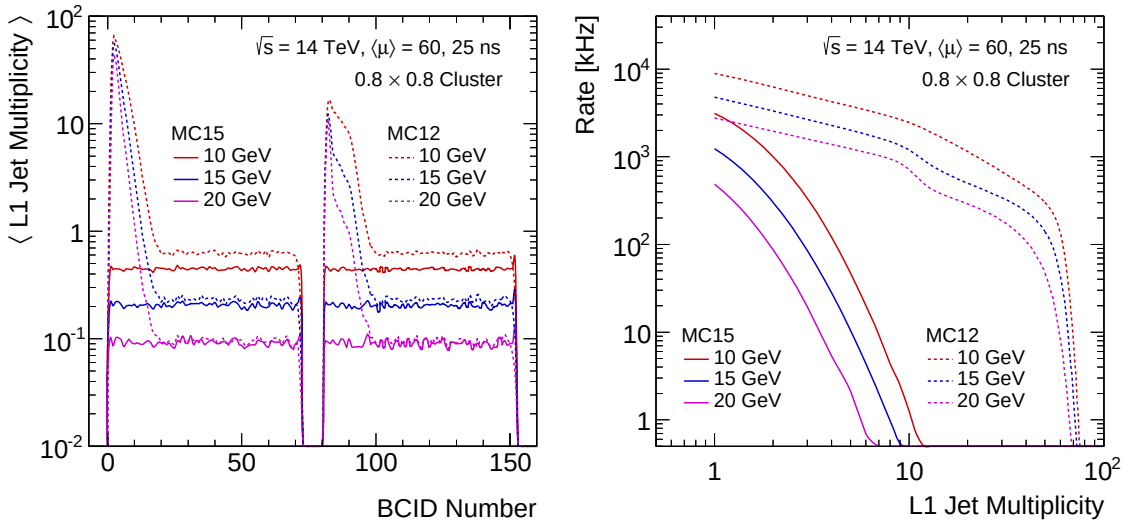

(a) (b)

Figure 7.6: Level 1 jet multiplicities passing different thresholds in the MC12 and MC15 simulation for minimum-bias events. Subfigure (a) shows the average number of Level 1 jets as a function of the BCID number for a bunch train proceeding a long and short gap. Subfigure (b) shows the inclusive rate at which Level 1 jet multiplicities are satisfied.

resulting in a fake trigger rate that, if significant, will limit the performance of the trigger. The mean number of jets in the stable region of the bunch train is consistently lower for the MC15 simulation, with this difference becoming increasingly smaller for higher E_{T} thresholds. This effect is driven by the generally larger noise cuts used in the MC15 simulation, but would otherwise be more significant if not for the better BCID efficiency of the autocorrelation filters. It is also worth noting that much smaller fluctuations in the jet multiplicity are observed in the MC15 simulation, indicating less sensitivity to noise and pile-up.

The optimisations in the MC15 simulation result in significantly better behaviour of the jet multiplicity triggers, where ultimately the pedestal correction is the most significant contributor. Substantial rate reductions are observed, for example the rate for at least four jets with $E_{\mathrm{T}} > 10$, 15 and 20 GeV is reduced by a factor of approximately 35, 81 and 277, respectively.

7.6.2 Spatial Resolution

The RoI coordinate resolution largely depends on the step size of the jet algorithm and RoI definition, both of which will remain the same in Run 2. However, the spatial resolution at low-E_{T} is more sensitive to noise contributions, and so the noise cuts and the performance of the trigger tower signal processing is important. It is necessary to provide accurate coordinates of the jet RoI for the HLT as these can be used in seeding HLT jet algorithms. There is an additional importance in Run 2, as the spatial resolution will have an effect on the formation of topological selections based on the angular distances between TOBs at the Level 1 trigger.

Figure 7.7 shows distributions of the angular distance measured between the RoI coordinate and the nearest calorimeter jet, normalised by the number of matched jets, for minimum-bias events in the offline E_{T} range $15 < E_{\mathrm{T}}^{\mathrm{jet}} < 50\,\mathrm{GeV}$. As mentioned previously, the lack of any resolution in η for jet RoIs which occur in FCal means that the $\Delta\phi$ has been plotted, rather than ΔR. There is a significant reduction in the tail of the ΔR distribution, resulting in the fraction of matched jets within 0.2 rad ($f^{0.2/0.4}$) improving by 8.3%, while the peak of the distributions remain closely matched as expected. The poor granularity available to the jet algorithm in the FCal means that any improvement is difficult to realise, but a gain of 4.6% in the fraction of matched jets within 0.2 rad is achieved.

The peaks of the distributions are firmly constrained by the jet algorithm itself and therefore will not change by much between the simulations. The peak of the ΔR distribution is fitted with a Landau function convolved with a Gaussian resolution, while the peak of the $\Delta\phi$ distribution is fitted with a double Gaussian function. As indicated on the plots, the ΔR distributions peak at values slightly larger than 0.1 rad, with the MC15 result shifted to slightly larger values. The $\Delta\phi$ distribution peaks are found to be slightly asymmetric, where once again the MC15 result is shifted to a greater value. This asymmetry can be explained by the nature of the RoI declustering algorithm that causes well-contained showers to be biased towards Level 1 coordinates with greater η and ϕ values [88,121]. It appears that the greater

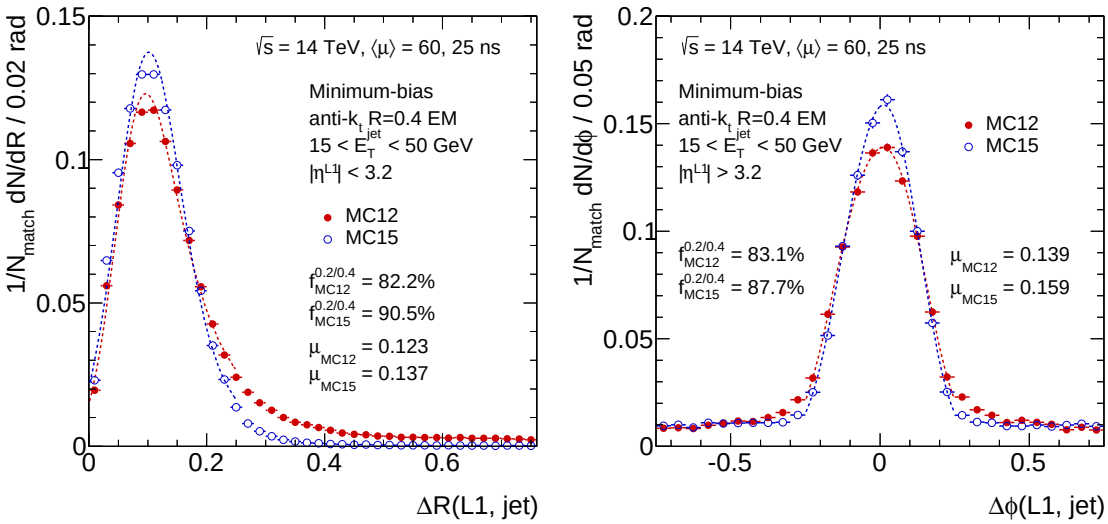

(a) (b)

Figure 7.7: Closest distance between Level 1 and calorimeter jets with $15 < E_{\mathrm{T}}^{\mathrm{jet}} < 50\,\mathrm{GeV}$, normalised to the number of matched jets for MC12 and MC15, using minimum-bias events. The ΔR for Level 1 RoIs outside FCal is shown in (a), while (b) shows the $\Delta\phi$ for Level 1 RoIs within FCal.

noise suppression in the MC15 simulation is acting to slightly enhance this bias.

7.6.3 Transverse Energy Linearity

It is generally expected that the jet E_{T} is underestimated by the Level 1 jet cluster as energy may leak outside the cluster window and smaller energy deposits further from the jet axis are easily lost due to finite BCID efficiency and noise cuts. Ultimately this is not a critical problem for the jet trigger as this fact is simply compensated for by setting lower E_{T} thresholds, which are easily configured in the trigger menu. Hence the jet E_{T} thresholds at Level 1 are dependent on the configuration of the Preprocessor. The trigger towers are also calibrated to the calorimeter EM-scale and so the energy deposits from hadronic showers are not properly compensated for. The possibility exists to use a non-linear LUT-scale in the nMCM during Run 2, which could better calibrate Level 1 jet clusters to the hadronic energy scale and therefore improve the jet resolution, but this is not considered here. The following compares the Level 1 jet cluster E_{T} to that of calorimeter jets, which are also calibrated to

the EM-scale and hence constitute the target jet E_{T} for the present trigger tower LUT calibration.

Figure 7.8 shows the E_{T} correlation between Level 1 jet clusters and reconstructed calorimeter jets for $t\bar{t}$ events in the MC12 and MC15 simulations. The long tails present in the MC12 correlation plot at lower E_{T} values are largely the result of the pedestal shift at the start of the bunch train. This effect is completely removed in the MC15 simulation, however there remains a residual tail that corresponds to where the anti-k_t algorithm has identified two or more jets in FCal with similar positions in ϕ and as a result of the poor granularity available to the Level 1 jet algorithm here, these are merged into a single jet RoI with a higher cluster E_{T}.

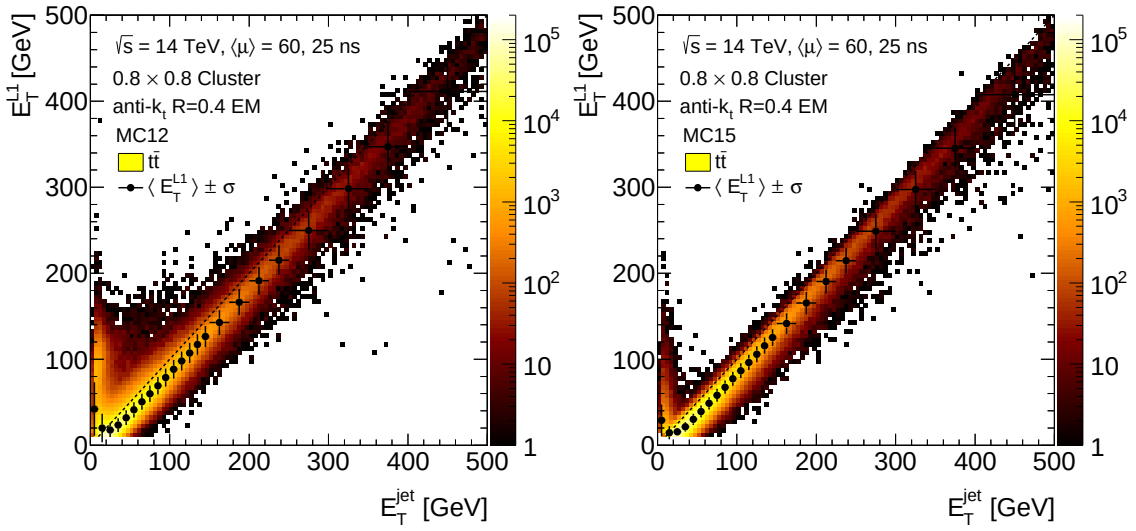

(a) (b)

Figure 7.8: Correlation between Level 1 and anti-k_t $R = 0.4$ EM-scale jets in $t\bar{t}$ events for (a) MC12 and (b) MC15 simulations. The overlaid data points and vertical error bars represent the mean and standard deviation of the distributions of Level 1 jet E_{T}, respectively.

The jet response ($\mathcal{R}$) is defined as the ratio between the Level 1 jet cluster E_{T} and the reference jet E_{T} reconstructed with the anti-k_t algorithm, and matched according to the criteria in Section 7.6. Figure 7.9 shows the distributions of the jet response to calorimeter jets for $15 < E_{\mathrm{T}}^{\mathrm{jet}} < 50\,\mathrm{GeV}$ that are separated by the position in the bunch train and pseudorapidity. A comparison between the mean and width of

the different distributions in each simulation is given in Table 7.5, where the results have been obtained by comparing the values measured from a Gaussian fit to the core of each distribution.

It is immediately clear that there is a much greater similarity between the distributions in the MC15 simulation, where the overall response is most consistent with that of MC12 central jets in the bulk of the bunch train. The MC12 distributions have a much larger mean response at the start of the bunch train, while jets present in the bulk of the bunch train have a slighter lower mean response, with respect to MC15. This is the result of the pedestal shifts experienced in different parts of the bunch train, which have been compensated for in MC15 by the average pedestal correction. The widths of the distributions are also improved on in MC15, except for central jets occurring in the bulk of the bunch train where there is no significant change. The improvement in resolution for forward jets in the bulk of the bunch train is due to the autocorrelation filters. On average the 0.8×0.8 jet cluster in the MC15 simulation underestimates the calorimeter jet E_{T} by about 14% in this low-E_{T} region.

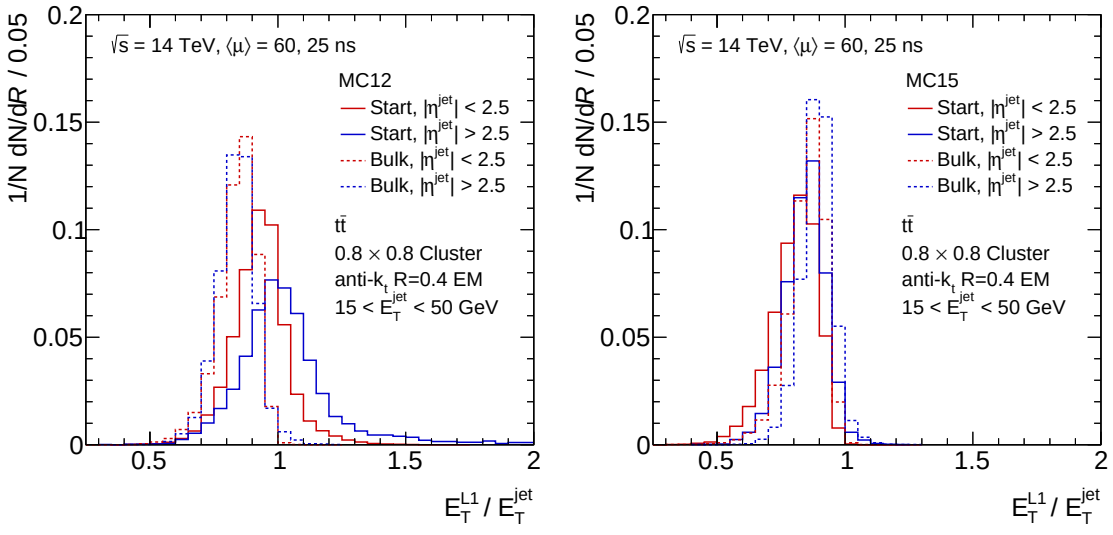

(a) (b)

Figure 7.9: Response distributions between Level 1 and anti-k_t $R = 0.4$ EM-scale jets with $15 < E_{\mathrm{T}}^{\mathrm{jet}} < 50\,\mathrm{GeV}$ for (a) MC12 and (b) MC15 using $t\bar{t}$ data. The distributions are separated by the position in the bunch train and for $|\eta| < 2.5$ and $|\eta| > 2.5$.

Table 7.5: Comparison between MC12 and MC15 of the fitted mean (μ) and standard deviation (σ) in the distributions of Figure 7.9.

Distribution	$\mu_{\mathrm{MC12}} - \mu_{\mathrm{MC15}}$	$\sigma_{\mathrm{MC15}}/\sigma_{\mathrm{MC12}}$
Start, $\lvert\eta\rvert < 2.5$	0.1163 ± 0.0006	0.898 ± 0.006
Start, $\lvert\eta\rvert > 2.5$	0.1461 ± 0.0024	0.619 ± 0.014
Bulk, $\lvert\eta\rvert < 2.5$	-0.0166 ± 0.0007	1.008 ± 0.011
Bulk, $\lvert\eta\rvert > 2.5$	-0.0537 ± 0.0011	0.793 ± 0.015

7.6.4 Transverse Energy Resolution

The precision of the jet transverse energy measurement is also of significant importance to the jet trigger in achieving sharp trigger turn-on, as well as an important contributor to the determination of the missing transverse energy. The following describes the measurement of the Level 1 jet resolution with respect to the truth jet E_{T}, where the jets were matched according to the method described in Section 7.6.

The jet energy resolution is measured from the E_{T} response distributions between matched pairs of Level 1 clusters and truth jets in bins of the truth jet energy, as well as for two different regions in $|\eta|$. To minimise the distortions to the jet resolution due to the pedestal shift, events occurring at the start of the bunch train have been discarded. The averaged jet response ($\langle\mathcal{R}\rangle$) is defined as the peak position of a Gaussian fit to the core of the jet response distribution and the jet resolution ($\sigma_{\langle\mathcal{R}\rangle}$) is given by the standard deviation of the fit. The fractional jet resolution ($\sigma_{\langle\mathcal{R}\rangle}/\langle\mathcal{R}\rangle = \sigma_{E_{\mathrm{T}}}/E_{\mathrm{T}}$) is used to determine the size of the fluctuations in the Level 1 jet energy cluster.

The fractional jet E_{T} resolution can be parameterised as a function of the truth jet E_{T} according to the standard calorimeter-based resolution function containing the noise (N), stochastic (S), and constant (C) terms:

$$\frac{\sigma_{E_{\mathrm{T}}}}{E_{\mathrm{T}}} = \frac{N}{E_{\mathrm{T}}} \oplus \frac{S}{\sqrt{E_{\mathrm{T}}}} \oplus C. \tag{7.1}$$

The N term includes noise sources from the calorimeter electronics and pile-up that dominate in the low-E_{T} region. The statistical fluctuations in the development of showers arising from the sampling nature of the calorimeters are represented by the S term, and are the main limiting factor in the intermediate E_{T} range. The C term contains sources independent of the jet E_{T} that include energy lost to the passive material in the detector. This term is important in the high-E_{T} region.

The fractional resolution curves for $|\eta| < 2.5$ and $|\eta| > 2.5$ are shown in Figure 7.10 for the MC12 and MC15 simulations. The bands mark the statistical uncertainty of the fitted points at the 68% confidence level and the values of the fitted parameters are given in Table 7.6. In general the S term is smaller for more central jets, but both the N and C terms are larger. The jet resolution is substantially improved in the MC15 simulation for the more forward region, due to improvements in both the N and S terms. There is an improvement in the S term in the central region, which leads to an improved resolution in the intermediate E_{T} range of $75 < E_{\mathrm{T}}^{\mathrm{truth}} < 300\,\mathrm{GeV}$ important for single jet thresholds, however the N and C terms are degraded and lead to poorer resolution elsewhere. The resolution for a 100 GeV truth jet in the central region is 21.1 GeV in the MC12 and 20.5 GeV in MC15. The corresponding resolutions for the forward region are 21.6 GeV in the MC12 and 18.3 GeV in MC15.

Table 7.6: Fitted values for the noise, sampling and constant terms in the jet E_{T} resolution parametrisation for the MC12 and MC15 simulations for the given ranges in $|\eta|$, taking E_{T} to be in units of GeV.

	MC12		MC15	
Term	$\lvert\eta\rvert < 2.5$	$2.5 < \lvert\eta\rvert < 4.9$	$\lvert\eta\rvert < 2.5$	$2.5 < \lvert\eta\rvert < 4.9$
N	14.8±0.1	11.8±0.2	16.7±0.1	10.8±0.2
S	1.41±0.02	1.81±0.02	0.94±0.04	1.48±0.02
C	0.053±0.002	0.010±0.002	0.073±0.002	0.010±0.003

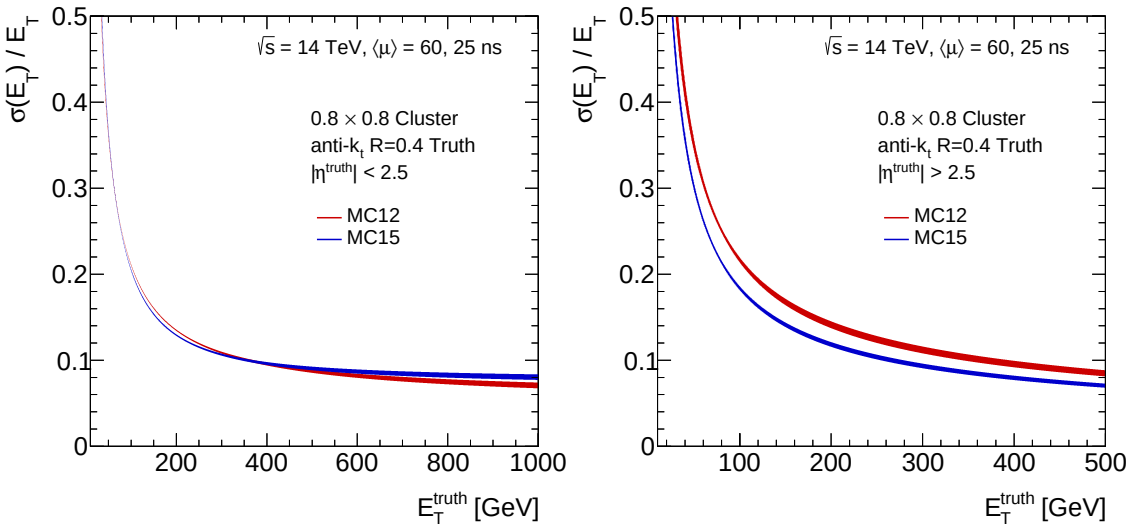

(a) (b)

Figure 7.10: Level 1 fractional jet E_{T} resolution in MC12 and MC15 as a function of $E_{\mathrm{T}}^{\mathrm{truth}}$ for (a) $|\eta| < 2.5$ and (b) $|\eta| > 2.5$.

7.6.5 Identification Efficiency

Another way to assess the jet trigger performance is to study the efficiency to identify individual jets as a function of the jet p_{T} and η. The difference between the per event and per jet approach is that all jets in the event that pass the trigger contribute to the efficiency per event, while only reference jets that are matched to trigger jets are considered in the per jet efficiency.

The efficiency of the jet trigger has been evaluated for truth jets reconstructed with the anti-k_t algorithm with radius parameter $R = 0.4$. The efficiency is defined as the fraction of truth jets that match a trigger jet, according to the method described in Section 7.6, and pass the corresponding trigger threshold. Examples of the jet identification efficiencies obtained for central and forward jets for a 15 GeV threshold are shown in Figure 7.11, for the MC12 and MC15 simulation as a function of the truth jet p_{T}. Only events occurring later in the bunch train have been considered in order to remove distortions to the turn-on curves at low-p_{T} in the MC12 simulation, due to pedestal shifts. The results therefore more closely reflect the differences in the filter performance and noise cuts than the pedestal correction. The efficiency

curves in Figure 7.11 have been described assuming Gaussian resolution using the following function:

$$\epsilon(x) = \frac{\varepsilon}{2}\left[1 + \mathrm{erf}\left(\frac{x-\mu}{\sqrt{2}\sigma}\right)\right], \tag{7.2}$$

where μ represents the efficiency mid-point, ε the plateau efficiency value and σ the turn-on width. In each case the turn-on width is improved by the MC15 simulation, most significantly in the more forward region.

Some efficiency is lost on the turn-on curve for jets with $|\eta| < 2.5$ due to fact the noise cuts are significantly larger in the MC15 simulation. However, after 50 GeV the difference is insignificant and the trigger reaches full efficiency at the same p_{T} in each of the simulations. The efficiency curve in the forward region has a slower turn-on due to the reduced trigger tower granularity, but the efficiency improvement in the MC15 simulation is considerable. The turn-on width is improved by 1.9 GeV and the 99% efficiency point is reached 9.7 GeV earlier. These gains are the result of the improved jet energy resolution from the much greater BCID efficiency and better pile-up noise suppression of the autocorrelation filters.

Figure 7.12 shows the jet efficiency as a function of $|\eta|$ for truth jets passing a 15 GeV threshold in the MC12 and MC15 simulation for the p_{T} ranges on the turn-on curve of $40 < p_{\mathrm{T}}^{\mathrm{truth}} < 70$ GeV and near plateau with $p_{\mathrm{T}}^{\mathrm{truth}} > 70$ GeV. The low-p_{T} region exhibits a strong dependence on $|\eta|$, particularly in the regions at $|\eta| \sim 1.5$ and 3.2, which correspond to the barrel–endcap and IW–FCal transition regions, as well as at high-$|\eta|$ where jets begin to fall outside the FCal acceptance. The poorer low-p_{T} performance of MC15 observed for the central region appears to be dominated by the barrel, while the improvement is evident everywhere in the forward region. For the high-p_{T} region the jet trigger begins to reach full efficiency for the whole calorimeter under both simulations.

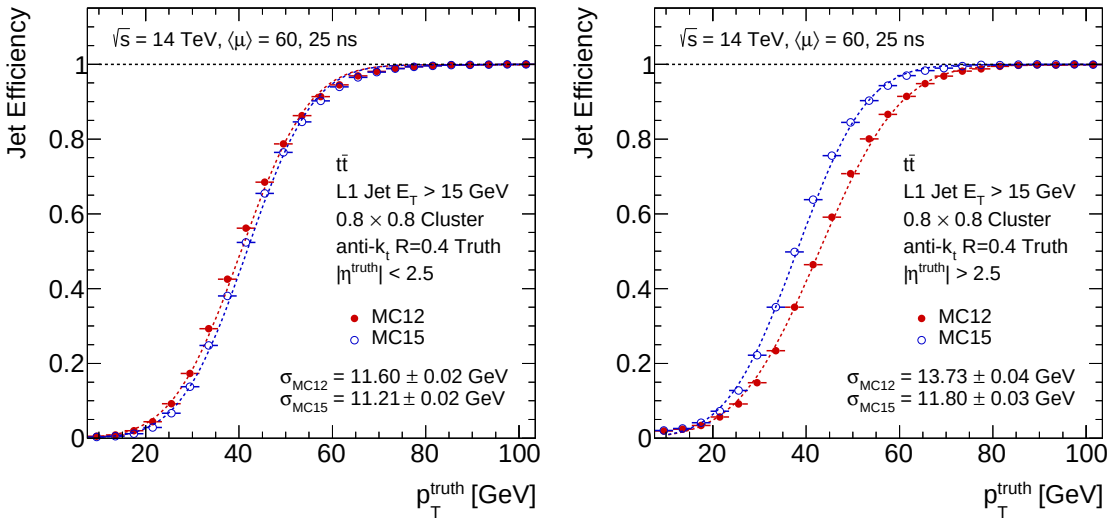

Figure 7.11: The efficiency in MC12 and MC15 for anti-k_t $R = 0.4$ truth jets in $t\bar{t}$ events to satisfy a Level 1 threshold of 15 GeV as a function of the truth jet p_{T}, integrating over (a) $|\eta| < 2.5$ and (b) $|\eta| > 2.5$. Only events occurring in later bunches in a train are used.

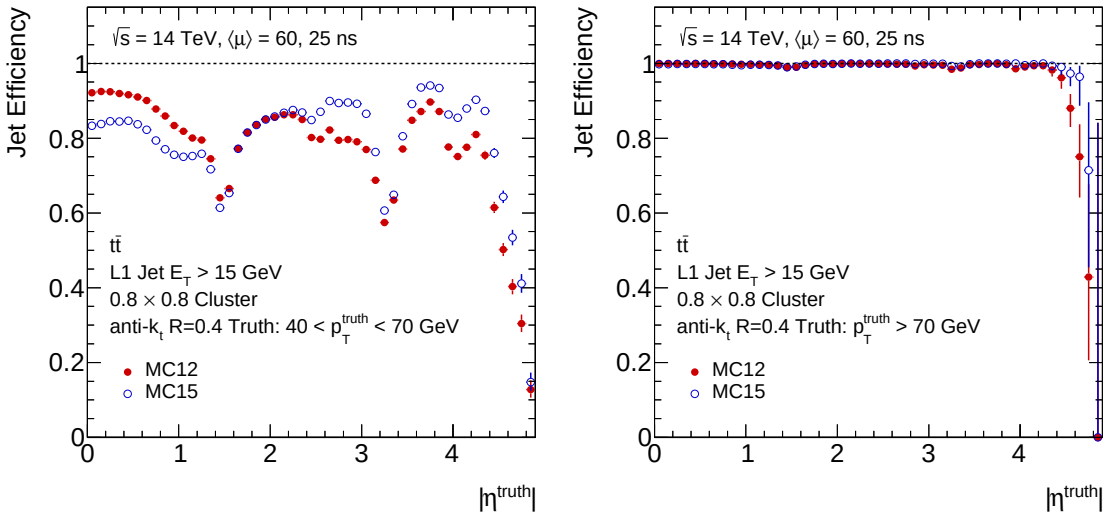

Figure 7.12: The efficiency in MC12 and MC15 for anti-k_t $R = 0.4$ truth jets in $t\bar{t}$ events to satisfy a Level 1 threshold of 15 GeV as a function of the truth jet $|\eta|$ for (a) $40 < p_{\mathrm{T}}^{\mathrm{truth}} < 70$ GeV and (b) $p_{\mathrm{T}}^{\mathrm{truth}} > 70$ GeV.

7.7 Missing Transverse Energy Performance

The goal of the $E_{\mathrm{T}}^{\mathrm{miss}}$ trigger is to select events with an imbalance in the total measured momentum due to non-interacting particles which pass through the detector. Large missing transverse energy is an important signature for the discovery of new physics at the LHC. Some 2012 Level 1 $E_{\mathrm{T}}^{\mathrm{miss}}$ triggers omitted the first three bunches in a train in order to reduce the fake $E_{\mathrm{T}}^{\mathrm{miss}}$ trigger rate due to pedestal shifts.

The $E_{\mathrm{T}}^{\mathrm{miss}}$ trigger performance is process-dependent and so a few different signatures have been considered. The simulated event samples used include minimum-bias events and processes with large jet multiplicities and/or large missing transverse momentum such as VBF $H \rightarrow \tau\tau$, $t\bar{t}$ and $ZH \rightarrow \nu\bar{\nu}b\bar{b}$. The $ZH \rightarrow \nu\bar{\nu}b\bar{b}$ decay was selected in 2012 by the $E_{\mathrm{T}}^{\mathrm{miss}}$ trigger with a Level 1 theshold set to 40 GeV. Increasing the $E_{\mathrm{T}}^{\mathrm{miss}}$ theshold at Level 1 rapidly suppresses signal acceptance. For Run 2, combinations of $E_{\mathrm{T}}^{\mathrm{miss}}$ and jet requirements along with topological selections can be used to suppress trigger rates. Ultimately it is likely that both standalone $E_{\mathrm{T}}^{\mathrm{miss}}$ triggers and combined topological triggers will be pursued.

Whenever a trigger tower is saturated or an overflow occurs, the corresponding Level 1 jet element is set to 1023 GeV and the energy sums (E_x, E_y, and $E_{\mathrm{T}}^{\mathrm{miss}}$) are set to 4032 GeV. In this situation the energy sums no longer represent true estimates and the triggering is instead handled by saturation flag bits. As a result, these events are rejected from the following results.

Even in events where there is no intrinsic $E_{\mathrm{T}}^{\mathrm{miss}}$, imperfect calorimeter resolution will give rise to non-zero values of $E_{\mathrm{T}}^{\mathrm{miss}}$. Figure 7.13 compares the Level 1 E_x^{miss}, E_y^{miss}, $E_{\mathrm{T}}^{\mathrm{miss}}$ and $\sum E_{\mathrm{T}}$ distributions in the MC12 and MC15 simulation for minimum-bias events. In each of the transverse energy distributions the MC12 simulation displays significant tails due to the pedestal shifts at the start of the bunch train. The distribution of $\sum E_{\mathrm{T}}$ is highly sensitive to noise and, as well as reducing the tail, the implementation of the autocorrelation filters and noise cuts has shifted the distribution peak to lower values.

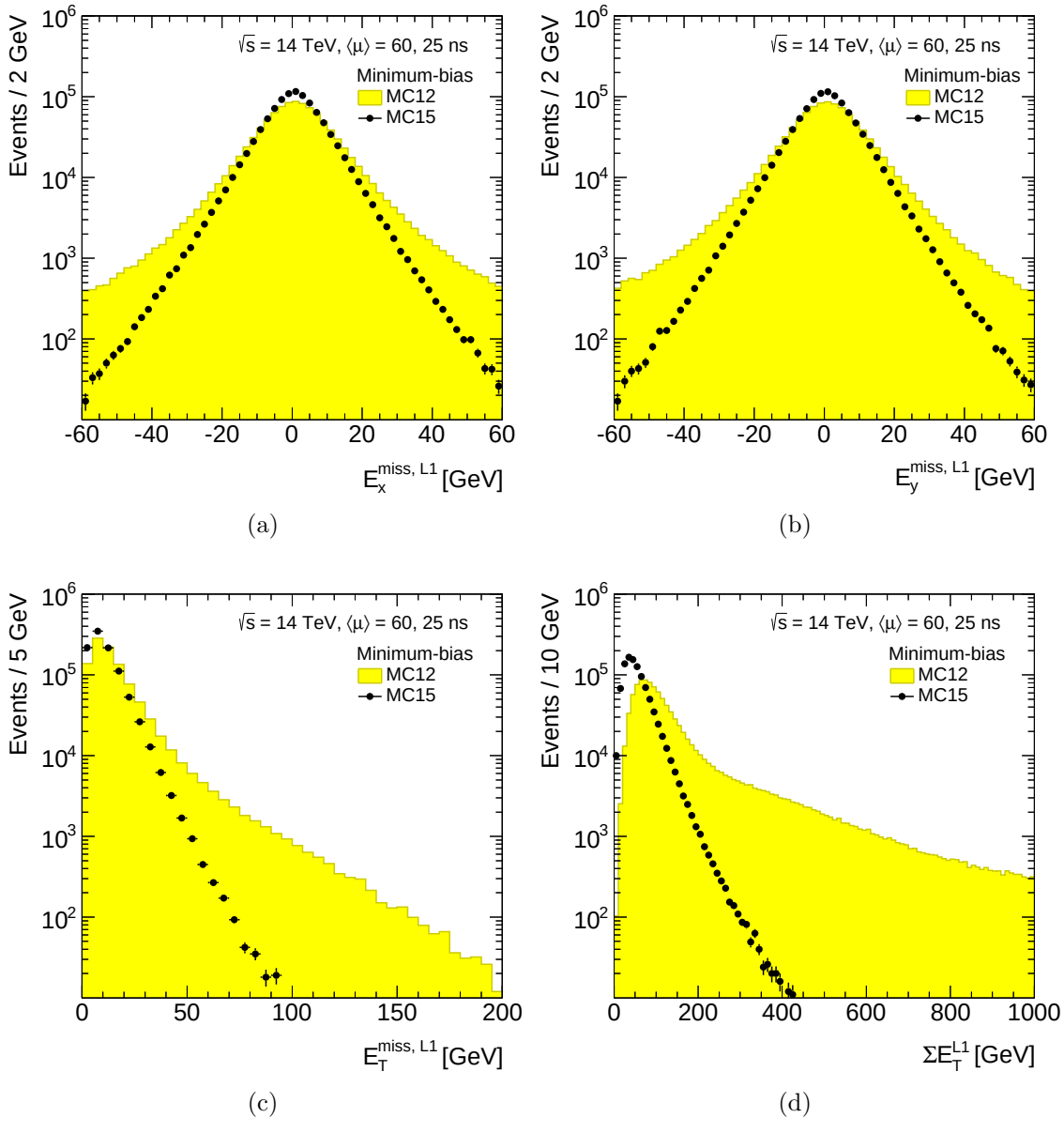

Figure 7.13: Distributions of the Level 1 (a) E_x^{miss}, (b) E_y^{miss}, (c) $E_{\text{T}}^{\text{miss}}$ and (d) $\sum E_{\text{T}}$ as measured in minimum-bias events for the MC12 and MC15 simulations.

7.7.1 Missing Transverse Energy Linearity

The reference offline $E_{\mathrm{T}}^{\mathrm{miss}}$ algorithm used in this study accounts for the energy deposited in topological clusters based on uncalibrated calorimeter energy measurements, referred to here as *Topo* $E_{\mathrm{T}}^{\mathrm{miss}}$. It provides the best offline performance for uncalibrated $E_{\mathrm{T}}^{\mathrm{miss}}$ measurements and it therefore constitutes the targeted $E_{\mathrm{T}}^{\mathrm{miss}}$ reconstruction for the Level 1 trigger. It is also the same algorithm used to calculate the $\sum E_{\mathrm{T}}$.

Figure 7.14 shows the $E_{\mathrm{T}}^{\mathrm{miss}}$ correlation between the Level 1 trigger and topological cluster estimates for $ZH \rightarrow \nu\bar{\nu}b\bar{b}$ events in the MC12 and MC15 simulations. Except for low values of $E_{\mathrm{T}}^{\mathrm{miss}}$ the Level 1 trigger underestimates the offline $E_{\mathrm{T}}^{\mathrm{miss}}$ on average. Similarly to the jet correlation plots, there are large tails in the MC12 distribution where the $E_{\mathrm{T}}^{\mathrm{miss}}$ is overestimated due to the large pedestal shift at the start of the bunch train. This effect is completely compensated for by the pedestal correction in the MC15 simulation.

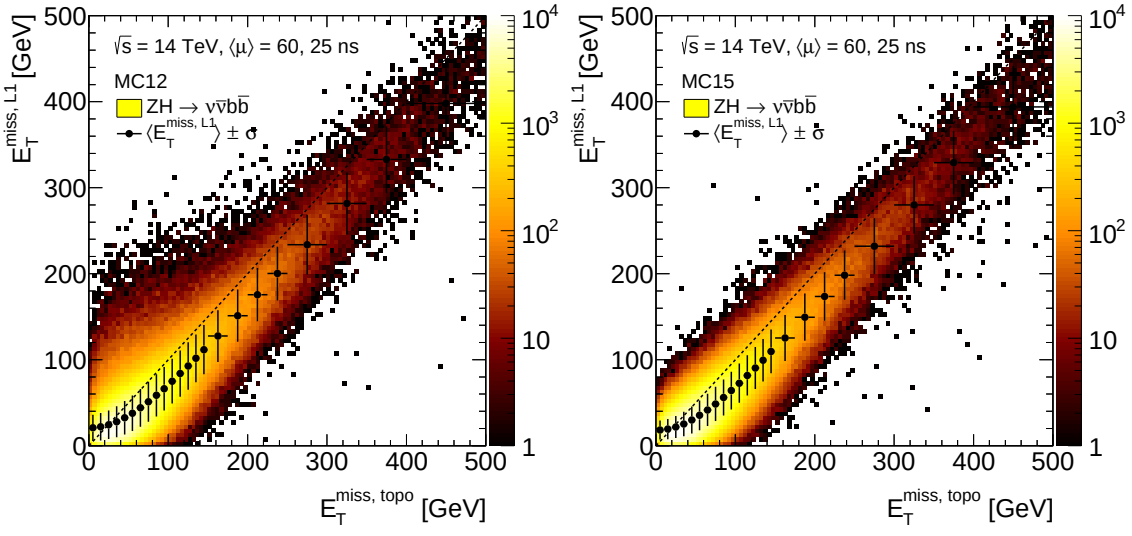

(a) (b)

Figure 7.14: Correlation between the Level 1 and Topo $E_{\mathrm{T}}^{\mathrm{miss}}$ for $ZH \rightarrow \nu\bar{\nu}b\bar{b}$ events in (a) the MC12 and (b) the MC15 simulations. The overlaid data points and vertical error bars represent the mean and standard deviation of the distributions of Level 1 $E_{\mathrm{T}}^{\mathrm{miss}}$, respectively.

The distributions of the difference between the Level 1 and truth $E_{\mathrm{T}}^{\mathrm{miss}}$ are shown in Figure 7.15 for $ZH \rightarrow \nu\bar{\nu}b\bar{b}$ and $t\bar{t}$ events with $E_{\mathrm{T}}^{\mathrm{miss,\ truth}} > 100\,\mathrm{GeV}$. The events have been divided according to whether they occurred at the start or within the bulk of the bunch train. In general the true $E_{\mathrm{T}}^{\mathrm{miss}}$ in the event is underestimated at Level 1 as it is based on the EM-scale provided by the trigger towers LUTs, rather than on calibrated trigger objects. The Level 1 $E_{\mathrm{T}}^{\mathrm{miss}}$ estimate is very dependent on the pedestal shift, with the distributions for the start of the bunch train in MC12 shifted to greater values by approximately 12 GeV for either process. There is even a small effect of around 1–2 GeV visible for the bulk of the bunch train where the pedestal correction has compensated for the shift in the opposite direction. The spread of the distributions depends on the amount of activity in the event, as greater activity causes the Level 1 $E_{\mathrm{T}}^{\mathrm{miss}}$ resolution to degrade.

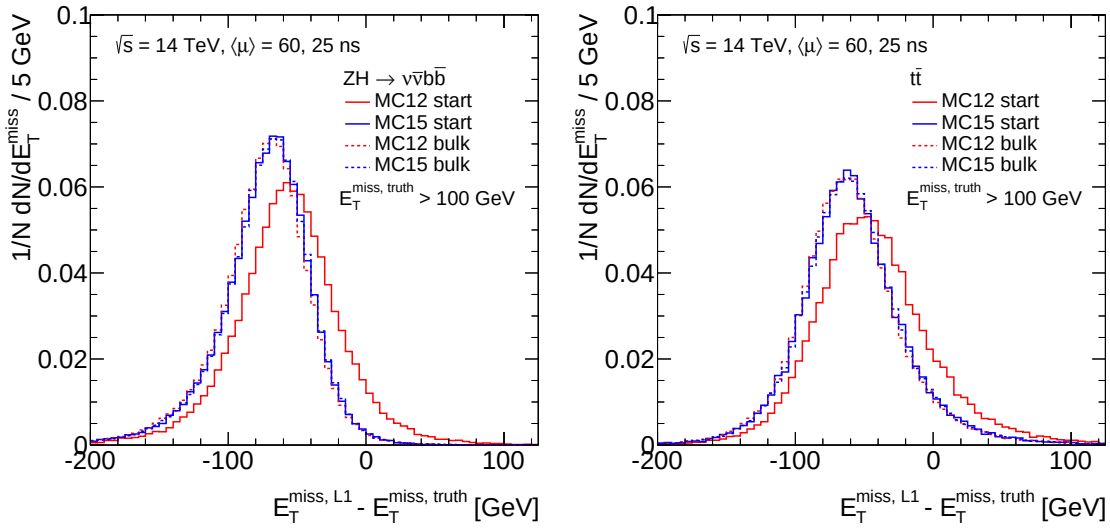

(a) (b)

Figure 7.15: Distributions of the difference between the Level 1 and Topo $E_{\mathrm{T}}^{\mathrm{miss}}$ for (a) $ZH \rightarrow \nu\bar{\nu}b\bar{b}$ events and (b) $t\bar{t}$ events in the MC12 and MC15 simulation with $E_{\mathrm{T}}^{\mathrm{miss,\ truth}} > 100\,\mathrm{GeV}$ and separated by the position in the bunch train.

7.7.2 Missing Transverse Energy Direction

For events with genuine missing transverse momentum, the $E_{\mathrm{T}}^{\mathrm{miss}}$ angular resolution depends in general on the event topology. Figure 7.16 shows the $E_{\mathrm{T}}^{\mathrm{miss}}$ azimuthal

resolution as a function of the true $E_{\mathrm{T}}^{\mathrm{miss}}$ for different physics processes in the MC12 and MC15 simulation. The resolution has been obtained from the width of a Gaussian fit to the core of the distributions of the minimum angular difference between the Level 1 and truth $E_{\mathrm{T}}^{\mathrm{miss}}$ vector directions. The accuracy of the direction measurement rapidly degrades for low values of $E_{\mathrm{T}}^{\mathrm{miss}}$, however at high $E_{\mathrm{T}}^{\mathrm{miss}}$ accuracies approaching the size of jet elements of 0.2 rad are achieved for all samples. The measurement of the $E_{\mathrm{T}}^{\mathrm{miss}}$ azimuth is clearly least accurate for $t\bar{t}$ events due to their complex topology, involving a significant amount of hadronic activity. In this case there is almost no difference in the direction resolution between MC12 and MC15. The resolutions for $ZH \rightarrow \nu\bar{\nu}b\bar{b}$ and VBF $H \rightarrow \tau_\ell\tau_h$ events are similar in size and for each process there is a small improvement in resolution, which becomes most significant at low $E_{\mathrm{T}}^{\mathrm{miss}}$.

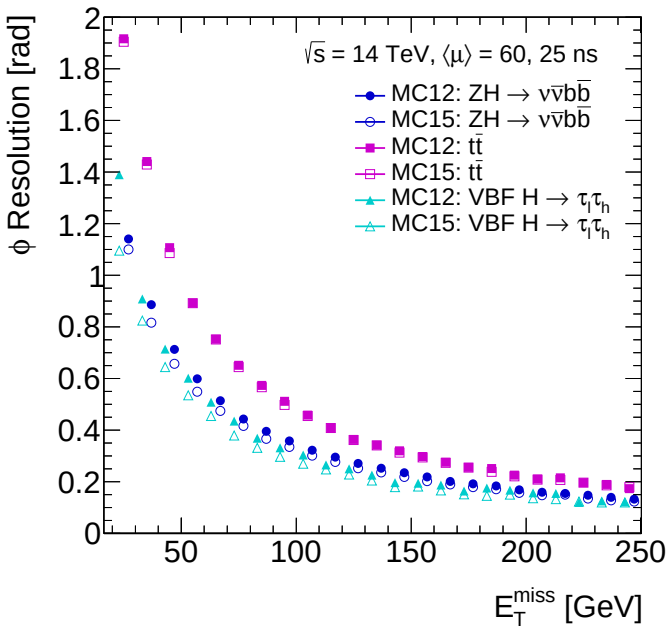

Figure 7.16: Azimuthal resolution of the $E_{\mathrm{T}}^{\mathrm{miss}}$ vector as a function of the true $E_{\mathrm{T}}^{\mathrm{miss}}$ in MC12 and MC15 for three different physics processes: $ZH \rightarrow \nu\bar{\nu}b\bar{b}$, semi-leptonic $t\bar{t}$ and VBF $H \rightarrow \tau_\ell\tau_h$ events. The data points for each process have different offsets with respect to the bin centre for clarity.

The improvement observed for $ZH \rightarrow \nu\bar{\nu}b\bar{b}$ events is of some benefit to triggering this process in Run 2. It has been proposed that in addition to the $E_{\mathrm{T}}^{\mathrm{miss}}$ trigger used in Run 1 these events can be selected by a combined trigger with topological

requirements to achieve a rate sufficiently low for incorporation into the menu [85]. The intention is to combine a lower $E_{\mathrm{T}}^{\mathrm{miss}}$ threshold of 50 GeV with an inclusive jet trigger with $p_{\mathrm{T}} > 40\,\mathrm{GeV}$. In this process the direction of the $E_{\mathrm{T}}^{\mathrm{miss}}$ is likely to point far away from any jet, which gives good discrimination against the QCD background. This fact can be exploited by requiring the presence of central jets with $p_{\mathrm{T}} > 20\,\mathrm{GeV}$ and $|\eta| < 2.5$, where the minimum value of the azimuthal angular distance between the Level 1 $E_{\mathrm{T}}^{\mathrm{miss}}$ and central jets, denoted $|\Delta\phi\ (E_{\mathrm{T}}^{\mathrm{miss}}, \text{jets})|$, is greater than 1.0. Lowering the $E_{\mathrm{T}}^{\mathrm{miss}}$ threshold significantly increases the signal acceptance while the additional jet and topological requirements suppress backgrounds by many times with very little loss in signal.

7.7.3 Missing Transverse Energy Resolution

A more quantitative evaluation of the $E_{\mathrm{T}}^{\mathrm{miss}}$ performance at Level 1 can be obtained by studying its resolution with respect to offline algorithms. The resolution of the E_x^{miss} and E_y^{miss} components of the $E_{\mathrm{T}}^{\mathrm{miss}}$ generally depends on the overall activity in the event, which can be quantified by the $\sum E_{\mathrm{T}}$ deposited in the calorimeters. The greater the activity present in the event, the more the observed $E_{\mathrm{T}}^{\mathrm{miss}}$ resolution is degraded, and the presence of large event pile-up only acts to degrade it further.

Non-zero values of $E_{\mathrm{T}}^{\mathrm{miss}}$ can arise for events which do not contain any non-interacting particles due to limited detector coverage, finite detector resolution, presence of dead material and different sources of noise producing fake $E_{\mathrm{T}}^{\mathrm{miss}}$. Therefore, minimum-bias data can be a useful indicator of the $E_{\mathrm{T}}^{\mathrm{miss}}$ resolution at low $\sum E_{\mathrm{T}}$, as well as those events which contain real $E_{\mathrm{T}}^{\mathrm{miss}}$. The results in this section calculate the resolution of the two $E_{\mathrm{T}}^{\mathrm{miss}}$ components using the offline Topo reconstruction and so similar resolutions should be observed for different processes.

The resolution is estimated by the width of a Gaussian fit to the core of the combined distribution of the differences between the Level 1 and Topo $E_{\mathrm{T}}^{\mathrm{miss}}$ components, for bins of the total transverse energy. The resolution of the two $E_{\mathrm{T}}^{\mathrm{miss}}$ components

approximately follows a stochastic behaviour as a function of the $\sum E_{\mathrm{T}}$, which can be modelled using the following function:

$$\sigma^{\mathrm{miss}}_{x\ (y)} = k \cdot \sqrt{\sum E_{\mathrm{T}}}, \tag{7.3}$$

where k is a fitting parameter which quantifies the $E^{\mathrm{miss}}_{\mathrm{T}}$ resolution that depends directly on the jet resolution. Deviations from this behaviour are expected for very low $\sum E_{\mathrm{T}}$, where noise contributions are important, and for very high values of $\sum E_{\mathrm{T}}$, where the constant term in the resolution of the calorimeter energy dominates.

Figure 7.17 shows the $E^{\mathrm{miss}}_{x,\,y}$ resolution as a function of the total transverse energy in the event for a number of different processes. A combined fit to the minimum-bias and signal processes is made for each simulation for values of $\sum E_{\mathrm{T}}$ between 400 and 1500 GeV and the values of k obtained are $0.993 \pm 0.001\,\mathrm{GeV}^{1/2}$ for the MC12 simulation and $0.9460 \pm 0.0005\,\mathrm{GeV}^{1/2}$ for MC15. The MC15 simulation shows an improvement in the resolution of approximately 5%.

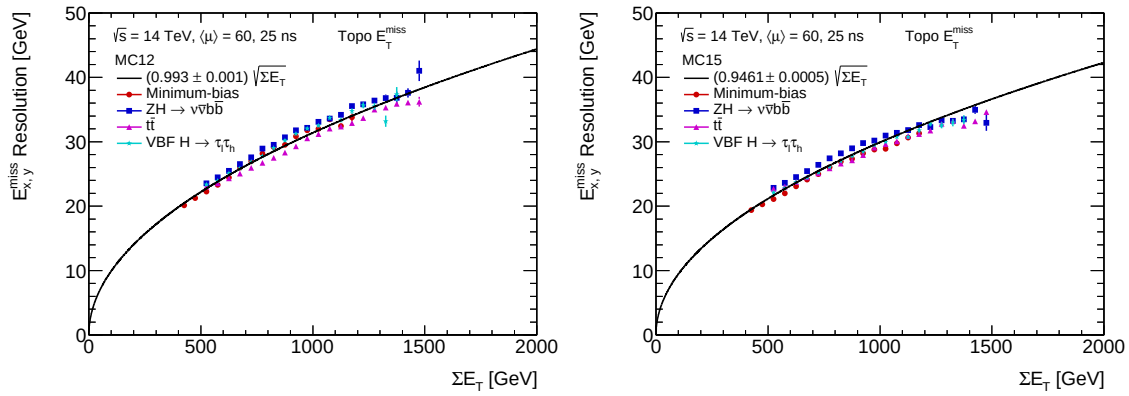

(a) (b)

Figure 7.17: $E^{\mathrm{miss}}_{x,\,y}$ resolution as a function of the total transverse energy in (a) MC12 and (b) MC15 for four different physics processes: minimum-bias, $ZH \to \nu\bar{\nu}b\bar{b}$, semi-leptonic $t\bar{t}$ and VBF $H \to \tau_\ell\tau_h$ events. The black line shows the combined fit to the data points and the value of the fitting parameter k is given in the legend.

In addition to the improvements discussed in this chapter relating to the trigger tower performance and optimisation of noise cuts, it is believed that further improvements in the $E^{\mathrm{miss}}_{\mathrm{T}}$ reconstruction at Level 1 can be achieved in Run 2 using a

Kalman filter method to obtain correction factors for jet TOBs as a function of p_{T} and η, which can be implemented within a LUT in L1Topo [122].

7.8 Results with Data

This section describes some of the early performance results of the Level 1 trigger with Run 2 data collected at $\sqrt{s} = 13\,\mathrm{TeV}$ during 2015. This data was collected using the strategy proposed in this thesis of autocorrelation filters operated in combination with an average pedestal correction and noise cuts derived for approximately 0.5% trigger tower occupancy. The performance is compared to that expected with the Run 1 filter coefficients and without the use of the pedestal correction. Figure 7.18 shows the normalised autocorrelation FIR coefficients obtained from 25 ns data for the EM and hadronic layers using the method presented in Section 6.8. The $|\eta|$ bins are numbered in order of increasing $|\eta|$, where the coefficients share the same characteristics as those derived by the ToyMC. The initial LUT calibration corresponding to these coefficients has been optimised according to the same pulse shape assumed in the derivation of the coefficients. The collected data will enable more detailed offline analysis methods [123] to refine this calibration further.

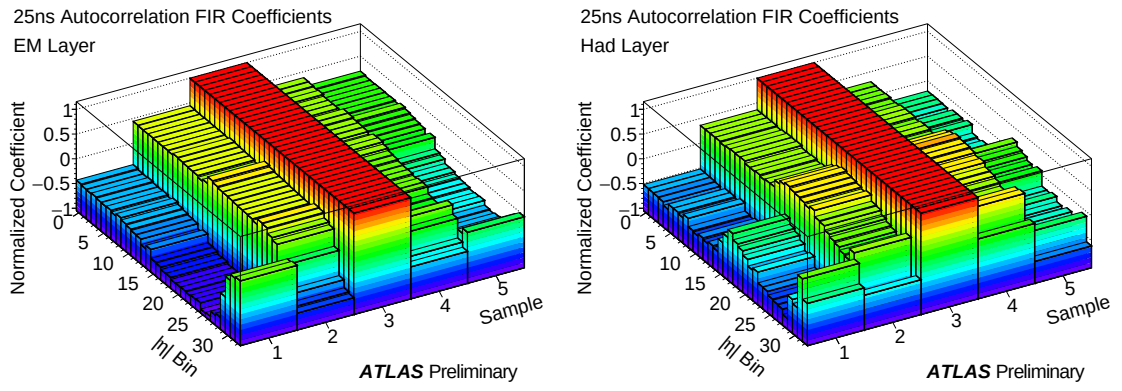

(a) (b)

Figure 7.18: Normalised autocorrelation FIR filter coefficients for a 25 ns bunch spacing for each $|\eta|$-bin in (a) the EM layer and (b) the hadronic layer [124].

A comparison of the matched and autocorrelation FIR filter BCID efficiency as a function of the offline calorimeter cell-based E_{T} estimate is shown in Figure 7.19 for trigger towers in the EMEC IW and the two most forward $|\eta|$-bins in FCal1. The matched filter performance has been obtained by emulating the filter behaviour in a reprocessing of the original ADC data with the Run 1 coefficients. As predicted by the ToyMC studies presented in Chapter 6, there is a significant performance gain by using autocorrelation filters in regions with substantial pile-up noise.

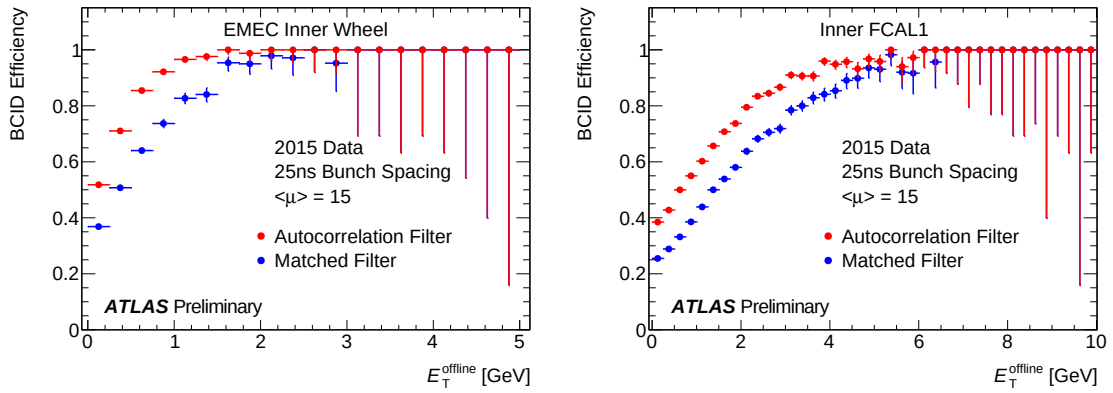

(a) (b)

Figure 7.19: The efficiency that a calorimeter pulse is identified in the correct bunch crossing as a function of the offline E_{T} [124]. The performance of the matched filter is compared to the autocorrelation filter for (a) the EMEC IW and (b) FCal1.

Figure 7.20 compares the Level 1 trigger rate per bunch as a function of the instantaneous luminosity per bunch for the $E_{\mathrm{T}}^{\mathrm{miss}}$ trigger with a 35 GeV threshold, with and without the application of the average pedestal correction. The trigger rates without the pedestal correction show that despite the use of autocorrelation filters, which are less sensitive to the pedestal shifts than the matched filters, a significant non-linear increase in the trigger rate is still observed as in Run 1. However, the application of the pedestal correction results in trigger rates that depend linearly on luminosity. In Run 1, the noise cuts applied in the forward region were relatively harsh in order to cope with the large pedestal shifts produced at the start of bunch trains at high luminosities. The consequence of this was that at lower luminosities the event rate was very low. The new noise cut strategy works well in combina-

tion with the pedestal correction as higher event rates can be accepted at lower luminosities without exceeding the bandwidth at high luminosity.

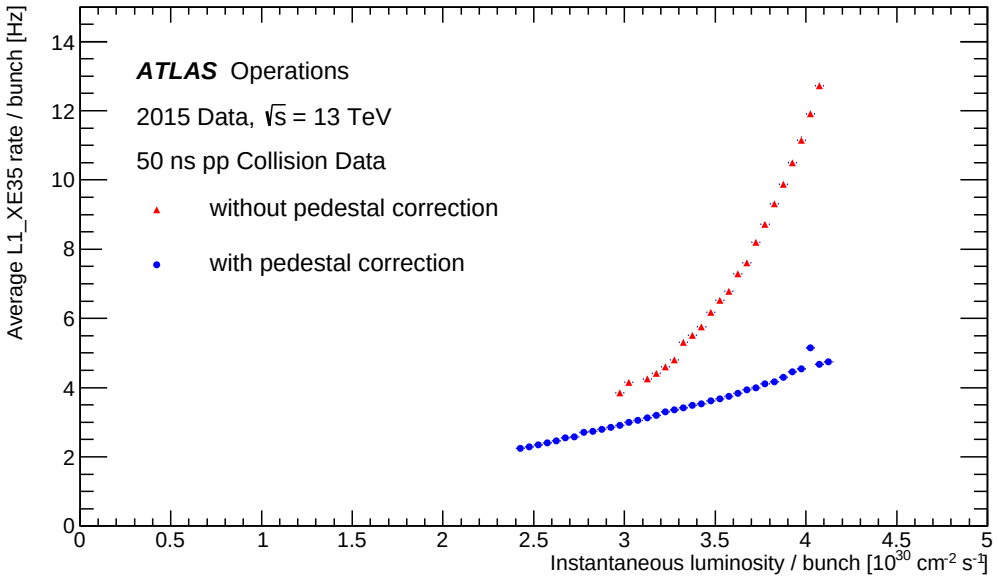

Figure 7.20: Level 1 trigger rate per bunch as a function of the instantaneous luminosity per bunch for the $E_{\mathrm{T}}^{\mathrm{miss}}$ trigger with a 35 GeV threshold [124]. The rates are shown with and without the pedestal correction applied.

7.9 Summary

In this chapter a new noise cut strategy was proposed for Run 2 that relies on the measurement of the trigger tower occupancy. The trigger performance was studied for a number of noise cut sets combined with autocorrelation filters and a pedestal correction. There are significant improvements found in almost all aspects of the jet and $E_{\mathrm{T}}^{\mathrm{miss}}$ trigger performance, especially in the uniformity of response with position in the bunch train. These proposals were used in 2015 data-taking and performed as predicted.

CHAPTER 8

SEARCH FOR HIGGS BOSON PAIR PRODUCTION

8.1 Introduction

Presented here are searches for the Higgs boson pair production in the $hh \to b\bar{b}\tau\tau$ decay channel for the final state where one tau lepton decays leptonically ($\tau \to \ell\nu\bar{\nu}$ with $\ell = e, \mu$) and the other decays hadronically ($\tau \to$ hadrons+ν). The nonresonant search includes the SM production modes where Higgs boson pairs are produced through Higgs boson self-coupling and the Higgs-fermion Yukawa interactions. The resonant production of Higgs boson pairs from the decay of a new heavy CP-even neutral Higgs boson is considered as part of the resonant search. In each of these searches only the gluon fusion production mechanism is assumed. The leading order Feynman diagrams for each of these processes are shown in Figure 8.1. The potential interference between nonresonant and resonant production is ignored.

The $b\bar{b}\tau\tau$ channel has the third largest branching ratio for the decays of Higgs boson

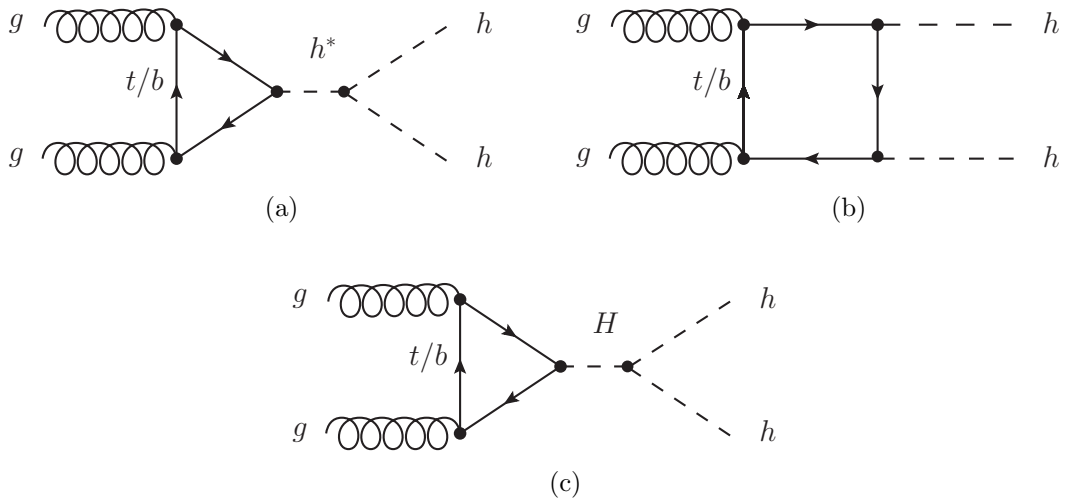

Figure 8.1: Leading order Feynman diagrams for the nonresonant production of Higgs boson pairs in the SM through (a) the Higgs boson self-coupling and (b) the Higgs-fermion Yukawa interactions and the BSM resonant Higgs boson production shown in (c).

pairs in the SM of approximately 7%. This channel can be divided into three final states depending on the decays of the tau leptons. The lepton-hadron, hadron-hadron and lepton-lepton final states occur around 45.6%, 41.9% and 12.4% of the time, respectively. The final states including an electron (muon) are referred to as $e\tau_{\text{had}}$ ($\mu\tau_{\text{had}}$). The larger branching ratio and clean lepton signature makes the lepton-hadron final state the most sensitive. Comparatively, the $b\bar{b}b\bar{b}$ channel has the largest branching ratio for the decays of Higgs boson pairs but suffers from large multijet backgrounds, and despite its clean signature the $b\bar{b}\gamma\gamma$ channel has a branching ratio more than 25 times smaller than that for decays to $b\bar{b}\tau\tau$. These factors combined with the accurate reconstruction of the ditau mass (discussed in Section 8.5) makes the $b\bar{b}\tau\tau$ decay a promising search channel.

Although the data collected during Run 1 is expected to be insensitive to the Higgs boson self-coupling in the SM [125], it is still important to quantify the sensitivity of this data set and develop the foundations of future measurements. Furthermore, enhancements in the rates of both nonresonant and resonant production are expected in alternative Higgs BSM models.

8.2 Background Processes

This analysis considers single SM Higgs boson production processes as background. Processes that contain one Higgs boson decaying to a pair of tau leptons or pair of b-quarks with one lepton in the final state are included. Therefore the production modes ggh, qqh, Vh and $t\bar{t}h$ are used for $h \to \tau\tau$ decays and Vh and $t\bar{t}h$ for $h \to b\bar{b}$ decays. Here V is used to indicate a W or Z vector boson.

The decays of $t\bar{t}$ events form the dominant background to this analysis. If both W bosons (from $t \to bW$) decay leptonically, these events create signatures with real $E_{\mathrm{T}}^{\mathrm{miss}}$, electrons, muons or tau leptons that can result in a visible final state that is identical to the signal. In addition, the hadronic decay products of a W boson can potentially be misidentified as a hadronic tau candidate. Single-top production via the s- or t-channel contributes to the background if the W boson decays leptonically and the tau lepton is faked by a misidentified hadronic jet. In the case of Wt production, the tau lepton comes from the decay of the second W boson.

$Z/\gamma^* \to \tau\tau$ plus heavy flavour events constitute a large irreducible background as they have two real tau leptons and produce the same final state as the signal. $Z/\gamma^* \to ee$ plus heavy flavour and $Z/\gamma^* \to \mu\mu$ plus heavy flavour events can also be background providing one of the leptons or an accompanying hadronic jet are misidentified as a tau lepton. For simplicity, these Z/γ^* processes are hereafter referred to as $Z \to \tau\tau$, $Z \to ee$ and $Z \to \mu\mu$, respectively.

W production in association with jets provides a significant source of background due to its relatively large cross section and the combination of a lepton and $E_{\mathrm{T}}^{\mathrm{miss}}$ from a leptonic decay of the W boson in the final state. Hadronic jets accompanying the W boson can be misidentified as hadronic tau decays and b-jets.

The EW production of pairs of vector bosons can contribute to the background. The production of ZZ can lead to $b\bar{b}\tau\tau$ final states if one of the Z bosons decays to a ditau pair and the other to a $b\bar{b}$ pair. In addition, WW and WZ processes can be

background if the events have one or two fake lepton/tau/b-jets. All of these sources contribute a relatively small background.

The large cross sections for QCD dijet or multijet processes result in a background contribution if one of the jets is misidentified as a hadronic tau decay and another jet as an electron or muon. In this case, the lepton can also arise from the semileptonic decays of b or c hadrons.

8.3 Data and Monte Carlo Samples

This analysis uses the full pp collision data set recorded in 2012 at a centre-of-mass energy of 8 TeV with the ATLAS detector, corresponding to an integrated luminosity of 20.3 fb^{-1}. Only data which pass the requirements for the normal operation of all subdetectors are included. The analysis uses events collected by the lowest threshold unprescaled electron and muon SLTs that pass into the `EGamma` and `Muon` data streams, respectively. The thresholds for both of these triggers are 24 GeV and both require isolated objects.

The MC samples for signal and background are simulated with different event generators each interfaced to Pythia8 [116] for parton shower, hadronisation and underlying event simulation. The events from minimum-bias interactions were simulated using the AU2 [126] parameter tuning of Pythia8. Tauola [127] and Photos [128] are used to simulate the tau decay and additional photon radiation from charged leptons to fit the data, respectively. The set of PDFs CT10 [129] is used for the Powheg samples, while CTEQ6L1 [130] is used for the Pythia8 and Alpgen samples. The detector simulation in all the MC samples is performed with Geant4 [111] and the reconstruction is made with the same software as is used for data. All MC samples are then corrected to better reproduce the data, using official recommendations from combined performance groups. An overview of the generators and PDFs used for the signal and background processes is given in Table 8.1.

Table 8.1: List of the MC generators and PDFs used to model the signal and background processes at $\sqrt{s} = 8\,\text{TeV}$ for the $hh \to b\bar{b}\tau\tau$ analysis.

Process	Event generator	PDF set
Background processes		
V + jets	Alpgen + Pythia8	CTEQ6L1
Diboson: WW	Powheg + Pythia8	CT10
Diboson: WZ	Powheg + Pythia8	CT10
Diboson: ZZ	Powheg + Pythia8	CT10
$t\bar{t}$	Powheg + Pythia8	CT10
Single top: t-channel	AcerMC + Pythia8	CTEQ6L1
Single top: s-channel	Powheg + Pythia8	CT10
Single top: Wt	Powheg + Pythia8	CT10
$gg \to h$	Powheg + Pythia8	CT10
$qq \to qqh$	Powheg + Pythia8	CT10
$qq \to Vh$	Pythia8	CTEQ6L1
$qq/gg \to t\bar{t}h$	Pythia8	CTEQ6L1
Signal processes		
Nonresonant $gg \to hh$	MadGraph5 + Pythia8	CTEQ6L1
Resonant $gg \to H \to hh$	MadGraph5 + Pythia8	CTEQ6L1

The nonresonant and resonant Higgs boson pair production signal processes are produced with the Leading Order (LO) MadGraph5 generator [131]. The nonresonant production is modelled using the SM di-Higgs model [132, 133]. The resonant production of the heavy scalar H decaying to two Higgs bosons is generated using the HeavyScalar model [134]. A narrow decay width of 10 MeV is assumed for the heavy scalar H, which is significantly smaller than the detector resolution.

The single SM Higgs background is simulated for each of the production mechanisms individually. The simulation of ggF and VBF process samples is based on the NLO perturbative calculation, including finite bottom quark and top quark mass effects [135], using the Powheg event generator [112, 113, 114]. The Higgs boson p_{T} spectrum of the ggF process is matched with the calculated spectrum at Next-to-Next-to-Leading Order (NNLO) and Next-to-Next-to-Leading Logarithm (NNLL) [136] in QCD corrections. The Pythia8 generator is used to simulate events for associated production and $t\bar{t}h$. These backgrounds are all normalised to the state-of-the-art theoretical cross sections provided by References [137, 39, 40].

The ALPGEN program [138] is used to produce the W + jets and Z + jets samples. This generator employs the MLM matching scheme [139] between the hard process, calculated with LO matrix elements for up to five jets, and the parton shower. The POWHEG generator is used to simulate $t\bar{t}$ events as well as the s-channel and Wt processes of single top production. The ACERMC program [140] is used to simulate the single top t-channel process. The diboson backgrounds are simulated with the POWHEG generator.

The $Z \to \tau\tau$ background sample is obtained using a hybrid data and MC technique known as *embedding* that was originally developed for the SM $H \to \tau\tau$ analysis and is described extensively in Reference [141]. This technique offers a way of modelling the $Z \to \tau\tau$ background in a largely data-driven approach, as existing MC simulations of Z + jets events have been shown not to be entirely consistent with data [142]. Due to the difficulties associated with obtaining a pure high statistics $Z \to \tau\tau$ sample in data without contamination of Higgs boson decays to tau lepton pairs, the embedding method works by tagging $Z \to \mu\mu$ events in data and replacing the muons with simulated tau lepton decays. The tau lepton kinematics are matched to the kinematics of the muons they are replacing accounting for the mass difference between the muons and the tau leptons. The small coupling of the Higgs boson to muons means that $Z \to \mu\mu$ events provide a virtually signal-free signature.

The $Z \to \mu\mu$ selection in data requires that collision events pass either a single muon trigger with a p_{T} threshold of 24 GeV, or a dimuon trigger with leading muon threshold of 18 GeV and a subleading muon threshold of 8 GeV. There must be at least two reconstructed muons with pseudorapidity of $|\eta| < 2.5$ and a leading (subleading) muon transverse momentum $p_{\mathrm{T}} > 20$ (15) GeV. The muons must have track isolation in a cone of size $\Delta R < 0.4$ to be less than 20% of the muon p_{T}. There must be at least one opposite-charge muon pair with invariant mass $m_{\mu\mu} > 40$ GeV. For events with more than two muon candidates, all possible oppositely-charged pairs with a common vertex are formed, and the muon pair with $m_{\mu\mu}$ closest to the Z boson resonance is chosen as the $Z \to \mu\mu$ candidate decay products.

8.4 Object Selection

The $hh \to b\bar{b}\tau\tau$ analysis uses a wide variety of physics objects that include electrons, muons, jets, hadronically decaying tau leptons and $E_{\mathrm{T}}^{\mathrm{miss}}$. In addition, this analysis required that jets are b-tagged using a specifically designed algorithm. This section briefly describes the reconstruction and identification of these physics objects by the ATLAS detector and the selection used in the $hh \to b\bar{b}\tau\tau$ analysis. The object definitions and event selection largely mirror those of the existing ATLAS SM $H \to \tau\tau$ analysis [143].

Electrons

Electron candidates are reconstructed from clusters of energy in the EM calorimeters matched to a track in the ID. The tracks are fitted using a Gaussian Sum Filter [144] that allows for energy losses due to bremsstrahlung to be accounted for. A set of cut-based identification criteria provide background discrimination from hadronic jets by using information about the longitudinal and transverse shower profiles available from the calorimeter and information about the ID track and high-threshold TRT hits.

Electrons are required to pass the *tight* identification criteria with a transverse energy $E_{\mathrm{T}} > 15\,\mathrm{GeV}$ and to be in the fiducial volume of the barrel or the endcaps, defined by $|\eta| < 1.37$ or $1.52 < |\eta| < 2.47$. The typical reconstruction and identification efficiencies for electrons satisfying these selection criteria range between approximately 65% and 85% depending on E_{T} and η [145]. Isolation is required such that the calorimeter energy in a cone of radius $\Delta R = 0.2$ around the electron is less than 6% of the electron's E_{T}. Additionally, track isolation is imposed by requiring that the p_{T} sum of additional tracks with $p_{\mathrm{T}} > 1\,\mathrm{GeV}$ in a cone of radius $\Delta R = 0.4$ is less than 6% of the electron's track p_{T}. Corrections are applied to MC to account for mismodelling of the electron reconstruction and identification efficiencies and calorimeter isolation.

Muons

Muon candidates are reconstructed using an algorithm that combines information from the MS and ID. Muon tracks are reconstructed in the MS by identifying local track segments in each of the chamber layers and combining these into a full MS track. The ID provides an independent measurement of the muon track close to the interaction point. Combined muons are identified by successfully matching an MS track with an ID track to form a combined measurement of the muon track parameters. Additional muon quality criteria on the number of ID hits is also applied to reduce the misidentification rate.

The analysis requires muons to have transverse momenta $p_{\mathrm{T}} > 10\,\mathrm{GeV}$ and pseudorapidity $|\eta| < 2.5$. The efficiencies for muons satisfying these selection criteria are typically above 95% [146]. Similarly as for electrons, calorimeter isolation is imposed by requiring that the additional energy deposited in the calorimeters in a cone of radius $\Delta R = 0.2$ around the muon is less than 6% of the muon's p_{T}. Track isolation is also required such that the p_{T} sum of additional tracks with $p_{\mathrm{T}} > 1\,\mathrm{GeV}$ in a cone of radius $\Delta R = 0.4$ is less than 6% of the muon's track p_{T}. Correction factors are applied to MC to account for observed differences in the p_{T} resolution and identification efficiency between data and simulation, as well as for calorimeter isolation.

Hadronic τ

In 65% of cases tau leptons decay hadronically, for which a specialised algorithm is required to reconstruct candidates [147]. The hadronic tau reconstruction starts from jets formed by the anti-k_t algorithm [118] with distance parameter $R = 0.4$, using calorimeter topoclusters [119] with a local hadronic calibration [148] as input. To seed a hadronic tau candidate the jets are required to have $p_{\mathrm{T}} > 10\,\mathrm{GeV}$ and $|\eta| < 2.5$. To improve reconstruction efficiency in increased pile-up the tau lepton production vertex is identified with a dedicated tau vertex association algorithm.

This enables the association of tracks with the reconstructed jet and to build the system in which identification variables are calculated. The hadronic decay products predominately contain either one or three charged pions which can be identified by the number of reconstructed tracks and are referred to as 1-track and 3-track hadronic taus, respectively. The tau reconstruction provides very little rejection against jet backgrounds. The offline tau identification uses various discriminating variables combined in separate Boosted Decision Trees (BDTs) to help discriminate against both jets and electrons.

The hadronic tau candidates in the $hh \rightarrow b\bar{b}\tau\tau$ analysis are required to have $p_{\mathrm{T}} > 20\,\mathrm{GeV}$ and to pass the *medium* jet discriminator identification. Additionally, they must have one or three associated tracks with a total charge of ± 1, determined by summing the charges of the associated tracks. Hadronic taus with 1-track are required to have a cluster within $|\eta| < 2.47$ and a track within $|\eta| < 2.47$, while 3-track hadronic taus need only a cluster within $|\eta| < 2.5$. The identification efficiency for hadronic tau candidates satisfying the *medium* criteria is of the order of 55–60% [147]. In the $e\tau_{\mathrm{had}}$ channel, hadronic tau candidates are additionally required to pass the *medium* electron discriminator.

Jets

Jets are reconstructed using the anti-k_t algorithm with distance parameter $R = 0.4$ using as input topological clusters calibrated with the local hadronic calibration scheme. The jet energies are corrected for contributions from pile-up using a technique based on jet area [149] and are calibrated using p_{T}- and η-dependent correction factors determined from data and simulation [150, 151].

Jets are required to have $p_{\mathrm{T}} > 30\,\mathrm{GeV}$ and $|\eta| < 4.5$. For those within the acceptance of the tracking detectors, the vertex information for associated tracks is used to compute the so-called Jet-Vertex Fraction (JVF). The JVF is defined as the ratio of the transverse momentum sum of the tracks matched to the jet that are associated

to the primary vertex and the transverse momentum sum of the tracks matched to the jet that are associated to any vertex in the event. Jets with $|\eta| < 2.4$ and $p_{\mathrm{T}} < 50\,\mathrm{GeV}$ are required to have $|\mathrm{JVF}| > 0.5$ in order to suppress pile-up contributions. Jets are explicitly used in the event selection and categorisation, and to propagate jet energy uncertainties to missing transverse momentum.

B-Tagging

The identification of jets originating from b-quarks is important to suppress background processes containing mainly light flavour jets. The relatively long lifetime of b-hadrons means they travel some distance before they decay, leaving a displaced secondary vertex. Different algorithms exist in ATLAS that exploit the main signatures of such decays and their outputs are combined to further improve the tagging efficiency and reduce the mistag rate [152].

This analysis uses the MV1 neural network based discriminator to tag b-jets [153]. Tagged jets are required to be in the pseudorapidity range $|\eta| < 2.5$, as the algorithms require tracking information, and to pass the 80% efficiency working point for b-jets in simulated $t\bar{t}$ events. The corresponding light-quark misidentification probability is around 10% depending on the p_{T} and η of the jet.

Overlap Removal

There is the possibility that multiple objects, as defined by the criteria given above, actually correspond to the same physical object in the detector. In such instances an "overlap removal" scheme is followed to retain the object most likely to be correct. Objects are considered to be overlapping if they lie within $\Delta R < 0.2$ and the overlap is resolved by selecting objects in the following order of priority: muons, electrons, tau leptons and then jet candidates. For the purpose of overlap removal, the isolation requirements are dropped from the muon and electron identification and the *loose* identification for electrons is used. Additionally, in order to improve the rejection of

fake tau candidates caused by misidentified low-p_{T} muons, the muon p_{T}-threshold is lowered to 4 GeV when checking for overlaps between muon and tau candidates only. To provide further rejection against tau candidates faked by electrons, electrons found in the transition region between the barrel and endcap calorimeters ($1.37 < |\eta| < 1.52$) fulfilling the *medium* identification are also used to check overlaps with tau candidates.

Missing Transverse Energy

The $E_{\mathrm{T}}^{\mathrm{miss}}$ is an event-level quantity based on the energy deposited in the calorimeters and on muons reconstructed in the MS [154]. Its magnitude and direction are constructed from the vector sums of visible calibrated objects and soft contributions from pile-up and the underlying event. The calorimeter energy deposits are calibrated according to the reconstructed physics object to which they belong, with the following precedence: electrons, photons, hadronically decaying tau leptons, jets and muons. Energy deposits not associated with these objects are taken into account in the soft term of the $E_{\mathrm{T}}^{\mathrm{miss}}$ calculation. This summation is performed over the range $|\eta| < 4.5$. The vector sum of calibrated muon transverse momenta is also added and the parameterised energy loss in the calorimeter associated with these muons is subtracted to avoid double counting.

In order to suppress pile-up in $E_{\mathrm{T}}^{\mathrm{miss}}$, each jet with $|\eta| < 2.4$ is weighted with the JVF (forward jets are taken uncorrected) and the energy contributions not associated to physics objects are scaled using the so-called Soft-Term Vertex-Fraction (STVF). The STVF is the ratio of the transverse momentum sum of the tracks unmatched to physics objects that are associated to the primary vertex and the transverse momentum sum of the tracks unmatched to physics objects that are associated to any vertex in the event [155]. In MC simulations, corrections applied to the energy of electrons and muons are propagated to the missing transverse momentum.

8.5 Mass Reconstruction

The motivation for and implementation of the ditau invariant mass reconstruction technique used in the $hh \to b\bar{b}\tau\tau$ analysis is detailed in [156]. The accurate reconstruction of a resonance decaying to a pair of tau leptons is complicated by the presence of one or two neutrinos per tau lepton decay. The simplest reconstruction methods rely on partial reconstruction of the ditau invariant mass, such as the mass of the visible decay products, while alternative approximations are based on assumptions about the invisible decay products, such as the collinear mass approximation [157]. Each of these techniques have drawbacks, including poor mass resolution, strong assumptions about the ditau system, or even lack of calculability in some cases.

In this analysis, the ditau invariant mass is fully reconstructed using the Missing Mass Calculator (MMC) [156] method, which has been successfully used in the SM $H \to \tau\tau$ analysis [143]. It has the benefit of making no assumptions about the ditau decay kinematics, while fully reconstructing an accurate invariant mass. This requires solving an underconstrained system of equations for seven unknowns: x-, y-, and z-components of the momentum carried by the neutrinos for each of the tau leptons in the event, and the invariant mass of the neutrinos from the leptonic tau decay. However, there are only four equations available:

$$
\begin{aligned}
E_x^{\text{miss}} &= p_{\text{miss}_1} \sin\theta_{\text{miss}_1} \cos\phi_{\text{miss}_1} + p_{\text{miss}_2} \sin\theta_{\text{miss}_2} \cos\phi_{\text{miss}_2} \\
E_y^{\text{miss}} &= p_{\text{miss}_1} \sin\theta_{\text{miss}_1} \sin\phi_{\text{miss}_1} + p_{\text{miss}_2} \sin\theta_{\text{miss}_2} \sin\phi_{\text{miss}_2} \\
m_{\tau_1}^2 &= m_{\text{miss}_1}^2 + m_{\text{vis}_1}^2 + 2\sqrt{p_{\text{vis}_1}^2 + m_{\text{vis}_1}^2}\sqrt{p_{\text{miss}_1}^2 + m_{\text{miss}_1}^2} - 2p_{\text{vis}_1}p_{\text{miss}_1}\cos\Delta\theta_{\text{vis-miss}_1} \\
m_{\tau_2}^2 &= m_{\text{miss}_2}^2 + m_{\text{vis}_2}^2 + 2\sqrt{p_{\text{vis}_2}^2 + m_{\text{vis}_2}^2}\sqrt{p_{\text{miss}_2}^2 + m_{\text{miss}_2}^2} - 2p_{\text{vis}_2}p_{\text{miss}_2}\cos\Delta\theta_{\text{vis-miss}_2}
\end{aligned}
$$

Here the E_x^{miss} and E_y^{miss} are the x- and y-components of the $E_{\text{T}}^{\text{miss}}$ vector, $p_{\text{vis}_{1,2}}$, $m_{\text{vis}_{1,2}}$, $\theta_{\text{vis}_{1,2}}$, $\phi_{\text{vis}_{1,2}}$ are the momenta, invariant masses, polar and azimuthal angles of the visible tau decay products, and m_τ is the tau lepton invariant mass. The rest of the variables constitute the unknowns, which are the combined invisible momenta

p_{miss} carried away by the neutrinos for each of the tau decays and the invariant mass of the neutrinos in the leptonic tau decay m_{miss_1}. Finally, $\Delta\theta_{\text{vis-miss}_{1,2}}$ is the angle between the p_{miss} and p_{vis} vectors for each of the tau leptons.

The calculation uses the constraints from the measured components of the $E_{\text{T}}^{\text{miss}}$ vector, and the visible masses of both tau lepton decays. A scan is performed over the two components of the $E_{\text{T}}^{\text{miss}}$ vector and the yet undetermined variables. These constraints are combined with a two-dimensional likelihood function to solve for the seven kinematic parameters. Each scan point is weighted by its probability according to the tau decay topologies and the $E_{\text{T}}^{\text{miss}}$ resolution. The most likely value for the ditau mass $m_{\tau\tau}^{\text{MMC}}$ is chosen.

The MMC algorithm is highly efficient at finding a valid solution for signal and $Z \to \tau\tau$ events, while a low efficiency is observed for background samples, providing an extra handle against them. As a result, events which fail the mass reconstruction are rejected from the analysis. The algorithm also gives a good mass resolution and discrimination between $Z \to \tau\tau$ events and the Higgs boson signal. This separation is demonstrated in Figure 8.2a for the reconstructed mass distributions in the nonresonant search for simulated signal and the tau-embedded background sample.

The dijet mass (m_{bb}) is calculated using the two leading b-tagged jets, if two or more jets are b-tagged, or from the b-tagged jet and the highest p_{T} untagged jet if only one jet is b-tagged. Similar resolutions are achieved by m_{bb} and $m_{\tau\tau}^{\text{MMC}}$ for the signal, however a longer tail is present in the m_{bb} distribution. The mass of the heavy resonance ($m_{bb\tau\tau}$) is reconstructed using the dijet and MMC ditau four-momenta. To improve the mass resolution a simple rescaling is applied to each of these of m_h/m_{bb} and $m_h/m_{\tau\tau}^{\text{MMC}}$ respectively, where m_h is set to the value used in the simulation of 125 GeV. Figure 8.2b shows the signal distributions for the reconstructed and constrained $bb\tau\tau$ mass in the resonant search. It is established from simulation studies that the resolution of $m_{bb\tau\tau}$ varies from 2.4% at $m_H = 260$ GeV to 4.8% at 1000 GeV. The rescaling improves the mass resolution most significantly at low mass and varies between a factor of three gain at 260 GeV to a third at 1000 GeV.

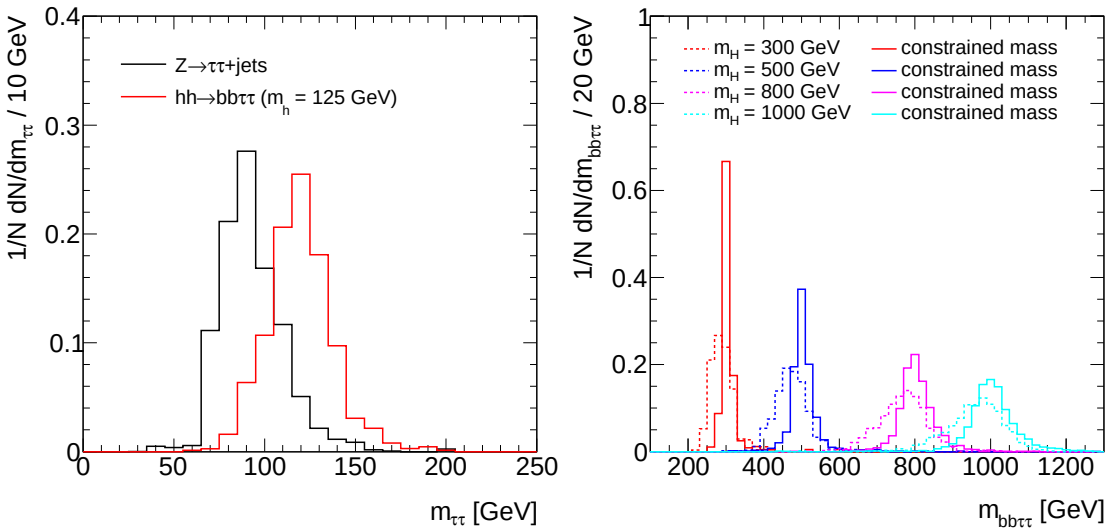

(a) (b)

Figure 8.2: Mass distributions of (a) the reconstructed $m_{\tau\tau}^{\mathrm{MMC}}$ for $hh \to b\bar{b}\tau\tau$ and $Z \to \tau\tau$ events in MC simulation and embedding respectively and (b) the reconstructed and constrained $m_{bb\tau\tau}$ for four simulated heavy Higgs boson masses.

8.6 Event Selection

As previously mentioned, the events used in this analysis are selected using the SLTs. To ensure that these triggers are nearly fully efficient for events passing the final selection the p_{T} requirements on the selected lepton are set at 2 GeV higher than the trigger threshold. This section describes the series of selection criteria imposed on these events, as well as the factors used to categorise them into different signal regions. The various background processes shown in the plots in this section are estimated with the methods described later in Section 8.7.

One of the limitations of this analysis is the relatively high SLTs thresholds for the leptonic tau decay without the inclusion of combined lepton and hadronic tau triggers to help improve the signal acceptance. This has an impact on the sensitivity of the analysis to lower mass resonances. Simulation studies indicate that if the SLT thresholds were lower by even 2 GeV there would be a relative improvement in the signal acceptance after the full analysis selection for a resonance of mass 300 GeV of around 10%.

8.6.1 Preselection

The event preselection is designed to select only the basic event topology. Each event requires a primary vertex with at least four tracks with transverse momentum $p_{\mathrm{T}} > 400\,\mathrm{MeV}$. This helps to reject non-collision events, such as cosmic rays and beam halo. If more than one such vertex exists, the vertex candidate with the largest sum of the squared transverse momenta of all the associated tracks is selected. Events are required to have exactly one isolated electron or muon with $p_{\mathrm{T}} > 26\,\mathrm{GeV}$ and exactly one hadronic tau with $p_{\mathrm{T}} > 20\,\mathrm{GeV}$ of opposite sign charge to the selected lepton. Events with more than one lepton passing the object preselection described in Section 8.4 are rejected to suppress $Z \to ee$, $Z \to \mu\mu$, $t\bar{t}$ and Wt single top processes. For the purpose of this dilepton veto, the isolation requirements are dropped from the electron and muon identification, and a looser identification requirement is used for electrons. The final requirement is for at least two jets with $p_{\mathrm{T}} > 30\,\mathrm{GeV}$, where between one and three of these selected jets must be b-tagged.

Figures 8.3a and 8.3b show the observed distributions in data and those expected from background events of the $m_{\tau\tau}^{\mathrm{MMC}}$ and m_{bb} after the preselection. The selection is dominated by contributions from top quark production and fake tau, and to a lesser degree $Z \to \tau\tau$ backgrounds. The distributions also contain signal for nonresonant Higgs boson pair production and a resonantly produced heavy Higgs signal with a mass of 300 GeV, both normalised to a production cross section of 20 pb. The signal yield for the nonresonant production is significantly larger than for lower mass resonances, assuming the same cross section. This is largely the result of the harder p_{T} spectrum of the Higgs boson in the nonresonant production. Data in all distributions are well modelled by the background predictions. Events passing the preselection cuts form the baseline event sample from which the final analysis categories and several control regions are defined, as described in the subsequent sections.

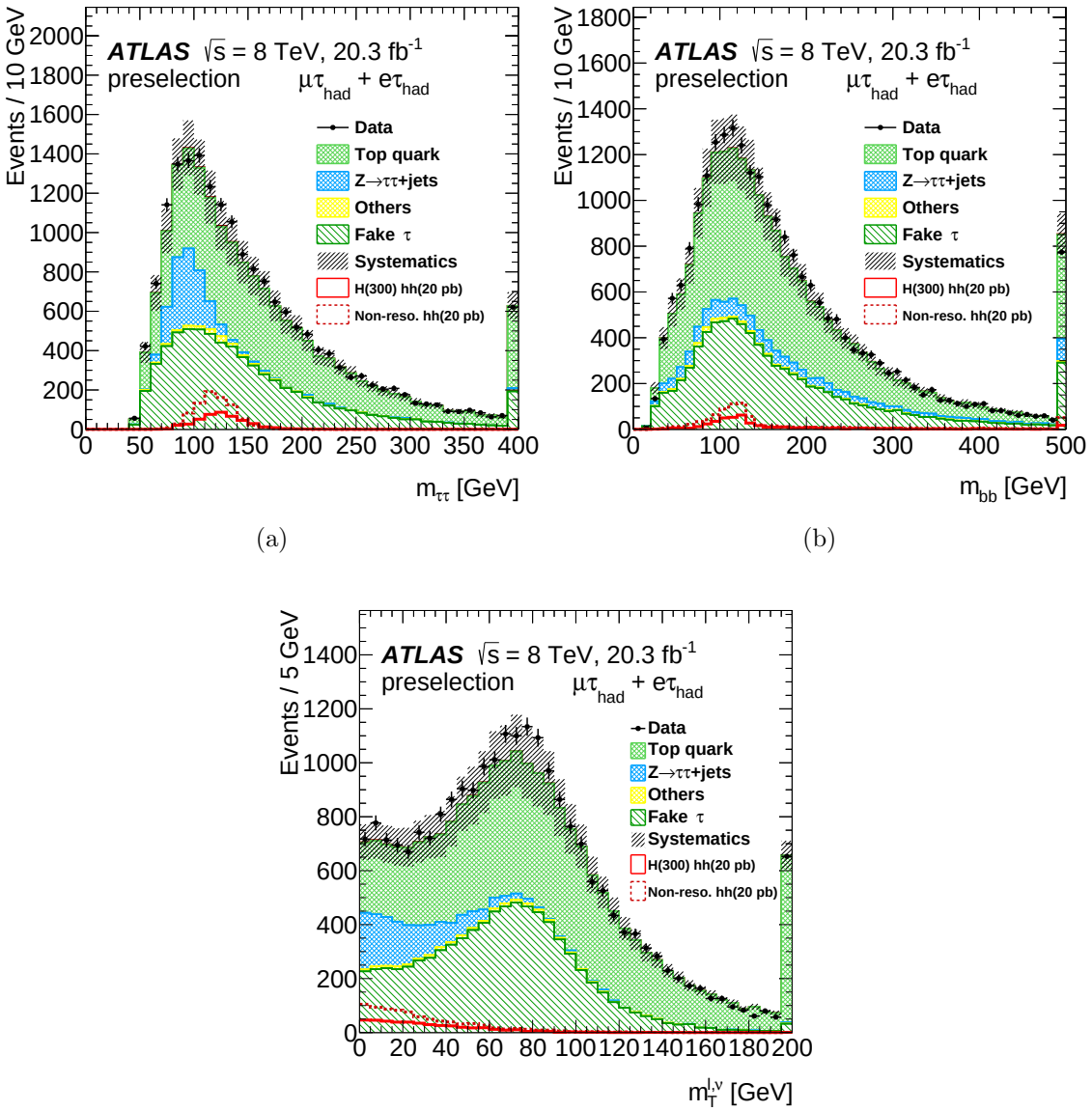

(a) (b)

(c)

Figure 8.3: Distributions after preselection comparing data with the expected background contributions: (a) ditau mass $m_{\tau\tau}$ reconstructed using the MMC method, (b) dijet mass m_{bb} and (c) the transverse mass $m_{\mathrm{T}}^{\ell\nu}$ of the lepton and the $E_{\mathrm{T}}^{\mathrm{miss}}$ system [8]. The top quark background includes contributions from both $t\bar{t}$ and the single top processes. The $Z \to \tau\tau$ + jets background is estimated using tau-embedded data. The background labelled as "Others" is composed of the diboson and $Z \to ee/\mu\mu$ contributions. The fake τ background is estimated with the fake factor method. Single SM Higgs boson contributions are included on these distributions, but are not significant enough to be visible. The uncertainties associated with the total background estimate is given by the black hatched bands. The expected signal distributions for simulated nonresonant and resonant Higgs boson pair production are overlaid assuming a production cross section of 20 pb. The resonant production signal shown here is for $m_H = 300\,\mathrm{GeV}$. The overflows are included in the last bin of each distribution.

8.6.2 Event Categorisation

To exploit the differences in contributions from signal and background in different kinematic regions, events passing the preselection are divided amongst four analysis categories according to the number of b-jets $n_{b\text{-jet}}$ and the transverse momentum of the ditau system $p_{\mathrm{T}}^{\tau\tau}$ for both the nonresonant and resonant searches. Although two b-jets are expected in the final state, events are categorised into those containing only one b-tagged jet and those with at least two b-tagged jets to maximise the signal efficiency. There is however a maximum of three b-tagged jets allowed, in order for this analysis to remain statistically independent of the $hh \to b\bar{b}b\bar{b}$ analysis in the Higgs pair production combination, presented in Chapter 9. Events are further divided into low and high $p_{\mathrm{T}}^{\tau\tau}$ categories defined by a cut at 100 GeV, where the value of $p_{\mathrm{T}}^{\tau\tau}$ used is that computed by the MMC. The four categories used in the final statistical fitting are summarised in Table 8.2.

Table 8.2: Summary of categories used in final statistical calculation, based on the number of b-tagged jets and transverse momentum of ditau system.

Category name	$n_{b\text{-jet}}$	$p_{\mathrm{T}}^{\tau\tau}$ (GeV)
1 b-tag, low $p_{\mathrm{T}}^{\tau\tau}$	1	< 100
1 b-tag, high $p_{\mathrm{T}}^{\tau\tau}$	1	> 100
2 b-tag, low $p_{\mathrm{T}}^{\tau\tau}$	2 or 3	< 100
2 b-tag, high $p_{\mathrm{T}}^{\tau\tau}$	2 or 3	> 100

Figure 8.4 shows the distibutions of $p_{\mathrm{T}}^{\tau\tau}$ after preselection for 1 b-tag and 2 b-tag category events. The background composition in each of these regions is very different. The categories with two or three b-tagged jets are more sensitive to signal events than those with one b-tagged jet, while higher resonant masses are more likely to have a large $p_{\mathrm{T}}^{\tau\tau}$, where the backgrounds are smaller. Although the categories with one b-tagged jet are less sensitive to signal, they will help constrain the background in the combined likelihood fit, discussed in Section 8.9.

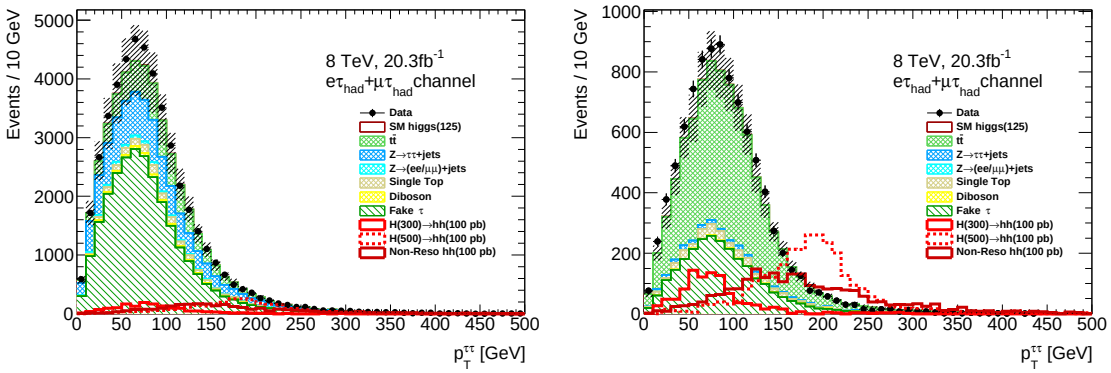

(a) (b)

Figure 8.4: Distributions of $p_{\mathrm{T}}^{\tau\tau}$ after preselection for (a) events with one b-tagged jet and (b) events with two or three b-tagged jets. The expected signal distributions for a cross section of 100 pb are overlaid for both nonresonant Higgs boson pair production and for 300 GeV and 500 GeV resonances.

8.6.3 Final Selection

To increase the sensitivity of the analysis, a set of additional kinematic cuts are considered after the preselection to further suppress backgrounds. The first of these cuts is on the transverse mass between the lepton and the $E_{\mathrm{T}}^{\mathrm{miss}}$ system, which helps to discriminate between signal and backgrounds with $W \to \ell\nu_\ell$. It is defined by:

$$m_{\mathrm{T}}^{\ell\nu} = \sqrt{2p_{\mathrm{T}}^{\ell}E_{\mathrm{T}}^{\mathrm{miss}}(1-\cos\Delta\phi)}, \tag{8.1}$$

where p_{T}^{ℓ} is the transverse momentum of the lepton and $\Delta\phi$ is the angle between the lepton and $E_{\mathrm{T}}^{\mathrm{miss}}$ in the plane perpendicular to the beam direction. It can be seen in Figure 8.3c that signal events are more likely to have small values of the transverse mass. This results in a cut requiring events to have $m_{\mathrm{T}}^{\ell\nu} < 60\,\mathrm{GeV}$ to reduce contributions from the fake tau and top quark background processes, while retaining an approximate signal efficiency of 90%.

Additional suppression of the top and W + jets background is provided by a requirement on the $E_{\mathrm{T}}^{\mathrm{miss}}$ ϕ centrality. It quantifies whether the $E_{\mathrm{T}}^{\mathrm{miss}}$ is between the lepton and tau in the transverse plane as is typical in true ditau systems. The variable is maximised when the $E_{\mathrm{T}}^{\mathrm{miss}}$ points directly between the lepton and tau

candidates, and minimised when it points directly opposite. Events are required to have $E_{\mathrm{T}}^{\mathrm{miss}}$ ϕ centrality > 1, which ensures that the $E_{\mathrm{T}}^{\mathrm{miss}}$ is between the lepton and tau candidates.

A significant source of the fake tau background is produced by the semileptonic decays of $t\bar{t}$ events, where one W boson decays leptonically and the other one decays hadronically. In this case, the reconstructed tau is a result of one of the jets from the hadronic decay of the W boson. To reduce this background source, a selection is made in the two-dimensional plane of the reconstructed W mass $m_{\tau j}$ and the reconstructed top mass $m_{\tau jb}$. The hadronic W mass is reconstructed using the tau jet and the nearest untagged jet. The top mass is reconstructed by the addition of the b-jet that minimises the mass sum $m_{\ell b}+m_{\tau b}$. The following elliptical requirement is imposed in the two-dimensional plane, taking the form of a χ^2:

$$\left(\frac{\Delta m_W \cos\theta - \Delta m_t \sin\theta}{28\,\mathrm{GeV}}\right)^2 + \left(\frac{\Delta m_W \sin\theta - \Delta m_t \cos\theta}{18\,\mathrm{GeV}}\right)^2 > 1 \qquad (8.2)$$

Here $\Delta m_W = m_{\tau j} - m_W$, $\Delta m_t = m_{\tau jb} - m_t$ and θ is a rotation angle given by $\tan\theta = m_t/m_W$ used to account for the average correlation between $m_{\tau j}$ and $m_{\tau jb}$. Figure 8.5 shows the reconstructed $m_{\tau j}$ versus $m_{\tau jb}$ for simulated semileptonic $t\bar{t}$ events and the resonant signal, where events inside the ellipse are rejected.

A cut is also made to improve the rejection of $t\bar{t}$ events whose decays produce an identical visible final state to the signal, in the case where one W decays to an electron or muon and the other to a tau lepton which then decays hadronically. In signal events the p_{T} of the lepton will tend to be softer than that of the hadronic tau due to there being more neutrinos in the leptonic decay of the tau. The p_{T} of the lepton or muon is therefore required to satisfy $p_{\mathrm{T}}^{\ell} < p_{\mathrm{T}}^{\tau} + 20\,\mathrm{GeV}$.

To be consistent with the expectation of the $h \to b\bar{b}$ decay, events must pass the mass window cut of $90 < m_{bb} < 160\,\mathrm{GeV}$. This is the final cut made in the nonresonant search and the final discriminant used to extract the signal is the ditau invariant mass $m_{\tau\tau}^{\mathrm{MMC}}$. The resonant search places an additional mass window cut to the ditau

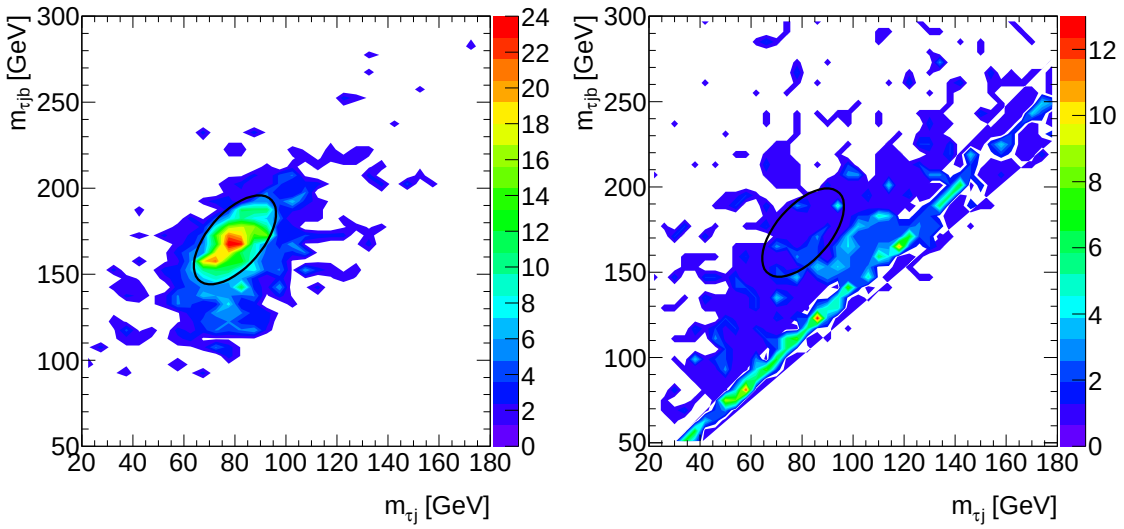

(a) (b)

Figure 8.5: Distribution of $m_{\tau j}$ versus $m_{\tau jb}$ for simulated (a) semileptonic $t\bar{t}$ events and (b) resonant signal with $m_H = 260\,\text{GeV}$ passing the preselection. The normalisation scales are arbitrary. Events falling inside the ellipse are rejected.

invariant mass of $100 < m_{\tau\tau}^{\text{MMC}} < 150\,\text{GeV}$ to ensure that events are consistent with the $h \to \tau\tau$ decay. The efficiency for the nonresonant signal after the full analysis selection is 0.57%. The resonant signal selection efficiency improves consistently for increasing values of m_H varying from 0.2% at 260 GeV to 1.5% at 1000 GeV.

8.7 Background Estimation

The estimation of the numbers of background events and their associated kinematic distributions is provided by a mixture of data-driven and simulation-based methods. The normalisation of the most important background contributions is performed by comparing the simulated samples of individual background sources to data in regions which have a small or negligible contamination from signal or other background events.

Background contributions from jets that are misidentified as hadronically decaying tau leptons (fake backgrounds) are estimated by using a *fake factor* method. The

$Z \rightarrow \tau\tau$ background kinematic distributions are provided by the tau-embedded data sample described in Section 8.3. Contributions from various other physics processes are estimated using the simulation and are normalised to the theoretical cross sections. The following sections discuss in more detail the estimation of the various background components.

8.7.1 Fake Factor Method

The fake factor method is used to derive estimates of the fake background resulting from jets misidentified as hadronic tau candidates that cause events to pass the analysis selection. It accounts for the QCD and multijet, W + jets, Z + jets, and semileptonic $t\bar{t}$ backgrounds. The fake factor method uses a control sample requiring that tau candidates pass the object selection criteria but fail the *medium* identification. These objects are referred to here as 'antitau' candidates. The antitau selection for the control sample is chosen to minimise the differences from identified tau leptons as far as possible, while maintaining sufficient statistics for a reliable background estimate. This is achieved by placing a lower cut on the hadronic tau identification BDT score of 0.7 × the *loose* identification working point.

The values of the identification cuts are dependant on the transverse momentum of the tau candidate as shown in Figure 8.6. This means that the antitau selection includes values that lie approximately between 0.35 and 0.65. The flavour composition of these candidates can be seen in Figure 8.7, where the antitau selection reduces the pile-up and gluon content to better resemble the *medium* identification region.

The fake tau background in the Signal Regions (SRs) is estimated with the following calculation:

$$n^{\text{SR}}_{\text{fake }\tau} = \left(n^{\text{SR, data}}_{\text{antitau}} - n^{\text{SR, real}}_{\text{antitau}}\right) \times \text{FF}, \tag{8.3}$$

where $n^{\text{SR, data}}_{\text{antitau}}$ is the antitau contribution from data, $n^{\text{SR, real}}_{\text{antitau}}$ accounts for events with real hadronic tau objects that fail identification and FF is the transfer factor referred to as the fake factor. The $n^{\text{SR, real}}_{\text{antitau}}$ component also includes contributions

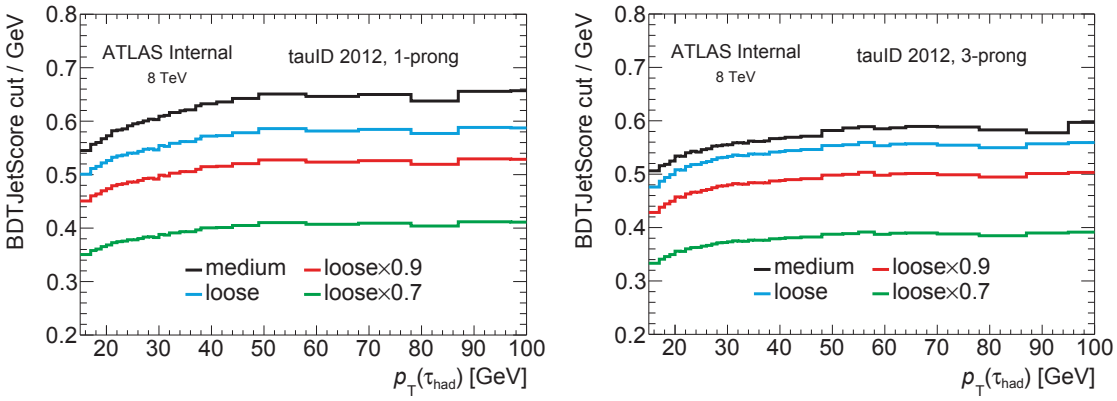

(a) 1-track (b) 3-track

Figure 8.6: Requirement on the hadronic tau jet discriminant for various operating points as a function of the candidate p_{T}.

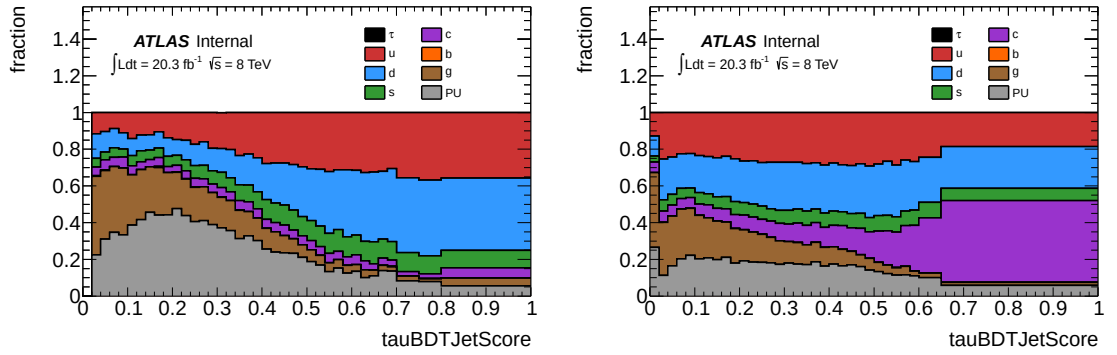

(a) 1-track (b) 3-track

Figure 8.7: Origin of the antitau candidates in terms of parton flavour and pile-up jets in simulated W + jets events.

from $\ell \rightarrow \tau_{\mathrm{had}}$ fakes and is estimated using MC and tau-embedded events. In events where there are more than one antitau candidate present, each is considered in a separate antitau event.

The fake factor is defined as the ratio of the number of reconstructed hadronic tau candidates passing the *medium* identification to the number satisfying the antitau selection discussed above:

$$\mathrm{FF} = \frac{n^{\mathrm{CR}}_{\tau_{\mathrm{had}}}}{n^{\mathrm{CR}}_{\mathrm{antitau}}}. \tag{8.4}$$

The fake factor estimate is derived for a Control Region (CR) that excludes events entering the signal region and should be void of signal. However, there are a number

of different processes that contribute significantly to antitau events in this analysis and so their fake factors must be considered individually. The fake factors were measured using data in the following dedicated control regions:

- QCD: Apply preselection, but with relaxed lepton isolation
- W + jets: Apply preselection without the b-tag selection and $m_{\mathrm{T}}^{\ell\nu} > 70\,\mathrm{GeV}$
- Z + jets: Apply preselection, but with the dilepton veto inverted
- Top: Apply preselection and require $m_{\mathrm{T}}^{\ell\nu} > 70\,\mathrm{GeV}$

The fake factor is determined for bins in p_{T} of the hadronic tau candidate, as well as for the number of tracks. Figure 8.8 shows the fake factor measured in data for each of the QCD, W + jets, Z + jets and top control regions for 1-tack and 3-track hadronic tau candidates. The values of the fake factor measured in the different control regions do not show significant deviation within statistical uncertainty.

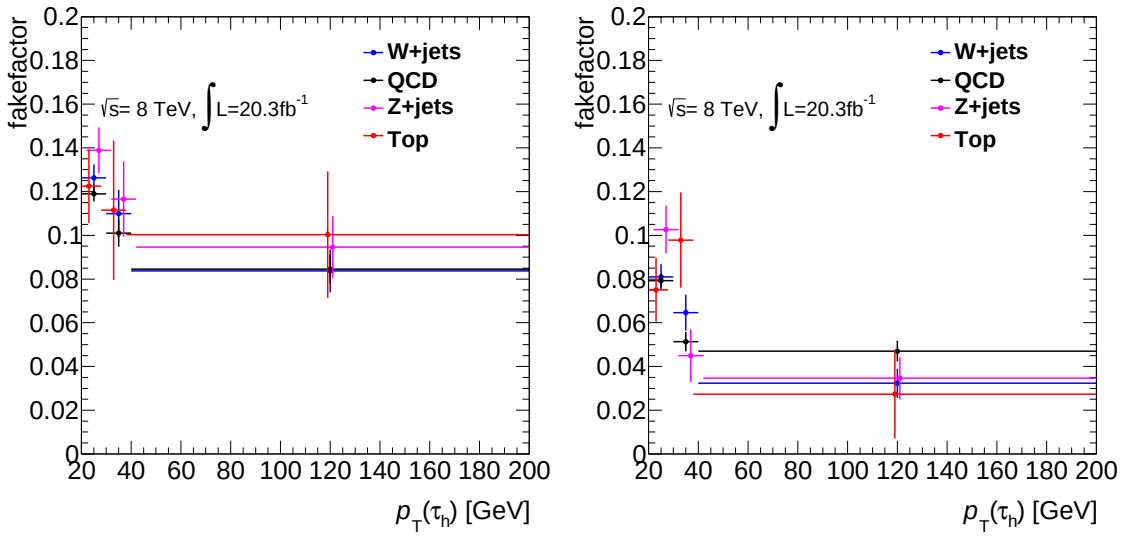

(a) 1-track (b) 3-track

Figure 8.8: Fake factors for the W + jets, QCD, Z + jets and top control regions as a function of the hadronic tau candidate p_{T}. The error bars show the statistical uncertainty only.

It is not possible to predetermine which process is responsible for an antitau event

and so a combined fake factor is used which accounts for the relative fraction of each process in the antitau sample. The combined fake factor is given by:

$$\mathrm{FF}(p_{\mathrm{T}}, n_{\mathrm{track}}) = \sum_{i}^{\mathrm{CR}} R_i \cdot \mathrm{FF}_i(p_{\mathrm{T}}, n_{\mathrm{track}}), \tag{8.5}$$

where R_i is the fraction of antitau events contributed by the background CR i and FF_i is the fake factor specific to that background CR. The values for R_i are determined using MC estimates for the antitau contribution of $Z+$jets and top processes, except for QCD and $W+$jets. For $W+$jets, this fraction is estimated using a data-driven technique involving the antitau $W+$jets control region and a MC-based extrapolation from the antitau $W+$jets control region to the antitau signal region:

$$R_{W+\mathrm{jets}} = \frac{n_{\mathrm{antitau}}^{\mathrm{SR},\ W+\mathrm{jets}}}{n_{\mathrm{antitau}}^{\mathrm{SR},\ W+\mathrm{jets}} + n_{\mathrm{antitau}}^{\mathrm{SR},\ \mathrm{QCD}}}, \tag{8.6}$$

where $n_{\mathrm{antitau}}^{\mathrm{SR},\ W+\mathrm{jets}}$ is estimated by

$$n_{\mathrm{antitau}}^{\mathrm{SR},\ W+\mathrm{jets}} = n_{\mathrm{antitau}}^{\mathrm{CR},\ W+\mathrm{jets\ data}} \times \frac{n_{\mathrm{antitau}}^{\mathrm{SR},\ W+\mathrm{jets\ MC}}}{n_{\mathrm{antitau}}^{\mathrm{CR},\ W+\mathrm{jets\ MC}}} \tag{8.7}$$

and $n_{\mathrm{antitau}}^{\mathrm{SR},\ \mathrm{QCD}}$ is estimated by

$$n_{\mathrm{antitau}}^{\mathrm{SR},\ W+\mathrm{jets}} = n_{\mathrm{antitau}}^{\mathrm{SR},\ \mathrm{data}} - \left(n_{\mathrm{antitau}}^{\mathrm{SR},\ W+\mathrm{jets}} + n_{\mathrm{antitau}}^{\mathrm{SR},\ \mathrm{real}} \right). \tag{8.8}$$

The value for R_{QCD} can then be obtained by requiring the ratios sum to unity:

$$R_{\mathrm{QCD}} = 1 - R_{W+\mathrm{jets}} - R_{Z+\mathrm{jets}} - R_{\mathrm{top}} \tag{8.9}$$

The values obtained for the background fractions are given in Table 8.3.

Table 8.3: Fraction of antitau candidates from different processes contributing to the fake tau background in the analysis signal regions.

Fraction	R_{QCD}	$R_{W+\mathrm{jets}}$	$R_{Z+\mathrm{jets}}$	R_{top}
Value	0.40	0.46	0.11	0.03

The background estimation is validated using a control region of events with a reconstructed lepton and hadronic tau that have same-sign charge. This type of event will be dominated by fake backgrounds, making an ideal control region. Figure 8.9 shows the distributions of $m_{\tau\tau}^{\text{MMC}}$ and $m_{bb\tau\tau}$ in the 1 b-tag and 2 b-tag categories. In order to maximise the available statistics, events used in these validation regions merge the low and high $p_{\text{T}}^{\tau\tau}$ categories. The fake factor uncertainty is taken into account as part of the method validation. Good agreement can be seen between the derived background estimation and the observed data, not only for the event yield but also for the shape of the distributions. The overall estimated yield is 132.4 ± 26.7 (32.9 ± 7.5) in 1 b-tag (2 b-tag) categories, these numbers agree well with the observation of 130 (33) events.

8.7.2 Top Background

The $t\bar{t}$ background is the largest contributor to the 2 b-tag category. The semileptonic $t\bar{t}$ estimate is accounted for in the fake tau estimate based on the fake factor method, while the dileptonic $t\bar{t}$ estimate is provided by MC, as described here. In addition to the typical corrections applied to the simulation, the MC is reweighted with a p_{T}-dependent correction factor derived from data to compensate for the mismodeling of the top and $t\bar{t}$ p_{T} distributions [158]. The top background estimate is validated using a control region defined by an inversion of the m_{bb} mass window cut as given in Section 8.6.3. In order to maximise the available statistics the low and high $p_{\text{T}}^{\tau\tau}$ categories are merged. Figure 8.10 shows the distributions in the top control region for the final discriminants in the nonresonant and resonant searches.

Good agreement can be seen between the derived background estimation and the observed data, not only for the event yield but also for the shape of the distribution. The total estimated event yield in the control region is 368.6 ± 37.1, which is in good agreement with the observation of 360 events. As a result, no additional normalisation is applied to the top background estimate.

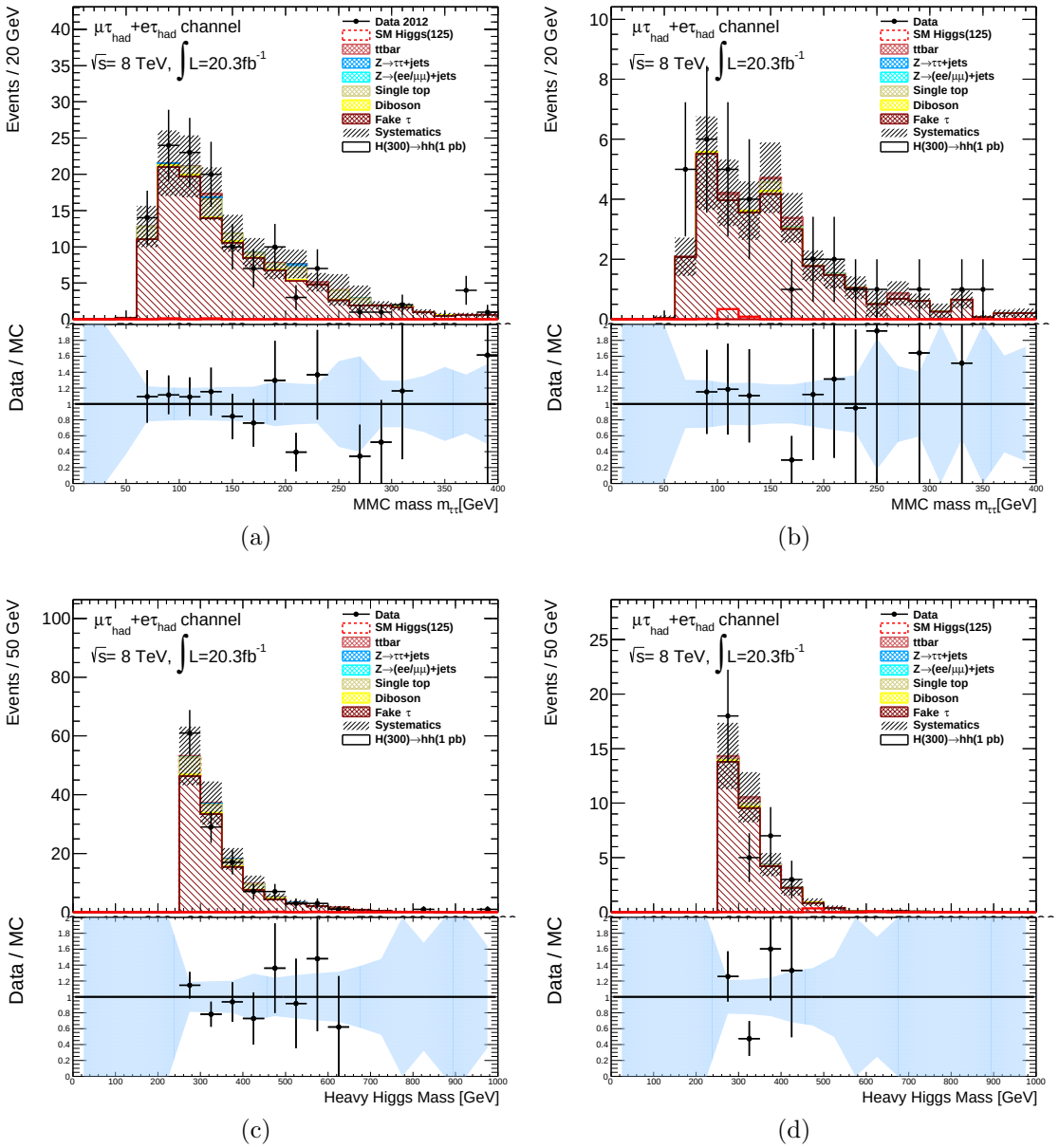

Figure 8.9: Distributions in the fake tau validation region defined by events with same-sign charge passing the nonresonant search selection. The $m_{\tau\tau}^{\mathrm{MMC}}$ distribution is shown for (a) events with one b-tagged jet and (b) events with two or three b-tagged jets. The $m_{bb\tau\tau}$ distribution for (c) events in the 1 b-tag categories and (d) events in the 2 b-tag categories.

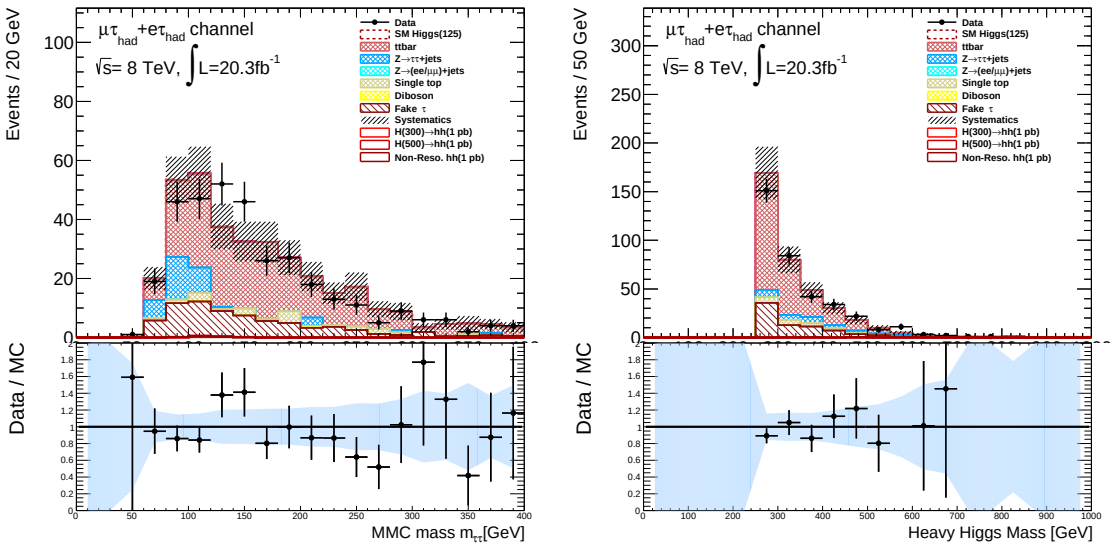

(a) (b)

Figure 8.10: Distributions in the top control region defined by an inversion of the m_{bb} mass window cut for (a) the $m_{\tau\tau}^{\mathrm{MMC}}$ and (b) the $m_{bb\tau\tau}$ for 2 b-tag category events.

8.7.3 $Z \to \tau\tau$ Background

The $Z \to \tau\tau$ background estimate is based on the tau-embedded data sample obtained from $Z \to \mu\mu$ collision data. The absolute normalisation for the embedded sample was determined with data, by using events in the $Z \to \tau\tau$-rich window of $40 < m_{\tau\tau}^{\mathrm{vis}} < 70\,\mathrm{GeV}$ after all the preselection requirements, except for the requirements on jets. The embedded sample predictions are normalised to be equal to the data in this mass window minus all other backgrounds. The fraction of signal events in this region is expected to be less than 0.01%. The normalisation factor applied to the embedded sample for the final state with an electron is 0.65 ± 0.05, while for the final state with a muon is 0.57 ± 0.04. The quoted errors are statistical in nature only.

It is observed that $t\bar{t}$ events containing two true tau leptons represent a non-negligible contribution to the tau-embedded sample. Therefore, to prevent double counting the MC prediction is subtracted. The advantage of using the tau-embedded sample with this normalisation procedure is that it results in a smaller systematic uncertainty with respect to using a $Z \to \tau\tau$ estimate from simulation.

8.7.4 Other Backgrounds

The $Z \to ee$ and $Z \to \mu\mu$ background estimates are based on the MC simulation and include dedicated corrections to better produce data. The corrections that account for the difference in the misidentification rate of hadronic tau candidates resulting from leptons were obtained from dedicated tag-and-probe studies of data [159, 160]. This is particularly important for $Z \to ee$ events where the misidentified hadronic tau candidate has originated from a true electron. The background for the case in which a jet is misidentified as a hadronic tau is included in the fake factor estimate, descibed earlier in Section 8.7.1. The diboson background estimate is taken directly from the MC simulation as this constitutes a relatively small background in this analysis, hence why the diboson background where a jet fakes a hadronic tau is not included in the fake factor estimate.

8.8 Systematic Uncertainties

This section provides an overview of the systematic uncertainties affecting the $hh \to b\bar{b}\tau\tau$ analysis that arise from either experimental, modelling or theoretical sources. These uncertainties enter into the final result as nuisance parameters in the fit model, as discussed in Section 8.9. The dominant experimental uncertainties arise from the jet and tau energy scales, the jet energy resolution and b-tagging. In general, the effects resulting from the uncertainties related to leptons are smaller than those from hadronic taus. The 2 b-tag categories typically are associated with larger systematic uncertainties, as are the high $p_{\mathrm{T}}^{\tau\tau}$ categories.

8.8.1 Luminosity

The uncertainty on the integrated luminosity of the 8 TeV data sample is $\pm 2.8\%$ and only affects the normalisation of those MC backgrounds that are not normalised

to data. This uncertainty is determined from the calibration of the luminosity scale with the vdM scans described in Section 4.7.1 that include effects such as the beam centring and stability, the fit model and dependence on the average number interactions per bunch crossing [93].

8.8.2 Lepton

The efficiencies for triggering, reconstructing and identifying electrons and muons as well as isolation are measured in dedicated tag-and-probe studies as described in References [145] and [146], respectively. The uncertainties with these studies arise from the selection choice of the tag object as well as uncertainties associated with the background estimation. The MC samples are corrected for the measured differences with respect to data and the associated uncertainties are propagated through the analysis by varying the corresponding scale factors accordingly. The uncertainties on the electron energy and muon momentum scales and resolution are obtained from calibration techniques using $Z \to \ell\ell$ and $J/\Psi \to \ell\ell$ events and are typically of the order of 1% [161, 146]. All of these uncertainties lead to normalisation effects on the total number of selected events of approximately 1–3%.

8.8.3 Hadronic Tau

The efficiencies of the reconstruction and identification algorithms are measured in collision data using a tag-and-probe technique described in Reference [147], from which the corresponding corrections to MC are obtained. A sample of enriched $Z \to \tau\tau$ events are used for this measurement. The total uncertainties on the scale factors for hadronic tau identification are 2.5% for 1-track hadronic tau objects and 4.0% for 3-track hadronic tau objects. The dominant uncertainties with this method come from the jet background model, the tau energy scale and shower model, the underlying event, and the statistics of the sample used. The electron veto efficiency measurement is based on another tag-and-probe technique, which uses a sample of

enriched $Z \rightarrow ee$ events. The total uncertainties on the scale factors vary in the range 8–30% depending on the η-range considered.

The uncertainty on the energy scale and resolution of hadronic tau decays was estimated using two complementary methods, both described in Reference [147]. The *deconvolution method* studies the uncertainties on the tau energy scale and the modelling, using dedicated measurements and simulation. It works by propagating the uncertainties associated with each of the hadronic tau decay products to the final tau energy scale. The *in-situ* method tests only the modelling and is based on the typical conditions for 2012 collision data. It evaluates the shift on the tau energy scale by reconstructing the visible mass peak in $Z \rightarrow \tau\tau$ events, where one tau decays hadronically and the other to a muon plus neutrinos. Both of these methods give consistent results, with uncertainties on the tau energy scale ranging from 2–4% depending on the number of tracks associated with the hadronic tau decay. The combined effect of these different uncertainties results in normalisation effects of less than 5%, as well as shape changing effects.

8.8.4 Jet Energy Scale and Resolution

There are multiple uncertainties assigned to the energy calibration of jets. These include uncertainties on the modelling of in-situ energy calibration, intercalibration across η bins, pile-up, as well as uncertainties on jet flavour composition and the varied detector response to different jet flavours [150, 151]. Only those components that have significant effect on the yield and shape are retained to prevent introducing noise into the fit, while preserving the jet energy scale uncertainty. The response of the calorimeters to jets is studied using data-driven techniques as a function of the jet p_{T} and pseudorapidity by examining the p_{T} balance in dijet events. The uncertainties on the calibration factors are typically less than 1% for central jets, but increase to 3.5% for low-p_{T} jets at high $|\eta|$ [151]. The jet energy resolution is determined by different in-situ measurements, with uncertainties arising from experimental selections and simulation modelling. Each of these uncertainties is

accounted for by varying and smearing the jet energy. The combined systematic uncertainty attributed to these effects leads to changes in the normalisation of 2–12%, as well as shape changing effects.

8.8.5 B-Tagging

The scale factors used to correct the difference in b-tagging efficiencies measured for data and MC are obtained using dileptonic $t\bar{t}$ events [162, 153]. The uncertainties in the b-tagging efficiency measurements are of around 2% for jets with transverse momenta up to 100 GeV. The effects on the normalisation of these are in the range 1–4%.

8.8.6 Missing Transverse Momentum

The uncertainty on the $E_{\mathrm{T}}^{\mathrm{miss}}$ is primarily the result on the uncertainties on the energy scales of the individual $E_{\mathrm{T}}^{\mathrm{miss}}$ components: electrons, hadronic tau leptons, and jets. These uncertainties are propagated through to the computation of the $E_{\mathrm{T}}^{\mathrm{miss}}$ vector as described in Section 8.4. Additionally, the $E_{\mathrm{T}}^{\mathrm{miss}}$ soft term scale and resolution uncertainties that arise from the MC modelling and pile-up are also considered. The combined effect of these on the normalisation is of 1–4%.

8.8.7 Fake Factor Method

An important systematic uncertainty on the background estimation comes from the estimated fake tau background. The two main components that enter into this uncertainty arise from the statistical uncertainty of the samples used to compute the fake factors and the dominant systematic uncertainty on the methodology itself that arises from the composition of the combined fake background. The statistical uncertainty is evaluated by varying the fake factor values within their statistical

uncertainty. This results in an uncertainty on the effective fake factor of 5.1%. The uncertainty on the composition is estimated by varying each fractional contribution by 50%, which affects the effective fake factor by 9.5%. These uncertainties propagate to give a 1–4% combined uncertainty on the prediction.

8.8.8 Top Background

A systematic uncertainty resulting from the top p_{T} reweighing of 1% (5%) is assigned for the low (high) $p_{\mathrm{T}}^{\tau\tau}$ categories. In addition, an uncertainty for the extrapolation between the control region and signal region is assigned based on the difference in expectation of the POWHEG and MC@NLO [163, 164] generators, corresponding to 2.0% (7.9%) for low (high) $p_{\mathrm{T}}^{\tau\tau}$ categories, in both the resonant and nonresonant search. The effect of these uncertainties combined leads to effects less than 7% on the normalisation.

8.8.9 $Z \to \tau\tau$ Embedding

There are two sources of systematic uncertainty considered relating to the tau-embedding procedure. The first source is associated with the $Z \to \mu\mu$ event selection and in particular to the isolation requirement applied to the muons. This uncertainty is estimated by comparing the sample with nominal selection to samples with relaxed and tightened isolation requirements. The second source of systematic uncertainty comes from the subtraction of energy deposits in calorimeter cells associated to the muon in the replacement of the muons with tau leptons. A conservative estimate of this uncertainty is obtained by comparing the nominal sample to that with the subtracted energy scaled up and down by 20%. These two sources result in around a 2% effect on the background normalisation. In addition, a systematic uncertainty of between 8% and 15% is assigned to the subtraction of the $t\bar{t}$ process, which leads to normalisation effects of less than 2%.

8.8.10 Theory

A number of theoretical sources also contribute to uncertainties in signal acceptance. The choice of PDF was evaluated by reweighing the signal samples at reconstruction level to compare the difference between the nominal PDFs and MSTW2008 [165] and NNPDF [166]. Other uncertainties considered in generating signal events include changes in the value of strong coupling constant α_s and the renormalisation and factorisation scales. These three sources are assigned uncertainties of 3%, 3% and 1% across all signal acceptances, respectively. The uncertainty on the branching ratios of $h \to b\bar{b}$ and $h \to \tau\tau$ were taken from the LHC Higgs cross section working group [40].

8.9 Signal Extraction

The discriminating variables used for the signal extraction in the nonresonant and resonant searches are the ditau mass reconstructed with the MMC and the constrained $m_{bb\tau\tau}$ respectively, for the four analysis categories. The statistical analysis of the data in both searches use methods commonly employed at the LHC [167].

Each analysis category gives a prediction for each bin of the expected number of the background events as well as possible Higgs boson pair production signal events. The consistency of the data with either the background-only or signal-plus-background hypotheses can then be determined using these binned distributions. The binning inherently takes into consideration the shape of the distributions of the discriminant as opposed to a simpler counting experiment.

The parameter of interest in the $hh \to b\bar{b}\tau\tau$ analysis is the signal strength μ, which represents the unknown rate of signal and can be given with respect to a specific benchmark. In the background hypothesis $\mu = 0$ and for any signal hypothesis $\mu > 0$, with the benchmark corresponding to $\mu = 1$. For the nonresonant search the parameter of interest is defined as $\sigma(gg \to hh)$ and for the resonant search as

$\sigma(gg \rightarrow H) \times \mathrm{BR}(H \rightarrow hh)$, both assuming a production cross section of 1 pb. The nuisance parameters θ account for the different systematic uncertainties and normalisations in the fit.

The statistical analysis of the data uses a binned likelihood function $\mathcal{L}(\mu, \theta)$, constructed as the product of Poission probability terms that represent the bins from all the analysis categories, considering all the systematics described in the previous section as nuisance parameters. Each nuisance parameter is constrained by a Gaussian probability density in the case of systematic uncertainties and a log-normal probability density in the case of a normalisation. Pulls in the nuisance parameters from their prefit prediction result in a penalty that increases the likelihood.

The test statistic is a single value that can be used to distinguish between two hypotheses and set upper limits on the rate of signal production. The test statistic q_μ is constructed according to the profile likelihood ratio:

$$q_\mu = \begin{cases} -2 \ln \frac{\mathcal{L}(\mu, \hat{\hat{\theta}}_\mu)}{\mathcal{L}(\hat{\mu}, \hat{\theta})} & \hat{\mu} \leq \mu \\ 0 & \hat{\mu} > \mu \end{cases} \tag{8.10}$$

where $\hat{\mu}$ and $\hat{\theta}$ are the best fit parameters that maximise the likelihood, and $\hat{\hat{\theta}}_\mu$ are the values of the nuisance parameters that maximise the likelihood for the given value of μ. The constraints imposed here avoid unphysical negative values of the signal strength and prevent the exclusion of any μ smaller than the best fit $\hat{\mu}$, ensuring the construction of a one-sided confidence interval. Large values of q_μ indicate poor compatibility between the μ hypothesis and data. The p-value of the signal-plus-background hypothesis can then be defined as the probability of finding a value of q_μ at least as large as the observed value q_μ^{obs}:

$$p_\mu = \int_{q_\mu^{\mathrm{obs}}}^{\infty} f(q_\mu|\mu) \, \mathrm{d}q_\mu, \tag{8.11}$$

where $f(q_\mu|\mu)$ is the probability density function for q_μ.

The procedure followed to set the 95% Confidence Level (CL) upper limit on the

production cross section is to determine the value of μ that gives a $p_\mu \leq 0.05$. Following this procedure alone can result in the exclusion of hypotheses with a small expected signal yield, due to downward statistical fluctuations of the data [168]. The CL_s method [169] was developed to address this issue by reweighting the exclusion p-value according to whether or not the background-only hypothesis also disagrees with the data:

$$p_{\mathrm{CL}_s} = \frac{p_\mu}{1 - p_b}, \tag{8.12}$$

where the p-value for the background-only hypothesis p_b is defined as:

$$p_b = \int_{-\infty}^{q_\mu^{\mathrm{obs}}} f(q_\mu|0)\ \mathrm{d}q_\mu. \tag{8.13}$$

Toy MC pseudo-data are generated from the sum of the signal and background or background-only expectations to determine the probability distribution of $f(q_\mu|\mu)$ and $f(q_\mu|0)$, respectively. It is useful to be able to indicate the sensitivity of an analysis by giving the expected significance that would be achieved under different signal hypotheses. Generating large numbers of toy experiments can be computationally expensive and time consuming. In the limit of a large data sample size, the distribution $f(q_\mu)$ can be computed with a formula known as the asymptotic limit approximation [170]. For these conditions the negative log-likelihood can be shown to follow a Gaussian distribution [171]:

$$-2\ln\frac{\mathcal{L}(\mu, \hat{\hat{\theta}}_\mu)}{\mathcal{L}(\hat{\mu}, \hat{\theta})} = \frac{(\mu - \hat{\mu})^2}{\sigma^2} + \mathcal{O}(1/\sqrt{N}). \tag{8.14}$$

The standard deviation σ can be obtained with a single representative data set that is widely known as the 'Asimov' data set.

The statistical significance of an observed signal can be quantified by means of a p-value. In the case an excess of events is observed, the p-value is used to express the compatibility of the result with the background-only hypothesis. For this, the

test statistic is changed to the following:

$$q_0 = \begin{cases} -2\ln\frac{\mathcal{L}(0,\hat{\hat{\theta}}_\mu)}{\mathcal{L}(\hat{\mu},\hat{\theta})} & \hat{\mu} \geq 0 \\ 0 & \hat{\mu} < 0 \end{cases} \tag{8.15}$$

Using this test, the data are not considered to disagree with the background-only hypothesis if the best fit value $\hat{\mu}$ is determined to be less than zero. The p-value to observe an excess as large or greater than the observed data can be defined as:

$$p_0 = \int_{q_0^{\text{obs}}}^{\infty} f(q_0|0)\ \mathrm{d}q_0 \tag{8.16}$$

8.9.1 Implementation and Nuisance Parameter Treatment

The fit model used for the $hh \to b\bar{b}\tau\tau$ analysis was implemented using the HistFactory software package [172] that relies on the RooFit/RooStats framework [173, 174]. It constructs the likelihood function based on input histograms of the expected event yields for all signal and background processes as well as for all systematic variations. All four analysis categories are used in separate combined likelihood fits for the nonresonant and resonant searches. The binning used for each discriminant is given in Table 8.4 and was chosen to minimise the number of expected background events in each bin, for the purpose of the fit. However, the binning could be better optimised to take full advantage of the expected signal resolution. For the resonant search in particular, the binning cannot effectively distinguish between signal masses greater than approximately 400 GeV.

All systematic uncertainties described in the preceding section enter the fit as nuisance parameters. Nuisance parameters that affect the normalisation are only included providing that their effect is greater than 0.05%. There are also nuisance parameters that affect the shape of the discriminant, such as systematics relating to Tau Energy Scale (TES), Jet Energy Scale (JES) and $E_{\text{T}}^{\text{miss}}$. Careful consideration is applied to the shape nuisance parameters as many of the samples contain rela-

Table 8.4: Bins of $m_{\tau\tau}^{\text{MMC}}$ and $m_{bb\tau\tau}$ in GeV used in the fits to extract the signal for the nonresonant and resonant search of the $b\bar{b}\tau\tau$ analysis. They are chosen to ensure a minimum number of events for the background prediction in each bin. The low and high $p_{\text{T}}^{\tau\tau}$ categories correspond to $p_{\text{T}}^{\tau\tau} < 100\,\text{GeV}$ and $p_{\text{T}}^{\tau\tau} > 100\,\text{GeV}$.

	hh				$H \to hh$			
Bin	$n_{b\text{-jet}} = 1$		$n_{b\text{-jet}} \geq 2$		$n_{b\text{-jet}} = 1$		$n_{b\text{-jet}} \geq 2$	
	low $p_{\text{T}}^{\tau\tau}$	high $p_{\text{T}}^{\tau\tau}$	low $p_{\text{T}}^{\tau\tau}$	high $p_{\text{T}}^{\tau\tau}$	low $p_{\text{T}}^{\tau\tau}$	high $p_{\text{T}}^{\tau\tau}$	low $p_{\text{T}}^{\tau\tau}$	high $p_{\text{T}}^{\tau\tau}$
1	0 – 80	0 – 90	0 – 80	0 – 90	0 – 275	0 – 350	0 – 257	0 – 290
2	80 – 90	90 – 100	80 – 90	90 – 110	275 – 295	350 – 360	257 – 260	290 – 310
3	90 – 100	100 – 125	90 – 100	110 – 120	295 – 315	360 – 370	260 – 270	310 – 335
4	100 – 105	125 – 135	100 – 105	120 – 130	315 – 400	370 – 2000	270 – 280	335 – 380
5	105 – 110	135 – 150	105 – 110	130 – 140	400 – 2000		280 – 290	380 – 2000
6	110 – 115	150 – 180	110 – 120	140 – 160			290 – 300	
7	115 – 120	180 – 600	120 – 125	160 – 600			300 – 310	
8	120 – 125		125 – 130				310 – 320	
9	125 – 130		130 – 135				320 – 400	
10	130 – 135		135 – 140				400 – 450	
11	135 – 140		140 – 160				450 – 2000	
12	140 – 160		160 – 600					
13	160 – 600							

tively low sample sizes after the full analysis selection and so fairly small systematic variations may be subject to significant statistical noise. To prevent noise being introduced into the fit that could potentially cause instabilities, without accidentally removing genuine shape variations, additional modelling steps are applied to the shape systematics before they are entered in the fit. These are summarised in the following:

- **Pruning:** The Kolmogorov-Smirnov compatibility test between the upwards and the downwards shape variation with respect to the nominal is performed. Providing that the result is less than a given probability threshold for either of the upward or downward variation, the shape systematic is retained.
- **Smoothing:** The ratio of the variation to nominal shape is smoothed using the `TH1::Smooth` method of ROOT [175]. The smoothed varied shape is then obtained by multiplying the nominal with the smoothed ratio.

8.10 Results

The distributions for the final discriminants in the nonresonant and resonant signal regions after the full analysis selection are shown in Figure 8.11. The observed distribution for the nonresonant search agrees well with expectation. However, there is a small deficit of observed data events for $m_{bb\tau\tau}$ around 300 GeV in the resonant signal region.

The expected event yields from background processes and observed in the data, broken down for each of the four categories after the nonresonant and resonant search selection, are summarised in Tables 8.5 and 8.6, respectively. No evidence of Higgs boson pair production is observed in data for any of the analysis categories belonging to either search. As a result, upper limits are set at the 95% CL on the production cross section for SM nonresonant Higgs boson pair production and on the cross section times branching fraction for resonant Higgs boson pair production,

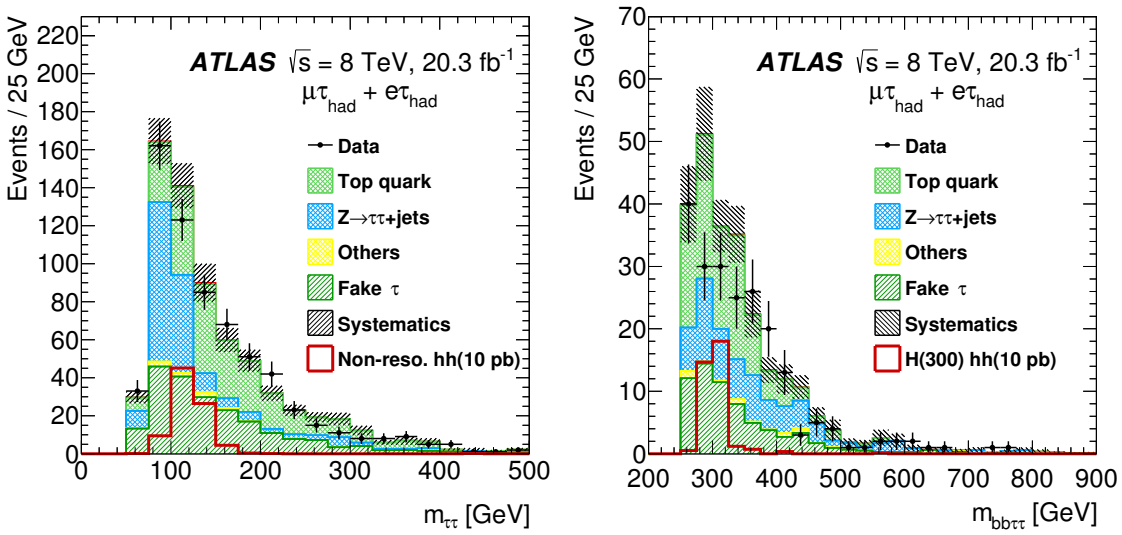

(a) (b)

Figure 8.11: Distributions of final discriminants combining all analysis categories: (a) $m_{\tau\tau}^{\mathrm{MMC}}$ for the nonresonant search and (b) $m_{bb\tau\tau}$ for the resonant search. The single SM Higgs boson background is too small to be seen and the nonresonant signal distribution is shown assuming a cross section of 10 pb for Higgs boson pair production.

using the CL_s technique described in Section 8.9.

As explained in the previous section, the signal for the nonresonant and resonant searches is extracted by dividing the events in these signals regions amongst four analysis categories, defined by the number of b-tagged jets and the transverse momentum of the ditau system. The distributions of the discriminating variable in each case are divided into a number of bins of variable mass widths, as defined in Table 8.4. Figures 8.12 and 8.13 show the rebinned distributions for each of the categories for the nonresonant and resonant searches, respectively.

The observed and expected 95% CL upper limits for nonresonant $gg \to hh$ production are 1.6 pb and 1.3 pb, respectively. The observed and expected 95% confidence level upper limits on the cross section times branching ratio for $gg \to H \to hh \to b\bar{b}\tau\tau$ are shown in Figure 8.14. The observed limits are shown to be considerably lower than the expectation for m_H around 300 GeV. This is consistent with the observed deficit of events in the combined $m_{bb\tau\tau}$ distribution around the same mass.

Table 8.5: The numbers of events predicted for different background processes as well as observed in data that pass the final selection for the four categories in the nonresonant analysis. The expected number of events for nonresonant production of a Higgs boson pair with a cross section of $\sigma(gg \to hh) = 1\,\text{pb}$ are also indicated. The errors show the combined statistical and systematic uncertainties.

	$n_{b\text{-jet}} = 1$		$n_{b\text{-jet}} \geq 2$	
Process	$p_{\text{T}}^{\tau\tau} < 100\,\text{GeV}$	$p_{\text{T}}^{\tau\tau} > 100\,\text{GeV}$	$p_{\text{T}}^{\tau\tau} < 100\,\text{GeV}$	$p_{\text{T}}^{\tau\tau} > 100\,\text{GeV}$
SM Higgs	0.7 ± 0.1	0.9 ± 0.2	0.2 ± 0.1	0.4 ± 0.1
Top quark	56.8 ± 7.1	51.6 ± 8.0	81.6 ± 11.8	74.5 ± 13.2
$Z \to \tau\tau$	96.4 ± 8.5	53.9 ± 6.9	16.8 ± 3.0	16.1 ± 3.5
Fake τ_{had}	117.4 ± 12.8	39.0 ± 4.6	34.8 ± 4.3	17.9 ± 2.4
Others	27.4 ± 7.1	9.2 ± 4.9	9.8 ± 3.8	2.6 ± 2.6
Total background	298.7 ± 18.4	154.6 ± 12.5	143.2 ± 13.4	111.5 ± 14.1
Data	266	157	118	118
Signal nonresonant	0.3 ± 0.1	2.3 ± 0.4	0.6 ± 0.1	5.2 ± 0.7

Table 8.6: The numbers of events predicted for different background processes as well as observed in data that pass the final selection for the four categories in the resonant analysis [8]. The expected number of events for the production of a $m_H = 300\,\text{GeV}$ resonance with a cross section of $\sigma(gg \to H) \times \text{BR}(H \to hh) = 1\,\text{pb}$ are also indicated. The errors show the combined statistical and systematic uncertainties.

	$n_{b\text{-jet}} = 1$		$n_{b\text{-jet}} \geq 2$	
Process	$p_{\text{T}}^{\tau\tau} < 100\,\text{GeV}$	$p_{\text{T}}^{\tau\tau} > 100\,\text{GeV}$	$p_{\text{T}}^{\tau\tau} < 100\,\text{GeV}$	$p_{\text{T}}^{\tau\tau} > 100\,\text{GeV}$
SM Higgs	0.5 ± 0.1	0.8 ± 0.1	0.1 ± 0.1	0.2 ± 0.1
Top quark	30.3 ± 3.6	19.6 ± 2.5	30.9 ± 3.0	23.6 ± 2.5
$Z \to \tau\tau$	38.1 ± 4.4	20.2 ± 3.7	6.8 ± 1.8	2.6 ± 1.0
Fake τ_{had}	37.0 ± 4.4	12.1 ± 1.7	13.7 ± 1.9	5.4 ± 1.0
Others	3.2 ± 3.7	0.5 ± 1.5	0.7 ± 1.6	0.2 ± 0.7
Total background	109.1 ± 8.6	53.1 ± 6.0	52.2 ± 8.2	32.1 ± 5.4
Data	92	46	35	35
Signal $m_H = 300\,\text{GeV}$	0.8 ± 0.2	0.4 ± 0.2	1.5 ± 0.3	0.9 ± 0.2

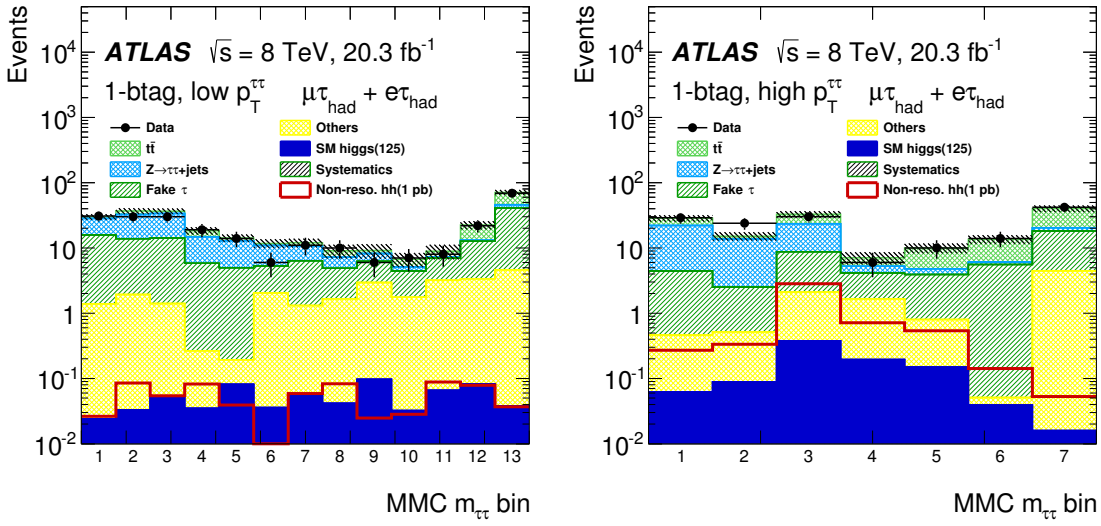

Figure 8.12: Rebinned $m_{\tau\tau}^{\mathrm{MMC}}$ distributions for the nonresonant signal region used in the fit to extract the signal for the (a) 1 b-tag low $p_{\mathrm{T}}^{\tau\tau}$ (b) 1 b-tag high $p_{\mathrm{T}}^{\tau\tau}$ (c) 2 b-tag low $p_{\mathrm{T}}^{\tau\tau}$ and (d) 2 b-tag high $p_{\mathrm{T}}^{\tau\tau}$ categories. The expected signal distribution for SM nonresonant Higgs boson pair production is shown assuming a cross section of 1 pb.

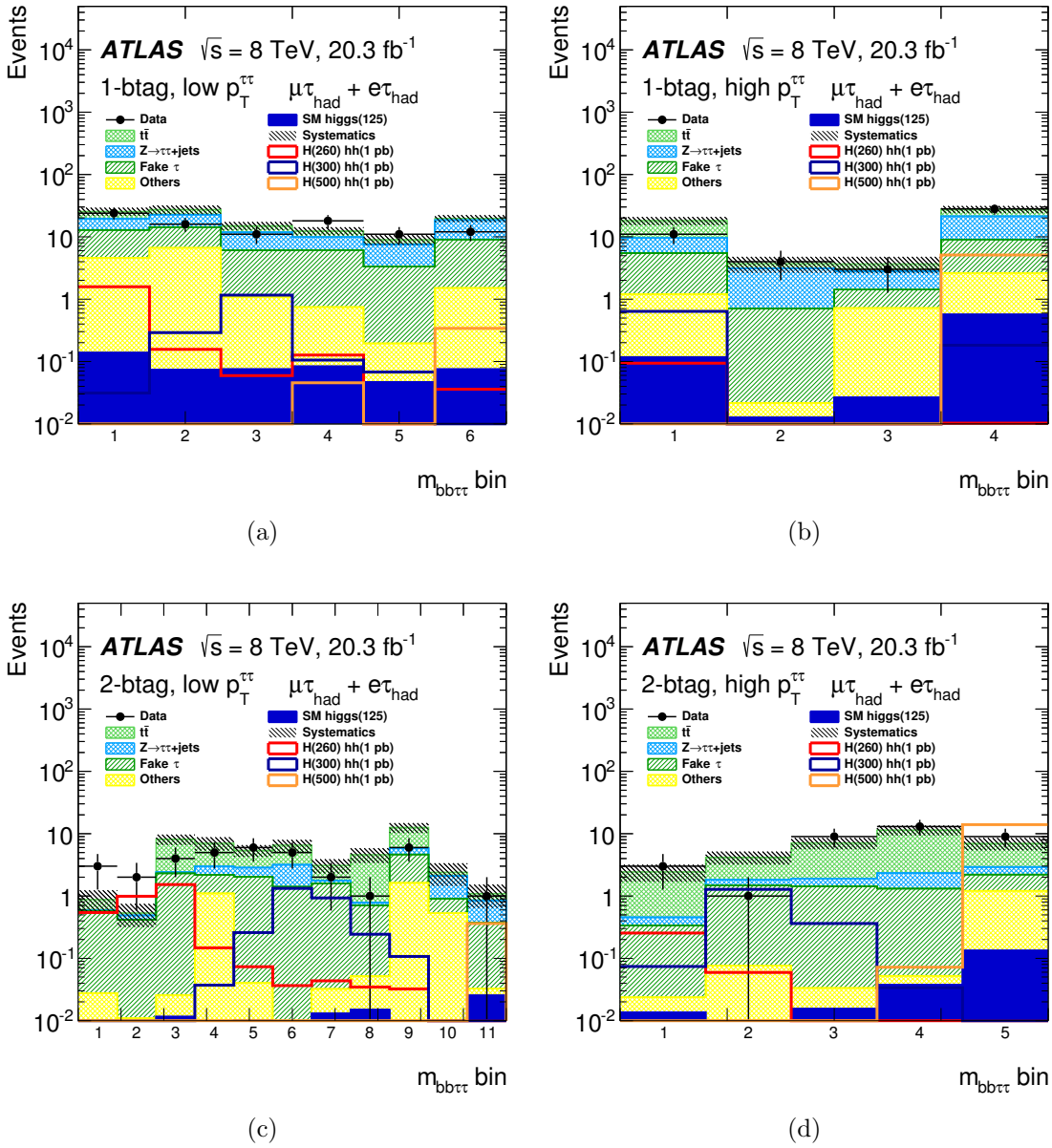

Figure 8.13: Rebined $m_{bb\tau\tau}$ distributions for the resonant signal region used in the fit to extract the signal for the (a) 1 b-tag low $p_{\mathrm{T}}^{\tau\tau}$ (b) 1 b-tag high $p_{\mathrm{T}}^{\tau\tau}$ (c) 2 b-tag low $p_{\mathrm{T}}^{\tau\tau}$ and (d) 2 b-tag high $p_{\mathrm{T}}^{\tau\tau}$ categories. The expected signal distributions are shown for $m_H = 260$, 300 and 500 GeV assuming a cross section of 1 pb for Higgs boson pair production.

The limits are correlated for m_H above 400 GeV as this represents a single bin in the statistical fitting of the $m_{bb\tau\tau}$ distribution. In general, the expected limits decrease for increasing values of m_H, which is directly related to the increase in selection efficiency for the signal.

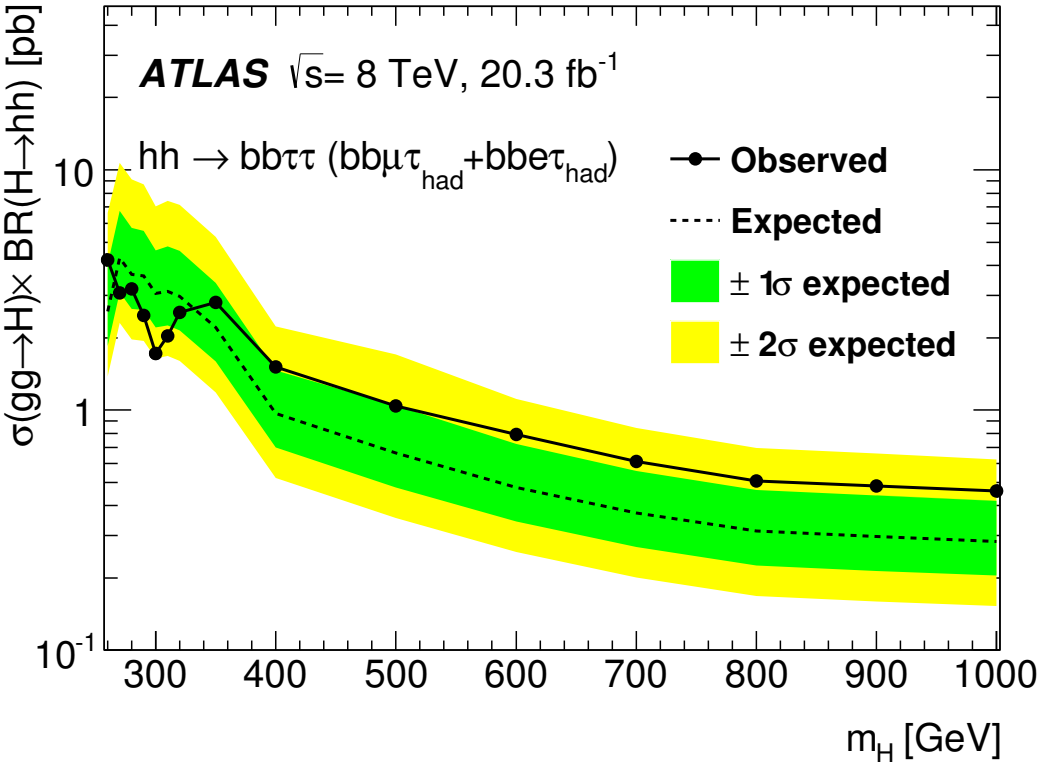

Figure 8.14: The observed and expected 95% CL upper limits on $\sigma(gg \to H) \times \mathrm{BR}(H \to hh)$ as a function of resonant mass m_H. The green and yellow bands represent the $\pm 1\sigma$ and $\pm 2\sigma$ uncertainty ranges of the expected limits.

CHAPTER 9

HIGGS BOSON PAIR PRODUCTION COMBINATION

9.1 Introduction

A number of searches have been performed by both the ATLAS and CMS collaborations for resonant and nonresonant Higgs boson pair production [176, 177, 178, 179]. This chapter presents the combined results of the different decay channels considered by ATLAS using the 8 TeV pp collision data set. The decay channels included in this combination are $hh \to WW^*\gamma\gamma \to \ell\nu qq'\gamma\gamma$, $hh \to b\bar{b}\gamma\gamma$, $hh \to b\bar{b}\tau\tau \to b\bar{b}\ell\tau_{\text{had}}3\nu$, and $hh \to b\bar{b}b\bar{b}$. The analysis overview and results for the $hh \to b\bar{b}\tau\tau$ channel have already been presented in Chapter 8. A summary of each of the other analyses in the combination and their results is given in the following sections. The combined results are used to set limits on the production of Higgs boson pairs and for resonant production the results are interpreted within two MSSM specific scenarios, known as hMSSM [69, 70] and low-tan β-high [63]. These scenarios attempt to accommodate

the observed Higgs boson at 125 GeV by making specific assumptions and/or choices of the parameters in the MSSM. Much of the material presented in this chapter on the combination of these searches is published in Reference [8].

9.2 Summary of $hh \to WW^*\gamma\gamma$

This section describes the search for Higgs boson pair production in the $hh \to WW^*\gamma\gamma$ channel, where one Higgs boson decays to a pair of W bosons and the other to a pair of photons. This channel benefits from the ability to tag the Higgs boson through the narrow diphoton mass resonance from the $h \to \gamma\gamma$ decay, as well as the excellent diphoton mass resolution of the ATLAS detector that aids to strongly suppress background contributions. In addition, the $h \to WW^*$ decay has the largest branching fraction after $h \to b\bar{b}$. The $WW^*\gamma\gamma$ analysis examines the final state in which one W boson decays to an electron or muon[1], while the other decays hadronically, resulting in the $\ell\nu qq'\gamma\gamma$ decay signature. This final state helps to maintain sensitivity while suppressing multijet background processes.

This analysis uses the full 8 TeV data set collected by ATLAS passing the data quality requirements, corresponding to 20.3 fb^{-1}. The events were recorded with diphoton triggers that are nearly fully efficient for events passing the offline photon selection. The ATLAS photon reconstruction and identification used in this analysis is discussed in Reference [8] and the photon selection largely follows that of the existing ATLAS $h \to \gamma\gamma$ production measurement [180]. Events are required to have a pair of isolated photons where the p_{T} of the leading and subleading photon candidates are greater than 35% and 25% of the diphoton invariant mass, respectively. The invariant mass of the photon pair must also fall within the diphoton mass window $105 < m_{\gamma\gamma} < 160$ GeV, from which the signal region and control regions for estimating the background contributions are defined.

The $h \to WW^* \to \ell\nu qq'$ decay signature is identified by also requiring events to

[1] either directly or through a tau lepton

contain two or more jets and exactly one muon or electron. In order to minimise contributions from top production, a veto on b-tagged jets is applied. Events are rejected if they contain any jet b-tagged using the MV1 algorithm at the 70% efficiency working point for jets origination from the b-quark decay in simulated $t\bar{t}$ events. The event selection finally requires a $E_{\mathrm{T}}^{\mathrm{miss}}$-significance of greater than one to reduce multijet backgrounds. The $E_{\mathrm{T}}^{\mathrm{miss}}$-significance is defined as $E_{\mathrm{T}}^{\mathrm{miss}}/\sigma(E_{\mathrm{T}}^{\mathrm{miss}})$ and takes into account the sensitivity of the $E_{\mathrm{T}}^{\mathrm{miss}}$ resolution to pile-up, which degrades proportionally with the square root of the total energy in the calorimeter.

There are only 13 events that are found to satisfy the above selection, from which the final $hh \to WW^*\gamma\gamma$ candidates are required to have a diphoton mass within a signal mass window defined by $\pm 2\sigma$ of the Higgs boson mass measured by the $h \to \gamma\gamma$ analysis [4], where the expected resolution is 1.7 GeV. A total of 4 candidate events fall into the signal mass window and due to the low statistics both nonresonant and resonant searches proceed as counting experiments. The signal selection efficiency for the SM nonresonant Higgs boson pair production is estimated to be 2.9% using simulation. The corresponding efficiencies for resonant production are found to vary between 1.7% at 260 GeV and 3.3% at 500 GeV.

This analysis considers background contributions from single SM Higgs boson production and continuum backgrounds. It is possible for events from single Higgs boson production to imitate the final state providing the Higgs boson decays to two photons, leading to a diphoton mass peak at m_h, and the event satisfies the $h \to WW^* \to \ell\nu qq'$ identification. The contributions from the various single SM Higgs boson decay mechanisms are estimated with MC simulated events normalised to the SM cross sections [40], where a total of 0.25 ± 0.07 events are expected in the signal mass window, with the ggF and VBF processes proving negligible contributors.

The continuum background estimate is based on a fit to sideband data within a relaxed control region, due to the low event yield observed after the full selection. The control region follows the same analysis selection but with the lepton and $E_{\mathrm{T}}^{\mathrm{miss}}$ requirements removed. From simulation studies, a major source of the continuum

background is expected to comprise of $W\gamma\gamma$ + jets events with a $W \to \ell\nu$ decay. The continuum background is modelled by an exponential function fitted to the diphoton mass distribution, excluding the region $m_h \pm 5\,\text{GeV}$ to minimise potential signal contamination in the sidebands. The total number of continuum background events expected in the signal mass window is calculated as:

$$N_{\text{bkg}} = N \times \frac{f}{1-f}, \tag{9.1}$$

where N is the number of events observed in the data sidebands after the full selection and f is the fraction of background events in $105 < m_{\gamma\gamma} < 160\,\text{GeV}$ that fall into the signal mass window, determined from the fit in the control region. Following this method, the continuum background is estimated to be 1.40 ± 0.47 events. The control region is shown in Figure 9.1a, where it is observed that the data favour a larger cross section for single SM Higgs boson production. This observation is consistent with that made in the measurement of the $h \to \gamma\gamma$ production cross section given in Reference [181].

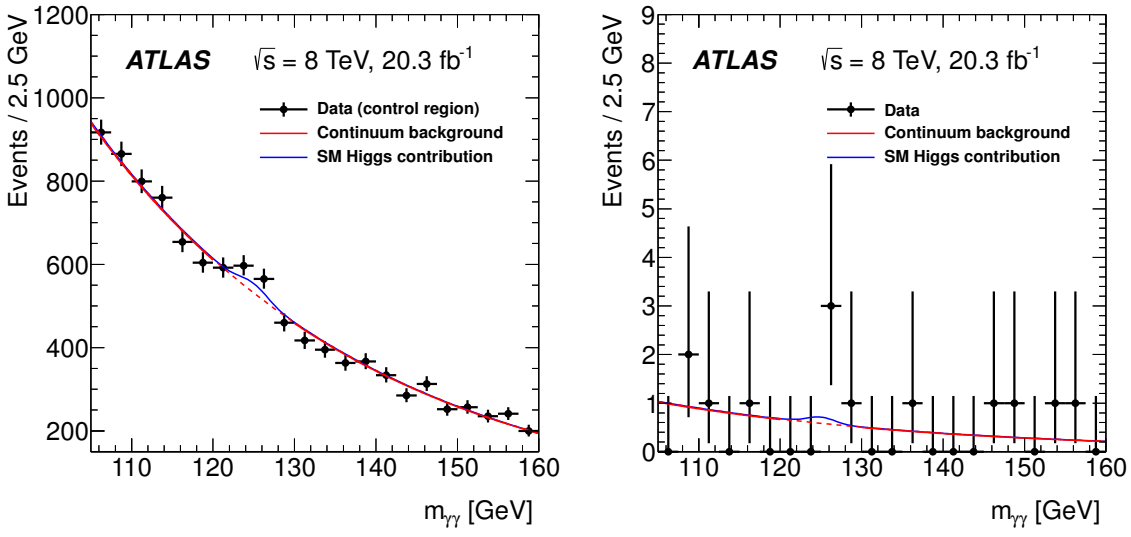

(a) (b)

Figure 9.1: Diphoton invariant mass distribution for events passing (a) the relaxed selection and (b) the final selection [8]. The relaxed selection excludes the lepton and $E_{\text{T}}^{\text{miss}}$ requirements. The red line represents the continuum background contribution, shown as a dashed line in the signal mass window. The blue line shows the expected contribution from single SM Higgs boson production.

The total experimental uncertainty for this analysis varies from 4% to 7% depending on the signal sample being considered, with the jet energy scale being the most dominant contributor. The uncertainties from theoretical sources are the same as those reported for the $hh \to b\bar{b}\tau\tau$ analysis in Section 8.8.10.

The $m_{\gamma\gamma}$ distribution for events passing the final selection is shown in Figure 9.1b, where a total of 13 events are found in the mass range $105 < m_{\gamma\gamma} < 160\,\text{GeV}$. Four events are observed in the signal mass window $m_h \pm 2\sigma$, where the expected number of events from the SM Higgs boson production and continuum background processes is 1.65 ± 0.47. The p-value of the background-only hypothesis is 3.8%. For nonresonant production, the number of expected signal events in this window is 0.64 ± 0.05. The event yields corresponding to resonances with a mass of 300 and 500 GeV are 0.47 ± 0.05 and 0.72 ± 0.06, respectively.

9.3 Summary of $hh \to b\bar{b}\gamma\gamma$

This section summaries the search for Higgs boson production in the $hh \to b\bar{b}\gamma\gamma$ channel, where one Higgs boson decays to a pair of b-quarks and the other to a pair of photons. The $b\bar{b}\gamma\gamma$ channel is a powerful test of Higgs pair production due to the large $h \to b\bar{b}$ branching ratio and the excellent diphoton invariant mass resolution of the ATLAS detector. Events containing this final state can be identified by tagging the $h \to \gamma\gamma$ decay with the use of clean diphoton triggers in the same way as the $WW^*\gamma\gamma$ channel, along with the identification of two b-tagged jets. This channel is particularly important in the low resonant mass range of $260 < m_H < 500\,\text{GeV}$, where backgrounds and combinatorics are more challenging for the $b\bar{b}b\bar{b}$ and $b\bar{b}\tau\tau$ channels.

The $b\bar{b}\gamma\gamma$ analysis [176] uses the full 8 TeV data set collected by ATLAS passing the data quality requirements, corresponding to $20.3\,\text{fb}^{-1}$. The events were selected using loose diphoton triggers that are nearly fully efficient for events passing the offline photon selection. The photon selection used by this analysis fundamentally

follows that mentioned for the $WW^*\gamma\gamma$ analysis, presented in the previous section. Events are required to contain a pair of isolated photon candidates, where the p_{T} of the leading and subleading photon candidates are greater than 35% and 25% of the diphoton invariant mass, which itself must fall within the range $105 < m_{\gamma\gamma} < 160\,\mathrm{GeV}$. In addition, selected events are required to contain two high-p_{T} b-tagged jets with the transverse momentum of the leading (subleading) jet required to be greater than 55 (35) GeV. The dijet mass must also fall within the range $95 < m_{bb} < 135\,\mathrm{GeV}$, to be consistent with the $h \to b\bar{b}$ decay. The b-tagging is performed by the MV1 algorithm at the 70% efficiency working point.

The backgrounds for the nonresonant and resonant analyses are divided between two different categories. The first of these is the signal region, where events are required to have at least two b-tagged jets, while the second category is a control region containing less than two b-tagged jets. The two categories are kinematically identical. The nonresonant analysis performs an unbinned signal-plus-background fit to the $m_{\gamma\gamma}$ distribution, comprised of the Higgs boson pair signal, the single SM Higgs boson background, and the continuum background. The $m_{\gamma\gamma}$ resonance is described by the sum of a Crystal Ball function and a wide Gaussian component, to model the tails of the distribution [180]. The continuum background is modelled by an exponential function with a common slope between the two categories, such that the control region constrains the background shape in the signal region. The combined acceptance and selection efficiency for the SM Higgs boson pair production signal is 7.4%. The fits to data in the nonresonant signal and control regions are shown in Figure 9.2a.

From simulation studies it is established that the continuum contribution to the signal region is divided between events with two photons and events with one photon in association with a jet fake. The b-tagged jets are comprised of both real heavy-flavour jets and mistagged light-flavour jets. The contributions of the dileptonic decays of $t\bar{t}$ events, where each lepton results in a photon fake is approximately 10% of the total background. The single Higgs boson background is evaluated directly from simulation for each analysis signal region. The contribution from

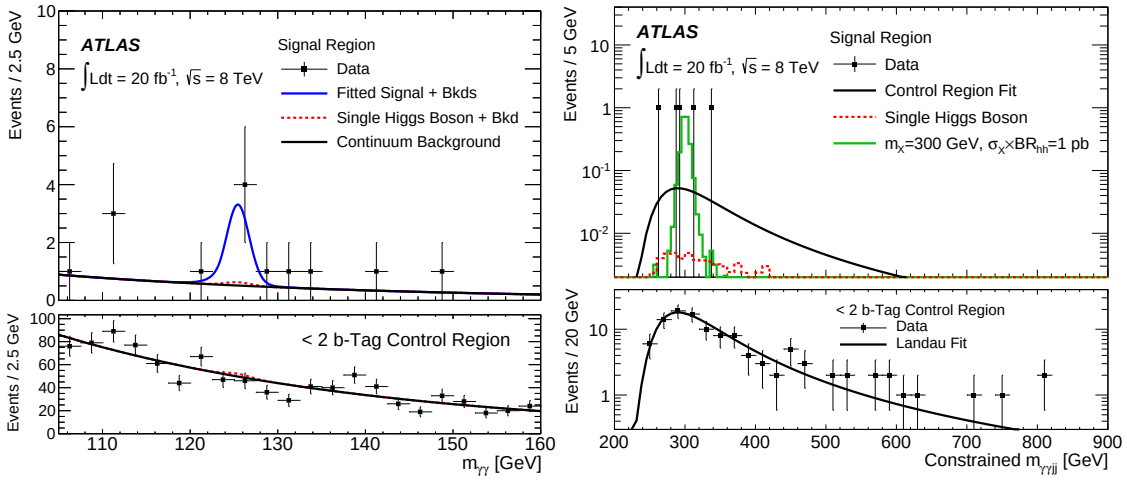

(a) (b)

Figure 9.2: The upper plot in (a) shows the diphoton invariant mass distribution for the nonresonant signal region with the combined signal-plus-background fit. The upper plot in (b) shows the constrained $m_{bb\gamma\gamma}$ distribution in the resonant signal region with a simulated signal for a $m_H = 300\,\text{GeV}$ resonance. The lower plots show the fitted continuum background shape for events in the corresponding fewer than 2 b-tag control region. Taken from [176].

other processes is considered to be negligible.

The resonant search starts with the same selection as for the nonresonant analysis, but imposes additional requirements on $m_{bb\gamma\gamma}$. The small number of events expected after these additional cuts requires that the resonant analysis proceeds as a counting experiment, rather than a simultaneous fit. The diphoton mass must be within a signal window $\pm 2\sigma$ of the Higgs boson mass (set to be $125.5\,\text{GeV}$)[2], where the expected resolution is $1.6\,\text{GeV}$. The four-momentum of the bb-system is constrained to m_h by applying a simple rescaling of m_h/m_{bb}, with m_h set to the value used in simulation of $125\,\text{GeV}$. This improves the $m_{bb\gamma\gamma}$ resolution by 30–60% depending on the resonant mass hypothesis, without introducing significant bias to the background shape. The requirements imposed on $m_{bb\gamma\gamma}$ are designed to select the smallest signal window that contains 95% of the simulated $H \to hh$ signal events, where the width depends linearly on the mass of the resonance being considered. The combined acceptance and selection efficiency for a resonant Higgs boson pair produced signal

[2]The combined mass measured in Reference [3]

varies from 3.8% at $m_H = 260\,\text{GeV}$ to 8.2% at $m_H = 500\,\text{GeV}$.

The continuum background in the resonant signal window is evaluated with data by combining estimates of the contribution entering the $m_{\gamma\gamma}$ signal window and the acceptance of the mass-dependent signal window in the resonant signal region. Firstly, the continuum background in the $m_{\gamma\gamma}$ signal window is extrapolated from the number of observed events in the $m_{\gamma\gamma}$ sidebands (N) and the fraction of background events in the $m_{\gamma\gamma}$ signal window ($f_{m_{\gamma\gamma}}$). The latter is measured by fitting an exponential function to the diphoton mass sidebands for events with fewer than two b-tagged jets, excluding the region $m_h \pm 5\,\text{GeV}$ to minimise contamination from resonant Higgs production. The acceptance of the signal window in $m_{bb\gamma\gamma}$ is measured using events that contain fewer than two b-tagged jets that pass the $m_{\gamma\gamma}$ signal window cut. The distribution is fitted with a Landau function and is integrated in the signal window to obtain $f_{m_{bb\gamma\gamma}}$ for each mass hypothesis. The total number of events expected as part of the continuum background is therefore given by:

$$N_{\text{bkg}} = N \times \frac{f_{m_{\gamma\gamma}}}{1 - f_{m_{\gamma\gamma}}} \times f_{m_{bb\gamma\gamma}}, \tag{9.2}$$

where N_{bkg} and $f_{m_{bb\gamma\gamma}}$ are both functions of m_H. Figure 9.2b shows the constrained $m_{bb\gamma\gamma}$ distribution of events in the resonant signal region that includes a simulated signal for a $m_H = 300\,\text{GeV}$ resonance, and the fitted distribution in the corresponding control region.

There are a large statistical uncertainties associated with the dominant continuum background of 33% as a result of how few events are present in the diphoton mass sideband. As a result, the majority of systematic uncertainties have very little effect on the final result. However, there are some systematic uncertainties with comparable effect that are part of the resonant search. Depending on the resonance mass hypothesis, uncertainties of up to 30% are assigned due to the modelling of the $m_{bb\gamma\gamma}$ shape based on the fewer than 2 b-tag control region. Additional uncertainties of 16–30% are included to account for the choice of analytic function used to parametrise the shape of $m_{bb\gamma\gamma}$.

The nonresonant analysis expects a total of 1.5 background events, with 1.3 ± 0.5 events from the continuum background and 0.17 ± 0.04 events from the single Higgs boson, which is dominated by $t\bar{t}h$ production. About 0.04 signal events are expected from Higgs boson pair production. A total of 5 events are observed, corresponding to a small excess of 2.4σ from the background-only hypothesis. The nonresonant search sets a 95% confidence level upper limit on the cross section of 2.2 (1.0) pb. The resonant search finds an observed (expected) exclusion on the production cross section of 2.3 (1.7) pb at $m_H = 260\,\text{GeV}$ and 0.7 (0.7) pb at $m_H = 500\,\text{GeV}$. The local p-value reaches a minimum at $m_H = 300\,\text{GeV}$, corresponding to a 3.0σ excess and a 2.1σ global excess after consideration of the look elsewhere effect [182, 183].

9.4 Summary of $hh \to b\bar{b}b\bar{b}$

This section summarises the search for Higgs boson production in the $hh \to b\bar{b}b\bar{b}$ channel, where each Higgs boson decays to a pair of b-quarks. Despite the fully-hadronic final state being subject to large multijet backgrounds, the ATLAS $hh \to b\bar{b}b\bar{b}$ analysis [177] has good sensitivity for the production of Higgs boson pairs and benefits significantly from the large $h \to b\bar{b}$ branching ratio. The analysis selects events with a pair of back-to-back, high momentum $b\bar{b}$ systems containing two b-tagged jets that have masses consistent with m_h. Selecting events with this topology gives excellent rejection of all backgrounds and minimises combinatorial ambiguity in forming Higgs boson candidates.

The data sample used in this analysis, after applying data quality requirements that include the availability of b-jet triggers, corresponds to an integrated luminosity of $19.5\,\text{fb}^{-1}$. A combination of five triggers requiring multiple jets or b-jets was used to select events to give a high signal efficiency. The selection of events for this analysis greatly benefits from the use of efficient b-tagged multijet triggers, where the b-jets are identified using a dedicated HLT algorithm [184].

Two different methods are employed when reconstructing the Higgs boson. The

'resolved' method attempts to reconstruct the $h \to b\bar{b}$ decay from a pair of separated nearby b-tagged jets, whereas the 'boosted' method identifies the $h \to b\bar{b}$ decay through a single reconstructed jet using a jet substructure technique. For resonance masses above approximately 1000 GeV decaying to a pair of high momentum Higgs bosons, the boosted method becomes particularly effective. The combination of the hh channels presented in this chapter is primarily concerned with masses below this, and so the more sensitive results obtained with the resolved method are used.

The resolved technique reconstructs Higgs bosons from pairs of nearby anti-k_t jets with radius parameter $R = 0.4$, that have been b-tagged with the MV1 algorithm at the 70% efficiency working point. The event selection requires at least four b-tagged jets, each with $p_{\mathrm{T}} > 40$ GeV. The four highest p_{T} b-tagged jets are selected to form two dijet systems, requiring that the angular separation ΔR between the two jets in each dijet system to be less than 1.5. The p_{T} of the leading and subleading dijet systems are also required to be greater than 200 GeV and 150 GeV, respectively. These selection criteria are partly driven by the corresponding jet trigger thresholds and the necessity to suppress backgrounds. This leads to a significant loss of signal acceptance for lower resonance masses and therefore the resonant search only considers masses above 500 GeV.

Due to the differing kinematics over the large resonant mass range, the selection uses mass dependent cuts that are chosen to maintain optimal sensitivity as a function of the four-jet mass m_{4b}. These additional cuts, applied to the leading and subleading dijet momentum as well as the maximum difference in pseudorapidity between the dijet systems, were optimised simultaneously in a three-dimensional scan of the threshold values.

After the selection of dijets satisfying the mass dependent requirements, the background composition of $t\bar{t}$ events is approximately 10%. The majority of these events arise from the hadronic decay of both top quarks, where the dijets are formed from the b-jet and a mistagged charm jet from the decay of the W boson. To reduce this background while retaining high signal efficiency the analysis utilises a '$t\bar{t}$ veto'.

Additional jets in the event are used to reconstruct the W and top candidates by combining them with each of the dijets. The compatibility with the top quark decay hypothesis is determined by the following expression:

$$\sqrt{\left(\frac{m_W - \tilde{m}_W}{\sigma_{m_W}}\right)^2 + \left(\frac{m_t - \tilde{m}_t}{\sigma_{m_t}}\right)^2} < 3.2, \tag{9.3}$$

where m_W and m_t are the invariant masses of the W and top candidates, $\tilde{m}_W$ and $\tilde{m}_t$ are the W and top quark masses, and σ_{m_W} and σ_{m_t} represent the dijet and three-jet system mass resolutions. The event is rejected if either dijet satisfies the expression for any possible combination with an extra jet.

The signal region is defined by a cut on the leading (m_{12}) and subleading (m_{34}) dijet invariant mass values such that they are consistent with the expectations of the $hh \to b\bar{b}b\bar{b}$ decay, as given by:

$$\sqrt{\left(\frac{m_{12} - \tilde{m}_{12}}{\sigma_{12}}\right)^2 + \left(\frac{m_{34} - \tilde{m}_{34}}{\sigma_{34}}\right)^2} < 1.6. \tag{9.4}$$

Here $\tilde{m}_{12}$ and $\tilde{m}_{34}$ give the peak values expected for the leading and subleading dijet pair from simulation, found to be 124 GeV and 115 GeV respectively, while σ_{12} and σ_{34} are the dijet mass resolutions, estimated from the simulation to be 10% of the dijet mass values. In the resonant production search a constraint is applied to the two dijet mass systems such that they are equal to the Higgs boson mass, in the same way as the $b\bar{b}\tau\tau$ analysis. This leads to an improvement of approximately 30% in the m_{4b} resolution, with a significant reduction in the low mass tails and little impact on the background. The nonresonant search proceeds as a counting experiment, while the resonant search uses the constrained four-jet invariant mass as the final discriminate in the signal region, from which the upper limit on the potential signal cross section is extracted.

The background composition after the full selection is expected to be more than 90% multijet events, with the remainder mostly originating from $t\bar{t}$ events. The contribution to the total background from Z + jets events is less than 1% and is

modelled using MC simulation. A data-driven approach is used to model the multijet background, based on a control sample of events passing the full selection except that only one of the two selected dijets is b-tagged. Corrections are applied to this control sample to account for differences caused by the additional b-tagging requirements in the signal sample. The $t\bar{t}$ background is estimated using MC simulations normalised to data in dedicated control regions. Figure 9.3a shows the m_{4b} distribution of events in the control region, where good agreement between the data and predicted background is observed.

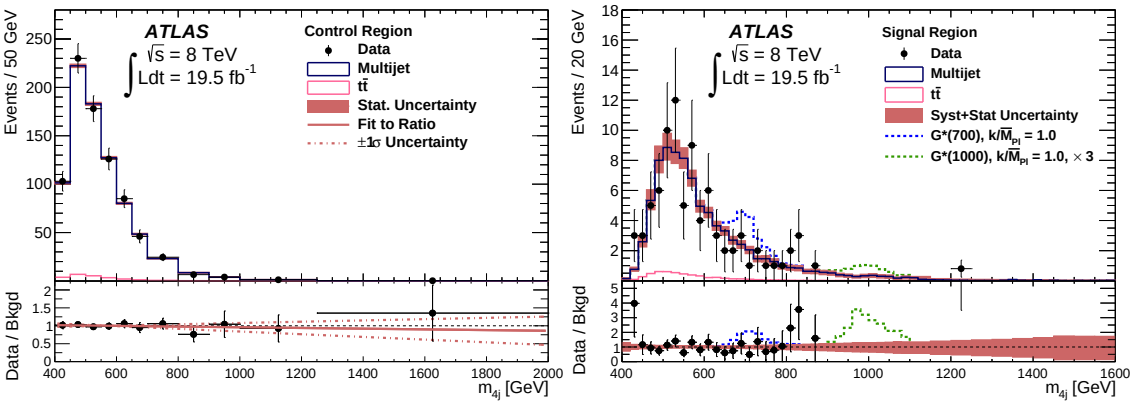

(a) (b)

Figure 9.3: The four-jet mass distributions in (a) the control region and (b) the signal region, including two simulated signals for a possible graviton model [177].

The b-tagging calibration and the multijet background modelling are the most dominant sources of systematic uncertainty in the analysis, where the impact on the sensitivity of the analysis from these sources in less than 10%. Other sources of systematic uncertainty that contribute at the percent level are the jet energy scale and resolution and $t\bar{t}$ modelling

A total of 87 events are observed in the data, which agrees well with the SM expectation of 87.0 ± 5.6 events. There are also no obviously significant local excesses observed in the four-jet invariant mass distribution, as shown in Figure 9.3b. For the nonresonant search, both the observed and expected 95% CL upper limit on the cross section $\sigma(pp \to hh \to b\bar{b}b\bar{b})$ is 202 fb. For the resonant search, the observed (expected) 95% CL upper limit on $\sigma(pp \to H \to hh \to b\bar{b}b\bar{b})$ ranges between

52 (56) fb at $m_H = 500\,\text{GeV}$ and 3.6 (5.8) fb at $m_H = 1000\,\text{GeV}$.

9.5 Combination Procedure

The combination is made from the results obtained in the signal regions of the four different analysis channels. The combination of the resonant searches considers a low and a high resonant mass region of between 260–500 GeV and 500–1000 GeV, respectively. Not all of the channels are included in the combination of each of these mass regions, either because their contribution to the final limit is insignificant or because of limitations in the analysis. Table 9.1 summarises the number of categories and final discriminants used for each analysis in either search, as well as the mass regions they contribute to in the resonant search.

Table 9.1: A summary of the number of categories and final discriminants used for both the nonresonant and resonant searches [8]. The mass ranges used in the combination of the resonant searches are also given.

Search	Channel	Categories	Discriminant	m_H [GeV]
hh	$WW^*\gamma\gamma$	1	event yields	–
	$b\bar{b}\gamma\gamma$	1	$m_{\gamma\gamma}$	–
	$b\bar{b}\tau\tau$	4	$m_{\tau\tau}^{\text{MMC}}$	–
	$b\bar{b}b\bar{b}$	1	event yields	–
$H \to hh$	$WW^*\gamma\gamma$	1	event yields	260–500
	$b\bar{b}\gamma\gamma$	1	event yields	260–500
	$b\bar{b}\tau\tau$	4	$m_{bb\tau\tau}$	260–1000
	$b\bar{b}b\bar{b}$	1	m_{4b}	500–1500

The CL_s method, as discussed in Section 8.9, is adopted for the limit setting. In the combination, different statistical treatments are applied depending on which analyses are included. The nature of the $b\bar{b}\gamma\gamma$ and $WW^*\gamma\gamma$ analyses means that the available statistics are very low and so toy MC pseudo-data is generated in order to obtain the limits and p-values. This technique is therefore applied to the nonresonant and low mass region of the resonant combination. In the high mass region only the $b\bar{b}b\bar{b}$ and $b\bar{b}\tau\tau$ channels are included and as both analyses have

sufficiently large statistics their combined limits and p-values can be obtained using the asymptotic approach. Smaller mass steps are used in the combination for the $b\bar{b}b\bar{b}$ and $b\bar{b}\gamma\gamma$ analyses, reflecting their better mass resolutions than those of the $b\bar{b}\tau\tau$ and $WW^*\gamma\gamma$ analyses.

The Parameters of Interest (PoIs) for each channel are defined as $\sigma(gg \to hh)$ for the nonresonant search and $\sigma(gg \to H) \times \mathrm{BR}(H \to hh)$ for the resonant search. Both of these are assumed to be 1 pb in the combination, where SM branching ratios are also assumed for the h decay. The results are all given for a common mass value of $m_h = 125.4$ GeV. After rescaling to the same definition, the PoIs are correlated across all channels in each search. Systematic uncertainties that affect two or more analysis channels in the combination are assigned common nuisance parameters. Examples include the luminosity, jet energy scale and resolution, and b-tagging uncertainties. The correlations between nuisance parameters are also checked under a fit to the Asimov data set for the background-only hypothesis to identify any strong correlations.

The different systematic uncertainties have been categorised into relevant groups with respect to their sources and the impact on the cross section limits have been assessed. This was achieved using the signal strength parameter μ, defined to be the ratio of the extracted to the assumed signal cross section. The shifts in μ are dependent on the value of the signal strength and for illustration these have been evaluated for $\mu = 1$ for a cross section of 1 pb, as in the limit setting. The influence of the most significant sources of systematic uncertainty are given in Table 9.2.

The largest contributors are the background modelling, b-tagging, the branching ratios of the h decay, and the jet and $E_{\mathrm{T}}^{\mathrm{miss}}$ uncertainties. The fact that the b-tagging systematic uncertainty has a significant impact in the nonresonant and high mass region of the resonant search is a reflection of the comparatively strong weight that the $hh \to b\bar{b}b\bar{b}$ analysis has in the combination.

Table 9.2: The percentage impact of the leading sources of systematic uncertainty on the signal strength parameter μ for the nonresonant and resonant signal, assuming a production cross section of 1 pb [8].

hh		$H \to hh$			
		$m_H = 300\,\text{GeV}$		$m_H = 600\,\text{GeV}$	
Source	$\Delta\mu/\mu$ (%)	Source	$\Delta\mu/\mu$ (%)	Source	$\Delta\mu/\mu$ (%)
Background model	11	Background model	15	b-tagging	10
b-tagging	7.9	Jet and $E_{\text{T}}^{\text{miss}}$	9.9	h BR	6.3
h BR	5.8	Lepton and τ_{had}	6.9	Jet and $E_{\text{T}}^{\text{miss}}$	5.5
Jet and $E_{\text{T}}^{\text{miss}}$	5.5	h BR	5.9	Luminosity	2.7
Luminosity	3.0	Luminosity	4.0	Background model	2.4
Total	16	Total	21	Total	14

9.6 Results

No significant excesses are observed in the nonresonant searches and so limits are set on the hh production cross section. The expected and observed 95% CL upper limits for each of the decay channels and their combination are given in Table 9.3. The table also shows the cross section limits relative to the SM expectation for the $gg \to hh$ process of $9.9 \pm 1.3\,\text{fb}$ [185] assuming $m_h = 125.4\,\text{GeV}$. The combined observed (expected) upper limit on $\sigma(gg \to hh)$ is 0.69 (0.47) pb, which corresponds to 70 (48) times the expected SM cross section. The channel with the greatest expected sensitivity is $b\bar{b}b\bar{b}$ and is followed by $b\bar{b}\gamma\gamma$, $b\bar{b}\tau\tau$ and lastly $WW^*\gamma\gamma$. The combined observed limit is somewhat higher than that for the $hh \to b\bar{b}b\bar{b}$ analysis alone, which is partly the result of the observed excess of events in the $hh \to b\bar{b}\gamma\gamma$ analysis. The compatibility of the combined result with the SM hypothesis as given by the p-value is found to be 4.4% or equivalently 1.7σ, where this low value is attributed to the same excess.

The upper limits for the resonant searches on the $\sigma(gg \to H) \times \text{BR}(H \to hh)$ are illustrated in Figure 9.4 as a function of the heavy Higgs boson mass m_H. It shows the expected limits for each of the analyses individually as well as the expected and observed limits of the combination. The $hh \to b\bar{b}\gamma\gamma$ analysis is the most significant contributor at low mass, while $b\bar{b}b\bar{b}$ is by far the most important channel in the high

Table 9.3: The observed and expected 95% CL upper limits on the cross section for nonresonant $gg \to hh$ production in each of the individual analyses and their combination [8]. The limits are also given with respect to the SM prediction.

Channel	σ [pb]		$\sigma/\sigma_{\mathrm{SM}}$	
	Observed	Expected	Observed	Expected
$WW^*\gamma\gamma$	11	6.7	1150	680
$b\bar{b}\gamma\gamma$	2.2	1.0	220	100
$b\bar{b}\tau\tau$	1.6	1.3	160	130
$b\bar{b}b\bar{b}$	0.62	0.62	63	63
Combined	0.69	0.47	70	48

mass range. The corresponding p-values are given in Figure 9.5. The most significant excess observed in the combination is at a mass of 300 GeV with a local significance of approximately 2.5σ. This is mostly the result of the 3.0σ excess observed in the $b\bar{b}\gamma\gamma$ analysis [176], but is reduced in the combination due to the deficit observed in the $b\bar{b}\tau\tau$ analysis at the same mass. The combined upper limit varies from 2.1 pb at 260 GeV to 0.011 pb at 1000 GeV.

9.7 Interpretation

The cross section limits are interpreted in the Higgs sectors of two simplified MSSM scenarios referred to as hMSSM and low-tan β-high that were introduced in Section 2.5.1. The results obtained for the upper limits on the $\sigma(gg \to H) \times \mathrm{BR}(H \to hh)$ are interpreted as regions of exclusion in the plane of (m_A, $\tan\beta$) for each of these scenarios. The combination has sensitivity in the region of $\tan\beta$ below two and for values of m_A in the range 200–350 GeV. Effects due to the natural width of the heavy Higgs boson in these scenarios can be neglected as they remain sufficiently small compared to the experimental resolution in the sensitive region of this combination.

Higgs boson production cross sections through the ggF process are calculated for both scenarios using SusHi [187, 188, 189]. The branching ratios are calculated

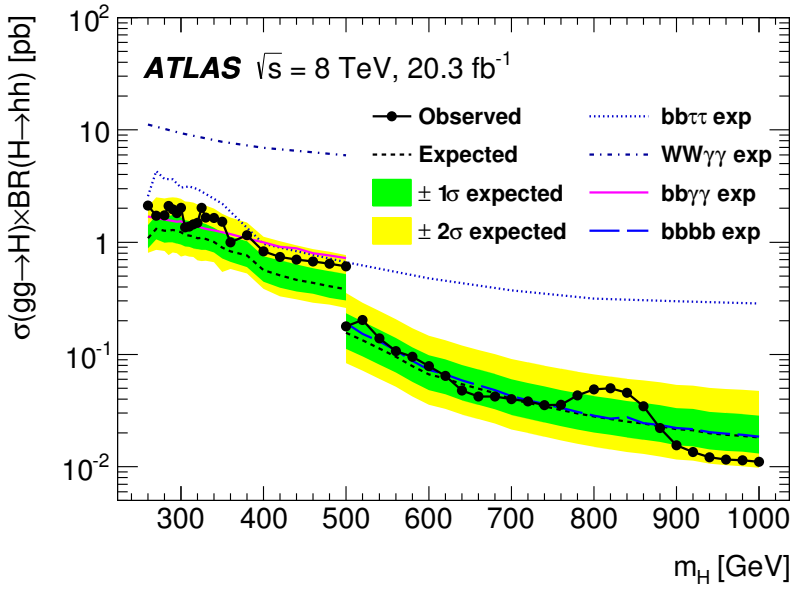

Figure 9.4: The observed and expected 95% CL upper limits on $\sigma(gg \to H) \times \mathrm{BR}(H \to hh)$ as a function of the heavy Higgs boson mass m_H, combining resonant searches in the $hh \to b\bar{b}\gamma\gamma$, $b\bar{b}b\bar{b}$, $b\bar{b}\tau\tau$ and $WW^*\gamma\gamma$ channels [8]. The expected limits for individual searches are also shown. The green and yellow bands show the $\pm 1\sigma$ and $\pm 2\sigma$ uncertainties on the expected limits of the combination. The disjoint at $m_H = 500\,\mathrm{GeV}$ reflects different m_H search ranges of the individual analyses.

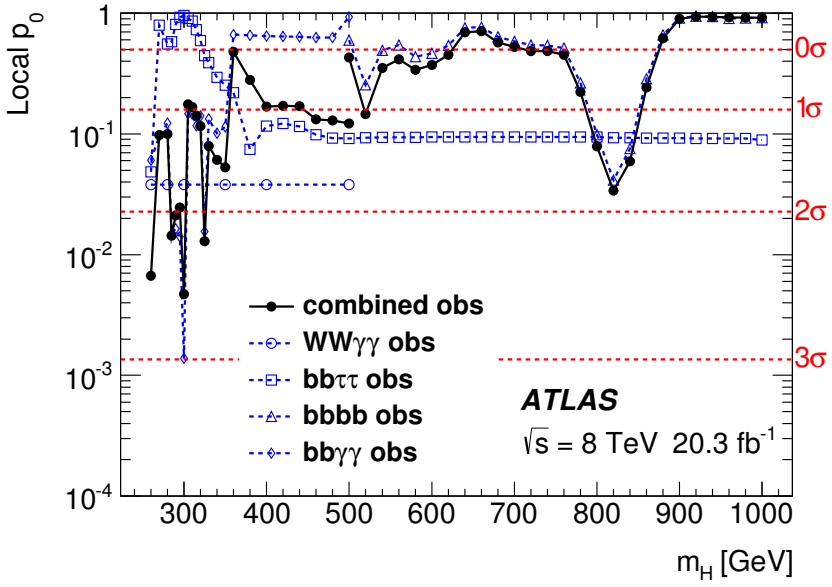

Figure 9.5: The local p-value as a function of the heavy Higgs boson mass m_H, combining resonant searches in the $hh \to b\bar{b}\gamma\gamma$, $b\bar{b}b\bar{b}$, $b\bar{b}\tau\tau$ and $WW^*\gamma\gamma$ channels [186]. The p-values for the individual searches are also shown with open markers.

with HDECAY [190] following the prescription of Reference [191] for the hMSSM scenario and with FeynHiggs [192] for the low-tan β-high scenario. The branching ratios of the light CP-even Higgs boson in these scenarios depend on m_A and $\tan\beta$ and are different from the corresponding SM values used to derive the upper limits shown in Figure 9.4. The branching ratios to gauge bosons are suppressed with respect to their SM value in each of the MSSM scenarios, while those to fermions are enhanced. They however begin to approach the SM values for increasing values of m_H. For example, this enhances the expected yields in the $b\bar{b}\tau\tau$ channel between approximately 60% to 20% in the hMSSM scenario and 55% to 15% in the low-tan β-high scenario, for the m_H range between 260 GeV and 500 GeV. The $b\bar{b}b\bar{b}$ and $b\bar{b}\tau\tau$ channels therefore have a relatively stronger weight in the exclusion limit, while the $WW^*\gamma\gamma$ and $b\bar{b}\gamma\gamma$ channels are strongly and slightly suppressed, respectively.

To simplify the computation of the exclusion, as this would require generating toy MC pseudo-data for every point in the (m_A, $\tan\beta$) plane, each of the hh branching fractions are fixed to their smallest values within expected sensitivity of $1 < \tan\beta < 2$ as a function of m_H. This procedure results in conservative exclusion regions.

The exclusion regions obtained for each of the scenarios are shown in Figure 9.6. Lines of constant m_H are indicated by grey dashes in the parameter space, as large differences between the values of m_A and m_H arise for decreasing values of m_A or $\tan\beta$. The region of exclusion in m_H lies between the kinematic threshold of the $H \to hh$ decay and the dominant $H \to t\bar{t}$ decay. The region shaded in grey in the low-tan β-high scenario indicates the exclusion due to the measured mass of the observed light CP-even Higgs boson of 125 GeV. For both of the scenarios presented, the observed exclusion region is smaller than the expectation, which proves consistent with the small excess observed in the data. The improvement in sensitivity of the expected exclusion following the m_H contour line at around 260 GeV corresponds to the same improvement in the expected limit on the cross section seen in Figure 9.4. In addition, the reduction in the observed exclusion following the m_H contour line at around 325 GeV is caused by the small excess in events observed at the same mass in the cross section limits.

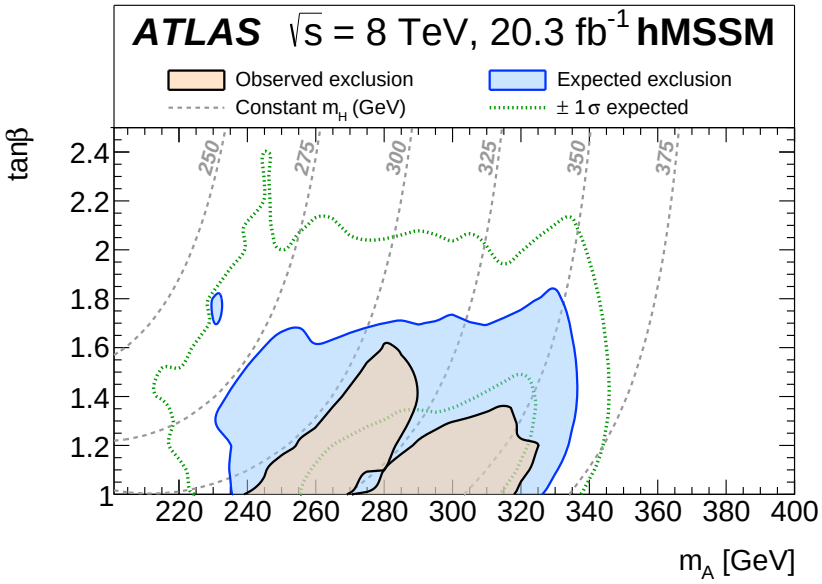

(a)

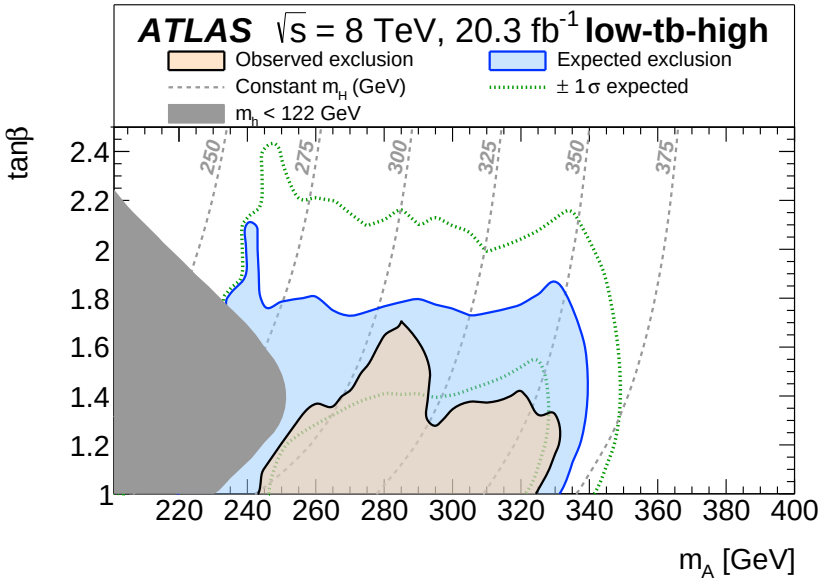

(b)

Figure 9.6: The observed and expected 95% CL exclusion regions in the (m_A, $\tan\beta$) plane of MSSM scenarios from the resonant search: (a) the hMSSM scenario and (b) the low-$\tan\beta$-high scenario [8]. The green dotted lines delimit the $\pm 1\sigma$ uncertainty ranges of the expected exclusion regions. The grey dashed lines show the constant values of the heavy CP-even Higgs boson mass.

The exclusion results obtained with the combination of the $H \to hh$ production channels in the hMSSM model can be compared to those obtained for other heavy Higgs boson searches performed by ATLAS. Figure 9.7 shows the 95% CL contours in the $(m_A, \tan\beta)$ plane for the expectation of the SM Higgs sector and the observed data, as marked by dashed lines and solid lines, respectively. The observed exclusions are indicated by the filled or hatched regions of the plot. The $H \to hh$ searches are complimentary to those of the $H \to WW$, $H \to ZZ$ and $A \to ZH$ channels. Further detail on these results can be found in Reference [193].

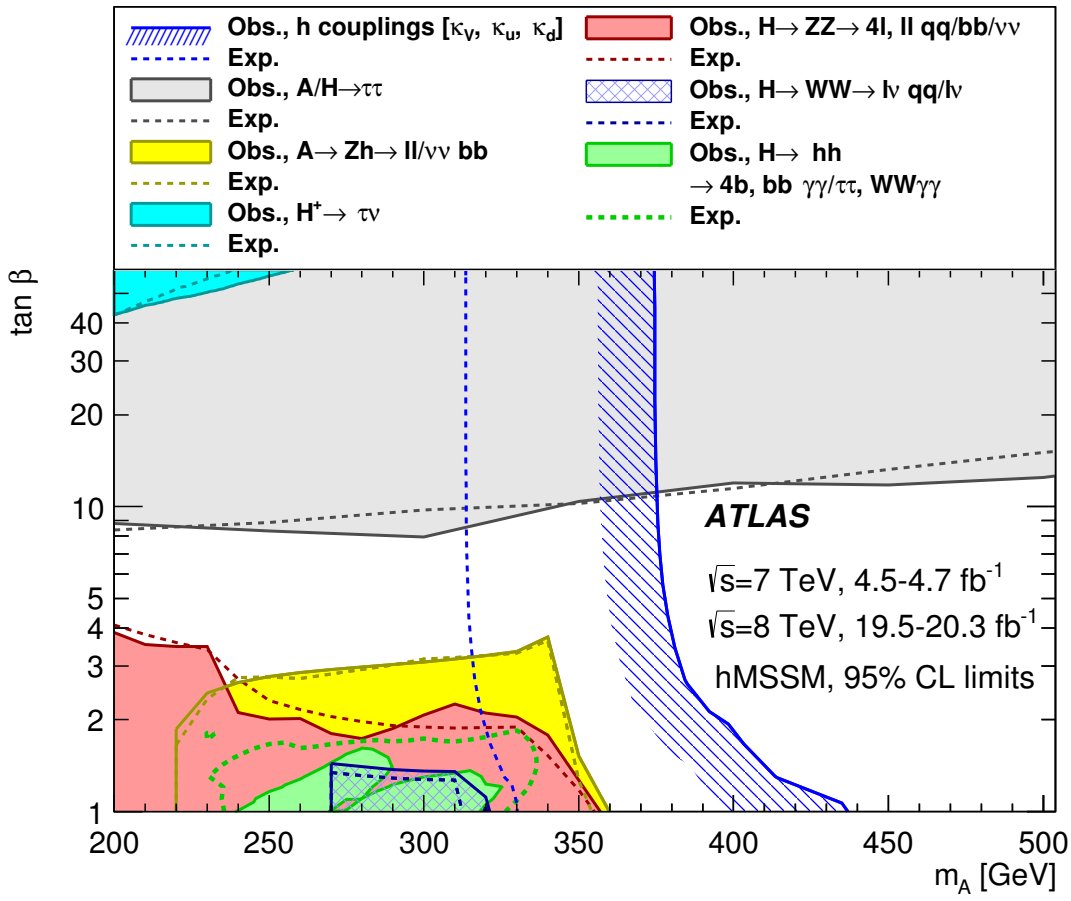

Figure 9.7: Regions of the $(m_A, \tan\beta)$ plane excluded in the hMSSM scenario from direct searches for heavy Higgs bosons and fits to the measured rates of observed Higgs boson production and decays. The observed exclusion region is indicated by the hashed line whereas the expected exclusion is delimited by the dashed line. Taken from [186].

CHAPTER 10

CONCLUSION

High luminosity conditions at the LHC present a challenging environment in which L1Calo must maintain high performance despite ever increasing pile-up. The most significant problem faced by L1Calo has been the large shifts in the average pedestal level at the start of bunch trains. This results in a non-linear scaling of low threshold jet and $E_{\mathrm{T}}^{\mathrm{miss}}$ trigger rates with luminosity, due to the large increase in fake triggers. Large pile-up noise also degrades the performance of the identification and E_{T} measurement for small signals.

The studies in this thesis have shown that autocorrelation FIR filters offer superior performance with respect to the matched filters used during Run 1. That is with the exception of the Tile calorimeter, where the performance is marginally worse. Despite advantages identified for operating the FIR filter at a higher frequency, it is concluded that the increased data volume would make this unfeasible. The crucial addition of a dynamic pedestal correction per bunch crossing to the signal processing has been very successfully demonstrated in simulation to control the trigger tower

E_{T} response. These features have been incorporated into the design of the upgraded version of the MCM. A new noise cut strategy based on the occupancy of trigger towers in $|\eta|$-bins was established and optimised using MC incorporating the new signal processing improvements. This determined that in order to sustain sensible multijet and $E_{\mathrm{T}}^{\mathrm{miss}}$ trigger rates at luminosities around $2 \times 10^{34}\,\mathrm{cm}^{-2}\,\mathrm{s}^{-1}$, a very low occupancy of trigger towers is required, in the region of 0.5%. The improvements in the signal processing are also shown to offer significant improvements in jet and $E_{\mathrm{T}}^{\mathrm{miss}}$ performance, particularly in the region $|\eta| > 2.5$. A very similar approach has been taken with regard to the signal processing and noise cuts for early Run 2 data with great success. Importantly, Level 1 triggers have been shown to no longer demonstrate non-linear behaviour with increasing luminosity.

The discovery of a Higgs boson by the ATLAS and CMS collaborations at a mass of around 125 GeV has been a remarkable success for the theory of EWSB. The new boson presents a great opportunity to test the predictions of the SM in this previously unexplored sector, as well as opening a new region in which to probe for new physics. This includes the possibility of extended Higgs sectors that are predicted by many BSM theories.

ATLAS has performed searches for Higgs boson pair production in a number of decay channels with part of the LHC Run 1 data set. These include the search for SM Higgs boson pair production and the search for a heavy CP-even Higgs boson that decays to a pair of light Higgs bosons. Although no evidence for such production mechanism is observed, the combined 95% CL upper limits of these results demonstrate the sensitivity of ATLAS with the Run 1 data set. The LHC has now started Run 2 operations with a much higher centre-of-mass energy of $\sqrt{s} = 13\,\mathrm{TeV}$ that will assist in greatly enhancing the signal rate for Higgs boson production. This new data will further test the compatibility of the Higgs boson with SM predictions to a greater precision and extend the reach for new physics, ensuring that this remains an interesting field of research for many years to come.

REFERENCES

[1] W. Buttinger, "The ATLAS Level-1 Trigger system," *J. Phys. Conf. Ser.*, vol. 396, p. 012010, 2012.

[2] O. Brandt, A. C. Daniells, D. I. Narrias Villar, V. Scharf, and M. Wessels, "Simulation and parametrisation of dynamic pile-up corrections in the ATLAS Level-1 Calorimeter Trigger," Tech. Rep. ATL-COM-DAQ-2015-120, CERN, Geneva, Jul 2015.

[3] ATLAS Collaboration, "Measurements of Higgs boson production and couplings in diboson final states with the ATLAS detector at the LHC," *Phys. Lett.*, vol. B726, pp. 88–119, 2013.

[4] ATLAS Collaboration, "Measurement of the Higgs boson mass from the $H \to \gamma\gamma$ and $H \to ZZ^* \to 4\ell$ channels with the ATLAS detector using 25 fb^{-1} of pp collision data," *Phys. Rev.*, vol. D90, no. 5, p. 052004, 2014.

[5] ATLAS Collaboration, "Measurements of Higgs boson production and couplings in the four-lepton channel in pp collisions at center-of-mass energies of 7 and 8 TeV with the ATLAS detector," *Phys. Rev.*, vol. D91, no. 1, p. 012006, 2015.

[6] ATLAS Collaboration, "Measurements of the properties of the Higgs-like boson in the four lepton decay channel with the ATLAS detector using 25 fb^{-1} of proton-proton collision data," Tech. Rep. ATLAS-CONF-2013-013, CERN, Geneva, Mar 2013.

[7] S. H. Abidi *et al.*, "Event selection and background estimation for the measurement of the properties of the Higgs particle in the four lepton decay channel with the ATLAS detector," Tech. Rep. ATL-PHYS-INT-2014-032, CERN, Geneva, Oct 2014.

[8] ATLAS Collaboration, "Searches for Higgs boson pair production in the $hh \to bb\tau\tau$, $\gamma\gamma WW^*$, $\gamma\gamma bb$, $bbbb$ channels with the ATLAS detector," *Phys. Rev.*, vol. D92, p. 092004, Nov 2015.

[9] J. Ebke, P. Waller, and T. Brooks, "Mcviz." `http://mcviz.net`. Version: 25/09/2011.

[10] J. J. Thomson, "Cathode Rays," *Philosophical Magazine*, vol. 44, p. 293, 1897.

[11] UA1 Collaboration, "Experimental Observation of Isolated Large Transverse Energy Electrons with Associated Missing Energy at $\sqrt{s} = 540$ GeV," *Phys. Lett.*, vol. B122, pp. 103–116, 1983.

[12] UA1 Collaboration, "Experimental Observation of Lepton Pairs of Invariant Mass Around 95 GeV/c^2 at the CERN SPS Collider," *Phys. Lett.*, vol. B126, pp. 398–410, 1983.

[13] UA2 Collaboration, "Observation of Single Isolated Electrons of High Transverse Momentum in Events with Missing Transverse Energy at the CERN $\bar{p}p$ Collider," *Phys. Lett.*, vol. B122, pp. 476–485, 1983.

[14] UA2 Collaboration, "Evidence for $Z^0 \to e^+e^-$ at the CERN $\bar{p}p$ Collider," *Phys. Lett.*, vol. B129, pp. 130–140, 1983.

[15] CDF Collaboration, "Observation of Top Quark Production in $\bar{p}p$ Collisions with the Collider Detector at Fermilab," *Phys. Rev. Lett.*, vol. 74, pp. 2626–2631, Apr 1995.

[16] DØ Collaboration, "Search for High Mass Top Quark Production in $p\overline{p}$ Collisions at $\sqrt{s} = 1.8$ TeV," *Phys. Rev. Lett.*, vol. 74, pp. 2422–2426, Mar 1995.

[17] Planck Collaboration, "Planck 2013 results. XVI. Cosmological parameters," *Astron. Astrophys.*, vol. 571, p. A16, 2014.

[18] "LHC sets new world record." `http://press-archive.web.cern.ch/press-archive/PressReleases/Releases2009/PR18.09E.html`. Accessed: 15 Aug 2015.

[19] ATLAS Collaboration, "Observation of a new χ_b state in radiative transitions to $\Upsilon(1S)$ and $\Upsilon(2S)$ at ATLAS," *Phys. Rev. Lett.*, vol. 108, p. 152001, 2012.

[20] CMS and LHCb Collaborations, "Observation of the rare $B_s^0 \to \mu^+\mu^-$ decay from the combined analysis of CMS and LHCb data," *Nature*, vol. 522, pp. 68–72, 2015.

[21] LEP Working Group for Higgs boson searches and ALEPH, DELPHI, L3, OPAL Collaborations, "Search for the standard model Higgs boson at LEP," *Phys. Lett.*, vol. B565, pp. 61–75, 2003.

[22] CDF and DØ Collaborations, "Higgs Boson Studies at the Tevatron," *Phys. Rev.*, vol. D88, no. 5, p. 052014, 2013.

[23] ATLAS Collaboration, "Observation of a new particle in the search for the Standard Model Higgs boson with the ATLAS detector at the LHC," *Phys. Lett.*, vol. B716, pp. 1–29, 2012.

[24] CMS Collaboration, "Observation of a new boson at a mass of 125 GeV with the CMS experiment at the LHC," *Phys. Lett.*, vol. B716, pp. 30–61, 2012.

[25] "The nobel prize in physics 2013." `http://www.nobelprize.org/nobel_prizes/physics/laureates/2013/`. Accessed: 25 Oct 2015.

[26] ATLAS Collaboration, "Jet and missing transverse momentum trigger improvements for supersymmetry signatures in 2012 with the ATLAS detector," Tech. Rep. ATL-DAQ-PUB-2012-002, CERN, Geneva, Nov 2012.

[27] "ATLAS Experiment Public Results." `https://twiki.cern.ch/twiki/bin/view/AtlasPublic`. Accessed: 31 Mar 2015.

[28] S. L. Glashow, "Partial symmetries of weak interactions," *Nucl. Phys.*, vol. 22, pp. 579–588, 1961.

[29] S. Weinberg, "A model of leptons," *Phys. Rev. Lett.*, vol. 19, pp. 579–588, 1967.

[30] A. Salam, "Weak and Electromagnetic Interactions," *Conf. Proc.*, vol. C680519, pp. 367–377, 1968.

[31] K. Olive *et al.*, "Review of particle physics," *Chin. Phys.*, vol. C38, p. 090001, 2014.

[32] ATLAS, CDF, CMS and DØ Collaborations, "First combination of Tevatron and LHC measurements of the top-quark mass," Tech. Rep. ATLAS-CONF-2014-008, CDF-NOTE-11071, CMS-PAS-TOP-13-014, D0-NOTE-6416, FERMILAB-TM-2582-E, 2014.

[33] I. J. R. Aitchison and A. J. G. Hey, *Gauge Theories in Particle Physics, 2 Volume Set*. Taylor & Francis, 3rd ed., 2004.

[34] F. Englert and R. Brout, "Broken Symmetry and the Mass of Gauge Vector Mesons," *Phys. Rev. Lett.*, vol. 13, pp. 321–323, 1964.

[35] P. Higgs, "Broken Symmetries and the Masses of Gauge Bosons," *Phys. Rev. Lett.*, vol. 13, pp. 508–509, 1964.

[36] G. Guralnik, C. Hagen, and T. Kibble, "Global Conservation Laws and Massless Particles," *Phys. Rev. Lett.*, vol. 13, pp. 585–587, 1964.

[37] L. Alvarez-Gaume and J. Ellis, "Eyes on a prize particle," *Nature Physics*, vol. 7, no. 1, pp. 2–3, 2011.

[38] W. J. Stirling, "Mstw pdfs : key plots." `https://mstwpdf.hepforge.org/plots/plots.html`. Accessed: 12 Feb 2015.

[39] LHC Higgs Cross Section Working Group, "Handbook of LHC Higgs Cross Sections: 2. Differential Distributions," Tech. Rep. CERN-2012-002, CERN, Geneva, 2012.

[40] LHC Higgs Cross Section Working Group, "Handbook of LHC Higgs Cross Sections: 3. Higgs Properties," Tech. Rep. CERN-2013-004, CERN, Geneva, 2013.

[41] ATLAS and CMS Collaborations, "Combined Measurement of the Higgs Boson Mass in pp Collisions at $\sqrt{s} = 7$ and 8 TeV with the ATLAS and CMS Experiments," *Phys. Rev. Lett.*, vol. 114, p. 191803, 2015.

[42] ATLAS and CMS collaborations, "Measurements of the Higgs boson production and decay rates and constraints on its couplings from a combined ATLAS and CMS analysis of the LHC pp collision data at $\sqrt{s} = 7$ and 8 TeV," Tech. Rep. ATLAS-CONF-2015-044, CERN, Geneva, Sep 2015.

[43] ATLAS Collaboration, "Evidence for the spin-0 nature of the Higgs boson using ATLAS data," *Phys. Lett.*, vol. B726, pp. 120–144, 2013.

[44] CMS Collaboration, "Constraints on the spin-parity and anomalous HVV couplings of the Higgs boson in proton collisions at 7 and 8 TeV," *Phys. Rev.*, vol. D92, p. 012004, 2015.

[45] ATLAS Collaboration, "Measurements of Higgs boson production and couplings in diboson final states with the ATLAS detector at the LHC," *Phys. Lett.*, vol. B726, p. 88, 2013.

[46] CMS Collaboration, "Precise determination of the mass of the Higgs boson and tests of compatibility of its couplings with the standard model predictions using proton collisions at 7 and 8 TeV," *Eur. Phys. J.*, vol. C75, p. 212, 2015.

[47] ATLAS Collaboration, "Search for the $b\bar{b}$ decay of the Standard Model Higgs boson in associated $(W/Z)H$ production with the ATLAS detector," *JHEP*, vol. 1501, p. 069, 2015.

[48] ATLAS Collaboration, "Evidence for the higgs-boson yukawa coupling to tau leptons with the atlas detector," *JHEP*, vol. 1504, p. 117, 2015.

[49] M. Slawinska, W. van den Wollenberg, B. van Eijk, and S. Bentvelsen, "Phenomenology of the trilinear Higgs coupling at proton-proton colliders," arXiv:1408.5010 [hep-ph].

[50] U. Baur, T. Plehn, and D. L. Rainwater, "Determining the Higgs Boson Self Coupling at Hadron Colliders," *Phys. Rev.*, vol. D67, p. 033003, 2003.

[51] J. Baglio, A. Djouadi, R. Grvber, M. M—hlleitner, J. Quevillon, *et al.*, "The measurement of the Higgs self-coupling at the LHC: theoretical status," *JHEP*, vol. 1304, p. 151, 2013.

[52] M. J. Dolan, C. Englert, and M. Spannowsky, "Higgs self-coupling measurements at the LHC," *JHEP*, vol. 1210, p. 112, 2012.

[53] J. Baglio, A. Djouadi, R. Grber, M. M. Mhlleitner, J. Quevillon, and M. Spira, "The measurement of the Higgs self-coupling at the LHC: theoretical status," *JHEP*, vol. 04, p. 151, 2013.

[54] H. E. Haber and G. L. Kane, "The search for supersymmetry: Probing physics beyond the standard model," *Phys. Rept.*, vol. 117, p. 75, 1985.

[55] Q. R. Ahmad *et al.*, "Direct evidence for neutrino flavor transformation from neutral current interactions in the Sudbury Neutrino Observatory," *Phys. Rev. Lett.*, vol. 89, p. 011301, 2002.

[56] U. Amaldi, W. de Boer, and H. Furstenau, "Comparison of grand unified theories with electroweak and strong coupling constants measured at LEP," *Phys. Lett.*, vol. B260, pp. 447–455, 1991.

[57] S. P. Martin, "A Supersymmetry primer," arXiv:hep-ph/9709356 [hep-ph].

[58] N. Seiberg, "Naturalness versus supersymmetric nonrenormalization theorems," *Phys. Lett.*, vol. B318, pp. 469–475, 1993.

[59] R. Barbieri and G. F. Giudice, "Upper Bounds on Supersymmetric Particle Masses," *Nucl. Phys.*, vol. B306, pp. 63–76, 1988.

[60] S. Dimopoulos and H. Georgi, "Softly Broken Supersymmetry and SU(5)," *Nucl. Phys.*, vol. B193, p. 150, 1981.

[61] A. Djouadi, "The Anatomy of electro-weak symmetry breaking. II. The Higgs bosons in the minimal supersymmetric model," *Phys. Rept.*, vol. 459, pp. 1–241, 2008.

[62] A. Arbey, M. Battaglia, A. Djouadi, F. Mahmoudi, and J. Quevillon, "Implications of a 125 GeV Higgs for supersymmetric models," *Phys. Lett.*, vol. B708, pp. 162–169, 2012.

[63] E. Bagnaschi, F. Frensch, S. Heinemeyer, G. Lee, S. R. Liebler, M. Muhlleitner, A. R. Mc Carn, J. Quevillon, N. Rompotis, P. Slavich, M. Spira, C. Wagner, and R. Wolf, "Benchmark scenarios for low $\tan\beta$ in the MSSM," Tech. Rep. LHCHXSWG-2015-002, CERN, Geneva, Aug 2015.

[64] M. Carena, S. Heinemeyer, O. Stl, C. E. M. Wagner, and G. Weiglein, "MSSM Higgs Boson Searches at the LHC: Benchmark Scenarios after the Discovery of a Higgs-like Particle," *Eur. Phys. J.*, vol. C73, no. 9, p. 2552, 2013.

[65] ATLAS Collaboration, "Search for neutral Higgs bosons of the minimal supersymmetric standard model in pp collisions at $\sqrt{s} = 8$ TeV with the ATLAS detector," *JHEP*, vol. 11, p. 056, 2014.

[66] CMS Collaboration, "Search for neutral MSSM Higgs bosons decaying to a pair of tau leptons in pp collisions," *JHEP*, vol. 10, p. 160, 2014.

[67] S. Schael *et al.*, "Search for neutral MSSM Higgs bosons at LEP," *Eur. Phys. J.*, vol. C47, pp. 547–587, 2006.

[68] A. Djouadi and J. Quevillon, "The MSSM Higgs sector at a high M_{SUSY}: reopening the low tanβ regime and heavy Higgs searches," *JHEP*, vol. 10, p. 028, 2013.

[69] A. Djouadi, L. Maiani, G. Moreau, A. Polosa, J. Quevillon, and V. Riquer, "The post-Higgs MSSM scenario: Habemus MSSM?," *Eur. Phys. J.*, vol. C73, p. 2650, 2013.

[70] A. Djouadi, L. Maiani, A. Polosa, J. Quevillon, and V. Riquer, "Fully covering the MSSM Higgs sector at the LHC," *JHEP*, vol. 06, p. 168, 2015.

[71] P. Watkins, *Story of the W and Z*. Cambridge University Press, 1986.

[72] S. Schael *et al.*, "Precision electroweak measurements on the Z resonance," *Phys. Rept.*, vol. 427, pp. 257–454, 2006.

[73] G. Baur *et al.*, "Production of antihydrogen," *Phys. Lett. B.*, vol. 368, no. 3, pp. 251–258, 1996.

[74] L. Evans and P. Bryant, "LHC Machine," *JINST*, vol. 3, no. 08, p. S08001, 2008.

[75] Wikimedia Commons, "Map of the CERN accelerator complex." `http://en.wikipedia.org/wiki/File:Cern-accelerator-complex.svg`. Accessed: 01 Feb 2012.

[76] ATLAS Collaboration, "The ATLAS Experiment at the CERN Large Hadron Collider," *JINST*, vol. 3, no. 08, p. S08003, 2008.

[77] CMS Collaboration, "The CMS experiment at the CERN LHC," *JINST*, vol. 3, no. 08, p. S08004, 2008.

[78] ALICE Collaboration, "The ALICE experiment at the CERN LHC," *JINST*, vol. 3, no. 08, p. S08002, 2008.

[79] LHCb Collaboration, "The LHCb Detector at the LHC," *JINST*, vol. 3, no. 08, p. S08002, 2008.

[80] TOTEM Collaboration, "The TOTEM Experiment at the CERN Large Hadron Collider," *JINST*, vol. 3, no. 08, p. S08007, 2008.

[81] LHCf Collaboration, "The LHCf detector at the CERN Large Hadron Collider," *JINST*, vol. 3, no. 08, p. S08006, 2008.

[82] MoEDAL Collaboration, "Technical Design Report of the MoEDAL Experiment," Tech. Rep. CERN-LHCC-2009-006; MoEDAL-TDR-001, CERN, Geneva, Jun 2009.

[83] R. Heuer, "LHC Schedule according to MTP2015, CERN Council 76th session." `http://indico.cern.ch/event/397373/session/0/contribution/9/2/material/slides/0.pdf`.

[84] "HL-LHC High Luminosity Large Hadron Collider: The HL-LHC project." `http://hilumilhc.web.cern.ch/about/hl-lhc-project`. Accessed: 21 Jul 2015.

[85] ATLAS Collaboration, "TDAQ Phase-I Upgrade Technical Design Report," Tech. Rep. CERN-LHCC-2013-018; ATLAS-TDR-023, CERN, Geneva, 2013.

[86] ATLAS Collaboration, "ATLAS Phase-II Upgrade Scoping Document," Tech. Rep. CERN-LHCC-2015-020; LHCC-G-166, CERN, Geneva, Sep 2015.

[87] ATLAS Collaboration, "ATLAS detector and physics performance: Technical Design Report, 1," Tech. Rep. CERN-LHCC-99-014; ATLAS-TDR-14, Geneva, 1999.

[88] ATLAS Collaboration, "ATLAS level-1 trigger: Technical Design Report," Tech. Rep. CERN-LHCC-98-014; ATLAS-TDR-12, Geneva, 1998.

[89] ATLAS Collaboration, "Performance of the ATLAS Electron and Photon Trigger in p-p Collisions at $\sqrt{s} = 7$ TeV in 2011," Tech. Rep. ATLAS-CONF-2012-048, CERN, Geneva, May 2012.

[90] ATLAS Collaboration, "Performance of the ATLAS muon trigger in pp collisions at $\sqrt{s} = 8$ TeV," *Eur. Phys. J.*, vol. C75, no. 3, p. 120, 2015.

[91] G. Pasztor, R. White, F. Monticelli, M. Wielers, T. Kono, F. Zhang, F. Wang, and K. Behr, "Electron trigger performance in 2012 ATLAS data," Tech. Rep. ATL-COM-DAQ-2015-091, CERN, Geneva, Jul 2015.

[92] S. van der Meer, "Calibration of the effective beam height in the ISR," Tech. Rep. CERN-ISR-PO-68-31; ISR-PO-68-31, CERN, Geneva, 1968.

[93] ATLAS Collaboration, "Improved luminosity determination in pp collisions at $\sqrt{s} = 7$ TeV using the ATLAS detector at the LHC," *Eur. Phys. J.*, vol. C73, no. 8, p. 2518, 2013.

[94] B. Åsman *et al.*, "The ATLAS Level-1 Calorimeter Trigger: PreProcessor implementation and performance," *JINST*, vol. 7, no. 12, p. P12008, 2012.

[95] T. Toifl, P. Moreira, A. Marchioro, and R. Vari, "4-channel rad hard delay generation ASIC with 1ns timing resolution for LHC," *IEEE Trans. Nucl. Sci.*, vol. 46, pp. 139–143, 1999.

[96] U. Pfeiffer and W. Htzel, "Bunch-Crossing Identification for saturated calorimeter signals," Tech. Rep. ATL-DAQ-99-009, CERN, Geneva, May 1999.

[97] H. Martinez, N. Besson, and N. Morange, "Update on the study and validation of the BCID of the L1Calo at very high transverse energies," Tech. Rep. ATL-LARG-INT-2012-005, CERN, Geneva, Oct 2012.

[98] W. R. Bennett, "Spectra of Quantized Signals," *Bell System Technical Journal*, vol. 27, pp. 446–472, July 1948.

[99] V. Andrei, P. Hanke, J. Jongmanns, A. Khomich, K. Meier, K. Schmitt, H. C. Schultz-Coulon, R. Stamen, P. Stock, and M. Wessels, "The upgrade of the PreProcessor system of the ATLAS level-1 calorimeter trigger," *JINST*, vol. 7, no. 12, p. C12026, 2012.

[100] ATLAS Collaboration, "ATLAS Insertable B-Layer Technical Design Report," Tech. Rep. CERN-LHCC-2010-013; ATLAS-TDR-19, CERN, Geneva, 2010.

[101] E. G. Stern, "Et Fluctuations in Pileup Events as a Function of Pseudorapidity," Tech. Rep. SSC-GEM-TN-92-111, 1992.

[102] ATLAS Collaboration, "ATLAS liquid-argon calorimeter: Technical Design Report," Tech. Rep. CERN-LHCC-96-041; ATLAS-TDR-2, Geneva, 1996.

[103] J. Garvey and D. Rees, "Bunch Crossing Identification for the ATLAS Level-1 Calorimeter Trigger," Tech. Rep. ATL-DAQ-96-051. ATL-D-PN-51, CERN, Geneva, May 1996.

[104] S. Chatterjee and A. S. Hadi, *Regression Analysis by Example*. Wiley, 5th ed., 2013.

[105] W. E. Cleland and E. G. Stern, "Signal processing considerations for liquid ionization calorimeters in a high rate environment," *Nucl. Instrum. Meth.*, vol. A338, no. 2–3, pp. 467–497, 1994.

[106] Y. Davygora and G. Unal, "Precision Timing of the ATLAS Level-1 Calorimeter Trigger: From Beam Splashes to High Luminosity ProtonProton Collisions," *J. Phys. Conf. Ser.*, vol. 404, no. 1, p. 012055, 2012.

[107] ATLAS Collaboration, "ATLAS Computing: technical design report," Tech. Rep. CERN-LHCC-2005-022; ATLAS-TRD-017, Geneva, 2005.

[108] G. Barrand *et al.*, "GAUDI — A software architecture and framework for building HEP data processing applications," *Comput. Phys. Commun.*, vol. 140, pp. 45–55, 2001.

[109] M. Dobbs and J. B. Hansen, "The HepMC C++ Monte Carlo event record for High Energy Physics," *Comput. Phys. Commun.*, vol. 134, pp. 41–46, 2001.

[110] ATLAS Collaboration, "The ATLAS Simulation Infrastructure," *Eur. Phys. J.*, vol. C70, pp. 823–874, 2010.

[111] S. Agostinelli *et al.*, "Geant4 — a simulation toolkit," *Nucl. Instrum. Meth.*, vol. A506, no. 3, pp. 250–303, 2003.

[112] P. Nason, "A New method for combining NLO QCD with shower Monte Carlo algorithms," *JHEP*, vol. 11, p. 040, 2004.

[113] S. Frixione, P. Nason, and C. Oleari, "Matching NLO QCD computations with Parton Shower simulations: the POWHEG method," *JHEP*, vol. 11, p. 070, 2007.

[114] S. Alioli, P. Nason, C. Oleari, and E. Re, "A general framework for implementing NLO calculations in shower Monte Carlo programs: the POWHEG BOX," *JHEP*, vol. 06, p. 043, 2010.

[115] J. M. Campbell, R. K. Ellis, P. Nason, and E. Re, "Top-pair production and decay at NLO matched with parton showers," *JHEP*, vol. 1504, p. 114, 2015.

[116] T. Sjostrand, S. Mrenna, and P. Z. Skands, "A Brief Introduction to PYTHIA 8.1," *Comput. Phys. Commun.*, vol. 178, pp. 852–867, 2008.

[117] T. Hryn'ova and K. Nagano, "Trigger Menu Strategy for Run 2," Tech. Rep. ATL-COM-DAQ-2014-054, CERN, Geneva, May 2014.

[118] M. Cacciari, G. P. Salam, and G. Soyez, "The Anti-k(t) jet clustering algorithm," *JHEP*, vol. 0804, p. 063, 2008.

[119] ATLAS Collaboration, "Topological cell clustering in the ATLAS calorimeters and its performance in LHC Run 1," arXiv:1603.02934 [hep-ex].

[120] ATLAS Collaboration, "Data-Quality Requirements and Event Cleaning for Jets and Missing Transverse Energy Reconstruction with the ATLAS Detector in Proton-Proton Collisions at a Center-of-Mass Energy of $\sqrt{s} = 7$ TeV," Tech. Rep. ATLAS-CONF-2010-038, CERN, Geneva, Jul 2010.

[121] ATLAS Collaboration, "Performance of the ATLAS jet trigger with pp collisions at $\sqrt{s} = 900$ GeV," Tech. Rep. ATLAS-CONF-2010-028, CERN, Geneva, Jul 2010.

[122] A. Mincer, F. U. Bernlochner, A. Struebig, J. Schouwenberg, and J. B. Beacham, "The ATLAS Transverse Momentum Trigger at the LHC," Tech. Rep. ATL-DAQ-PROC-2015-028, CERN, Geneva, Sep 2015.

[123] M. Wessels, "Calibration and Performance of the ATLAS Level-1 Calorimeter Trigger with LHC Collision Data," *Phys. Procedia*, vol. 37, pp. 1841–1848, 2012.

[124] V. Kouskoura, F. Bartels, V. Scharf, and T. M. Spieker, "L1Calo Performance Plots," Tech. Rep. ATL-COM-DAQ-2015-150, CERN, Geneva, Sep 2015.

[125] S. Dawson *et al.*, "Working Group Report: Higgs Boson," arXiv:1310.8361 [hep-ex].

[126] ATLAS Collaboration, "Summary of ATLAS Pythia 8 tunes," Tech. Rep. ATL-PHYS-PUB-2012-003, CERN, Geneva, Aug 2012.

[127] Z. Was, "TAUOLA the library for tau lepton decay, and KKMC / KORALB / KORALZ /... status report," *Nucl. Phys. Proc. Suppl.*, vol. 98, pp. 96–102, 2001.

[128] N. Davidson, T. Przedzinski, and Z. Was, "PHOTOS Interface in C++: Technical and Physics Documentation," arXiv:1011.0937 [hep-ph].

[129] H.-L. Lai, M. Guzzi, J. Huston, Z. Li, P. M. Nadolsky, *et al.*, "New parton distributions for collider physics," *Phys. Rev.*, vol. D82, p. 074024, 2010.

[130] J. Pumplin, D. Stump, J. Huston, H. Lai, P. M. Nadolsky, *et al.*, "New generation of parton distributions with uncertainties from global QCD analysis," *JHEP*, vol. 0207, p. 012, 2002.

[131] J. Alwall, M. Herquet, F. Maltoni, O. Mattelaer, and T. Stelzer, "MadGraph 5: going beyond," *JHEP*, vol. 1106, p. 128, 2011.

[132] T. Plehn, M. Spira, and P. Zerwas, "Pair production of neutral Higgs particles in gluon-gluon collisions," *Nucl. Phys.*, vol. B479, p. 46, 1996.

[133] R. Frederix, S. Frixione, V. Hirschi, F. Maltoni, O. Mattelaer, *et al.*, "Higgs pair production at the LHC with NLO and parton-shower effects," *Phys. Lett.*, vol. B732, p. 142, 2014.

[134] B. Hespel and E. Vryonidou, "Higgs Pair Production." `http://cp3.irmp.ucl.ac.be/projects/madgraph/wiki/HiggsPairProduction`. Accessed: 13 Jul 2016.

[135] M. Grazzini and H. Sargsyan, "Heavy-quark mass effects in Higgs boson production at the LHC," *JHEP*, vol. 1309, p. 129, 2013.

[136] D. de Florian, G. Ferrera, M. Grazzini, and D. Tommasini, "Higgs boson production at the LHC: transverse momentum resummation effects in the $H \to 2\gamma$, $H \to WW \to \ell\nu\ell'\nu'$ and $H \to ZZ \to 4\ell$ decay modes," *JHEP*, vol. 1206, p. 132, 2012.

[137] LHC Higgs Cross Section Working Group, "Handbook of LHC Higgs Cross Sections: 1. Inclusive Observables," Tech. Rep. CERN-2011-002, CERN, Geneva, 2011.

[138] M. L. Mangano, M. Moretti, F. Piccinini, R. Pittau, and A. D. Polosa, "ALPGEN, a generator for hard multiparton processes in hadronic collisions," *JHEP*, vol. 0307, p. 001, 2003.

[139] J. Alwall *et al.*, "Comparative study of various algorithms for the merging of parton showers and matrix elements in hadronic collisions," *Eur. Phys. J.*, vol. C53, pp. 473–500, 2008.

[140] B. P. Kersevan and E. Richter-Was, "The Monte Carlo event generator AcerMC versions 2.0 to 3.8 with interfaces to PYTHIA 6.4, HERWIG 6.5 and ARIADNE 4.1," *Comput. Phys. Commun.*, vol. 184, p. 919, 2013.

[141] ATLAS Collaboration, "Modelling $Z \to \tau\tau$ processes in ATLAS with τ-embedded $Z \to \mu\mu$ data," *JINST*, vol. 10, no. 09, p. P09018, 2015.

[142] ATLAS Collaboration, "Measurement of the electroweak production of dijets in association with a Z-boson and distributions sensitive to vector boson fusion in proton-proton collisions at $\sqrt{s} = 8$ TeV using the ATLAS detector," *JHEP*, vol. 04, p. 031, 2014.

[143] ATLAS Collaboration, "Evidence for the Higgs-boson Yukawa coupling to tau leptons with the ATLAS detector," *JHEP*, vol. 04, p. 117, 2015.

[144] ATLAS Collaboration, "Improved electron reconstruction in ATLAS using the Gaussian Sum Filter-based model for bremsstrahlung," Tech. Rep. ATLAS-CONF-2012-047, CERN, Geneva, May 2012.

[145] ATLAS Collaboration, "Electron efficiency measurements with the ATLAS detector using the 2012 LHC proton-proton collision data," Tech. Rep. ATLAS-CONF-2014-032, CERN, Geneva, Jun 2014.

[146] ATLAS Collaboration, "Measurement of the muon reconstruction performance of the ATLAS detector using 2011 and 2012 LHC proton-proton collision data," *Eur. Phys. J.*, vol. C74, no. 11, p. 3130, 2014.

[147] ATLAS Collaboration, "Identification and energy calibration of hadronically decaying tau leptons with the ATLAS experiment in pp collisions at $\sqrt{s} =$ 8 TeV," *Eur. Phys. J.*, vol. C75, no. 7, p. 303, 2015.

[148] ATLAS Collaboration, "Local Hadronic Calibration," Tech. Rep. ATL-LARG-PUB-2009-001-2, CERN, Geneva, Jun 2008.

[149] M. Cacciari and G. P. Salam, "Pileup subtraction using jet areas," *Phys. Lett.*, vol. B659, pp. 119–126, 2008.

[150] ATLAS Collaboration, "Jet energy measurement and its systematic uncertainty in proton-proton collisions at $\sqrt{s} = 7$ TeV with the ATLAS detector," *Eur. Phys. J.*, vol. C75, no. 1, p. 17, 2015.

[151] ATLAS Collaboration, "Data-driven determination of the energy scale and resolution of jets reconstructed in the ATLAS calorimeters using dijet and multijet events at $\sqrt{s} = 8$ TeV," Tech. Rep. ATLAS-CONF-2015-017, CERN, Geneva, Apr 2015.

[152] ATLAS Collaboration, "Performance of b-Jet Identification in the ATLAS Experiment," *JINST*, vol. 11, no. 04, p. P04008, 2016.

[153] ATLAS Collaboration, "Calibration of the performance of b-tagging for c and light-flavour jets in the 2012 ATLAS data," Tech. Rep. ATLAS-CONF-2014-046, CERN, Geneva, Jul 2014.

[154] ATLAS Collaboration, "Performance of Missing Transverse Momentum Reconstruction in ATLAS studied in Proton-Proton Collisions recorded in 2012 at 8 TeV," Tech. Rep. ATLAS-CONF-2013-082, CERN, Geneva, Aug 2013.

[155] ATLAS Collaboration, "Pile-up Suppression in Missing Transverse Momentum Reconstruction in the ATLAS Experiment in Proton-Proton Collisions at $\sqrt{s}$ = 8 TeV," Tech. Rep. ATLAS-CONF-2014-019, CERN, Geneva, May 2014.

[156] A. Elagin, P. Murat, A. Pranko, and A. Safonov, "A New Mass Reconstruction Technique for Resonances Decaying to di-tau," *Nucl. Instrum. Meth.*, vol. A654, pp. 481–489, 2011.

[157] R. K. Ellis, I. Hinchliffe, M. Soldate, and J. J. van der Bij, "Higgs Decay to $\tau^+\tau^-$: A possible signature of intermediate mass Higgs bosons at high energy hadron colliders," *Nucl. Phys.*, vol. B297, p. 221, 1988.

[158] ATLAS Collaboration, "Measurements of normalized differential cross sections for $t\bar{t}$ production in pp collisions at $\sqrt{s} = 7$ TeV using the ATLAS detector," *Phys. Rev.*, vol. D90, no. 7, p. 072004, 2014.

[159] ATLAS Collaboration, "Search for the Standard Model Higgs boson in the H to $\tau^+\tau^-$ decay mode in $\sqrt{s} = 7$ TeV pp collisions with ATLAS," *JHEP*, vol. 09, p. 070, 2012.

[160] ATLAS Collaboration, "Measurement of the Z to tau tau Cross Section with the ATLAS Detector," *Phys. Rev.*, vol. D84, p. 112006, 2011.

[161] ATLAS Collaboration, "Electron and photon energy calibration with the ATLAS detector using LHC Run 1 data," *Eur. Phys. J.*, vol. C74, no. 10, p. 3071, 2014.

[162] ATLAS Collaboration, "Calibration of b-tagging using dileptonic top pair events in a combinatorial likelihood approach with the ATLAS experiment," Tech. Rep. ATLAS-CONF-2014-004, CERN, Geneva, Feb 2014.

[163] S. Frixione and B. R. Webber, "Matching NLO QCD computations and parton shower simulations," *JHEP*, vol. 06, p. 029, 2002.

[164] S. Frixione, P. Nason, and B. R. Webber, "Matching NLO QCD and parton showers in heavy flavor production," *JHEP*, vol. 08, p. 007, 2003.

[165] A. Martin, W. Stirling, R. Thorne, and G. Watt, "Parton distributions for the LHC," *Eur. Phys. J.*, vol. C63, p. 189, 2009.

[166] R. D. Ball, S. Carrazza, L. Del Debbio, S. Forte, J. Gao, *et al.*, "Parton distribution benchmarking with LHC data," *JHEP*, vol. 1304, p. 125, 2013.

[167] ATLAS Collaboration, CMS Collaboration and LHC Higgs Combination Group, "Procedure for the LHC Higgs boson search combination in Summer 2011," Tech. Rep. ATL-PHYS-PUB-2011-11; CMS-NOTE-2011-005, CERN, Geneva, Aug 2011.

[168] G. Zech, "Upper limits in experiments with background or measurement errors," *Nucl. Instrum. Meth.*, vol. A277, p. 608. 6 p, Nov 1988.

[169] A. L. Read, "Presentation of search results: The CL(s) technique," *J. Phys.*, vol. G28, pp. 2693–2704, 2002.

[170] G. Cowan, K. Cranmer, E. Gross, and O. Vitells, "Asymptotic formulae for likelihood-based tests of new physics," *Eur. Phys. J.*, vol. C71, p. 1554, 2011.

[171] A. Wald, "Tests of statistical hypotheses concerning several parameters when the number of observations is large," *Trans. Amer. Math. Soc.*, vol. 54, no. 3, pp. 426–482, 1943.

[172] K. Cranmer, G. Lewis, L. Moneta, A. Shibata, and W. Verkerke, "HistFactory: A tool for creating statistical models for use with RooFit and RooStats," Tech. Rep. CERN-OPEN-2012-016, New York U., New York, Jan 2012.

[173] W. Verkerke and D. P. Kirkby, "The RooFit toolkit for data modeling," *eConf*, vol. C0303241, p. MOLT007, 2003.

[174] L. Moneta, K. Belasco, K. S. Cranmer, S. Kreiss, A. Lazzaro, D. Piparo, G. Schott, W. Verkerke, and M. Wolf, "The RooStats Project," *PoS*, vol. ACAT2010, p. 057, 2010.

[175] R. Brun and F. Rademakers, "Root — an object oriented data analysis framework," *Nucl. Instrum. Meth.*, vol. A389, no. 1–2, pp. 81–86, 1997.

[176] ATLAS Collaboration, "Search for Higgs Boson Pair Production in the $\gamma\gamma b\bar{b}$ Final State Using pp Collision Data at $\sqrt{s} = 8$ TeV from the ATLAS Detector," *Phys. Rev. Lett.*, vol. 114, p. 081802, 2015.

[177] ATLAS Collaboration, "Search for Higgs boson pair production in the $b\bar{b}b\bar{b}$ final state from pp collisions at $\sqrt{s} = 8$ TeV with the ATLAS detector," *Eur. Phys. J.*, vol. C75, no. 9, p. 412, 2015.

[178] CMS Collaboration, "Search for the resonant production of two Higgs bosons in the final state with two photons and two bottom quarks," Tech. Rep. CMS-PAS-HIG-13-032, CERN, Geneva, 2014.

[179] CMS Collaboration, "Search for resonant pair production of Higgs bosons decaying to two bottom quarkantiquark pairs in protonproton collisions at 8 TeV," *Phys. Lett.*, vol. B749, pp. 560–582, 2015.

[180] ATLAS Collaboration, "Measurement of Higgs boson production in the diphoton decay channel in pp collisions at center-of-mass energies of 7 and 8 TeV with the ATLAS detector," *Phys. Rev.*, vol. D90, no. 11, p. 112015, 2014.

[181] ATLAS Collaboration, "Measurements of fiducial and differential cross sections for Higgs boson production in the diphoton decay channel at $\sqrt{s} = 8$ TeV with ATLAS," *JHEP*, vol. 09, p. 112, 2014.

[182] L. Lyons, "Open statistical issues in particle physics," *Ann. Appl. Stat.*, vol. 2, pp. 887–915, Sep 2008.

[183] E. Gross and O. Vitells, "Trial factors or the look elsewhere effect in high energy physics," *Eur. Phys. J.*, vol. C70, pp. 525–530, 2010.

[184] D. Madaffari, "Real-time flavor tagging selection in ATLAS," Tech. Rep. ATL-DAQ-PROC-2014-036, CERN, Geneva, Oct 2014.

[185] D. de Florian and J. Mazzitelli, "Higgs Boson Pair Production at Next-to-Next-to-Leading Order in QCD," *Phys. Rev. Lett.*, vol. 111, p. 201801, 2013.

[186] "Searches for Higgs boson pair production in the $hh \to bb\tau\tau$, $\gamma\gamma WW^*$, $\gamma\gamma bb$, $bbbb$ channels with the ATLAS detector." `https://atlas.web.cern.ch/Atlas/GROUPS/PHYSICS/PAPERS/HIGG-2013-33/`. Accessed: 24 Nov 2015.

[187] R. V. Harlander, S. Liebler, and H. Mantler, "SusHi: A program for the calculation of Higgs production in gluon fusion and bottom-quark annihilation in the Standard Model and the MSSM," *Comput. Phys. Commun.*, vol. 184, p. 1605, 2013.

[188] R. V. Harlander and W. B. Kilgore, "Next-to-next-to-leading order Higgs production at hadron colliders," *Phys. Rev. Lett.*, vol. 88, p. 201801, 2002.

[189] U. Aglietti, R. Bonciani, G. Degrassi, and A. Vicini, "Two loop light fermion contribution to Higgs production and decays," *Phys. Lett.*, vol. B595, pp. 432–441, 2004.

[190] A. Djouadi, J. Kalinowski, and M. Spira, "HDECAY: a program for Higgs boson decays in the Standard Model and its supersymmetric extension," *Comput. Phys. Commun.*, vol. 108, p. 56, 1998.

[191] A. Djouadi, L. Maiani, A. Polosa, J. Quevillon, and V. Riquer, "Fully covering the MSSM Higgs sector at the LHC," *JHEP*, vol. 06, p. 168, 2015.

[192] S. Heinemeyer, W. Hollik, and G. Weiglein, "FeynHiggs: a program for the calculation of the masses of the neutral CP-even Higgs bosons in the MSSM," *Comput. Phys. Commun.*, vol. 124, p. 76, 2000.

[193] ATLAS Collaboration, "Constraints on new phenomena via Higgs boson couplings and invisible decays with the ATLAS detector," *JHEP*, vol. 11, p. 206, 2015.

[194] S. Alioli, P. Nason, C. Oleari, and E. Re, "NLO vector-boson production matched with shower in POWHEG," *JHEP*, vol. 0807, p. 060, 2008.

[195] ATLAS Collaboration, "New ATLAS event generator tunes to 2010 data," Tech. Rep. ATL-PHYS-PUB-2011-008, CERN, Geneva, Apr 2011.

[196] G. Corcella, I. Knowles, G. Marchesini, S. Moretti, K. Odagiri, *et al.*, "HERWIG 6: An Event generator for hadron emission reactions with interfering gluons (including supersymmetric processes)," *JHEP*, vol. 0101, p. 010, 2001.

[197] J. Butterworth, J. R. Forshaw, and M. Seymour, "Multiparton interactions in photoproduction at HERA," *Z. Phys.*, vol. C72, pp. 637–646, 1996.

[198] ATLAS Collaboration, "ATLAS tunes of PYTHIA 6 and Pythia 8 for MC11," Tech. Rep. ATL-PHYS-PUB-2011-009, CERN, Geneva, Jul 2011.

APPENDIX A

$H \to ZZ^{(*)} \to 4\ell$ LEPTON SELECTION EFFICIENCIES

A.1 Introduction

The SM Higgs boson production rate and couplings in the decay channel $H \to ZZ^{(*)} \to 4\ell$ (where $\ell = e$ or μ) have been measured by ATLAS using the Run 1 dataset [5]. Typically, the Combined Performance groups make recommendations on how to correct MC to match the performance measured in data for different sets of object definitions, however all leptons passing the $H \to ZZ^{(*)} \to 4\ell$ analysis selection are subject to additional isolation and impact parameter cuts on top of the lepton identification requirements. It is therefore important to determine whether further efficiency corrections are required for these additional selection cuts as well as the associated uncertainties. Such corrections, based on the ratio of the efficiencies measured in data and MC, are often referred to as Scale Factors (SFs).

Presented here is the study of the lepton selection efficiencies of the isolation and impact parameter cuts specific to this analysis for the 8 TeV dataset. SFs and their estimated uncertainties are determined for the barrel and endcap detector regions as a function of the electron E_{T} and muon p_{T}, as well as the dependence on the number of reconstructed primary vertices (N_{vtx}). The performance of the lepton selection is obtained with a tag-and-probe technique using decays of the Z bosons to electron and muon pairs. Such decays are ideal for this study as they result in a clean signature in much the same way as the decay of $H \to ZZ^{(*)} \to 4\ell$.

A.2 Data and Monte Carlo Samples

This study is performed on the total 20.3 fb^{-1} data sample recorded in 2012 at a centre-of-mass energy of 8 TeV, where all events must pass the data-quality requirements of the main analysis. A number of important backgrounds to the decays of $Z \to \ell\ell$ are considered. These include $Z \to \tau\tau$ events, where both tau leptons decay leptonically, $t\bar{t}$ production, where the leptons result from either the leptonic decay of the W boson or the hadronisation of the b-quark, and QCD processes which fake the final state.

The $Z \to ee$ and $Z \to \mu\mu$ signals are both modelled by the POWHEG event generator [112, 113, 114, 194], which provides up to NLO calculations for vector boson production. This is interfaced to PYTHIA8 [116] to perform showering and hadronization using the AU2 generator tune [126] and the CT10 PDF set [129], which is in turn interfaced to PHOTOS [128] for QED radiative corrections in the final state. The $Z \to ee$ sample also includes the latest detector geometry definition, which has an improved description of the material present in front of the endcap calorimeter [161]. The $t\bar{t}$ background sample is produced in much the same way [115], but using the Perugia2011C [195] generator tune and the CTEQ6L1 PDF set [130]. The simulation of $Z \to \tau\tau$ events uses instead the ALPGEN [138] tree-level matrix element calculator in the initial generation step and is interfaced through TAUOLA [127] for the decays of the tau lepton. Each MC sample is simulated for a bunch-spacing of 50 ns and events are weighted to reproduce the distribution of the average number of interactions per bunch crossing observed in data.

A data-driven estimate of the QCD background shape is obtained from events with same flavour and same charge leptons. To reduce the contamination fraction from true $Z \to ee$ events in the QCD background shape a looser cut on the electron Likelihood (LH) identification discriminant is used. The electron LH identification is described in detail in Reference [145]. The background modelling is discussed in more detail in the following section.

A.3 Muon Reconstruction

The ATLAS experiment uses information from the MS, ID and to some extent the calorimeter to identify and reconstruct muons. Muon tracks are reconstructed in the MS by identifying local track segments in each of the chamber layers and combining these into a full MS track. The ID provides an independent measurement of the muon track close to the interaction point. Typically muons are identified by matching full or partial MS tracks with ID tracks, however other criteria are used in areas which lack coverage from either of these systems. This leads to four types of muon candidates which are distinguished by the following reconstruction criteria.

- **Combined**: Combined muons are the primary muon type used in ATLAS analyses and also have the highest purity. These muons are identified by successfully matching an MS track with an ID track to form a combined measurement of the muon track parameters.

- **Segment-tagged**: The segment-tagged muon reconstruction is used to identify muons which cross only one layer of MS chambers, either because they have low p_{T} or because their trajectories pass through a region of reduced MS acceptance. Segment-tagged muons are identified by an ID track, when extrapolated to the MS is matched to at least one local track segment. The ST muon adopts the measured parameters of the associated ID track.

- **Standalone**: The standalone muon reconstruction is solely based on the tracks reconstructed in the MS. The parameters of the muon track are determined by extrapolating back to the point of closest approach to the beam line, taking into account the energy loss associated with the traversed calorimeter material. Standalone muons are mainly used to extend the acceptance beyond the ID coverage in the region $2.5 < |\eta| < 2.7$.

- **Calorimeter-tagged**: An ID track is identified as a muon if it can be associated to an energy deposit in the calorimeter compatible with a minimising ionising particle. These muons have the lowest purity of all and are primarily used to recover acceptance in the partially instrumented region of the MS for $|\eta| < 0.1$ with a track $p_{\mathrm{T}} > 15\,\mathrm{GeV}$. The muon track parameters are assigned using the ID track.

A.4 Tag-And-Probe Method

The tag-and-probe method is a data-driven technique used for measuring the efficiency of a set of selection criteria. It relies on the preparation of an unbiased sample of *probe* objects, from which the efficiencies of the requirements under study can be calculated. Events are selected by means of an independent and well defined *tag* object which satisfies a set of strict selection criteria. This study uses the invariant mass distribution of the well-known Standard Model process $Z \to \ell\ell$ to estimate the efficiency of the $H \to ZZ^{(*)} \to 4\ell$ selection criteria on probe leptons.

A.4.1 Event Selection

Dilepton events were selected with a combination of the relevant single-lepton triggers, identical to those used in the main analysis, and must contain a primary vertex with at least three associated tracks. For the 8 TeV dataset the p_{T} threshold of the single-muon triggers and E_{T} threshold for the single-electron triggers were each 24 GeV.

To remove bias in the selection of the probe, the first reconstructed lepton is always taken to be the tag. If that lepton fails to satisfy the tag requirements the event is discarded. The tag must pass the appropriate lepton identification with p_{T} or $E_{\mathrm{T}} > 26\,\mathrm{GeV}$, to ensure fully efficient triggering, and longitudinal impact parameter with respect to the primary vertex of less than 10 mm, to assure association to the primary vertex. The tag must also be the lepton which triggered the event and have relative track isolation within a cone of $\Delta R < 0.2$ of less than 0.05.

A tag muon is required to be a combined muon satisfying the inner detector hit requirements and $|\eta| < 2.7$. Tag electrons must pass the LOOSE LH identification and in order to improve the signal-to-background ratio below the Z peak for low probe E_{T}, the $|\eta|$-range of the tag is made dependent on the selection range of the probe. This is achieved by selecting electron tags within the barrel region $|\eta| < 1.37$ when considering probes in the endcap acceptance of $1.37 < |\eta| < 2.47$, and when considering probes in the barrel acceptance of $|\eta| < 1.37$, tags must fall in the endcap region $1.37 < |\eta| < 2.47$. This approach satisfies the requirement to increase the signal significance at low invariant mass, while maintaining sufficient statistics.

The probe is the remaining highest p_{T} or E_{T} lepton passing the selection requirements of the $H \to ZZ^{(*)} \to 4\ell$ analysis. These requirements are that muons must be either combined or segment-tagged with $p_{\mathrm{T}} > 6\,\mathrm{GeV}$ and $|\eta| < 2.7$, calorimeter-tagged with $p_{\mathrm{T}} > 15\,\mathrm{GeV}$ and $|\eta| < 0.1$, or standalone with $p_{\mathrm{T}} > 6\,\mathrm{GeV}$ and $2.5 < |\eta| < 2.7$. Standalone muons must pass the Muon System hits requirements, while the others must satisfy the Inner Detector hits requirements. Probe electrons are required to pass the LOOSE LH identification with $E_{\mathrm{T}} > 7\,\mathrm{GeV}$ and $|\eta| < 2.47$.

Care is also taken to remove overlaps between lepton tracks. For the case where two electron candidates share the same Inner Detector track, the electron with the lowest E_{T} is removed from the selection. When electron and muon candidates share a common track, the electron is removed from the selection. Additionally standalone muons must have $\Delta R > 0.2$ from the closest segment-tagged muon. Having applied the tag and probe selection, dilepton tag-and-probe pairs are formed with a same flavour and opposite charge requirement.

A.4.2 Isolation and Impact Parameter Cuts

Described here are the additional isolation and impact parameter cuts applied to muons and electrons in the $H \to ZZ^{(*)} \to 4\ell$ selection.

- **Impact parameter significance** ($|d_0|/\sigma_{d_0}$): the significance of the transverse impact parameter of the track with respect to the primary vertex, where d_0 is the distance of closest approach on the transverse plane and σ_{d_0} the corresponding uncertainty. For muons this must be less than 3.5 and less than 6.5 for electrons.

- **Relative track isolation**: the sum of the transverse momenta of tracks included in a cone of size $\Delta R = 0.2$ around the lepton, excluding the lepton track, divided by the transverse momentum of the track must be less than 0.15.

- **Relative calorimetric isolation**: for electrons it is computed as the sum of the cluster transverse energies deposited in the calorimeter inside a cone of size $\Delta R = 0.2$ around the electron, divided by the electron E_{T} and must be less than 0.2. For muons it is defined as the sum of the calorimeter cells inside a cone of size $\Delta R = 0.2$ around the muon direction, divided by the muon p_{T} and must be less than 0.3 (0.15 in the case of a standalone muon).

A.4.3 Fit Procedure

A fit to the invariant mass distribution of the tag-and-probe pairs is performed in the mass range 66–116 GeV. In order to minimize the uncertainty of the background estimation, the signal-like lepton yield is estimated within a narrow mass window extending 5 GeV above and below the Z mass peak, taken to be 91.0 GeV in the context of this study. The efficiency estimate is achieved by comparing the yields in this mass window before and after the application of the additional isolation and impact parameter cuts.

The efficiencies are determined in binned intervals of the probe electron E_{T} and muon p_{T} separately for probe leptons in either the barrel or endcap detector regions. For muons (electrons) the barrel region is defined as $|\eta| < 1.05$ ($|\eta| < 1.37$) and the endcap region as $1.05 < |\eta| < 2.7$ ($1.37 < |\eta| < 2.47$). Additionally efficiencies are estimated for data binned in N_{vtx}.

The data fit model is comprised of templates for the $Z \to \ell\ell$ signal and background contributions, obtained from the data samples covered in Section A.2. The $Z \to \ell\ell$ signal template as well as the $t\bar{t}$ and $Z \to \tau\tau$ background templates are obtained from MC, while the QCD background is described using a template from data of the same charge combination invariant mass distribution before the application of the additional selection cuts. The normalisation for both $t\bar{t}$ and $Z \to \tau\tau$ backgrounds is fixed to the integrated luminosity, but the $Z \to \ell\ell$ signal and QCD background normalisations are left free in the fit.

The signal-like event yield in data is therefore determined as the total sum of events in data, subtracting the contributions of each of the background yields in the given mass window. For MC it is possible to obtain an estimate of the signal event yield directly from the $Z \to \ell\ell$ template and therefore no fit is required. The efficiency is simply computed as the signal yield for probe leptons surviving the selection cuts, divided by the yield before the selection in the mass window. Finally, the scale factors are obtained by simply taking the ratio of the data and MC efficiencies.

A demonstration of the fitting procedure is shown in Figure A.1 for probe electrons with transverse energy between 11 GeV and 15 GeV. Presented are the results of the fits on the opposite and same charge combination distributions before and after applying all the isolation and impact parameter cuts. The total fit model, shown as a solid red line, is found to describe well the invariant mass distribution of the tag-and-probe pairs observed in data, both before and after the selection cuts. Additionally each component of the model is shown, where the backgrounds are marked as dashed lines and the $Z \rightarrow ee$ signal is shown as a blue solid line. It is apparent that particularly the QCD background is significantly reduced after the application of the additional selection cuts.

Figures A.2 and A.3 show the fits for some example distributions after the application of the additional selection cuts for intervals of the probe p_{T} or E_{T} and N_{vtx} for probe muons and electrons respectively. The backgrounds are shown to be relatively small and the QCD contributions become much less significant for higher p_{T} or E_{T} probes.

A.5 Systematic Uncertainties

Different sources of systematic uncertainty are taken into account in the efficiency and scale factor estimates, relating to particular choices made in the fitting procedure. For the evaluation of each systematic uncertainty, the standard fit procedure is followed and the difference each effect has on the result is evaluated independently. The sources considered are as follows:

- **Mass window:** the mass window used is varied from the standard 5 GeV window above and below the Z mass peak to larger windows of 15 and 25 GeV.
- **Fit range:** the standard fit range of 66–116 GeV is expanded to 56–126 GeV.
- Z **signal shape:** an alternative MC sample is used for the signal templates. This sample was generated using ALPGEN interfaced to Herwig [196] for parton shower hadronisation and to Jimmy [197] for the underlying event simulation, using the AUET2 tune [198] and the CTEQ6L1 PDF set.

The final uncertainty for each bin is obtained by combining the largest estimate of each uncertainty in quadrature, where typically the most dominant source comes from the mass window used. The contribution from different mass windows is not included in the efficiency systematics since the actual efficiency is varying when changing the window. This is particularly important in the lowest p_{T} bin, where in numerous cases the leptons have suffered final state radiation. However, this contribution is included on the systematic uncertainty evaluated for the scale factor.

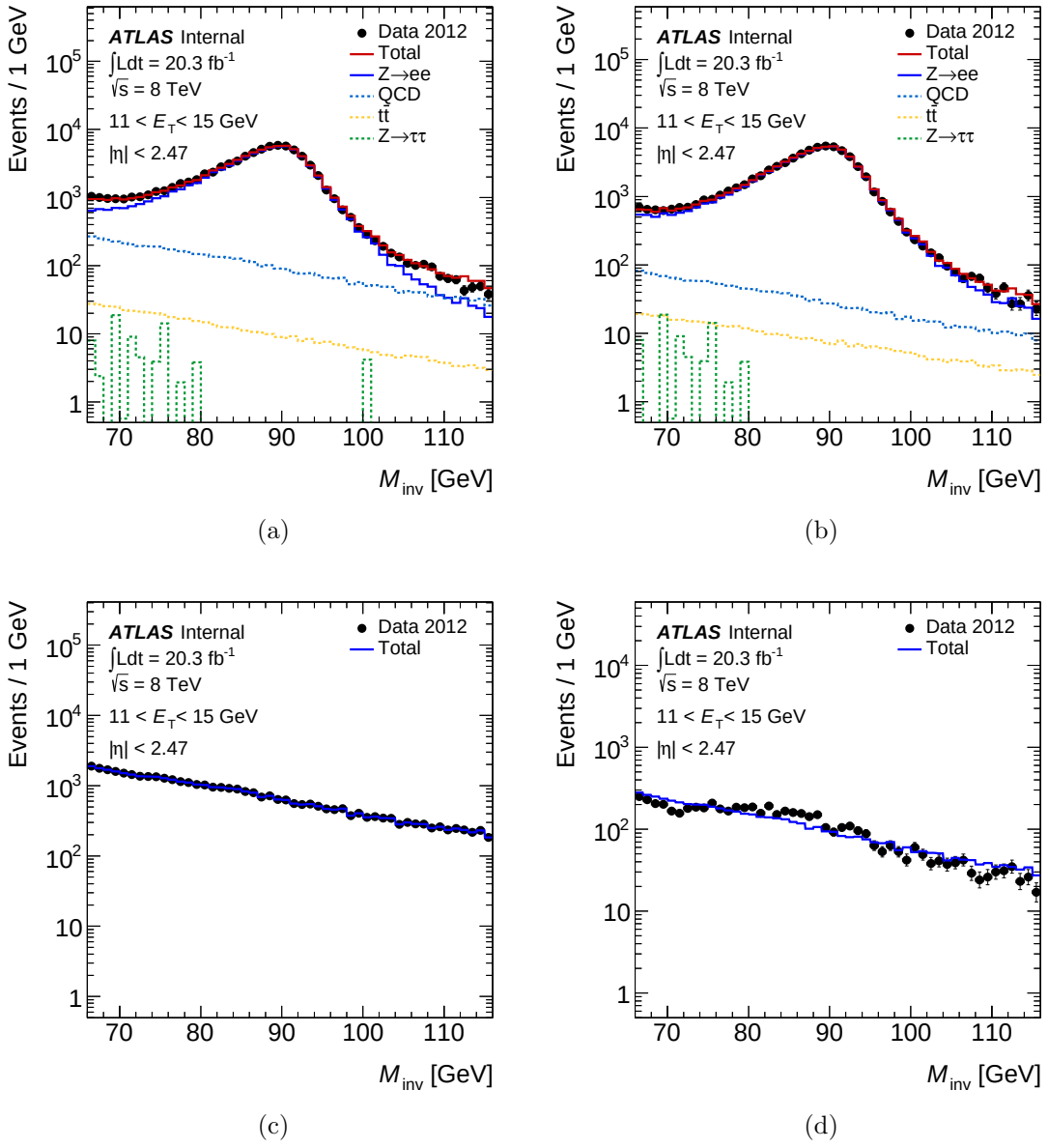

Figure A.1: The invariant mass distributions for the tag and probe pairs in data, where the probe has a transverse energy between 11 GeV and 15 GeV. The distributions for opposite charge combinations before (a) and after (b) applying all cuts, and for the same charge combinations before (c) and after (d) all cuts. The distribution tails and background composition are clearly illustrated by the logarithmic scale. The QCD background shape derived from the same charge data is shown by teal dashed lines and the green and yellow dashed lines correspond to the $Z \to \tau\tau$ and $t\bar{t}$ background contributions respectively. The total fit is given as a solid red line.

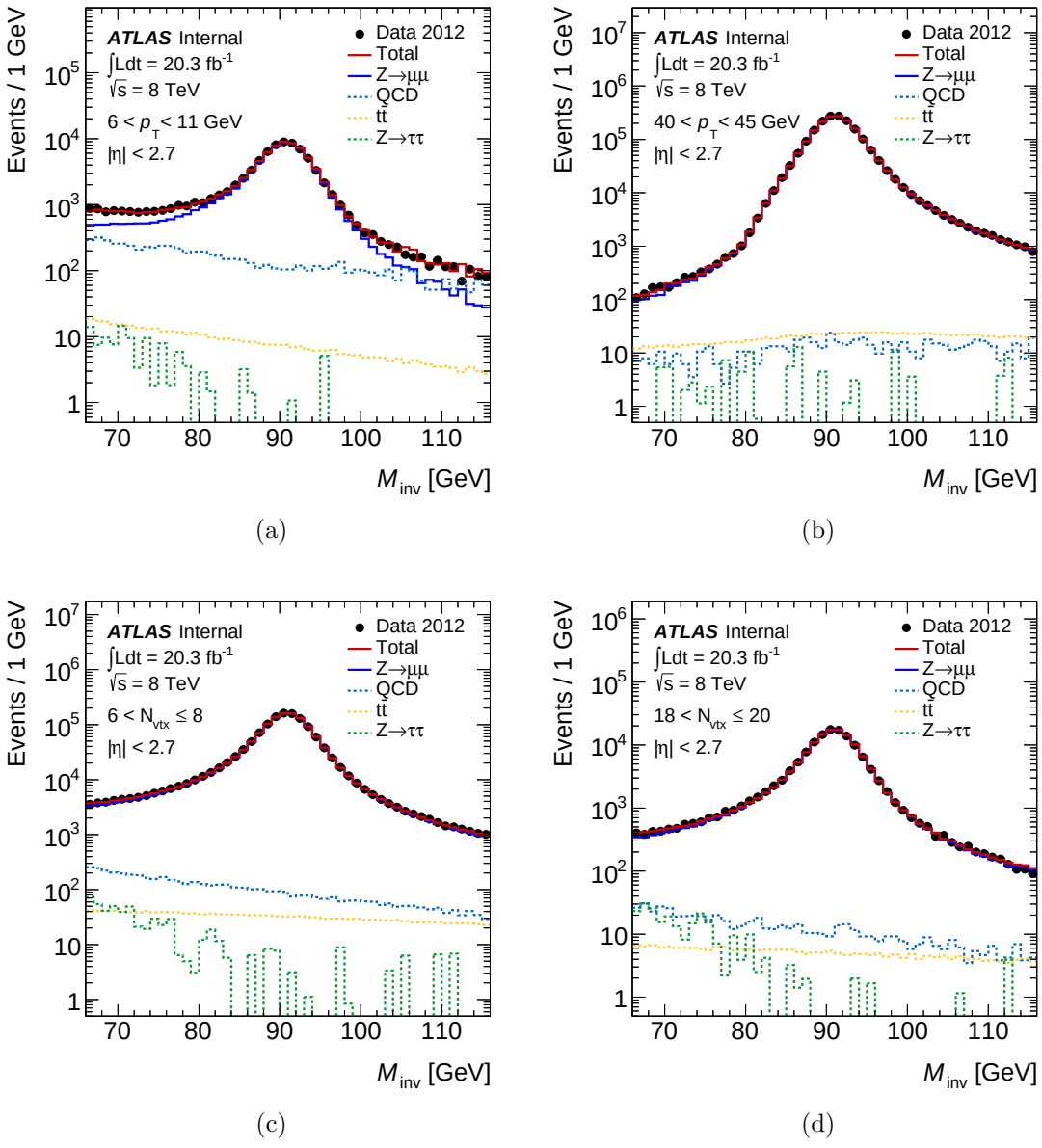

Figure A.2: The fits to the tag-and-probe invariant mass of the $Z \to \mu\mu$ signal after all the impact parameter significance and isolation cuts are applied. The results are given for the p_{T} bins (a) $6 < p_{\mathrm{T}} < 11\,\mathrm{GeV}$ and (b) $40 < p_{\mathrm{T}} < 45\,\mathrm{GeV}$, as well as for bins of the number of reconstructed primary vertices (c) $6 < N_{\mathrm{vtx}} < 8$ and (d) $18 < N_{\mathrm{vtx}} < 20$ in the region $|\eta| < 2.47$.

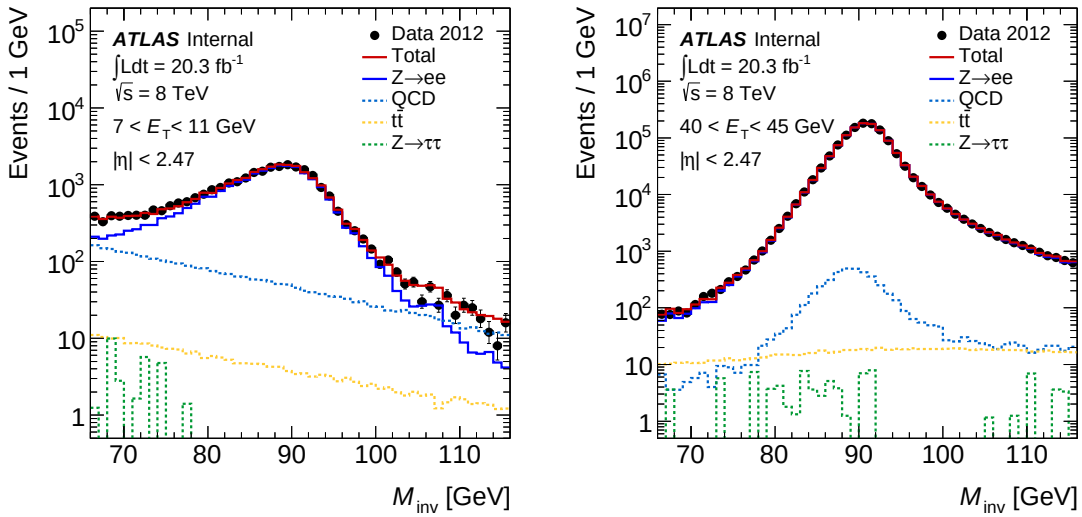

(a)

(b)

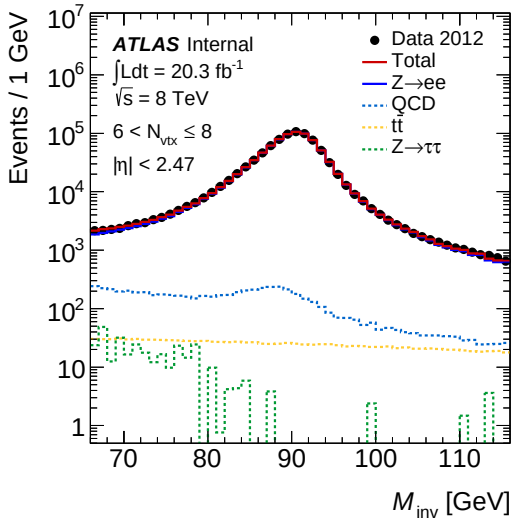

(c)

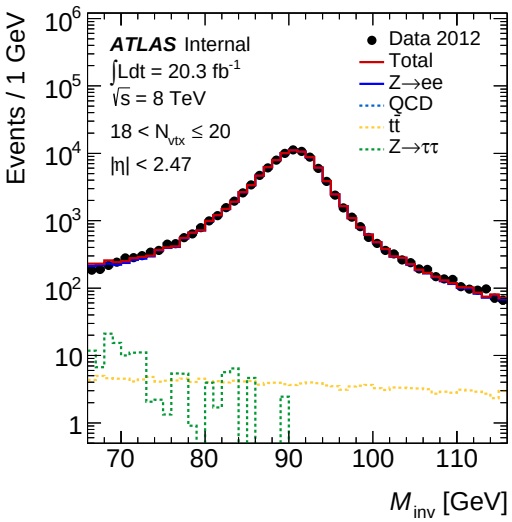

(d)

Figure A.3: The fits to the tag-and-probe invariant mass of the $Z \to ee$ signal after all the impact parameter significance and isolation cuts are applied. The results are given for the p_{T} bins (a) $7 < p_{\mathrm{T}} < 11\,\mathrm{GeV}$ and (b) $40 < p_{\mathrm{T}} < 45\,\mathrm{GeV}$, as well as for bins of the number of reconstructed primary vertices (c) $6 < N_{\mathrm{vtx}} < 8$ and (d) $18 < N_{\mathrm{vtx}} < 20$ in the region $|\eta| < 2.47$.

A.6 Results

The efficiency estimates for both data and MC can be seen in Figure A.4 as a function of the probe muon p_{T} and the probe electron E_{T} for each of the isolation and impact parameter cuts independently. The effect of the impact parameter cut on probe muons and electrons is less than 1% even for the lowest p_{T} or E_{T} bin. The largest efficiency loss observed for probe muons results from the track isolation cut, while for probe electrons this occurs after the application of the calorimeter isolation cut.

Figure A.5 shows the efficiency estimates for both data and MC with all the isolation and impact parameter cuts combined, in different detector regions as a function of the probe p_{T} or E_{T}. The efficiencies for probe muons remain significantly higher in the endcap region compared to barrel region for $p_{\mathrm{T}} < 20\,\mathrm{GeV}$, while the a similar but smaller effect is present for electrons with $E_{\mathrm{T}} < 15\,\mathrm{GeV}$. For the inclusive cases the selection efficiency is around 94% for the lowest p_{T} muons and 91% for the lowest E_{T} electrons.

Another important consideration is how the efficiency of the cuts depends on the pile-up. This is demonstrated in Figure A.6 as a function of N_{vtx}. The trend is that as the pile-up increases the efficiency of the cuts reduces, however the effect is very small at approximately 0.5% over the full range of the sample in either case.

In general the efficiency results for data and MC are found to be fairly consistent within uncertainties. The results for the scale factors for the barrel and endcap regions as a function of the probe muon p_{T} and electron E_{T} are shown in Figure A.7 with their total uncertainties. A full break down of these results, including their statistical and systematic uncertainties is given in Table A.1, inclusively as well as for the barrel and endcap. The differences between the data and MC are found to be much less than 1% in almost all cases. The largest differences are observed for electrons in the endcap region of the detector for $E_{\mathrm{T}} < 15\,\mathrm{GeV}$ and also have some of the largest systematic uncertainties.

The results for the scale factors and their total uncertainties as a function of N_{vtx} are given in Figure A.8. The agreement between data and simulation on the pile-up dependence of the cuts is excellent with small uncertainties estimated for both muons and electrons.

A.7 Summary

In all cases the scale factors obtained from the data and MC comparisons are found to be consistent with unity. As a result, no scale factors are applied in the $H \to ZZ^{(*)} \to 4\ell$ analysis to correct for the additional isolation and impact parameter cuts and systematics are assigned based on the results of the tag-and-probe study.

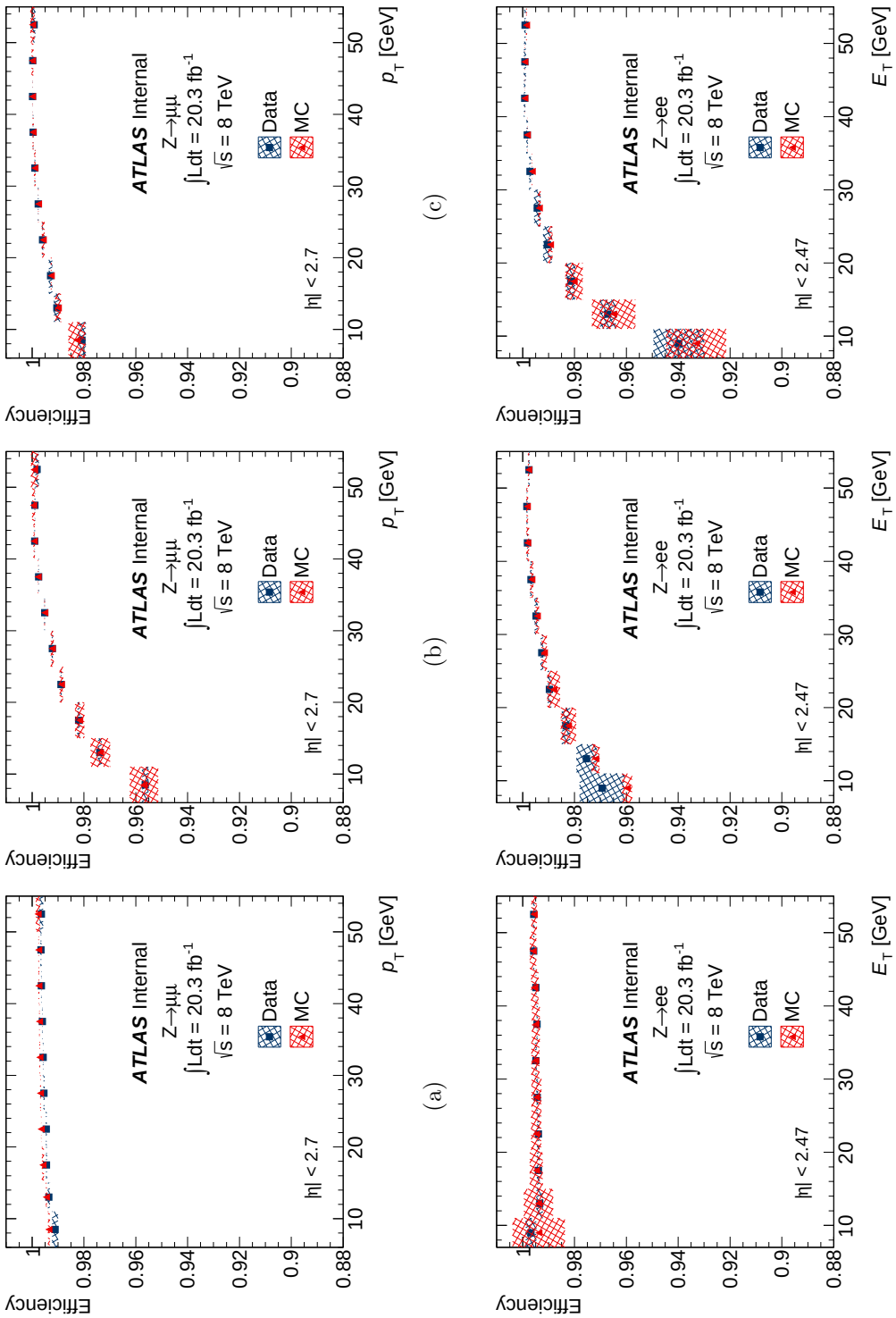

Figure A.4: The efficiencies measured in data and MC for probe muons (electrons) after (a) ((d)) the impact parameter significance cut, (b) ((e)) the track isolation cut, and (c) ((f)) the calorimeter isolation cut are applied individually. The last bin represents the efficiency for probes with transverse energy or momenta greater than 50 GeV.

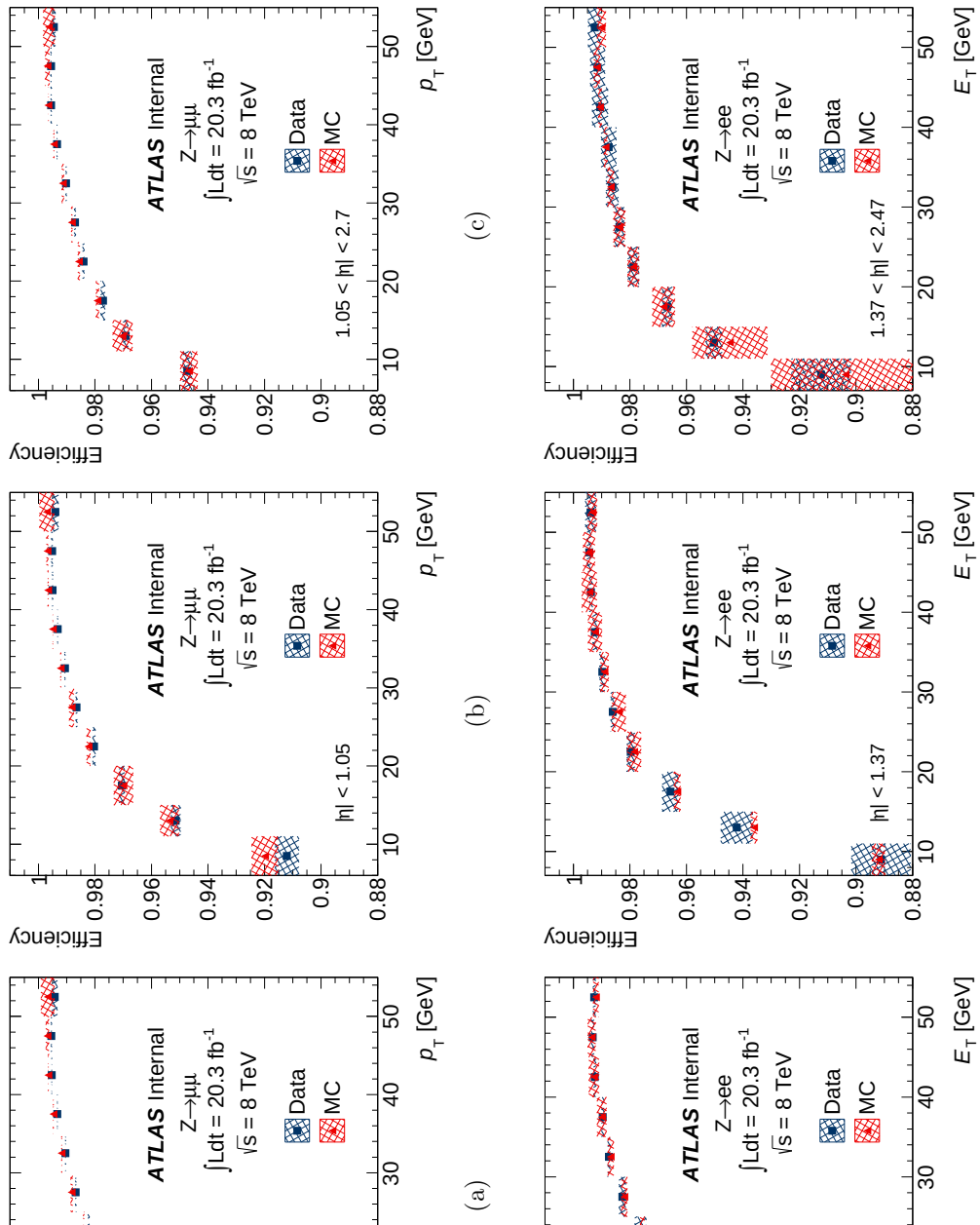

Figure A.5: The efficiencies measured in data and MC for probe muons (electrons) in (a) ((d)) the full acceptance range, (b) ((e)) the barrel region, and (c) ((f)) the endcap region. The last bin represents the efficiency for probes with transverse energy or momenta greater than 50 GeV.

Table A.1: Scale factors and their statistical and systematic uncertainties for the barrel, endcap and inclusive detector regions in intervals of muon probe p_{T} and electron probe E_{T}.

p_{T} or E_{T}	Barrel			Endcap			Inclusive		
(GeV)	SF	stat.	syst.	SF	stat.	syst.	SF	stat.	syst.
				Muons					
6 - 11	0.992	0.003	0.010	0.999	0.001	0.004	0.998	0.001	0.004
11 - 15	0.998	0.001	0.006	1.000	0.001	0.004	0.998	0.001	0.005
15 - 20	1.001	0.001	0.004	1.000	0.000	0.002	0.999	0.000	0.003
20 - 25	0.998	0.000	0.001	1.000	0.000	0.001	0.998	0.000	0.001
25 - 30	0.998	0.000	0.001	1.000	0.000	0.001	0.999	0.000	0.001
30 - 35	0.998	0.000	0.001	0.999	0.000	0.000	0.999	0.000	0.000
35 - 40	0.998	0.000	0.000	0.999	0.000	0.000	0.999	0.000	0.000
40 - 45	0.998	0.000	0.000	0.999	0.000	0.000	0.999	0.000	0.000
45 - 50	0.998	0.000	0.000	0.999	0.000	0.001	0.999	0.000	0.001
> 50	0.997	0.000	0.004	0.998	0.000	0.002	0.998	0.000	0.003
				Electrons					
7 - 11	0.999	0.004	0.013	1.010	0.004	0.025	1.012	0.003	0.027
11 - 15	1.007	0.002	0.007	1.006	0.002	0.012	1.005	0.002	0.016
15 - 20	1.003	0.001	0.004	0.999	0.001	0.004	1.000	0.001	0.006
20 - 25	1.001	0.001	0.002	1.000	0.000	0.002	1.001	0.000	0.002
25 - 30	1.002	0.000	0.003	1.000	0.000	0.002	1.001	0.000	0.002
30 - 35	1.001	0.000	0.002	0.999	0.000	0.002	1.001	0.000	0.001
35 - 40	1.000	0.000	0.003	0.999	0.000	0.003	1.000	0.000	0.001
40 - 45	0.999	0.000	0.003	1.000	0.000	0.003	1.000	0.000	0.001
45 - 50	1.000	0.001	0.003	1.000	0.001	0.004	1.000	0.000	0.001
> 50	1.001	0.001	0.003	1.002	0.001	0.004	1.001	0.000	0.001

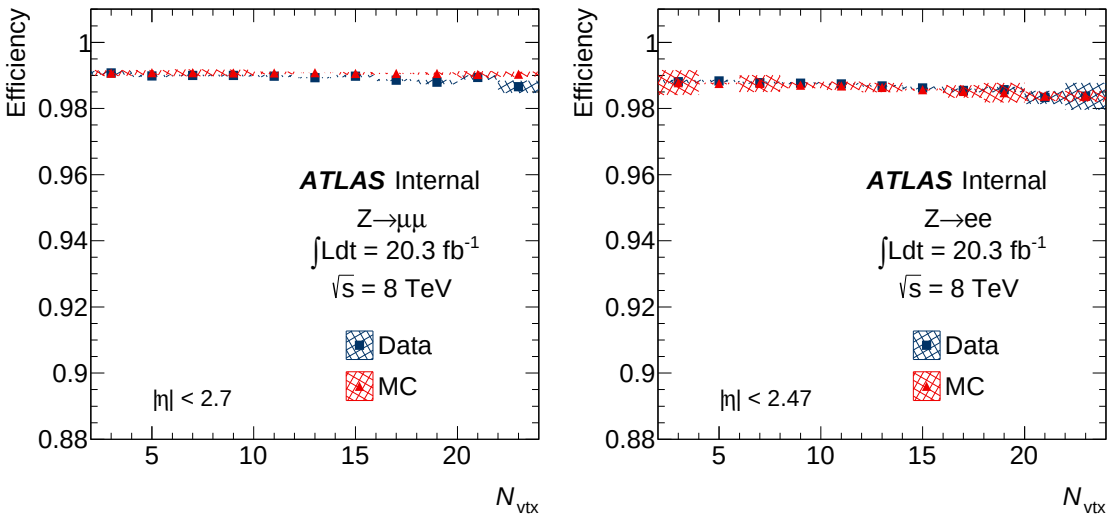

(a) (b)

Figure A.6: The efficiencies measured in data and MC after the application of all the isolation and impact parameter cuts as a function of the number of reconstructed primary vertices for (a) probe muons and (b) probe electrons.

A nuisance parameter is applied to the measurements made in the $H \to ZZ^{(*)} \to 4\ell$ channel to take into account the largest systematic uncertainties for electrons, associated with the first two E_{T} bins as shown in Table A.1. For electrons in the barrel region an uncertainty of 1.3% is assigned for $7 < E_{\mathrm{T}} < 11\,\mathrm{GeV}$ and 0.7% for the interval $11 < E_{\mathrm{T}} < 15\,\mathrm{GeV}$. For electrons in the endcap region an uncertainty of 2.5% is assigned for $7 < E_{\mathrm{T}} < 11\,\mathrm{GeV}$ and 1.2% for $11 < E_{\mathrm{T}} < 15\,\mathrm{GeV}$. The systematic uncertainty associated with the isolation and impact parameter cuts on the signal yield for the $4e$, $2\mu 2e$ and $2e2\mu$ final states as a function of the SM Higgs boson mass m_H is shown in Figure A.9. For a Higgs boson mass $m_H = 125\,\mathrm{GeV}$ the systematic uncertainties on the expected signal yield is 1.18% for decays to $4e$, 0.07% for decays to $2e2\mu$, and 1.10% for decays to $2\mu 2e$.

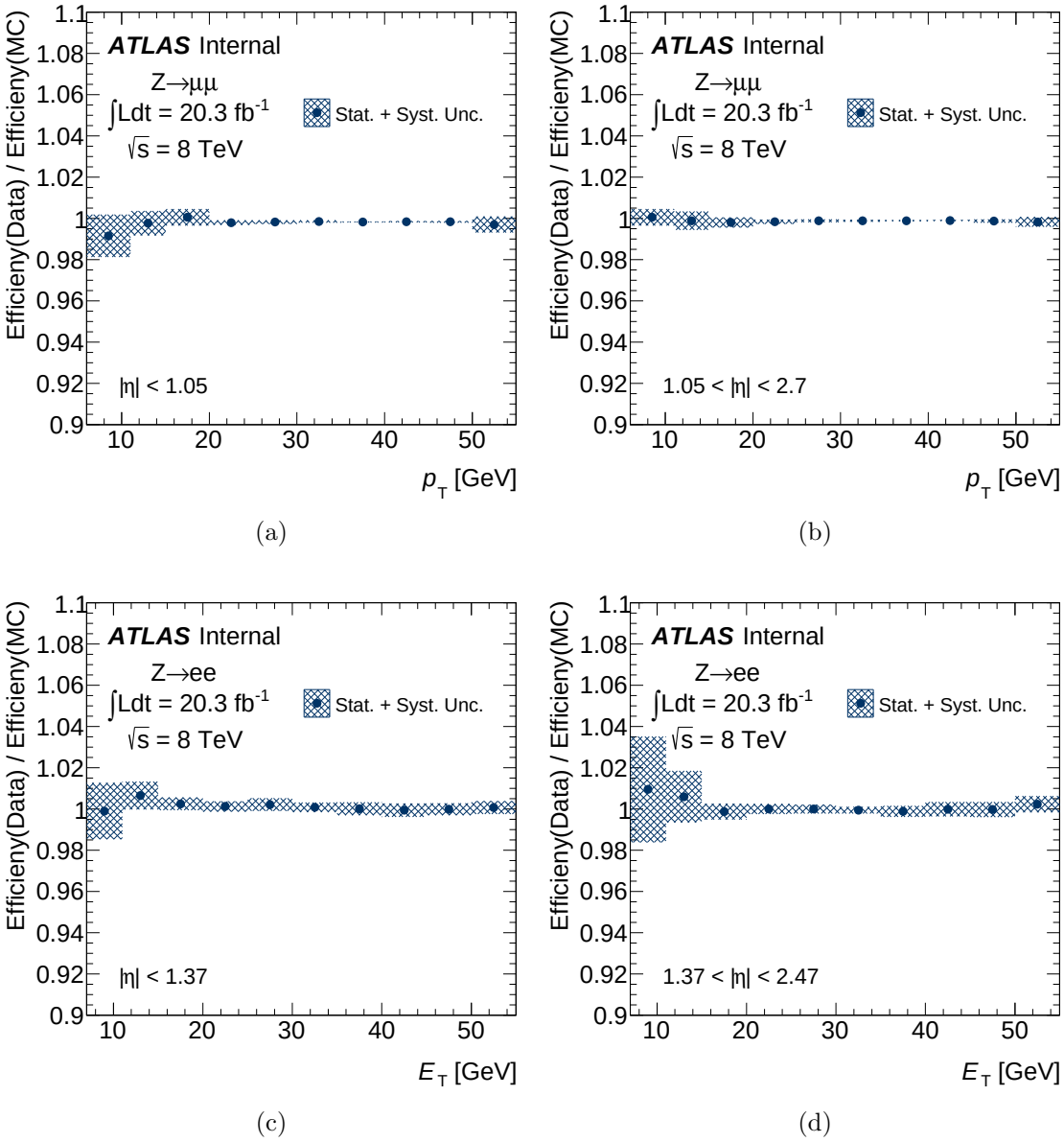

Figure A.7: The ratios between the efficiencies measured in data and simulation for electrons and muons after all the impact parameter significance and isolation cuts are applied, shown for (a) and (c) the barrel, and (b) and (d) endcap regions.

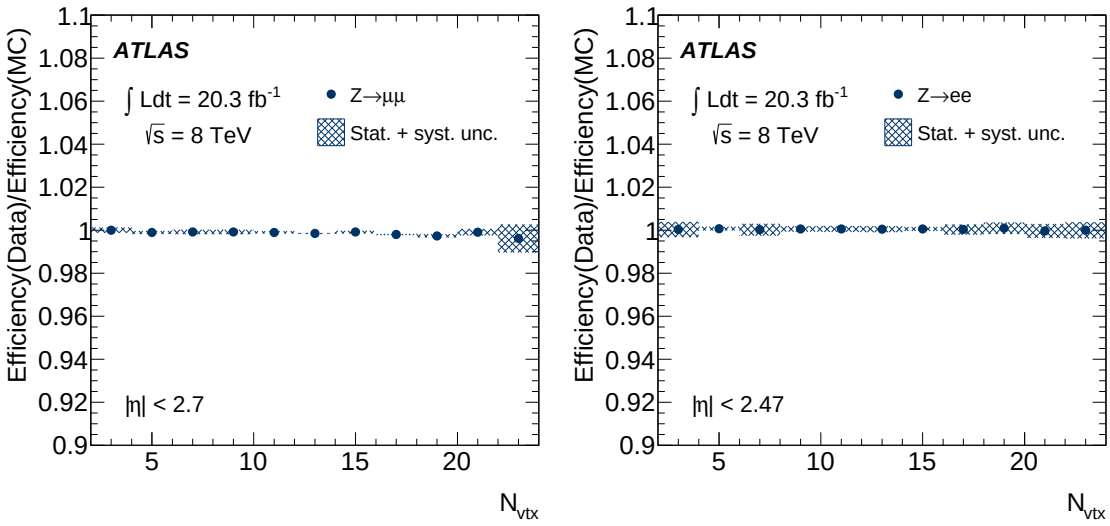

(a) (b)

Figure A.8: The ratios between the efficiencies measured in data and simulation for (a) muons and (b) electrons after all the impact parameter significance and isolation cuts are applied as a function of the number of reconstructed primary vertices in the event.

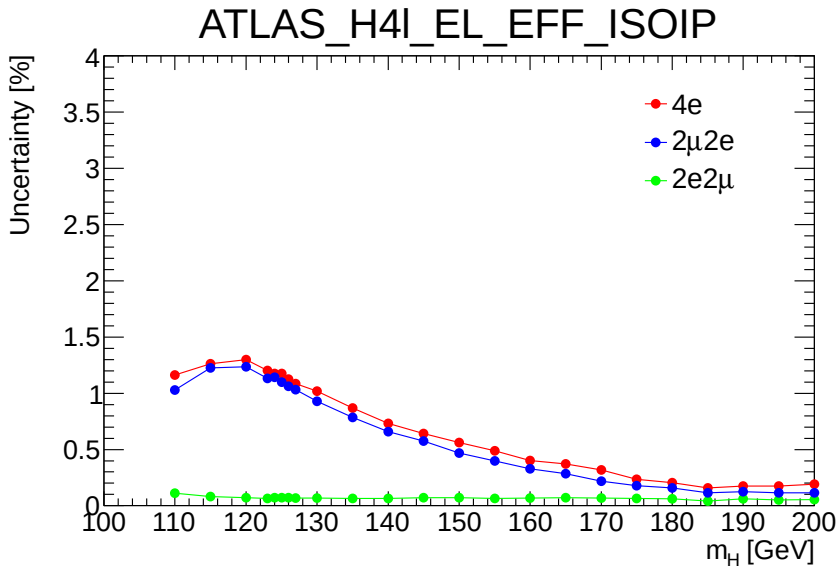

Figure A.9: Systematic uncertainties on the signal yield of the electron isolation and impact parameter cut efficiency nuisance parameter (`ATLAS_H4l_EL_EFF_ISOIP`) as a function of the Higgs mass m_H for the $4e$, $2\mu 2e$ and $2e2\mu$ final states [7].

APPENDIX B

ANALYSIS PAPER

Here follows the $hh \to b\bar{b}\tau\tau$ analysis and its combination with the other searches for Higgs boson pair production presented in this thesis, as published in
Phys. Rev. D **92**, 092004 (2015)

PHYSICAL REVIEW D **92,** 092004 (2015)

Searches for Higgs boson pair production in the $hh \to bb\tau\tau$, $\gamma\gamma WW^*$, $\gamma\gamma bb$, $bbbb$ channels with the ATLAS detector

G. Aad *et al.*[*]
(ATLAS Collaboration)
(Received 16 September 2015; published 5 November 2015)

Searches for both resonant and nonresonant Higgs boson pair production are performed in the $hh \to bb\tau\tau$, $\gamma\gamma WW^*$ final states using 20.3 fb^{-1} of pp collision data at a center-of-mass energy of 8 TeV recorded with the ATLAS detector at the Large Hadron Collider. No evidence of their production is observed and 95% confidence-level upper limits on the production cross sections are set. These results are then combined with the published results of the $hh \to \gamma\gamma bb$, $bbbb$ analyses. An upper limit of 0.69 (0.47) pb on the nonresonant hh production is observed (expected), corresponding to 70 (48) times the SM $gg \to hh$ cross section. For production via narrow resonances, cross-section limits of hh production from a heavy Higgs boson decay are set as a function of the heavy Higgs boson mass. The observed (expected) limits range from 2.1 (1.1) pb at 260 GeV to 0.011 (0.018) pb at 1000 GeV. These results are interpreted in the context of two simplified scenarios of the Minimal Supersymmetric Standard Model.

DOI: 10.1103/PhysRevD.92.092004 PACS numbers: 12.60.Fr, 14.80.Bn, 14.80.Ec

I. INTRODUCTION

The Higgs boson discovered at the LHC in 2012 [1,2] opens a window for testing the scalar sector of the Standard Model (SM) and its possible extensions. Since the discovery, significant progress has been made in measuring its coupling strengths to fermions and vector bosons [3–6] as well as in studying its spin and its charge-conjugate and parity (CP) properties [7,8]. All results are consistent with those expected for the SM Higgs boson (here denoted by h). Within the SM, the existence of the Higgs boson is a consequence of the electroweak symmetry breaking (EWSB). This also predicts self-coupling between Higgs bosons, the measurement of which is crucial in testing the mechanism of EWSB. The self-coupling is one mechanism for Higgs boson pair production as shown in Fig. 1(a). Higgs boson pairs can also be produced through other interactions such as the Higgs-fermion Yukawa interactions [Fig. 1(b)] in the Standard Model. These processes are collectively referred to as nonresonant production in this paper.

Higgs boson pair production at the LHC as a probe of the self-coupling has been extensively studied in the literature [9–13]. One conclusion [14] is that the data collected so far (approximately 25 fb^{-1} in total) are insensitive to the self-coupling in the SM, because of the expected small signal rates [15–17] and large backgrounds. However, it is essential to quantify the sensitivity of the current data set and to develop tools for future measurements. Moreover, physics beyond the Standard Model (BSM) can potentially enhance the production rate and alter the event kinematics. For example, in the Minimal Supersymmetric Standard Model (MSSM) [18], a heavy CP-even neutral Higgs boson H can decay to a pair of lighter Higgs bosons. Production of H followed by its decay $H \to hh$ would lead to a new resonant process of Higgs boson pair production, in contrast to the nonresonant hh production predicted by the SM (Fig. 1). In composite Higgs models such as those discussed in Refs. [19,20], increased production of nonresonant Higgs boson pairs is also expected.

Both the ATLAS and CMS collaborations have searched for nonresonant and/or resonant Higgs boson pair production [21–23]. In particular, ATLAS has published the results of searches in the $hh \to \gamma\gamma bb$ [21] and $hh \to bbbb$ [22] decay channels.[1] In this paper, searches in two additional hh decay final states, $bb\tau\tau$ and $\gamma\gamma WW^*$, are reported. For the $hh \to bb\tau\tau$ analysis, one tau lepton is required to decay to an electron or a muon, collectively referred to as ℓ, and the other tau lepton decays to hadrons (τ_{had}). For $hh \to \gamma\gamma WW^*$, the $h \to WW^* \to \ell\nu qq'$ decay signature is considered in this study. The results of these new analyses are combined with the published results of $hh \to \gamma\gamma bb$ and $hh \to bbbb$ for both nonresonant and resonant production. The resonance mass m_H considered in this paper ranges from 260 to 1000 GeV. The lower bound is dictated by the $2m_h$ threshold while the upper bound is set by the search range of the $hh \to bb\tau\tau$ analysis. The light Higgs boson mass m_h is assumed to be 125.4 GeV, the central value of the ATLAS measurement [24]. At this mass value, the SM predictions [25–27] for the

[*]Full author list given at the end of the article.

[1]Notations indicating particle charges or antiparticles are generally omitted throughout this paper.

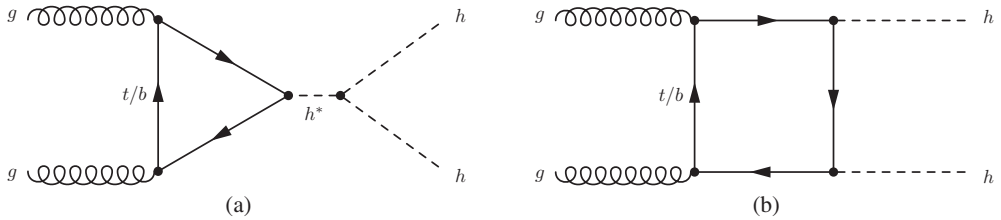

FIG. 1. Leading-order Feynman diagrams of the nonresonant production of Higgs boson pairs in the Standard Model through (a) the Higgs boson self-coupling and (b) the Higgs-fermion Yukawa interactions only.

decay fractions of $hh \to bbbb$, $bb\tau\tau$, $bb\gamma\gamma$ and $\gamma\gamma WW^*$ are, respectively, 32.6%, 7.1%, 0.26%, and 0.10%. The resonant search assumes that gluon fusion is the production mechanism for a heavy Higgs boson that can subsequently decay to a pair of lighter Higgs bosons, i.e., $gg \to H \to hh$. Furthermore, the heavy Higgs boson is assumed to have a width significantly smaller than the detector resolution, which is approximately 1.5% in the best case (the $hh \to \gamma\gamma bb$ analysis). The potential interference between nonresonant and resonant production is ignored.

This paper is organized as follows. For the $hh \to bb\tau\tau$ and $hh \to \gamma\gamma WW^*$ analyses, data and Monte Carlo (MC) samples are described in Sec. II and the object reconstruction and identification are outlined in Sec. III. In Secs. IV and V, the separately published $hh \to \gamma\gamma bb$ and $hh \to bbbb$ analyses are briefly summarized. The $hh \to bb\tau\tau$ and $hh \to \gamma\gamma WW^*$ analyses including event selection, background estimations, and systematic uncertainties are presented in Secs. VI and VII, respectively. The statistical and combination procedure is described in Sec. VIII. The results of the $hh \to bb\tau\tau$ and $hh \to \gamma\gamma WW^*$ analyses, as well as their combinations with the published analyses are reported in Sec. IX. The implications of the resonant search for two specific scenarios of the MSSM, hMSSM [28,29], and low-tb-high [30] are discussed in Sec. X. These scenarios make specific assumptions and/or choices of MSSM parameters to accommodate the observed Higgs boson. Finally, a summary is given in Sec. XI.

II. DATA AND MONTE CARLO SAMPLES

The data used in the searches were recorded in 2012 with the ATLAS detector at the Large Hadron Collider in proton-proton collisions at a center-of-mass energy of 8 TeV and correspond to an integrated luminosity of 20.3 fb^{-1}. The ATLAS detector is described in detail in Ref. [31]. Only data recorded when all subdetector systems were properly functional are used.

Signal and background MC samples are simulated with various event generators, each interfaced to Pythia v8.175 [32] for parton showers, hadronization and underlying-event simulation. Parton distribution functions (PDFs) CT10 [33] or CTEQ6L1 [34] for the proton are used depending on the generator in question. MSTW2008 [35] and NNPDF [36] PDFs are used to evaluate systematic uncertainties. Table I gives a brief overview of the event

TABLE I. List of MC generators and parton distribution functions of the signal and background processes used by the $hh \to bb\tau\tau$ and $hh \to \gamma\gamma WW^*$ analyses. SM cross sections used for the normalization are also given. For the WZ and ZZ processes, contributions from γ^* are included and the cross sections quoted are for $m_{Z/\gamma^*} > 20$ GeV.

Process	Event generator	PDF set	Cross section [pb]
Background processes			
V + jets	Alpgen+Pythia8	CTEQ6L1	normalized to data
Diboson: WW	Powheg+Pythia8	CT10	55.4
Diboson: WZ	Powheg+Pythia8	CT10	22.3
Diboson: ZZ	Powheg+Pythia8	CT10	7.3
$t\bar{t}$	Powheg+Pythia8	CT10	253
Single top: t-channel	AcerMC+Pythia8	CTEQ6L1	87.8
Single top: s-channel	Powheg+Pythia8	CT10	5.6
Single top: Wt	Powheg+Pythia8	CT10	22.0
$gg \to h$	Powheg+Pythia8	CT10	19.2
$q\bar{q}' \to q\bar{q}'h$	Powheg+Pythia8	CT10	1.6
$q\bar{q} \to Vh$	Pythia8	CTEQ6L1	1.1
$q\bar{q}/gg \to t\bar{t}h$	Pythia8	CTEQ6L1	0.13
Signal processes			
Nonresonant $gg \to hh$	MadGraph5+Pythia8	CTEQ6L1	0.0099
Resonant $gg \to H \to hh$	MadGraph5+Pythia8	CTEQ6L1	model dependent

generators, PDFs and cross sections used for the $hh \to bb\tau\tau$ and $hh \to \gamma\gamma WW^*$ analyses. All MC samples are passed through the ATLAS detector simulation program [37] based on GEANT4 [38].

Signal samples for both nonresonant and resonant Higgs boson pair production are generated using the leading-order MadGraph5 v1.5.14 [39] program. The nonresonant production is modeled using the SM DiHiggs model [40,41] while the resonant production is realized using the HeavyScalar model [42], both implemented in MadGraph5. The heavy scalar H is assumed to have a narrow decay width of 10 MeV, much smaller than the experimental resolution. The SM prediction for the nonresonant $gg \to hh$ production cross section is 9.9 ± 1.3 fb [17] with $m_h = 125.4$ GeV from the next-to-next-to-leading-order calculation in QCD.

Single SM Higgs boson production is considered as a background. The Powheg r1655 generator [43–45] is used to produce gluon fusion (ggF) and vector-boson fusion (VBF) events. This generator calculates QCD corrections up to next-to-leading order (NLO), including finite bottom- and top-quark mass effects [46]. The Higgs boson transverse momentum (p_{T}) spectrum of the ggF process is matched to the calculated spectrum at next-to-next-to-leading order (NNLO) and next-to-next-to-leading logarithm (NNLL) [47] in QCD corrections. Events of associated production $q\bar{q} \to Vh$ (here $V = W$ or Z) and $q\bar{q}/gg \to t\bar{t}h$ are produced using the Pythia8 generator [32]. All of these backgrounds are normalized using the state-of-the-art theoretical cross sections (see Table I) and their uncertainties compiled in Refs. [25–27].

The Alpgen v2.1.4 program [48] is used to produce the V + jets samples. The Powheg generator is used to simulate top quark pair production ($t\bar{t}$) as well as the s-channel and Wt processes of single top production; the t-channel process of single top production is simulated using the AcerMC v38 program [49]. The $t\bar{t}$ cross section has been calculated up to NNLO and NNLL in QCD corrections [50]. Cross sections for the three single-top processes have been calculated at (approximate) NNLO accuracy [51–53]. The Powheg generator is used to simulate diboson backgrounds (WW, WZ, and ZZ). The diboson production cross sections are calculated at NLO in QCD corrections using the MCFM program [54,55].

III. OBJECT IDENTIFICATION

In this section, object reconstruction and identification for the $hh \to bb\tau\tau$ and $hh \to \gamma\gamma WW^*$ analyses are discussed. The $hh \to bb\tau\tau$ and $hh \to \gamma\gamma WW^*$ analyses are developed following the $h \to \tau\tau$ [6] and $h \to \gamma\gamma$ [56] studies of single Higgs bosons, respectively, and use much of their methodology.

Electrons are reconstructed from energy clusters in the electromagnetic calorimeter matched to tracks in the inner tracker. The calorimeter shower profiles of electron candidates must be consistent with those expected from electromagnetic interactions. Electron candidates are identified using tight and medium criteria [57] for the $hh \to bb\tau\tau$ and $hh \to \gamma\gamma WW^*$ analyses, respectively. The selected candidates are required to have transverse momenta[2] $p_{\mathrm{T}} > 15$ GeV and be within the detector fiducial volume of $|\eta| < 2.47$ excluding $1.37 < |\eta| < 1.52$, the transition region between the barrel and endcap calorimeters. Muons are identified by matching tracks or segments reconstructed in the muon spectrometer with tracks reconstructed in the inner tracker. They are required to have $p_{\mathrm{T}} > 10$ GeV and $|\eta| < 2.5$. Both the electrons and muons must satisfy calorimeter and track isolation requirements. The calorimeter isolation requires that the energy deposited in the calorimeter in a cone of size $\Delta R \equiv \sqrt{(\Delta\eta)^2 + (\Delta\phi)^2} = 0.2$ around the lepton (electron or muon), excluding the energy deposited by the lepton itself, is less than 6% (20%) of the p_{T} of the lepton for the $hh \to bb\tau\tau$ ($hh \to \gamma\gamma WW^*$) analysis. The track isolation is defined similarly: the scalar p_{T} sum of additional tracks originating from the primary vertex with $p_{\mathrm{T}} > 1$ GeV in a cone of size $\Delta R = 0.4$ around the lepton is required to be less than 6% (15%) of the p_{T} of the lepton track for the $hh \to bb\tau\tau$ ($hh \to \gamma\gamma WW^*$) analysis.

Photons are reconstructed from energy clusters in the electromagnetic calorimeter with their shower profiles consistent with electromagnetic showers. A significant fraction of photons convert into e^+e^- pairs inside the inner tracker. Thus photon candidates are divided into unconverted and converted categories. Clusters without matching tracks are considered as unconverted photons, while clusters matched to tracks consistent with conversions are considered as converted photons. Photon candidates must fulfill the tight identification criteria [58] and are required to have $p_{\mathrm{T}} > 25$ GeV and $|\eta| < 2.37$ (excluding the transition region $1.37 < |\eta| < 1.52$) and must satisfy both calorimeter and track isolation. The calorimeter isolation requires the additional energy in a cone of $\Delta R = 0.4$ around the photon candidate to be less than 6 GeV while the track isolation requires the scalar p_{T} sum of additional tracks in a cone of $\Delta R = 0.2$ around the photon to be less than 2.6 GeV.

Jets are reconstructed using the anti-k_t algorithm [59] with a radius parameter of $R = 0.4$. Their energies are corrected for the average contributions from pileup interactions. Jets are required to have $p_{\mathrm{T}} > 30$ GeV and $|\eta| < 4.5$. For the $hh \to \gamma\gamma WW^*$ analysis, a lower p_{T} requirement of 25 GeV is applied for jets in the central region of $|\eta| < 2.4$. To suppress contributions from pileup interactions, jets with $p_{\mathrm{T}} < 50$ GeV and within

[2]ATLAS uses a right-hand coordinate system with the interaction point as its origin and the beam line as its z axis. The x axis points to the center of the LHC ring and y axis points upwards. The pseudorapidity η is defined as $\eta = -\ln\tan(\theta/2)$, where θ is the polar angle measured with respect to the z axis. The transverse momentum p_{T} is calculated from the momentum p: $p_{\mathrm{T}} = p\sin\theta$.

the acceptance of the inner tracker ($|\eta| < 2.4$) must have over 50% of the scalar sum of the p_{T} of their associated tracks contributed by those originating from the primary vertex. Jets containing b-hadrons are identified using a multivariate algorithm (b-tagging) [60]. The algorithm combines information such as the explicit reconstruction of the secondary decay vertices and track impact-parameter significances. The operating point chosen for both $hh \to bb\tau\tau$ and $hh \to \gamma\gamma WW^*$ analyses has an efficiency of 80% for the b-quark jets in $t\bar{t}$ events.

Hadronically decaying τ candidates (τ_{had}) are reconstructed using clusters in the electromagnetic and hadronic calorimeters [61]. The tau candidates are required to have $p_{\mathrm{T}} > 20$ GeV and $|\eta| < 2.5$. The number of tracks with $p_{\mathrm{T}} > 1$ GeV associated with the candidates must be one or three and the total charge determined from these tracks must be ± 1. The tau identification uses calorimeter cluster as well as tracking-based variables, combined using a boosted-decision-tree method [61]. Three working points, labeled loose, medium, and tight [61], corresponding to different identification efficiencies are used. Dedicated algorithms that suppress electrons and muons misidentified as τ_{had} candidates are applied as well.

The missing transverse momentum (with magnitude $E_{\mathrm{T}}^{\mathrm{miss}}$) is the negative of the vector sum of the transverse momenta of all photon, electron, muon, τ_{had}, and jet candidates, as well as the p_{T} of all calorimeter clusters not associated with these reconstructed objects, called the soft-term contribution [62]. The $hh \to bb\tau\tau$ analysis uses the version of the $E_{\mathrm{T}}^{\mathrm{miss}}$ calculation in the $h \to \tau\tau$ analysis [6]. In this calculation, the soft-term contribution is scaled by a vertex fraction, defined as the ratio of the summed scalar p_{T} of all tracks from the primary vertex not matched with the reconstructed objects to the summed scalar p_{T} of all tracks in the event. The $hh \to \gamma\gamma WW^*$ analysis, on the other hand, uses the $E_{\mathrm{T}}^{\mathrm{miss}}$-significance employed by the $h \to \gamma\gamma$ study [56]. It is defined as the ratio of the measured $E_{\mathrm{T}}^{\mathrm{miss}}$ to its expected resolution estimated using the square root of the scalar sum of the transverse energies of all objects contributing to the $E_{\mathrm{T}}^{\mathrm{miss}}$ calculation.

IV. SUMMARY OF $hh \to \gamma\gamma bb$

The $hh \to \gamma\gamma bb$ analysis, published in Ref. [21], largely follows the ATLAS analysis of the Higgs boson discovery in the $h \to \gamma\gamma$ decay channel [1,56]. The search is performed in the $\sqrt{s} = 8$ TeV data set corresponding to an integrated luminosity of 20.3 fb^{-1}. The data were recorded with diphoton triggers that are nearly 100% efficient for events satisfying the photon requirements. Events must contain two isolated photons. The p_{T} for the leading (subleading) photon must be larger than 35% (25%) of the diphoton invariant mass $m_{\gamma\gamma}$, which itself must be in the range of $105 < m_{\gamma\gamma} < 160$ GeV. Events must also contain two energetic b-tagged jets; the leading (subleading) jet must have $p_{\mathrm{T}} > 55\,(35)$ GeV, and the dijet mass must fall within a window $95 < m_{bb} < 135$ GeV, as expected from the $h \to bb$ decay. A multivariate b-tagging algorithm [60] that is 70% efficient for the b-quark jets in $t\bar{t}$ events is applied.

Backgrounds for both the resonant and nonresonant analyses are divided into two categories: events containing a single real Higgs boson (with $h \to \gamma\gamma$), and the continuum background of events not containing a Higgs boson. The former are evaluated purely from simulation, and are small compared to the continuum background, which is evaluated from data in the diphoton mass sidebands (the $m_{\gamma\gamma}$ range of 105–160 GeV excluding the region of $m_h \pm 5$ GeV). In the nonresonant analysis, an unbinned signal-plus-background fit is performed on the observed $m_{\gamma\gamma}$ distribution, with the background from single Higgs bosons constrained to the expectation from the SM. The continuum background is modeled with an exponential function; the shape of the exponential function is taken from data containing a diphoton and dijet pair where fewer than two jets are b-tagged.

The resonant search proceeds in a similar manner, although it is ultimately a counting experiment, with an additional requirement on the four-object invariant mass $m_{\gamma\gamma bb}$, calculated with the bb mass constrained to m_h. This requirement on $m_{\gamma\gamma bb}$ varies with the resonance mass hypothesis under evaluation, and is defined as the smallest window containing 95% of the signal events based on MC simulation. As in the nonresonant search, the number of background events with real Higgs bosons is estimated from simulation. The continuum background in the $m_{\gamma\gamma}$ signal window is extrapolated from the diphoton mass sidebands. A resonance with mass between 260 and 500 GeV is considered in the search.

The small number of events (nine) in the diphoton mass sideband leads to large statistical uncertainties (33%) on the dominant continuum background, so that most systematic uncertainties have a small effect on the final result. For the resonant search, however, systematic uncertainties with comparable effect remain. Uncertainties of 0%–30% (depending on the resonance mass hypothesis under consideration) are assigned due to the modeling of the $m_{\gamma\gamma bb}$ shape using the data with less than two b-tagged jets. Additional uncertainties of 16%–30% arise from the choice of functional form used to parametrize the shape of $m_{\gamma\gamma bb}$.

In the nonresonant analysis, extrapolating the sidebands into the diphoton mass window of the signal selection leads to a prediction of 1.3 continuum background events. An additional contribution of 0.2 events is predicted from single Higgs boson production. A total of five events are observed, representing an excess of 2.4 standard deviations (σ). A 95% confidence level (C.L.) upper limit of 2.2 (1.0) pb is observed (expected) for $\sigma(gg \to hh)$, the cross section of nonresonant Higgs boson pair production. For the resonant searches, the observed (expected) upper limits

on $\sigma(gg \to H) \times \mathrm{BR}(H \to hh)$ are 2.3 (1.7) pb at $m_H = 260$ GeV and 0.7 (0.7) pb at $m_H = 500$ GeV.

V. SUMMARY OF $hh \to bbbb$

The $hh \to bbbb$ analysis [22] benefits from the large branching ratio of $h \to bb$. The analysis employs resolved as well as boosted Higgs boson reconstruction methods. The resolved method attempts to reconstruct and identify separate b-quark jets from the $h \to bb$ decay, while the boosted method uses a jet substructure technique to identify the $h \to bb$ decay reconstructed as a single jet. The latter is expected if the Higgs boson h has a high momentum. The boosted method is particularly suited to the search for a resonance with mass above approximately 1000 GeV decaying to a pair of SM Higgs bosons. For the combinations presented in this paper, resonances below this mass are considered and the resolved method is used as it is more sensitive.

The analysis with the resolved method searches for two back-to-back and high-momentum bb systems with their masses consistent with m_h in a data set at $\sqrt{s} = 8$ TeV corresponding to an integrated luminosity of 19.5 fb^{-1} for the triggers used. The data were recorded with a combination of multijet triggers using information including the b-quark jet tagging. The trigger is $> 99.5\%$ efficient for signal events satisfying the offline selection. Candidate events are required to have at least four b-tagged jets, each with $p_{\mathrm{T}} > 40$ GeV. As in the $hh \to \gamma\gamma bb$ analysis, a multivariate b-tagging algorithm [60] with an estimated efficiency of 70% is used to tag jets containing b-hadrons. The four highest-p_{T} b-tagged jets are then used to form two dijet systems, requiring the angular separation ΔR in (η, ϕ) space between the two jets in each of the two dijet systems to be smaller than 1.5. The transverse momenta of the leading and subleading dijet systems must be greater than 200 and 150 GeV, respectively. These selection criteria, driven partly by the corresponding jet trigger thresholds and partly by the necessity to suppress the backgrounds, lead to significant loss of signal acceptance for lower resonance masses. The resonant search only considers masses above 500 GeV. The leading (m_{12}) and subleading (m_{34}) dijet invariant mass values are required to be consistent with those expected for the $hh \to bbbb$ decay, satisfying the requirement:

$$\sqrt{\left(\frac{m_{12} - m_{12}^0}{\sigma_{12}}\right)^2 + \left(\frac{m_{34} - m_{34}^0}{\sigma_{34}}\right)^2} < 1.6.$$

Here m_{12}^0 (124 GeV) and m_{34}^0 (115 GeV) are the expected peak values from simulation for the leading and subleading dijet pair, respectively, and σ_{12} and σ_{34} are the dijet mass resolutions, estimated from the simulation to be 10% of the dijet mass values. More details about the selection can be found in Ref. [22].

After the full selection, more than 90% of the total background in the signal region is estimated to be multijet events, while the rest is mostly $t\bar{t}$ events. The Z + jets background constitutes less than 1% of the total background and is modeled using MC simulation. The multijet background is modeled using a fully data-driven approach in an independent control sample passing the same selection as the signal except that only one of the two selected dijets is b-tagged. This control sample is corrected for the kinematic differences arising from the additional b-tagging requirements in the signal sample. The $t\bar{t}$ contribution is taken from MC simulations normalized to data in dedicated control samples.

The dominant sources of systematic uncertainty in the analysis are the b-tagging calibration and the modeling of the multijet background. The degradation in the analysis sensitivity from these uncertainties is below 10%. Other sources of systematic uncertainty include the $t\bar{t}$ modeling, and the jet energy scale and resolution, which are all at the percent level. A total of 87 events are observed in the data, in good agreement with the SM expectation of 87.0 ± 5.6 events. Good agreement is also observed in the four-jet invariant mass distribution, thus there is no evidence of Higgs boson pair production. For the nonresonant search, both the observed and expected 95% C.L. upper limit on the cross section $\sigma(pp \to hh \to bbbb)$ is 202 fb. For the resonant search, the invariant mass of the four jets is used as the final discriminant from which the upper limit on the potential signal cross section is extracted. The resulting observed (expected) 95% C.L. upper limit on $\sigma(pp \to H \to hh \to bbbb)$ ranges from 52 (56) fb, at $m_H = 500$ GeV, to 3.6 (5.8) fb, at $m_H = 1000$ GeV.

VI. $hh \to bb\tau\tau$

This section describes the search for Higgs boson pair production in the $hh \to bb\tau\tau$ decay channel, where only the final state where one tau lepton decays hadronically and the other decays leptonically, $bb\ell\tau_{\mathrm{had}}$, is used. The data were recorded with triggers requiring at least one lepton with $p_{\mathrm{T}} > 24$ GeV. These triggers are nearly 100% efficient for events passing the final selection. Candidate $bb\ell\tau_{\mathrm{had}}$ events are selected by requiring exactly one lepton with $p_{\mathrm{T}} > 26$ GeV, one hadronically decaying tau lepton of the opposite charge with $p_{\mathrm{T}} > 20$ GeV meeting the medium criteria [61], and two or more jets with $p_{\mathrm{T}} > 30$ GeV. In addition, between one and three of the selected jets must be b-tagged using the multivariate b-tagger. The upper bound on the number of b-tagged jets is designed to make this analysis statistically independent of the $hh \to bbbb$ analysis summarized in Sec. V. These criteria are collectively referred to as the "preselection".

The backgrounds from W + jets, $Z \to \tau\tau$, diboson (WW, WZ, and ZZ), and top quark (both $t\bar{t}$ and single top quark) production dominate the surviving sample and their contributions are derived from a mixture of data-driven

methods and simulation. The contribution from events with a jet misidentified as a τ_{had}, referred to as the fake τ_{had} background, are estimated using data with a "fake-factor" method. The method estimates contributions from $W+$jets, multijet, $Z+$jets, and top quark events that pass the event selection due to misidentified τ_{had} candidates. The fake factor is defined as the ratio of the number of τ_{had} candidates identified as medium, to the number satisfying the loose, but not the medium, criteria [61]. The p_{T}-dependent fake factors are measured in data control samples separately for the τ_{had} candidates with one or three tracks and for $W+$jets, multijet, $Z+$jets, and top quark contributions. The $W+$jets, multijet, $Z+$jets, and top quark control samples are selected by reversing the m_T cut (see below), relaxing the lepton isolation requirement, reversing the dilepton veto or by requiring b-tagged jets, respectively. The fake factors determined from these control samples are consistent within their statistical uncertainties. They are then applied to the signal control sample, i.e., events passing the selection, except that the τ_{had} candidate is required to satisfy the loose, but not the medium, τ_{had} identification, to estimate the fake τ_{had} background. The composition of the sample is determined from a mixture of data-driven methods and MC simulations and it is found that the sample is dominated by the $W+$jets and multijet events. Details of the method can be found in Ref. [61]. The method is validated using the same-sign $\ell\tau_{\text{had}}$ events that are otherwise selected in the same way as the signal candidates.

The $Z \to \tau\tau$ background is modeled using selected $Z \to \mu\mu$ events in data through embedding [63], where the muon tracks and associated energy depositions in the calorimeters are replaced by the corresponding simulated signatures of the final-state particles of tau decays. In this approach, the kinematics of the produced boson, the hadronic activity of the event (jets and underlying event) as well as pileup are taken from data [6]. Other processes passing the $Z \to \mu\mu$ selection, primarily from top quark production, are subtracted from the embedded data sample using simulation. Their contributions are approximately 2% for events with one b-tagged jet and 25% for events with two or more b-tagged jets. The $Z \to \tau\tau$ background derived is found to be in a good agreement with that obtained from the MC simulation.

The remaining backgrounds, mostly $t\bar{t}$ and diboson events with genuine $\ell\tau_{\text{had}}$ in their decay final states, are estimated using simulation. The small contributions from single SM Higgs boson production and from $Z(\to ee/\mu\mu)+$jets events (in which one of the electrons or muons is misidentified as τ_{had}) are also estimated from simulation. The production rates of these processes are normalized to the theoretical cross sections discussed in Sec. II. For the simulation of the $t\bar{t}$ process, the top quark p_{T} distribution is corrected for the observed difference between data and simulation [64]. The background from misidentified leptons is found to be negligible.

Figures 2(a) and 2(b) compare the observed ditau ($m_{\tau\tau}$) and dijet (m_{bb}) mass distributions with those expected from background events after the preselection discussed above. The sample is dominated by contributions from top quark production, fake τ_{had}, and $Z \to \tau\tau$ backgrounds. Also shown in the figures are the expected signal distributions for a Higgs boson pair production cross section of 20 pb as an illustration. The yield of the nonresonant production is significantly higher than that of the resonant production for the same cross section, largely due to the harder p_{T} spectrum of the Higgs boson h of the nonresonant production. The ditau invariant mass is reconstructed from the electron or muon, τ_{had}, and $E_{\text{T}}^{\text{miss}}$ using a method known as the missing mass calculator (MMC) [65]. The MMC solves an underconstrained system of equations with solutions weighted by $E_{\text{T}}^{\text{miss}}$ resolution and the tau-lepton decay topologies. It returns the most probable value of the ditau mass, assuming that the observed lepton, τ_{had} and $E_{\text{T}}^{\text{miss}}$ stem from a $\tau\tau$ resonance. The dijet mass is calculated from the two leading b-tagged jets, or using also the highest-p_{T} untagged jet if only one jet is b-tagged.

Additional topological requirements are applied to reduce the background. As shown in Fig. 2(c), the signal events tend to have small values of the transverse mass $m_{\text{T}}^{\ell\nu}$ calculated from the lepton and $E_{\text{T}}^{\text{miss}}$ system. Consequently, a requirement of $m_{\text{T}}^{\ell\nu} < 60$ GeV is applied, which reduces the background significantly with only a small loss of the signal efficiency. In addition, the angular separation in the transverse plane between the $E_{\text{T}}^{\text{miss}}$ and τ_{had} is required to be larger than one radian to reduce the fake τ_{had} background.

Background events from $t\bar{t} \to WWbb \to \ell\nu\tau\nu bb$ decay have an identical visible final state to the signal if the tau lepton decays hadronically. For signal $h \to \tau\tau \to \ell\tau_{\text{had}}$ events, however, the p_{T} of the lepton tends to be softer than that of the τ_{had} due to the presence of more neutrinos in the $\tau \to \ell$ decays. Thus the p_{T} of the electron or muon is required to satisfy $p_{\text{T}}(\ell) < p_{\text{T}}(\tau_{\text{had}}) + 20$ GeV. The $t\bar{t}$ events of the $t\bar{t} \to WWbb \to \ell\nu qq'bb$ final state with a misidentified τ_{had} candidate remain a large background. To reduce its contribution, a W boson candidate is reconstructed from the τ_{had} candidate and its closest untagged jet and its mass $m_{\tau j}$ is calculated. The W candidate is then paired with a b-tagged jet to form the top quark candidate with a reconstructed mass $m_{\tau jb}$. The pairing is chosen to minimize the mass sum $m_{\ell b} + m_{\tau b}$ for events with two or more b-tagged jets. If only one jet is b-tagged, one of the b-jets in the mass sum is replaced by the highest-p_{T} untagged jet. An elliptical requirement in the form of a χ^2 in the $(m_{\tau j}, m_{\tau jb})$ plane:

$$\left(\frac{\Delta m_W \cos\theta - \Delta m_t \sin\theta}{28\ \text{GeV}}\right)^2 + \left(\frac{\Delta m_W \sin\theta + \Delta m_t \cos\theta}{18\ \text{GeV}}\right)^2 > 1$$

is applied to reject events with $(m_{\tau j}, m_{\tau jb})$ consistent with the hypothesis (m_W, m_t), the masses of the W boson and

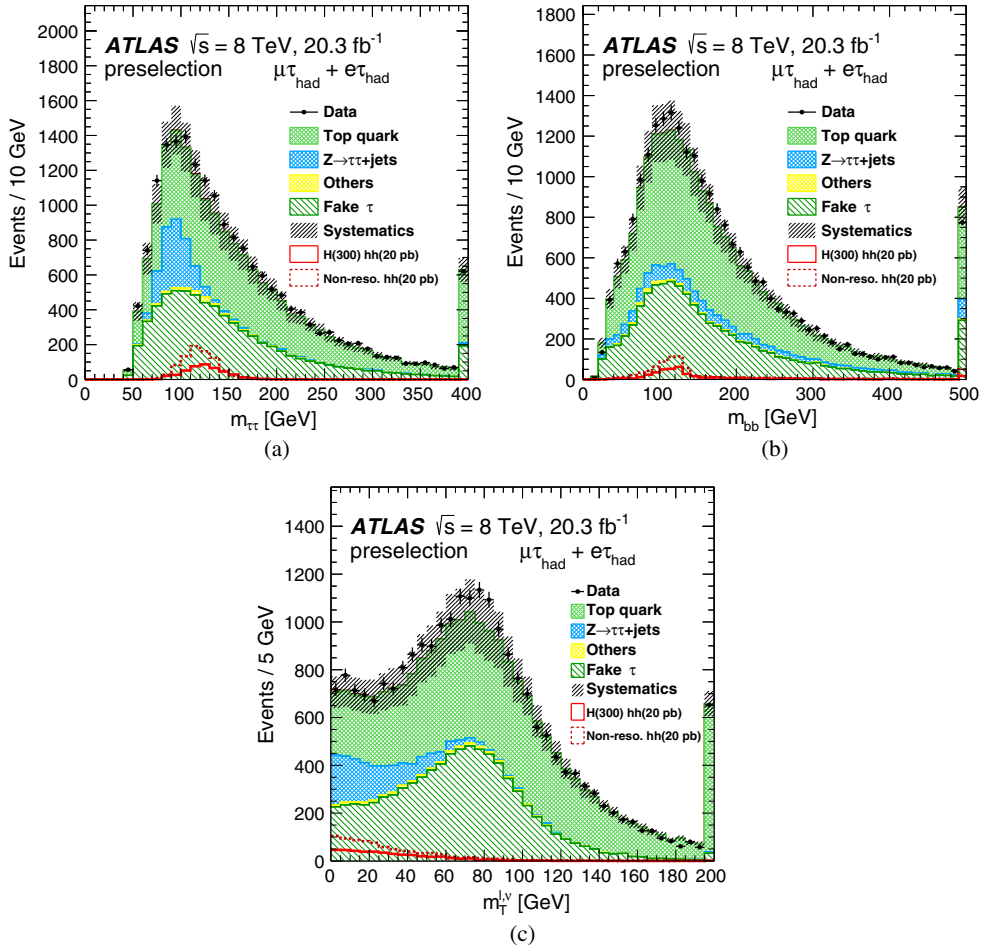

FIG. 2 (color online). Kinematic distributions of the $hh \to bb\tau\tau$ analysis after the preselection (see text) comparing data with the expected background contributions: (a) ditau mass $m_{\tau\tau}$ reconstructed using the MMC method, (b) dijet mass m_{bb}, and (c) the transverse mass $m_{\mathrm{T}}^{\ell\nu}$ of the lepton and the $E_{\mathrm{T}}^{\mathrm{miss}}$ system. The top quark background includes contributions from both $t\bar{t}$ and the single top-quark production. The background category labeled "Others" comprises diboson and $Z \to ee/\mu\mu$ contributions. Contributions from single SM Higgs boson production are included in the background estimates, but are too small to be visible on these distributions. As illustrations, expected signal distributions for a Higgs boson pair production cross section of 20 pb are overlaid for both nonresonant and resonant Higgs boson pair production. A mass of $m_H = 300$ GeV is assumed for the resonant production. The last bin in all distributions represents overflows. The gray hatched bands represent the uncertainties on the total background contributions. These uncertainties are largely correlated from bin to bin.

the top quark. Here $\Delta m_W = m_{\tau j} - m_W$, $\Delta m_t = m_{\tau jb} - m_t$ and θ is a rotation angle given by $\tan\theta = m_t/m_W$ to take into account the average correlation between $m_{\tau j}$ and $m_{\tau jb}$.

Finally, the remaining events must have $90 < m_{bb} < 160$ GeV, consistent with the expectation for the $h \to bb$ decay. For the nonresonant search, $m_{\tau\tau}$ is used as the final discriminant to extract the signal, and its distribution is shown in Fig. 3(a). The selection efficiency for the $gg \to hh \to bb\tau\tau$ signal is 0.57%. For the resonant search, the MMC mass is required to be in the range of $100 < m_{\tau\tau} < 150$ GeV. The mass resolutions of m_{bb} and $m_{\tau\tau}$ are comparable for the signal, but the m_{bb} distribution has a longer tail. The resonance mass $m_{bb\tau\tau}$ reconstructed from the dijet and ditau system is used as the discriminant. To improve the mass resolution of the heavy resonances, scale factors of m_h/m_{bb} and $m_h/m_{\tau\tau}$ are applied respectively to the four-momenta of the bb and $\tau\tau$ systems, where m_h is set to the value of 125 GeV used in the simulation. The resolution of $m_{bb\tau\tau}$ is found from simulation studies to vary from 2.4% at $m_H = 260$ GeV to 4.8% at 1000 GeV. The improvement in the resolution from the rescaling is largest at low mass and varies from approximately a factor of 3 at 260 GeV to about 30% at 1000 GeV. The reconstructed $m_{bb\tau\tau}$ distribution for events passing all the selections is shown in Fig. 3(b). The efficiency for the $gg \to H \to hh \to bb\tau\tau$ signal varies from 0.20% at 260 GeV to 1.5% at 1000 GeV. These efficiencies include branching ratios of

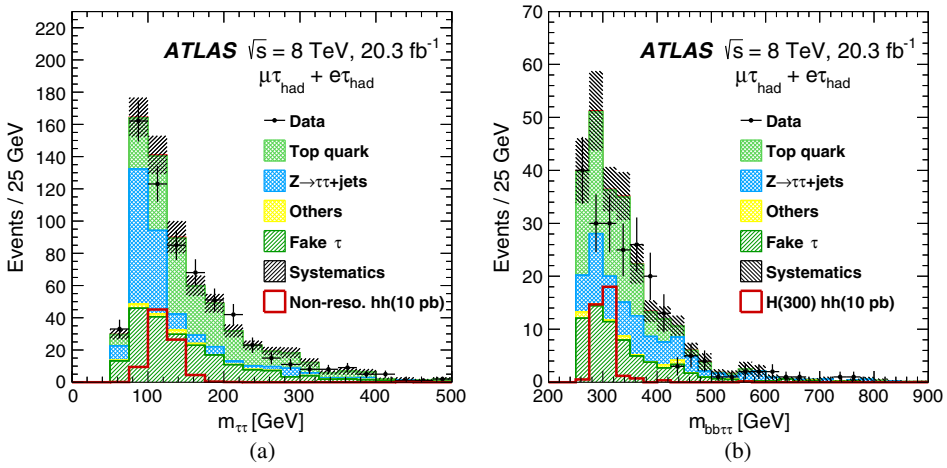

FIG. 3 (color online). Distributions of the final discriminants used to extract the signal: (a) $m_{\tau\tau}$ for the nonresonant search and (b) $m_{bb\tau\tau}$ for the resonant search. The top quark background includes contributions from both $t\bar{t}$ and the single top-quark production. The background category labeled "Others" comprises diboson and $Z \to ee/\mu\mu$ contributions. Contributions from single SM Higgs boson production are included in the background estimates, but are too small to be visible on these distributions. As illustrations, the expected signal distributions assume a cross section of 10 pb for Higgs boson pair production for both the nonresonant and resonant searches. In (b), a resonance mass of 300 GeV is assumed. The gray hatched bands represent the uncertainties on the total backgrounds. These uncertainties are largely correlated from bin to bin.

the tau lepton decays, but not those of heavy or light Higgs bosons.

To take advantage of different signal-to-background ratios in different kinematic regions, the selected events are divided into four categories based on the ditau transverse momentum $p_{\mathrm{T}}^{\tau\tau}$ (less than or greater than 100 GeV) and the number of b-tagged jets ($n_b = 1$ or ≥ 2) for both the nonresonant and resonant searches. The numbers of events expected from background processes and observed in the data passing the resonant $hh \to bb\tau\tau$ selection are summarized in Table II for each of the four categories. The expected number of events from the production of a Higgs boson with $m_H = 300$ GeV and a cross section of $\sigma(gg \to H) \times \mathrm{BR}(H \to hh) = 1$ pb for each category is also shown for comparison.

Systematic uncertainties from the trigger, luminosity, object identification, background estimate as well as Monte Carlo modeling of signal and background processes are taken into account in the background estimates and the calculation of signal yields. The impact of these systematic uncertainties varies for different background components and event categories. For the most sensitive $n_b \geq 2$ categories, the main background contributions are from top quark, fake τ_{had}, and $Z \to \tau\tau$. The jet energy scale and resolution is the largest uncertainty for the top-quark contribution, ranging between 10% and 19% for the nonresonant and resonant searches. The leading source of systematic uncertainty for the fake τ_{had} background is the "fake-factor" determination, due to the uncertainties of the sample composition. Varying the composition of W + jets,

TABLE II. The numbers of events predicted from background processes and observed in the data passing the final selection of the resonant search for the four categories. The top quark background includes contributions from both $t\bar{t}$ and the single top-quark production. The "others" background comprises diboson and $Z \to ee/\mu\mu$ contributions. The numbers of events expected from the production of a $m_H = 300$ GeV Higgs boson with a cross section of $\sigma(gg \to H) \times \mathrm{BR}(H \to hh) = 1$ pb are also shown as illustrations. The uncertainties shown are the total uncertainties, combining statistical and systematic components.

	$n_b = 1$		$n_b \geq 2$	
Process	$p_{\mathrm{T}}^{\tau\tau} < 100$ GeV	$p_{\mathrm{T}}^{\tau\tau} > 100$ GeV	$p_{\mathrm{T}}^{\tau\tau} < 100$ GeV	$p_{\mathrm{T}}^{\tau\tau} > 100$ GeV
SM Higgs	0.5 ± 0.1	0.8 ± 0.1	0.1 ± 0.1	0.2 ± 0.1
Top quark	30.3 ± 3.6	19.6 ± 2.5	30.9 ± 3.0	23.6 ± 2.5
$Z \to \tau\tau$	38.1 ± 4.4	20.2 ± 3.7	6.8 ± 1.8	2.6 ± 1.0
Fake τ_{had}	37.0 ± 4.4	12.1 ± 1.7	13.7 ± 1.9	5.4 ± 1.0
Others	3.2 ± 3.7	0.5 ± 1.5	0.7 ± 1.6	0.2 ± 0.7
Total background	109.1 ± 8.6	53.1 ± 6.0	52.2 ± 8.2	32.1 ± 5.4
Data	92	46	35	35
Signal $m_H = 300$ GeV	0.8 ± 0.2	0.4 ± 0.2	1.5 ± 0.3	0.9 ± 0.2

$Z+$jets, top quark and multijet events in the control samples by $\pm 50\%$ leads to a change in the estimated fake τ_{had} background by 9.5%. The most important source of systematic uncertainty for the $Z \to \tau\tau$ background is the $t\bar{t}$ subtraction from the $Z \to \mu\mu$ sample used for the embedding, due to the uncertainty on the $t\bar{t}$ normalization. Its effect ranges from 8% to 15%. The overall systematic uncertainties on the total background contributions to the high (low) $p_{\text{T}}^{\tau\tau}$ category of $n_b \geq 2$ are 12% (9%) for the nonresonant search and 14% (14%) for the resonant search. The largest contributions are from jet and tau energy scales and b-tagging. The modeling of top quark production is also an important systematic uncertainty for the category with two or more b-tagged jets and high $p_{\text{T}}^{\tau\tau}$.

The uncertainties on the signal acceptances are estimated from experimental as well as theoretical sources. The total experimental systematic uncertainties vary between 12% and 24% for the categories with two or more b-tagged jets, and are dominated by the jet and tau energy scales and b-tagging. Theoretical uncertainties arise from the choice of parton distribution functions, the renormalization and factorization scales as well as the value of strong coupling constant α_s used to generate the signal events. Uncertainties of 3%, 1%, and 3% from the three sources, respectively, are assigned to all signal acceptances.

For the nonresonant search, the observed ditau mass distribution agrees well with that of the estimated background events as shown in Fig. 3(a). For the resonant search, a small deficit with a local significance of approximately 2σ is observed in the data relative to the background expectation at $m_{bb\tau\tau} \sim 300$ GeV as is shown in Fig. 3(b). No evidence of Higgs boson pair production is present in the data. The resulting upper limits on Higgs boson pair production from these searches are described in Sec. IX.

VII. $hh \to \gamma\gamma WW^*$

This section describes the search for Higgs boson pair production in the $hh \to \gamma\gamma WW^*$ decay channel, where one Higgs boson decays to a pair of photons and the other decays to a pair of W bosons. The $h \to \gamma\gamma$ decay is well suited for tagging the Higgs boson. The small Higgs boson width together with the excellent detector resolution for the diphoton mass strongly suppresses background contributions. Moreover, the $h \to WW^*$ decay has the largest branching ratio after $h \to bb$. To reduce multijet backgrounds, one of the W bosons is required to decay to an electron or a muon (either directly or through a tau lepton) whereas the other is required to decay hadronically, leading to the $\gamma\gamma\ell\nu qq'$ final state.

The data used in this analysis were recorded with diphoton triggers with an efficiency close to 100% for diphoton events passing the final offline selection. The diphoton selection follows closely that of the ATLAS measurement of the $h \to \gamma\gamma$ production rate [56] and that of the $hh \to \gamma\gamma bb$ analysis [21]. Events are required to have two or more identified photons with the leading and subleading photon candidates having $p_{\text{T}}/m_{\gamma\gamma} > 0.35$ and 0.25, respectively, where $m_{\gamma\gamma}$ is the invariant mass of the two selected photons. Only events with $m_{\gamma\gamma}$ in the range of $105 < m_{\gamma\gamma} < 160$ GeV are considered.

Additional requirements are applied to identify the $h \to WW^* \to \ell\nu qq'$ decay signature. Events must have two or more jets, and exactly one lepton, satisfying the identification criteria described in Sec. III. To reduce multijet backgrounds, the events are required to have $E_{\text{T}}^{\text{miss}}$ with significance greater than one. Events with any b-tagged jet are vetoed to reduce contributions from top quark production.

A total of 13 events pass the above selection. The final $hh \to \gamma\gamma WW^*$ candidates are selected by requiring the diphoton mass $m_{\gamma\gamma}$ to be within a $\pm 2\sigma$ window of the Higgs boson mass in $h \to \gamma\gamma$ where σ is taken to be 1.7 GeV. Due to the small number of events, both nonresonant and resonant searches proceed as counting experiments. The selection efficiency for the $hh \to \gamma\gamma WW^*$ signal of SM nonresonant Higgs boson pair production is estimated using simulation to be 2.9%. For the resonant production, the corresponding efficiency varies from 1.7% at 260 GeV to 3.3% at 500 GeV. These efficiencies include the branching ratios of the W boson decays, but not those of the Higgs boson decays.

The background contributions considered are single SM Higgs boson production (gluon fusion, vector-boson fusion, and associated production of Wh, Zh, and $t\bar{t}h$) and continuum backgrounds in the $m_{\gamma\gamma}$ spectrum. Events from single Higgs boson production can mimic the $hh \to \gamma\gamma WW^*$ signal if, for example, the Higgs boson decays to two photons and the rest of the event satisfies the $h \to WW^* \to \ell\nu qq'$ identification. These events would exhibit a diphoton mass peak at m_h. As in the $hh \to bb\tau\tau$ analysis, their contributions are estimated from simulation using the SM cross sections [27]. The systematic uncertainty on the total yield of these backgrounds is estimated to be 29%, dominated by the modeling of jet production (27%). The total number of events expected from single SM Higgs production is therefore 0.25 ± 0.07 with contributions of 0.14, 0.08, and 0.025 events from Wh, $t\bar{t}h$, and Zh processes, respectively. Contributions from gluon and vector-boson fusion processes are negligible.

The background that is nonresonant in the $\gamma\gamma$ mass spectrum is measured using the continuum background in the $m_{\gamma\gamma}$ spectrum. The major source of these backgrounds is $W\gamma\gamma+$jets events with a $W \to \ell\nu$ decay. These events are expected to have a diphoton mass distribution with no resonant structure at m_h and their contribution ($N_{\text{SR}}^{\text{est}}$) in the signal region, $m_{\gamma\gamma} \in m_h \pm 2\sigma$, is estimated from the $m_{\gamma\gamma}$ sidebands in the data:

$$N_{\text{SR}}^{\text{est}} = N_{\text{SB}}^{\text{Data}} \times \frac{f_{\text{SB}}}{1 - f_{\text{SB}}}.$$

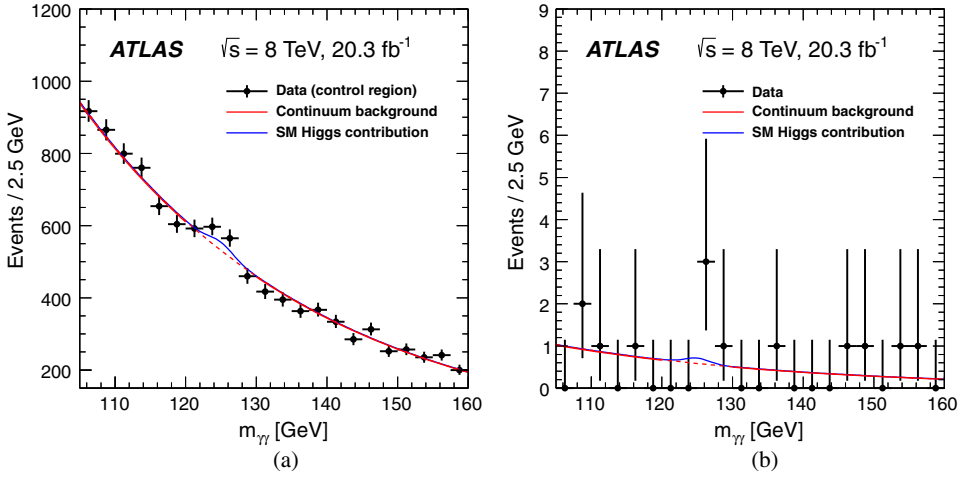

FIG. 4 (color online). The distribution of the diphoton invariant mass for events passing (a) the relaxed requirements and (b) the final selection. The relaxed requirements include all final selections except those on the lepton and $E_{\mathrm{T}}^{\mathrm{miss}}$. The red curves represent the continuum background contributions and the blue curves include the contributions expected from single SM Higgs boson production estimated from simulation. The continuum background contributions in the signal $m_{\gamma\gamma}$ mass window are shown as dashed lines.

Here $N_{\mathrm{SB}}^{\mathrm{Data}}$ is the number of events in the data sidebands, defined as the mass region $105 < m_{\gamma\gamma} < 160$ GeV excluding the signal region. The quantity f_{SB} is the fraction of background events in $105 < m_{\gamma\gamma} < 160$ GeV falling into the signal mass window, and can in principle be determined from a fit of the observed $m_{\gamma\gamma}$ distribution to an ansatz function. However, the small number of events after the final selection makes such a fit unsuitable. Instead, f_{SB} is determined in a data control sample, selected as the signal sample without the lepton and $E_{\mathrm{T}}^{\mathrm{miss}}$ requirements. Figure 4(a) shows the $m_{\gamma\gamma}$ distribution of events in the control sample. For the fit, an exponential function is used to model the sidebands and a wider region of $m_h \pm 5$ GeV is excluded to minimize potential signal contamination in the sidebands. The fit yields a value of $f_{\mathrm{SB}} = 0.1348 \pm 0.0001$. Varying the fit range of the sidebands leads to negligible changes. Different fit functions, such as a second-order polynomial or an exponentiated second-order polynomial, lead to a difference of 1.4% in f_{SB}. To study the sample dependence of f_{SB}, the fit is repeated for the control sample without the jet and $E_{\mathrm{T}}^{\mathrm{miss}}$ requirements and a difference of only 2% is observed. Simulation studies show that the continuum background is dominated by $W(\ell\nu)\gamma\gamma +$ jets production. The $\gamma\gamma\ell\nu +$ jets events generated using MadGraph reproduce well the observed $m_{\gamma\gamma}$ distribution. The potential difference between $\gamma\gamma +$ jets and $\gamma\gamma\ell\nu +$ jets samples is studied using simulation. A difference below 1% is observed. Taking all these differences as systematic uncertainties, the fraction of background events in the signal mass window is $f_{\mathrm{SB}} = 0.135 \pm 0.004$. With 9 ($N_{\mathrm{SB}}^{\mathrm{Data}}$) events observed in the data sidebands, it leads to $N_{\mathrm{SR}}^{\mathrm{est}} = 1.40 \pm 0.47$ events from the continuum background. Figure 4(a) also shows the contribution expected from single SM Higgs boson production. The data prefer a larger cross section than the SM prediction for single Higgs boson production, consistent with the measurement reported in Ref. [66].

The uncertainties on the signal acceptances are estimated following the same procedure as the $hh \to bb\tau\tau$ analysis. The total experimental uncertainty is found to vary between 4% and 7% for different signal samples under consideration, dominated by the contribution from the jet energy scale. The theoretical uncertainties from PDFs, the renormalization and factorization scales, and the strong coupling constant are 3%, 1%, and 3%, respectively, the same as for the $hh \to bb\tau\tau$ analysis.

The $m_{\gamma\gamma}$ distribution of the selected events in the data is shown in Fig. 4(b). In total, 13 events are found with $105 < m_{\gamma\gamma} < 160$ GeV. Among them, 4 events are in the signal mass window of $m_h \pm 2\sigma$ compared with 1.65 ± 0.47 events expected from single SM Higgs boson production and continuum background processes. The p-value of the background-only hypothesis is 3.8%, corresponding to 1.8 standard deviations.

Assuming a cross section of 1 pb ($\sigma(gg \to hh)$ or $\sigma(gg \to H) \times \mathrm{BR}(H \to hh)$) for Higgs boson pair production, the expected number of signal events is 0.64 ± 0.05 for the nonresonant production. For the resonant production, the corresponding numbers of events are 0.47 ± 0.05 and 0.72 ± 0.06 for a resonance mass of 300 GeV and 500 GeV, respectively. The implications of the search for Higgs boson pair production are discussed in Sec. IX.

VIII. COMBINATION PROCEDURE

The statistical analysis of the searches is based on the framework described in Refs. [67–70]. Profile-likelihood-ratio test statistics are used to measure the compatibility of the background-only hypothesis with the observed data

TABLE III. An overview of the number of categories and final discriminant distributions used for both the nonresonant and resonant searches. Shown in the last column are the mass ranges of the resonant searches.

hh	Nonresonant search		Resonant search		
Final state	Categories	Discriminant	Categories	Discriminant	m_H [GeV]
$\gamma\gamma b\bar{b}$	1	$m_{\gamma\gamma}$	1	event yields	260–500
$\gamma\gamma WW^*$	1	event yields	1	event yields	260–500
$b\bar{b}\tau\tau$	4	$m_{\tau\tau}$	4	$m_{bb\tau\tau}$	260–1000
$b\bar{b}b\bar{b}$	1	event yields	1	m_{bbbb}	500–1500

and to test the hypothesis of Higgs boson pair production with its cross section as the parameter of interest. Additional nuisance parameters are included to take into account systematic uncertainties and their correlations. The likelihood is the product of terms of the Poisson probability constructed from the final discriminant and of nuisance parameter constraints with either Gaussian, log-normal, or Poisson distributions. Upper limits on the Higgs boson pair production cross section are derived using the CL_s method [71]. For the combinations, systematic uncertainties that affect two or more analyses (such as those of luminosity, jet energy scale and resolutions, b-tagging, etc.) are modeled with common nuisance parameters.

For the $hh \to bb\tau\tau$ analysis, Poisson probability terms are calculated for the four categories separately from the mass distributions of the ditau system for the nonresonant search [Fig. 3(a)] and of the $bb\tau\tau$ system for the resonant search [Fig. 3(b)]. The $m_{bb\tau\tau}$ distributions of the resonant search are rebinned to ensure a sufficient number of events for the background prediction in each bin, in particular a single bin is used for $m_{bb\tau\tau} \gtrsim 400$ GeV for each category. For the $hh \to \gamma\gamma WW^*$ analysis, event yields are used to calculate Poisson probabilities without exploiting shape information. The $hh \to \gamma\gamma bb$ and $hh \to bbbb$ analyses are published separately in Refs. [21,22]. However, the results are quoted at slightly different values of the Higgs boson mass m_h and, therefore, have been updated using a common mass value of $m_h = 125.4$ GeV [24] for the combinations. The decay branching ratios of the Higgs boson h and their uncertainties used in the combinations are taken from Ref. [27]. Table III is a summary of the number of categories and final discriminants used for each analysis.

The four individual analyses are sensitive to different kinematic regions of the hh production and decays. The combination is performed assuming that the relative contributions of these regions to the total cross section are modeled by the MadGraph5 [39] program used to simulate the hh production.

IX. RESULTS

In this section, the limits on the nonresonant and resonant searches are derived. The results of the $hh \to bb\tau\tau$ and $hh \to \gamma\gamma WW^*$ analyses are first determined and then combined with previously published results of the $hh \to \gamma\gamma bb$ and $hh \to bbbb$ analyses. The impact of the leading systematic uncertainties is also discussed.

The observed and expected upper limits at 95% C.L. on the cross section of nonresonant production of a Higgs boson pair are shown in Table IV. These limits are to be compared with the SM prediction of 9.9 ± 1.3 fb [17] for $gg \to hh$ production with $m_h = 125.4$ GeV. Only the gluon fusion production process is considered. The observed (expected) cross-section limits are 1.6 (1.3) pb and 11.4 (6.7) pb from the $hh \to bb\tau\tau$ and $hh \to \gamma\gamma WW^*$ analyses, respectively. Also shown in the table are the cross-section limits relative to the SM expectation. The results are combined with those of the $hh \to \gamma\gamma bb$ and $hh \to bbbb$ analyses. The p-value of compatibility of the combination with the SM hypothesis is 4.4%, equivalent to 1.7 standard deviations. The low p-value is a result of the excess of events observed in the $hh \to \gamma\gamma bb$ analysis. The combined observed (expected) upper limit on $\sigma(gg \to hh)$ is 0.69 (0.47) pb, corresponding to 70 (48) times the cross

TABLE IV. The expected and observed 95% C.L. upper limits on the cross sections of nonresonant $gg \to hh$ production at $\sqrt{s} = 8$ TeV from individual analyses and their combinations. SM values are assumed for the h decay branching ratios. The cross-section limits normalized to the SM value are also included.

Analysis	$\gamma\gamma bb$	$\gamma\gamma WW^*$	$bb\tau\tau$	$bbbb$	Combined
	Upper limit on the cross section [pb]				
Expected	1.0	6.7	1.3	0.62	0.47
Observed	2.2	11	1.6	0.62	0.69
	Upper limit on the cross section relative to the SM prediction				
Expected	100	680	130	63	48
Observed	220	1150	160	63	70

TABLE V. The impact of the leading systematic uncertainties on the signal-strength parameter μ of a hypothesized signal for both the nonresonant and resonant ($m_H = 300$, 600 GeV) searches. For the signal hypothesis, a Higgs boson pair production cross section [$\sigma(gg \to hh)$ or $\sigma(gg \to H) \times \mathrm{BR}(H \to hh)$] of 1 pb is assumed.

Nonresonant search		Resonant search			
		$m_H = 300$ GeV		$m_H = 600$ GeV	
Source	$\Delta\mu/\mu$ [%]	Source	$\Delta\mu/\mu$ [%]	Source	$\Delta\mu/\mu$ [%]
Background model	11	Background model	15	b-tagging	10
b-tagging	7.9	Jet and $E_{\mathrm{T}}^{\mathrm{miss}}$	9.9	h BR	6.3
h BR	5.8	Lepton and τ_{had}	6.9	Jet and $E_{\mathrm{T}}^{\mathrm{miss}}$	5.5
Jet and $E_{\mathrm{T}}^{\mathrm{miss}}$	5.5	h BR	5.9	Luminosity	2.7
Luminosity	3.0	Luminosity	4.0	Background model	2.4
Total	16	Total	21	Total	14

section predicted by the SM. The $hh \to bbbb$ analysis has the best expected sensitivity followed by the $hh \to \gamma\gamma bb$ analysis. The observed combined limit is slightly weaker than that of the $hh \to bbbb$ analysis, largely due to the aforementioned excess.

The impact of systematic uncertainties on the cross-section limits is studied using the signal-strength parameter μ, defined as the ratio of the extracted to the assumed signal cross section [times branching ratio $\mathrm{BR}(H \to hh)$ for the resonant search]. The resulting shifts in μ depend on the actual signal-strength value. For illustration, they are evaluated using a cross section of 1 pb for $gg \to (H \to)hh$, comparable to the limits set. The effects of the most important uncertainty sources are shown in Table V. The leading contributions are from the background modeling, b-tagging, the h decay branching ratios, jet and $E_{\mathrm{T}}^{\mathrm{miss}}$ measurements. The large impact of the b-tagging systematic uncertainty reflects the relatively large weight of the $hh \to bbbb$ analysis in the combination. For the $hh \to bb\tau\tau$ analysis alone, the three leading systematic sources are the background estimates, jet and $E_{\mathrm{T}}^{\mathrm{miss}}$ measurements, and lepton and τ_{had} identifications. For the $hh \to \gamma\gamma WW^*$ analysis, they are the background estimates, jet and $E_{\mathrm{T}}^{\mathrm{miss}}$ measurements and theoretical uncertainties of the decay branching ratios of the Higgs boson h.

For the resonant production, limits are set on the cross section of $gg \to H$ production of the heavy Higgs boson times its branching ratio $\mathrm{BR}(H \to hh)$ as a function of the heavy Higgs boson mass m_H. The observed (expected) limits of the $hh \to bb\tau\tau$ and $hh \to \gamma\gamma WW^*$ analyses are illustrated in Fig. 5 and listed in Table VI (along with results from the $hh \to \gamma\gamma bb$ and $hh \to bbbb$ analyses). The m_H search ranges are 260–1000 GeV for $hh \to bb\tau\tau$ and 260–500 GeV for $hh \to \gamma\gamma WW^*$. For the $hh \to bb\tau\tau$ analysis, the observed limit around $m_H \sim 300$ GeV is considerably lower than the expectation, reflecting the deficit in the observed $m_{bb\tau\tau}$ distribution. At high mass, the limits are correlated since a single bin is used for $m_{bb\tau\tau} \gtrsim 400$ GeV. The decrease in the limit as m_H increases is a direct consequence of increasing selection efficiency for the signal. This is also true for the $hh \to \gamma\gamma WW^*$ analysis as the event selection is independent of m_H.

The $hh \to \gamma\gamma bb$ and $hh \to bbbb$ analyses are published separately and the mass range covered by the two analyses

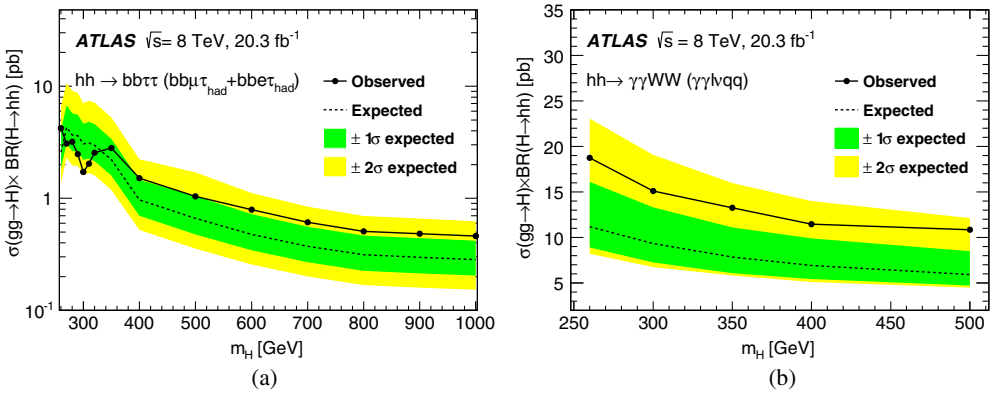

FIG. 5 (color online). The observed and expected upper limit at 95% C.L. on $\sigma(gg \to H) \times \mathrm{BR}(H \to hh)$ at $\sqrt{s} = 8$ TeV as a function of m_H from the resonant (a) $hh \to bb\tau\tau$ and (b) $hh \to \gamma\gamma WW^*$ analyses. The search ranges of the resonance mass are 260–1000 GeV for $hh \to bb\tau\tau$ and 260–500 GeV for $hh \to \gamma\gamma WW^*$. The green and yellow bands represent $\pm 1\sigma$ and $\pm 2\sigma$ ranges on the expected limits, respectively.

TABLE VI. The expected and observed 95% C.L. upper limits on $\sigma(gg \to H) \times \mathrm{BR}(H \to hh)$ in pb at $\sqrt{s} = 8$ TeV from individual analyses and their combinations. The SM branching ratios are assumed for the light Higgs boson decay.

m_H	Expected limit [pb]					Observed limit [pb]				
[GeV]	$\gamma\gamma bb$	$\gamma\gamma WW^*$	$bb\tau\tau$	$bbbb$	Combined	$\gamma\gamma bb$	$\gamma\gamma WW^*$	$bb\tau\tau$	$bbbb$	Combined
260	1.70	11.2	2.6	⋯	1.1	2.29	18.7	4.2	⋯	2.1
300	1.53	9.3	3.1	⋯	1.2	3.54	15.1	1.7	⋯	2.0
350	1.23	7.8	2.2	⋯	0.89	1.44	13.3	2.8	⋯	1.5
400	1.00	6.9	0.97	⋯	0.56	1.00	11.5	1.5	⋯	0.83
500	0.72	5.9	0.66	⋯	0.38	0.71	10.9	1.0	⋯	0.61
500	⋯	⋯	0.66	0.17	0.16	⋯	⋯	1.0	0.16	0.18
600	⋯	⋯	0.48	0.070	0.067	⋯	⋯	0.79	0.072	0.079
700	⋯	⋯	0.31	0.041	0.040	⋯	⋯	0.61	0.038	0.040
800	⋯	⋯	0.31	0.028	0.028	⋯	⋯	0.51	0.046	0.049
900	⋯	⋯	0.30	0.022	0.022	⋯	⋯	0.48	0.015	0.015
1000	⋯	⋯	0.28	0.018	0.018	⋯	⋯	0.46	0.011	0.011

are 260–500 GeV and 500–1500 GeV, respectively. The results of these four analyses, summarized in Table VI, are combined for the mass range 260–1000 GeV assuming the SM values of the h decay branching ratios. To reflect the better mass resolutions of the $hh \to bbbb$ and $hh \to \gamma\gamma bb$ analyses, the combination is performed with smaller mass steps than those of the $hh \to bb\tau\tau$ and $hh \to \gamma\gamma WW^*$ analyses. The most significant excess in the combined results is at a resonance mass of 300 GeV with a local significance of 2.5σ, largely due to the 3.0σ excess observed in the $hh \to \gamma\gamma bb$ analysis [21]. The upper limit on $\sigma(gg \to H) \times \mathrm{BR}(H \to hh)$ varies from 2.1 pb at 260 GeV to 0.011 pb at 1000 GeV. These limits are shown in Fig. 6 as a function of m_H. For the low-mass region of 260–500 GeV, both the $hh \to \gamma\gamma bb$ and $hh \to bb\tau\tau$ analyses contribute significantly to the combined sensitivities. Above 500 GeV, the sensitivity is dominated by the $hh \to bbbb$ analysis. Table V shows the impact of the leading systematic uncertainties for a heavy Higgs boson mass of 300 and 600 GeV. As in the nonresonant search, the systematic uncertainties with the largest impact on the sensitivity are from the uncertainties on the background modeling, b-tagging, jet and $E_{\mathrm{T}}^{\mathrm{miss}}$ measurements, and the h decay branching ratios. These limits are directly applicable to models such as those of Refs. [72–77] in which the Higgs boson h has the same branching ratios as the SM Higgs boson.

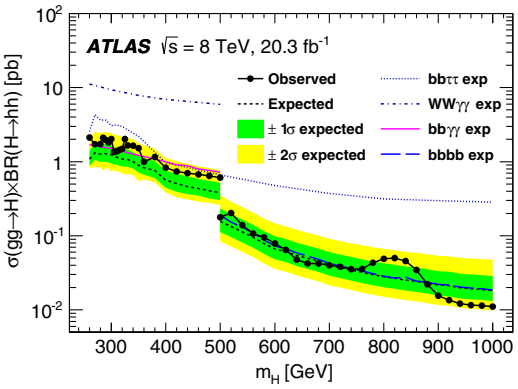

FIG. 6 (color online). The observed and expected 95% C.L. upper limits on $\sigma(gg \to H) \times \mathrm{BR}(H \to hh)$ at $\sqrt{s} = 8$ TeV as functions of the heavy Higgs boson mass m_H, combining resonant searches in $hh \to \gamma\gamma bb$, $bbbb$, $bb\tau\tau$, and $\gamma\gamma WW^*$ final states. The expected limits from individual analyses are also shown. The combination assumes SM values for the decay branching ratios of the lighter Higgs boson h. The green and yellow bands represent $\pm 1\sigma$ and $\pm 2\sigma$ uncertainty ranges of the expected combined limits. The improvement above $m_H = 500$ GeV is due to the sensitivity of the $hh \to bbbb$ analysis. The more finely spaced mass points of the combination reflect the better mass resolutions of the $hh \to \gamma\gamma bb$ and $hh \to bbbb$ analyses than those of the $hh \to bb\tau\tau$ and $hh \to \gamma\gamma WW^*$ analyses.

X. INTERPRETATION

The upper cross-section limits of the resonant search are interpreted in two MSSM scenarios, one referred to as the hMSSM [28,29] and the other as the low-tb-high [30]. In the interpretation, the CP-even light and heavy Higgs bosons of the MSSM are assumed to be the Higgs bosons h and H of the search, respectively. The natural width of the heavy Higgs boson H where limits are set in these scenarios is sufficiently smaller than the experimental resolution, which is at best 1.5%, that its effect can be neglected.

In the hMSSM scenario, the mass of the light CP-even Higgs boson is fixed to 125 GeV in the whole parameter space. This is achieved by implicitly allowing the supersymmetry-breaking scale m_{S} to be very large, which is especially true in the low $\tan\beta$ region where $m_{\mathrm{S}} \gg 1$ TeV, and making assumptions about the CP-even Higgs boson mass matrix and its radiative corrections, as well as the Higgs boson coupling dependence on the MSSM parameters. Here $\tan\beta$ is the ratio of the vacuum expectation values of the two doublet Higgs fields. The "low-tb-high" MSSM scenario follows a similar approach, differing in that explicit choices are made for the supersymmetry-breaking

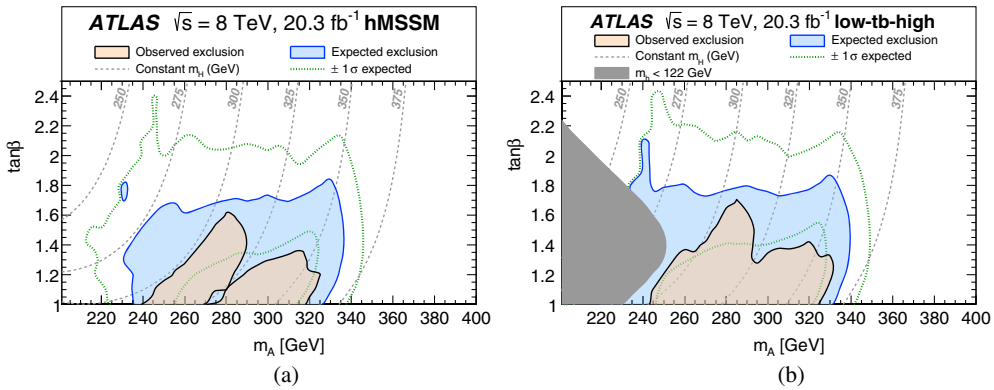

FIG. 7 (color online). The observed and expected 95% C.L. exclusion regions in the $(\tan\beta, m_A)$ plane of MSSM scenarios from the resonant search: (a) the hMSSM scenario and (b) the low-tb-high scenario. The green dotted lines delimit the $\pm 1\sigma$ uncertainty ranges of the expected exclusion regions. The gray dashed lines show the constant values of the heavy *CP*-even Higgs boson mass. The improved sensitivity in the expected exclusion on the contour line of $m_H \sim 260$ GeV reflects the improved expected limit on the cross section while the hole or the wedge around the $m_H \sim 325$ GeV contour line in the observed exclusion is the result of a small excess at this mass; see Fig. 6. The gray shaded region in (b) shows the region where the mass of the light *CP*-even Higgs boson is inconsistent with the measured value of 125.4 GeV. There is no such region in (a) by construction.

parameters [30]. The mass of the light Higgs boson is not fixed in this scenario, but is approximately 125 GeV in most of the parameter space. The m_h value grows gradually from 122 GeV at $m_A \sim 220$ GeV to 125 GeV as m_A approaching infinity. Higgs boson production cross sections through the gluon-fusion process are calculated with SusHi 1.4.1 [78–80] for both scenarios. Higgs boson decay branching ratios are calculated with HDECAY 6.42 [81] following the prescription of Ref. [29] for the hMSSM scenario and with FeynHiggs 2.10.0 [82–84] for the low-tb-high scenario.

The upper limits on $\sigma(gg \to H) \times \mathrm{BR}(H \to hh)$ can be interpreted as exclusion regions in the $(\tan\beta, m_A)$ plane. In both scenarios, the Higgs boson pair production rate $\sigma(gg \to H) \times \mathrm{BR}(H \to hh)$ depends on $\tan\beta$ and the mass of the *CP*-odd Higgs boson (m_A), and so does the mass of the heavy *CP*-even Higgs boson H. The values of m_A and m_H are generally different: m_H can be as much as 70 GeV above m_A in the parameter space relevant for this publication with the difference in masses decreasing for increasing values of $\tan\beta$ or m_A. Constant m_H lines for a few selected values are shown in Fig. 7. The decay branching ratios of the light Higgs boson in these scenarios depend on $\tan\beta$ and m_A and are different from the corresponding SM values used to derive the upper limits shown in Table VI. The upper limits, as functions of m_H, are recomputed; the hh decay fractions for each final state are fixed to their smallest value found in $1 < \tan\beta < 2$, the range of the expected sensitivity. This approach yields conservative limits, but simplifies the computation as the limit calculation does not have to be repeated at each $\tan\beta$ value. The results are used to set exclusions in the $(\tan\beta, m_A)$ plane as shown in Fig. 7. The analysis is sensitive to the region of low $\tan\beta$ and m_A values in the range $\sim 200 - 350$ GeV. For $m_A \lesssim 200$ GeV, m_H is typically below the $2m_h$ threshold of the $H \to hh$ decay, whereas above 350 GeV, the $H \to hh$ decay is suppressed because of the dominance of the $H \to t\bar{t}$ decay. The observed exclusion region in the $(\tan\beta, m_A)$ plane is smaller than the expectation, reflecting the small excess observed in the data.

XI. SUMMARY

This paper summarizes the search for both nonresonant and resonant Higgs boson pair production in proton-proton collisions from approximately 20 fb^{-1} of data at a center-of-mass energy of 8 TeV recorded by the ATLAS detector at the LHC. The search is performed in $hh \to bb\tau\tau$ and $\gamma\gamma WW^*$ final states. No significant excess is observed in the data beyond the background expectation. Upper limits on the hh production cross section are derived. Combining with the $hh \to \gamma\gamma bb$, $bbbb$ searches, a 95% C.L. upper limit of 0.69 pb on the cross section of the nonresonant hh production is observed compared with the expected limit of 0.47 pb. This observed upper limit is approximately 70 times the SM $gg \to hh$ production cross section. For the production of a narrow heavy resonance decaying to a pair of light Higgs bosons, the observed (expected) upper limit on $\sigma(gg \to H) \times \mathrm{BR}(H \to hh)$ varies from 2.1 (1.1) pb at 260 GeV to 0.011 (0.018) pb at 1000 GeV. These limits are obtained assuming SM values for the h decay branching ratios. Exclusion regions in the parameter space of simplified MSSM scenarios are also derived.

ACKNOWLEDGMENTS

We thank CERN for the very successful operation of the LHC, as well as the support staff from our institutions without whom ATLAS could not be operated efficiently. We acknowledge the support of ANPCyT, Argentina;

YerPhI, Armenia; ARC, Australia; BMWFW and FWF, Austria; ANAS, Azerbaijan; SSTC, Belarus; CNPq and FAPESP, Brazil; NSERC, NRC and CFI, Canada; CERN; CONICYT, Chile; CAS, MOST and NSFC, China; COLCIENCIAS, Colombia; MSMT CR, MPO CR and VSC CR, Czech Republic; DNRF, DNSRC, Denmark and Lundbeck Foundation, Denmark; IN2P3-CNRS, CEA-DSM/IRFU, France; GNSF, Georgia; BMBF, HGF, and MPG, Germany; GSRT, Greece; RGC, Hong Kong SAR, China; ISF, I-CORE and Benoziyo Center, Israel; INFN, Italy; MEXT and JSPS, Japan; CNRST, Morocco; FOM and NWO, Netherlands; RCN, Norway; MNiSW and NCN, Poland; FCT, Portugal; MNE/IFA, Romania; MES of Russia and NRC KI, Russian Federation; JINR; MESTD, Serbia; MSSR, Slovakia; ARRS and MIZŠ, Slovenia; DST/NRF, South Africa; MINECO, Spain; SRC and Wallenberg Foundation, Sweden; SERI, SNSF and Cantons of Bern and Geneva, Switzerland; MOST, Taiwan; TAEK, Turkey; STFC, United Kingdom; DOE and NSF, United States of America. In addition, individual groups and members have received support from BCKDF, the Canada Council, CANARIE, CRC, Compute Canada, FQRNT, and the Ontario Innovation Trust, Canada; EPLANET, ERC, FP7, Horizon 2020 and Marie Skłodowska-Curie Actions, European Union; Investissements d'Avenir Labex and Idex, ANR, Region Auvergne and Fondation Partager le Savoir, France; DFG and AvH Foundation, Germany; Herakleitos, Thales and Aristeia programmes co-financed by EU-ESF and the Greek NSRF; BSF, GIF and Minerva, Israel; BRF, Norway; the Royal Society and Leverhulme Trust, United Kingdom. The crucial computing support from all WLCG partners is acknowledged gratefully, in particular from CERN and the ATLAS Tier-1 facilities at TRIUMF (Canada), NDGF (Denmark, Norway, Sweden), CC-IN2P3 (France), KIT/GridKA (Germany), INFN-CNAF (Italy), NL-T1 (Netherlands), PIC (Spain), ASGC (Taiwan), RAL (UK) and BNL (USA) and in the Tier-2 facilities worldwide.

[1] ATLAS Collaboration, Observation of a new particle in the search for the standard model Higgs boson with the ATLAS detector at the LHC, Phys. Lett. B **716**, 1 (2012).
[2] CMS Collaboration, Observation of a new boson at a mass of 125 GeV with the CMS experiment at the LHC, Phys. Lett. B **716**, 30 (2012).
[3] ATLAS Collaboration, Measurements of Higgs boson production and couplings in diboson final states with the ATLAS detector at the LHC, Phys. Lett. B **726**, 88 (2013).
[4] CMS Collaboration, Precise determination of the mass of the Higgs boson and tests of compatibility of its couplings with the standard model predictions using proton collisions at 7 and 8 TeV, Eur. Phys. J. C **75**, 212 (2015).
[5] ATLAS Collaboration, Search for the $b\bar{b}$ decay of the standard model Higgs boson in associated $(W/Z)H$ production with the ATLAS detector, J. High Energy Phys. 01 (2015) 069.
[6] ATLAS Collaboration, Evidence for the Higgs-boson Yukawa coupling to tau leptons with the ATLAS detector, J. High Energy Phys. 04 (2015) 117.
[7] ATLAS Collaboration, Evidence for the spin-0 nature of the Higgs boson using ATLAS data, Phys. Lett. B **726**, 120 (2013).
[8] CMS Collaboration, Constraints on the spin-parity and anomalous HVV couplings of the Higgs boson in proton collisions at 7 and 8 TeV, Phys. Rev. D **92**, 012004 (2015).
[9] U. Baur, T. Plehn, and D. L. Rainwater, Determining the Higgs boson self-coupling at hadron colliders, Phys. Rev. D **67**, 033003 (2003).
[10] U. Baur, T. Plehn, and D. L. Rainwater, Probing the Higgs self-coupling at hadron colliders using rare decays, Phys. Rev. D **69**, 053004 (2004).
[11] M. J. Dolan, C. Englert, and M. Spannowsky, Higgs self-coupling measurements at the LHC, J. High Energy Phys. 10 (2012) 112.
[12] J. Baglio, A. Djouadi, R. Gröber, M. M. Mühlleitner, J. Quevillon, and M. Spira, The measurement of the Higgs self-coupling at the LHC: Theoretical status, J. High Energy Phys. 04 (2013) 151.
[13] L.-C. Lu *et al.*, Searching for heavier Higgs boson via di-Higgs production at LHC run-2, arXiv:1507.02644.
[14] S. Dawson *et al.*, Higgs Working Group report, arXiv:1310.8361.
[15] S. Dawson, S. Dittmaier, and M. Spira, Neutral Higgs-boson pair production at hadron colliders: QCD corrections, Phys. Rev. D **58**, 115012 (1998).
[16] J. Grigo, J. Hoff, K. Melnikov, and M. Steinhauser, On the Higgs boson pair production at the LHC, Nucl. Phys. **B875**, 1 (2013).
[17] D. de Florian and J. Mazzitelli, Higgs Boson Pair Production at Next-to-Next-to-Leading Order in QCD, Phys. Rev. Lett. **111**, 201801 (2013).
[18] H. E. Haber and G. L. Kane, The search for supersymmetry: Probing physics beyond the standard model, Phys. Rep. **117**, 75 (1985).
[19] R. Grober and M. Muhlleitner, Composite Higgs boson pair production at the LHC, J. High Energy Phys. 06 (2011) 020.
[20] R. Contino, M. Ghezzi, M. Moretti, G. Panico, F. Piccinini, and A. Wulzer, Anomalous couplings in double Higgs production, J. High Energy Phys. 08 (2012) 154.
[21] ATLAS Collaboration, Search for Higgs Boson Pair Production in the $\gamma\gamma b\bar{b}$ Final State Using pp Collision Data at $\sqrt{s} = 8$ TeV from the ATLAS Detector, Phys. Rev. Lett. **114**, 081802 (2015).

[22] ATLAS Collaboration, Search for Higgs boson pair production in the $b\bar{b}b\bar{b}$ final state from pp collisions at $\sqrt{s} = 8$ TeV with the ATLAS detector, Eur. Phys. J. C **75**, 412 (2015).

[23] CMS Collaboration, Search for resonant pair production of Higgs bosons decaying to two bottom quark-antiquark pairs in proton-proton collisions at 8 TeV, Phys. Lett. B **749**, 560 (2015).

[24] ATLAS Collaboration, Measurement of the Higgs boson mass from the $H \to \gamma\gamma$ and $H \to ZZ^* \to 4\ell$ channels in pp collisions at center-of-mass energies of 7 and 8 TeV with the ATLAS detector, Phys. Rev. D **90**, 052004 (2014).

[25] S. Dittmaier *et al.*, Handbook of LHC Higgs cross sections: 1. Inclusive observables, arXiv:1101.0593.

[26] S. Dittmaier *et al.*, Handbook of LHC Higgs cross sections: 2. Differential distributions, arXiv:1201.3084.

[27] S. Heinemeyer *et al.*, Handbook of LHC Higgs cross sections: 3. Higgs properties, arXiv:1307.1347.

[28] A. Djouadi, L. Maiani, G. Moreau, A. Polosa, J. Quevillon, and V. Riquer, The post-Higgs MSSM scenario: Habemus MSSM?, Eur. Phys. J. C **73**, 2650 (2013).

[29] A. Djouadi, L. Maiani, A. Polosa, J. Quevillon, and V. Riquer, Fully covering the MSSM Higgs sector at the LHC, J. High Energy Phys. 06 (2015) 168.

[30] E. Bagnaschi *et al.*, CERN Report No. LHCHXSWG-2015-002, 2015, http://cds.cern.ch/record/2039911.

[31] ATLAS Collaboration, The ATLAS experiment at the CERN Large Hadron Collider, JINST **3**, S08003 (2008).

[32] T. Sjostrand, S. Mrenna, and P. Z. Skands, A brief introduction to PYTHIA 8.1, Comput. Phys. Commun. **178**, 852 (2008).

[33] H.-L. Lai, M. Guzzi, J. Huston, Z. Li, P. M. Nadolsky, J. Pumplin, and C.-P. Yuan, New parton distributions for collider physics, Phys. Rev. D **82**, 074024 (2010).

[34] J. Pumplin, D. R. Stump, J. Huston, H.-L. Lai, P. Nadolsky, and W.-K. Tung, New Generation of Parton Distributions with Uncertainties from Global QCD Analysis, J. High Energy Phys. 07 (2002) 012.

[35] A. D. Martin, W. J. Stirling, R. S. Thorne, and G. Watt, Parton distributions for the LHC, Eur. Phys. J. C **63**, 189 (2009).

[36] R. D. Ball *et al.*, Parton distribution benchmarking with LHC data, J. High Energy Phys. 04 (2013) 125.

[37] ATLAS Collaboration, The ATLAS simulation infrastructure, Eur. Phys. J. C **70**, 823 (2010).

[38] S. Agostinelli *et al.*, GEANT4: A simulation toolkit, Nucl. Instrum. Methods Phys. Res., Sect. A **506**, 250 (2003).

[39] J. Alwall, M. Herquet, F. Maltoni, O. Mattelaer, and T. Stelzer, MadGraph 5: Going beyond, J. High Energy Phys. 06 (2011) 128.

[40] T. Plehn, M. Spira, and P. Zerwas, Pair production of neutral Higgs particles in gluon-gluon collisions, Nucl. Phys. **B479**, 46 (1996).

[41] R. Frederix, S. Frixione, V. Hirschi, F. Maltoni, O. Mattelaer, P. Torrielli, E. Vryonidou, and M. Zaro, Higgs pair production at the LHC with NLO and parton-shower effects, Phys. Lett. B **732**, 142 (2014).

[42] B. Hespel and E. Vryonidou, Higgs Pair Production, http://cp3.irmp.ucl.ac.be/projects/madgraph/wiki/HiggsPairProduction.

[43] P. Nason, A new method for combining NLO QCD with shower Monte Carlo algorithms, J. High Energy Phys. 11 (2004) 040.

[44] S. Frixione, P. Nason, and C. Oleari, Matching NLO QCD computations with parton shower simulations: The POWHEG method, J. High Energy Phys. 11 (2007) 070.

[45] S. Alioli, P. Nason, C. Oleari, and E. Re, A general framework for implementing NLO calculations in shower Monte Carlo programs: The POWHEG BOX, J. High Energy Phys. 06 (2010) 043.

[46] M. Grazzini and H. Sargsyan, Heavy-quark mass effects in Higgs boson production at the LHC, J. High Energy Phys. 09 (2013) 129.

[47] D. de Florian, G. Ferrera, M. Grazzini, and D. Tommasini, Higgs boson production at the LHC: Transverse momentum resummation effects in the $H \to 2\gamma$, $H \to WW \to \ell\nu\ell'\nu'$ and $H \to ZZ \to 4\ell$ decay modes, J. High Energy Phys. 06 (2012) 132.

[48] M. L. Mangano, F. Piccinini, A. D Polosa, M. Moretti, and R. Pittau, ALPGEN, a generator for hard multiparton processes in hadronic collisions, J. High Energy Phys. 07 (2003) 001.

[49] B. P. Kersevan and E. Richter-Was, The Monte Carlo event generator AcerMC versions 2.0 to 3.8 with interfaces to PYTHIA 6.4, HERWIG 6.5 and ARIADNE 4.1, Comput. Phys. Commun. **184**, 919 (2013).

[50] M. Czakon, P. Fiedler, and A. Mitov, Total Top-Quark Pair-Production Cross Section at Hadron Colliders through $O(\alpha_S^4)$, Phys. Rev. Lett. **110**, 252004 (2013).

[51] N. Kidonakis, Next-to-next-to-leading-order collinear and soft gluon corrections for t-channel single top quark production, Phys. Rev. D **83**, 091503 (2011).

[52] N. Kidonakis, Next-to-next-to-leading logarithm resummation for s-channel single top quark production, Phys. Rev. D **81**, 054028 (2010).

[53] N. Kidonakis, Two-loop soft anomalous dimensions for single top quark associated production with a W^- or H^-, Phys. Rev. D **82**, 054018 (2010).

[54] J. M. Campbell and R. Ellis, MCFM for the Tevatron and the LHC, Nucl. Phys. B, Proc. Suppl. **205–206**, 10 (2010).

[55] J. M. Campbell, R. K. Ellis, and C. Williams, Vector boson pair production at the LHC, J. High Energy Phys. 07 (2011) 018.

[56] ATLAS Collaboration, Measurement of Higgs boson production in the diphoton decay channel in pp collisions at center-of-mass energies of 7 and 8 TeV with the ATLAS detector, Phys. Rev. D **90**, 112015 (2014).

[57] ATLAS Collaboration, ATLAS Report No. ATLAS-CONF-2014-032, 2014, http://cds.cern.ch/record/1706245.

[58] ATLAS Collaboration, ATLAS Report No. ATLAS-CONF-2012-123, 2012, http://cds.cern.ch/record/1473426.

[59] M. Cacciari, G. P. Salam, and G. Soyez, The anti-k_t jet clustering algorithm, J. High Energy Phys. 04 (2008) 063.

[60] ATLAS Collaboration, ATLAS Report No. ATLAS-CONF-2014-046, 2014, http://cds.cern.ch/record/1741020.

[61] ATLAS Collaboration, Identification and energy calibration of hadronically decaying tau leptons with the ATLAS experiment in pp collisions at $\sqrt{s} = 8$ TeV, Eur. Phys. J. C **75**, 303 (2015).

[62] ATLAS Collaboration, Performance of missing transverse momentum reconstruction in proton-proton collisions at 7 TeV with ATLAS, Eur. Phys. J. C **72**, 1844 (2012).

[63] ATLAS Collaboration, Modelling $Z \to \tau\tau$ processes in ATLAS with τ-embedded $Z \to \mu\mu$ data, JINST **10**, P09018 (2015).
[64] ATLAS Collaboration, Measurements of normalized differential cross sections for $t\bar{t}$ production in pp collisions at $\sqrt{s} = 7$ TeV using the ATLAS detector, Phys. Rev. D **90**, 072004 (2014).
[65] A. Elagin, P. Murat, A. Pranko, and A. Safonov, A new mass reconstruction technique for resonances decaying to $\tau\tau$, Nucl. Instrum. Methods Phys. Res., Sect. A **654**, 481 (2011).
[66] ATLAS Collaboration, Measurements of fiducial and differential cross sections for Higgs boson production in the diphoton decay channel at $\sqrt{s} = 8$ TeV with ATLAS, J. High Energy Phys. 09 (2014) 112.
[67] ATLAS Collaboration, Combined search for the Standard Model Higgs boson in pp collisions at $\sqrt{s} = 7$ TeV with the ATLAS detector, Phys. Rev. D **86**, 032003 (2012).
[68] L. Moneta *et al.*, The RooStats Project, *Proc. Sci.*, ACAT2010 (2010) 057.
[69] W. Verkerke and D. P. Kirkby, The RooFit toolkit for data modeling, eConf C0303241 (2003), p. MOLT007; http://inspirehep.net/record/621398.
[70] G. Cowan, K. Cranmer, E. Gross, and O. Vitells, Asymptotic formulae for likelihood-based tests of new physics, Eur. Phys. J. C **71**, 11554 (2011).
[71] A. L. Read, Presentation of search results: The CL_s technique, J. Phys. G **28**, 2693 (2002).
[72] A. Hill and J. J. van der Bij, Strongly interacting singlet-double Higgs model, Phys. Rev. D **36**, 3463 (1987).
[73] T. Binoth and J. J. van der Bij, Influence of strongly coupled, hidden scalars on Higgs signals, Z. Phys. C **75**, 17 (1997).
[74] R. Schabinger and J. D. Wells, Minimal spontaneously broken hidden sector and its impact on Higgs boson physics at the CERN Large Hadron Collider, Phys. Rev. D **72**, 093007 (2005).
[75] B. Patt and F. Wilczek, Higgs-field portal into hidden sectors, arXiv:hep-ph/0605188.
[76] G. M. Pruna and T. Robens, Higgs singlet extension parameter space in the light of the LHC discovery, Phys. Rev. D **88**, 115012 (2013).
[77] T. Robens and T. Stefaniak, Status of the Higgs singlet extension of the standard model after LHC run 1, Eur. Phys. J. C **75**, 104 (2015).
[78] R. V. Harlander, S. Liebler, and H. Mantler, SusHi: A program for the calculation of Higgs production in gluon fusion and bottom-quark annihilation in the Standard Model and the MSSM, Comput. Phys. Commun. **184**, 1605 (2013).
[79] R. V. Harlander and W. B. Kilgore, Next-to-Next-to-Leading Order Higgs Production at Hadron Colliders, Phys. Rev. Lett. **88**, 201801 (2002).
[80] U. Aglietti, R. Bonciani, G. Degrassi, and A. Vicini, Two-loop light fermion contribution to Higgs production and decays, Phys. Lett. B **595**, 432 (2004).
[81] A. Djouadi, J. Kalinowski, and M. Spira, HDECAY: A program for Higgs boson decays in the Standard Model and its supersymmetric extension, Comput. Phys. Commun. **108**, 56 (1998).
[82] S. Heinemeyer, W. Hollik, and G. Weiglein, FeynHiggs: A program for the calculation of the masses of the neutral *CP*-even Higgs bosons in the MSSM, Comput. Phys. Commun. **124**, 76 (2000).
[83] G. Degrassi, S. Heinemeyer, W. Hollik, P. Slavich, and G. Weiglein, Towards high-precision predictions for the MSSM Higgs sector, Eur. Phys. J. C **28**, 133 (2003).
[84] T. Hahn, S. Heinemeyer, W. Hollik, H. Rzehak, and G. Weiglein, High-Precision Predictions for the Light *CP*-Even Higgs Boson Mass of the Minimal Supersymmetric Standard Model, Phys. Rev. Lett. **112**, 141801 (2014).

G. Aad,[85] B. Abbott,[113] J. Abdallah,[151] O. Abdinov,[11] R. Aben,[107] M. Abolins,[90] O. S. AbouZeid,[158] H. Abramowicz,[153] H. Abreu,[152] R. Abreu,[116] Y. Abulaiti,[146a,146b] B. S. Acharya,[164a,164b,b] L. Adamczyk,[38a] D. L. Adams,[25] J. Adelman,[108] S. Adomeit,[100] T. Adye,[131] A. A. Affolder,[74] T. Agatonovic-Jovin,[13] J. Agricola,[54] J. A. Aguilar-Saavedra,[126a,126f] S. P. Ahlen,[22] F. Ahmadov,[65,c] G. Aielli,[133a,133b] H. Akerstedt,[146a,146b] T. P. A. Åkesson,[81] A. V. Akimov,[96] G. L. Alberghi,[20a,20b] J. Albert,[169] S. Albrand,[55] M. J. Alconada Verzini,[71] M. Aleksa,[30] I. N. Aleksandrov,[65] C. Alexa,[26b] G. Alexander,[153] T. Alexopoulos,[10] M. Alhroob,[113] G. Alimonti,[91a] L. Alio,[85] J. Alison,[31] S. P. Alkire,[35] B. M. M. Allbrooke,[149] P. P. Allport,[18] A. Aloisio,[104a,104b] A. Alonso,[36] F. Alonso,[71] C. Alpigiani,[138] A. Altheimer,[35] B. Alvarez Gonzalez,[30] D. Álvarez Piqueras,[167] M. G. Alviggi,[104a,104b] B. T. Amadio,[15] K. Amako,[66] Y. Amaral Coutinho,[24a] C. Amelung,[23] D. Amidei,[89] S. P. Amor Dos Santos,[126a,126c] A. Amorim,[126a,126b] S. Amoroso,[48] N. Amram,[153] G. Amundsen,[23] C. Anastopoulos,[139] L. S. Ancu,[49] N. Andari,[108] T. Andeen,[35] C. F. Anders,[58b] G. Anders,[30] J. K. Anders,[74] K. J. Anderson,[31] A. Andreazza,[91a,91b] V. Andrei,[58a] S. Angelidakis,[9] I. Angelozzi,[107] P. Anger,[44] A. Angerami,[35] F. Anghinolfi,[30] A. V. Anisenkov,[109,d] N. Anjos,[12] A. Annovi,[124a,124b] M. Antonelli,[47] A. Antonov,[98] J. Antos,[144b] F. Anulli,[132a] M. Aoki,[66] L. Aperio Bella,[18] G. Arabidze,[90] Y. Arai,[66] J. P. Araque,[126a] A. T. H. Arce,[45] F. A. Arduh,[71] J-F. Arguin,[95] S. Argyropoulos,[63] M. Arik,[19a] A. J. Armbruster,[30] O. Arnaez,[30] H. Arnold,[48] M. Arratia,[28] O. Arslan,[21] A. Artamonov,[97] G. Artoni,[23] S. Asai,[155] N. Asbah,[42] A. Ashkenazi,[153] B. Åsman,[146a,146b] L. Asquith,[149] K. Assamagan,[25] R. Astalos,[144a] M. Atkinson,[165] N. B. Atlay,[141] K. Augsten,[128] M. Aurousseau,[145b] G. Avolio,[30] B. Axen,[15] M. K. Ayoub,[117]

G. Azuelos,[95,e] M. A. Baak,[30] A. E. Baas,[58a] M. J. Baca,[18] C. Bacci,[134a,134b] H. Bachacou,[136] K. Bachas,[154] M. Backes,[30] M. Backhaus,[30] P. Bagiacchi,[132a,132b] P. Bagnaia,[132a,132b] Y. Bai,[33a] T. Bain,[35] J. T. Baines,[131] O. K. Baker,[176] E. M. Baldin,[109,d] P. Balek,[129] T. Balestri,[148] F. Balli,[84] W. K. Balunas,[122] E. Banas,[39] Sw. Banerjee,[173] A. A. E. Bannoura,[175] L. Barak,[30] E. L. Barberio,[88] D. Barberis,[50a,50b] M. Barbero,[85] T. Barillari,[101] M. Barisonzi,[164a,164b] T. Barklow,[143] N. Barlow,[28] S. L. Barnes,[84] B. M. Barnett,[131] R. M. Barnett,[15] Z. Barnovska,[5] A. Baroncelli,[134a] G. Barone,[23] A. J. Barr,[120] F. Barreiro,[82] J. Barreiro Guimarães da Costa,[57] R. Bartoldus,[143] A. E. Barton,[72] P. Bartos,[144a] A. Basalaev,[123] A. Bassalat,[117] A. Basye,[165] R. L. Bates,[53] S. J. Batista,[158] J. R. Batley,[28] M. Battaglia,[137] M. Bauce,[132a,132b] F. Bauer,[136] H. S. Bawa,[143,f] J. B. Beacham,[111] M. D. Beattie,[72] T. Beau,[80] P. H. Beauchemin,[161] R. Beccherle,[124a,124b] P. Bechtle,[21] H. P. Beck,[17,g] K. Becker,[120] M. Becker,[83] M. Beckingham,[170] C. Becot,[117] A. J. Beddall,[19b] A. Beddall,[19b] V. A. Bednyakov,[65] C. P. Bee,[148] L. J. Beemster,[107] T. A. Beermann,[30] M. Begel,[25] J. K. Behr,[120] C. Belanger-Champagne,[87] W. H. Bell,[49] G. Bella,[153] L. Bellagamba,[20a] A. Bellerive,[29] M. Bellomo,[86] K. Belotskiy,[98] O. Beltramello,[30] O. Benary,[153] D. Benchekroun,[135a] M. Bender,[100] K. Bendtz,[146a,146b] N. Benekos,[10] Y. Benhammou,[153] E. Benhar Noccioli,[49] J. A. Benitez Garcia,[159b] D. P. Benjamin,[45] J. R. Bensinger,[23] S. Bentvelsen,[107] L. Beresford,[120] M. Beretta,[47] D. Berge,[107] E. Bergeaas Kuutmann,[166] N. Berger,[5] F. Berghaus,[169] J. Beringer,[15] C. Bernard,[22] N. R. Bernard,[86] C. Bernius,[110] F. U. Bernlochner,[21] T. Berry,[77] P. Berta,[129] C. Bertella,[83] G. Bertoli,[146a,146b] F. Bertolucci,[124a,124b] C. Bertsche,[113] D. Bertsche,[113] M. I. Besana,[91a] G. J. Besjes,[36] O. Bessidskaia Bylund,[146a,146b] M. Bessner,[42] N. Besson,[136] C. Betancourt,[48] S. Bethke,[101] A. J. Bevan,[76] W. Bhimji,[15] R. M. Bianchi,[125] L. Bianchini,[23] M. Bianco,[30] O. Biebel,[100] D. Biedermann,[16] S. P. Bieniek,[78] N. V. Biesuz,[124a,124b] M. Biglietti,[134a] J. Bilbao De Mendizabal,[49] H. Bilokon,[47] M. Bindi,[54] S. Binet,[117] A. Bingul,[19b] C. Bini,[132a,132b] S. Biondi,[20a,20b] D. M. Bjergaard,[45] C. W. Black,[150] J. E. Black,[143] K. M. Black,[22] D. Blackburn,[138] R. E. Blair,[6] J.-B. Blanchard,[136] J. E. Blanco,[77] T. Blazek,[144a] I. Bloch,[42] C. Blocker,[23] W. Blum,[83,a] U. Blumenschein,[54] S. Blunier,[32a] G. J. Bobbink,[107] V. S. Bobrovnikov,[109,d] S. S. Bocchetta,[81] A. Bocci,[45] C. Bock,[100] M. Boehler,[48] J. A. Bogaerts,[30] D. Bogavac,[13] A. G. Bogdanchikov,[109] C. Bohm,[146a] V. Boisvert,[77] T. Bold,[38a] V. Boldea,[26b] A. S. Boldyrev,[99] M. Bomben,[80] M. Bona,[76] M. Boonekamp,[136] A. Borisov,[130] G. Borissov,[72] S. Borroni,[42] J. Bortfeldt,[100] V. Bortolotto,[60a,60b,60c] K. Bos,[107] D. Boscherini,[20a] M. Bosman,[12] J. Boudreau,[125] J. Bouffard,[2] E. V. Bouhova-Thacker,[72] D. Boumediene,[34] C. Bourdarios,[117] N. Bousson,[114] S. K. Boutle,[53] A. Boveia,[30] J. Boyd,[30] I. R. Boyko,[65] I. Bozic,[13] J. Bracinik,[18] A. Brandt,[8] G. Brandt,[54] O. Brandt,[58a] U. Bratzler,[156] B. Brau,[86] J. E. Brau,[116] H. M. Braun,[175,a] W. D. Breaden Madden,[53] K. Brendlinger,[122] A. J. Brennan,[88] L. Brenner,[107] R. Brenner,[166] S. Bressler,[172] T. M. Bristow,[46] D. Britton,[53] D. Britzger,[42] F. M. Brochu,[28] I. Brock,[21] R. Brock,[90] J. Bronner,[101] G. Brooijmans,[35] T. Brooks,[77] W. K. Brooks,[32b] J. Brosamer,[15] E. Brost,[116] P. A. Bruckman de Renstrom,[39] D. Bruncko,[144b] R. Bruneliere,[48] A. Bruni,[20a] G. Bruni,[20a] M. Bruschi,[20a] N. Bruscino,[21] L. Bryngemark,[81] T. Buanes,[14] Q. Buat,[142] P. Buchholz,[141] A. G. Buckley,[53] S. I. Buda,[26b] I. A. Budagov,[65] F. Buehrer,[48] L. Bugge,[119] M. K. Bugge,[119] O. Bulekov,[98] D. Bullock,[8] H. Burckhart,[30] S. Burdin,[74] C. D. Burgard,[48] B. Burghgrave,[108] S. Burke,[131] I. Burmeister,[43] E. Busato,[34] D. Büscher,[48] V. Büscher,[83] P. Bussey,[53] J. M. Butler,[22] A. I. Butt,[3] C. M. Buttar,[53] J. M. Butterworth,[78] P. Butti,[107] W. Buttinger,[25] A. Buzatu,[53] A. R. Buzykaev,[109,d] S. Cabrera Urbán,[167] D. Caforio,[128] V. M. Cairo,[37a,37b] O. Cakir,[4a] N. Calace,[49] P. Calafiura,[15] A. Calandri,[136] G. Calderini,[80] P. Calfayan,[100] L. P. Caloba,[24a] D. Calvet,[34] S. Calvet,[34] R. Camacho Toro,[31] S. Camarda,[42] P. Camarri,[133a,133b] D. Cameron,[119] R. Caminal Armadans,[165] S. Campana,[30] M. Campanelli,[78] A. Campoverde,[148] V. Canale,[104a,104b] A. Canepa,[159a] M. Cano Bret,[33e] J. Cantero,[82] R. Cantrill,[126a] T. Cao,[40] M. D. M. Capeans Garrido,[30] I. Caprini,[26b] M. Caprini,[26b] M. Capua,[37a,37b] R. Caputo,[83] R. M. Carbone,[35] R. Cardarelli,[133a] F. Cardillo,[48] T. Carli,[30] G. Carlino,[104a] L. Carminati,[91a,91b] S. Caron,[106] E. Carquin,[32a] G. D. Carrillo-Montoya,[30] J. R. Carter,[28] J. Carvalho,[126a,126c] D. Casadei,[78] M. P. Casado,[12] M. Casolino,[12] E. Castaneda-Miranda,[145a] A. Castelli,[107] V. Castillo Gimenez,[167] N. F. Castro,[126a,h] P. Catastini,[57] A. Catinaccio,[30] J. R. Catmore,[119] A. Cattai,[30] J. Caudron,[83] V. Cavaliere,[165] D. Cavalli,[91a] M. Cavalli-Sforza,[12] V. Cavasinni,[124a,124b] F. Ceradini,[134a,134b] B. C. Cerio,[45] K. Cerny,[129] A. S. Cerqueira,[24b] A. Cerri,[149] L. Cerrito,[76] F. Cerutti,[15] M. Cerv,[30] A. Cervelli,[17] S. A. Cetin,[19c] A. Chafaq,[135a] D. Chakraborty,[108] I. Chalupkova,[129] Y. L. Chan,[60a] P. Chang,[165] J. D. Chapman,[28] D. G. Charlton,[18] C. C. Chau,[158] C. A. Chavez Barajas,[149] S. Cheatham,[152] A. Chegwidden,[90] S. Chekanov,[6] S. V. Chekulaev,[159a] G. A. Chelkov,[65,i] M. A. Chelstowska,[89] C. Chen,[64] H. Chen,[25] K. Chen,[148] L. Chen,[33d,j] S. Chen,[33c] S. Chen,[155] X. Chen,[33f] Y. Chen,[67] H. C. Cheng,[89] Y. Cheng,[31] A. Cheplakov,[65] E. Cheremushkina,[130] R. Cherkaoui El Moursli,[135e] V. Chernyatin,[25,a] E. Cheu,[7] L. Chevalier,[136] V. Chiarella,[47] G. Chiarelli,[124a,124b] G. Chiodini,[73a] A. S. Chisholm,[18] R. T. Chislett,[78] A. Chitan,[26b] M. V. Chizhov,[65] K. Choi,[61] S. Chouridou,[9] B. K. B. Chow,[100] V. Christodoulou,[78] D. Chromek-Burckhart,[30] J. Chudoba,[127] A. J. Chuinard,[87]

J. J. Chwastowski,[39] L. Chytka,[115] G. Ciapetti,[132a,132b] A. K. Ciftci,[4a] D. Cinca,[53] V. Cindro,[75] I. A. Cioara,[21] A. Ciocio,[15] F. Cirotto,[104a,104b] Z. H. Citron,[172] M. Ciubancan,[26b] A. Clark,[49] B. L. Clark,[57] P. J. Clark,[46] R. N. Clarke,[15] C. Clement,[146a,146b] Y. Coadou,[85] M. Cobal,[164a,164c] A. Coccaro,[49] J. Cochran,[64] L. Coffey,[23] J. G. Cogan,[143] L. Colasurdo,[106] B. Cole,[35] S. Cole,[108] A. P. Colijn,[107] J. Collot,[55] T. Colombo,[58c] G. Compostella,[101] P. Conde Muiño,[126a,126b] E. Coniavitis,[48] S. H. Connell,[145b] I. A. Connelly,[77] V. Consorti,[48] S. Constantinescu,[26b] C. Conta,[121a,121b] G. Conti,[30] F. Conventi,[104a,k] M. Cooke,[15] B. D. Cooper,[78] A. M. Cooper-Sarkar,[120] T. Cornelissen,[175] M. Corradi,[20a] F. Corriveau,[87,l] A. Corso-Radu,[163] A. Cortes-Gonzalez,[12] G. Cortiana,[101] G. Costa,[91a] M. J. Costa,[167] D. Costanzo,[139] D. Côté,[8] G. Cottin,[28] G. Cowan,[77] B. E. Cox,[84] K. Cranmer,[110] G. Cree,[29] S. Crépé-Renaudin,[55] F. Crescioli,[80] W. A. Cribbs,[146a,146b] M. Crispin Ortuzar,[120] M. Cristinziani,[21] V. Croft,[106] G. Crosetti,[37a,37b] T. Cuhadar Donszelmann,[139] J. Cummings,[176] M. Curatolo,[47] J. Cúth,[83] C. Cuthbert,[150] H. Czirr,[141] P. Czodrowski,[3] S. D'Auria,[53] M. D'Onofrio,[74] M. J. Da Cunha Sargedas De Sousa,[126a,126b] C. Da Via,[84] W. Dabrowski,[38a] A. Dafinca,[120] T. Dai,[89] O. Dale,[14] F. Dallaire,[95] C. Dallapiccola,[86] M. Dam,[36] J. R. Dandoy,[31] N. P. Dang,[48] A. C. Daniells,[18] M. Danninger,[168] M. Dano Hoffmann,[136] V. Dao,[48] G. Darbo,[50a] S. Darmora,[8] J. Dassoulas,[3] A. Dattagupta,[61] W. Davey,[21] C. David,[169] T. Davidek,[129] E. Davies,[120,m] M. Davies,[153] P. Davison,[78] Y. Davygora,[58a] E. Dawe,[88] I. Dawson,[139] R. K. Daya-Ishmukhametova,[86] K. De,[8] R. de Asmundis,[104a] A. De Benedetti,[113] S. De Castro,[20a,20b] S. De Cecco,[80] N. De Groot,[106] P. de Jong,[107] H. De la Torre,[82] F. De Lorenzi,[64] D. De Pedis,[132a] A. De Salvo,[132a] U. De Sanctis,[149] A. De Santo,[149] J. B. De Vivie De Regie,[117] W. J. Dearnaley,[72] R. Debbe,[25] C. Debenedetti,[137] D. V. Dedovich,[65] I. Deigaard,[107] J. Del Peso,[82] T. Del Prete,[124a,124b] D. Delgove,[117] F. Deliot,[136] C. M. Delitzsch,[49] M. Deliyergiyev,[75] A. Dell'Acqua,[30] L. Dell'Asta,[22] M. Dell'Orso,[124a,124b] M. Della Pietra,[104a,k] D. della Volpe,[49] M. Delmastro,[5] P. A. Delsart,[55] C. Deluca,[107] D. A. DeMarco,[158] S. Demers,[176] M. Demichev,[65] A. Demilly,[80] S. P. Denisov,[130] D. Derendarz,[39] J. E. Derkaoui,[135d] F. Derue,[80] P. Dervan,[74] K. Desch,[21] C. Deterre,[42] K. Dette,[43] P. O. Deviveiros,[30] A. Dewhurst,[131] S. Dhaliwal,[23] A. Di Ciaccio,[133a,133b] L. Di Ciaccio,[5] A. Di Domenico,[132a,132b] C. Di Donato,[132a,132b] A. Di Girolamo,[30] B. Di Girolamo,[30] A. Di Mattia,[152] B. Di Micco,[134a,134b] R. Di Nardo,[47] A. Di Simone,[48] R. Di Sipio,[158] D. Di Valentino,[29] C. Diaconu,[85] M. Diamond,[158] F. A. Dias,[46] M. A. Diaz,[32a] E. B. Diehl,[89] J. Dietrich,[16] S. Diglio,[85] A. Dimitrievska,[13] J. Dingfelder,[21] P. Dita,[26b] S. Dita,[26b] F. Dittus,[30] F. Djama,[85] T. Djobava,[51b] J. I. Djuvsland,[58a] M. A. B. do Vale,[24c] D. Dobos,[30] M. Dobre,[26b] C. Doglioni,[81] T. Dohmae,[155] J. Dolejsi,[129] Z. Dolezal,[129] B. A. Dolgoshein,[98,a] M. Donadelli,[24d] S. Donati,[124a,124b] P. Dondero,[121a,121b] J. Donini,[34] J. Dopke,[131] A. Doria,[104a] M. T. Dova,[71] A. T. Doyle,[53] E. Drechsler,[54] M. Dris,[10] E. Dubreuil,[34] E. Duchovni,[172] G. Duckeck,[100] O. A. Ducu,[26b,85] D. Duda,[107] A. Dudarev,[30] L. Duflot,[117] L. Duguid,[77] M. Dührssen,[30] M. Dunford,[58a] H. Duran Yildiz,[4a] M. Düren,[52] A. Durglishvili,[51b] D. Duschinger,[44] B. Dutta,[42] M. Dyndal,[38a] C. Eckardt,[42] K. M. Ecker,[101] R. C. Edgar,[89] W. Edson,[2] N. C. Edwards,[46] W. Ehrenfeld,[21] T. Eifert,[30] G. Eigen,[14] K. Einsweiler,[15] T. Ekelof,[166] M. El Kacimi,[135c] M. Ellert,[166] S. Elles,[5] F. Ellinghaus,[175] A. A. Elliot,[169] N. Ellis,[30] J. Elmsheuser,[100] M. Elsing,[30] D. Emeliyanov,[131] Y. Enari,[155] O. C. Endner,[83] M. Endo,[118] J. Erdmann,[43] A. Ereditato,[17] G. Ernis,[175] J. Ernst,[2] M. Ernst,[25] S. Errede,[165] E. Ertel,[83] M. Escalier,[117] H. Esch,[43] C. Escobar,[125] B. Esposito,[47] A. I. Etienvre,[136] E. Etzion,[153] H. Evans,[61] A. Ezhilov,[123] L. Fabbri,[20a,20b] G. Facini,[31] R. M. Fakhrutdinov,[130] S. Falciano,[132a] R. J. Falla,[78] J. Faltova,[129] Y. Fang,[33a] M. Fanti,[91a,91b] A. Farbin,[8] A. Farilla,[134a] T. Farooque,[12] S. Farrell,[15] S. M. Farrington,[170] P. Farthouat,[30] F. Fassi,[135e] P. Fassnacht,[30] D. Fassouliotis,[9] M. Faucci Giannelli,[77] A. Favareto,[50a,50b] L. Fayard,[117] O. L. Fedin,[123,n] W. Fedorko,[168] S. Feigl,[30] L. Feligioni,[85] C. Feng,[33d] E. J. Feng,[30] H. Feng,[89] A. B. Fenyuk,[130] L. Feremenga,[8] P. Fernandez Martinez,[167] S. Fernandez Perez,[30] J. Ferrando,[53] A. Ferrari,[166] P. Ferrari,[107] R. Ferrari,[121a] D. E. Ferreira de Lima,[53] A. Ferrer,[167] D. Ferrere,[49] C. Ferretti,[89] A. Ferretto Parodi,[50a,50b] M. Fiascaris,[31] F. Fiedler,[83] A. Filipčič,[75] M. Filipuzzi,[42] F. Filthaut,[106] M. Fincke-Keeler,[169] K. D. Finelli,[150] M. C. N. Fiolhais,[126a,126c] L. Fiorini,[167] A. Firan,[40] A. Fischer,[2] C. Fischer,[12] J. Fischer,[175] W. C. Fisher,[90] N. Flaschel,[42] I. Fleck,[141] P. Fleischmann,[89] G. T. Fletcher,[139] G. Fletcher,[76] R. R. M. Fletcher,[122] T. Flick,[175] A. Floderus,[81] L. R. Flores Castillo,[60a] M. J. Flowerdew,[101] A. Formica,[136] A. Forti,[84] D. Fournier,[117] H. Fox,[72] S. Fracchia,[12] P. Francavilla,[80] M. Franchini,[20a,20b] D. Francis,[30] L. Franconi,[119] M. Franklin,[57] M. Frate,[163] M. Fraternali,[121a,121b] D. Freeborn,[78] S. T. French,[28] F. Friedrich,[44] D. Froidevaux,[30] J. A. Frost,[120] R. Fuchi,[160] C. Fukunaga,[156] E. Fullana Torregrosa,[83] B. G. Fulsom,[143] T. Fusayasu,[102] J. Fuster,[167] C. Gabaldon,[55] O. Gabizon,[175] A. Gabrielli,[20a,20b] A. Gabrielli,[15] G. P. Gach,[18] S. Gadatsch,[30] S. Gadomski,[49] G. Gagliardi,[50a,50b] P. Gagnon,[61] C. Galea,[106] B. Galhardo,[126a,126c] E. J. Gallas,[120] B. J. Gallop,[131] P. Gallus,[128] G. Galster,[36] K. K. Gan,[111] J. Gao,[33b,85] Y. Gao,[46] Y. S. Gao,[143,f] F. M. Garay Walls,[46] F. Garberson,[176] C. García,[167] J. E. García Navarro,[167] M. Garcia-Sciveres,[15] R. W. Gardner,[31] N. Garelli,[143] V. Garonne,[119] C. Gatti,[47] A. Gaudiello,[50a,50b] G. Gaudio,[121a] B. Gaur,[141] L. Gauthier,[95]

P. Gauzzi,[132a,132b] I. L. Gavrilenko,[96] C. Gay,[168] G. Gaycken,[21] E. N. Gazis,[10] P. Ge,[33d] Z. Gecse,[168] C. N. P. Gee,[131] Ch. Geich-Gimbel,[21] M. P. Geisler,[58a] C. Gemme,[50a] M. H. Genest,[55] S. Gentile,[132a,132b] M. George,[54] S. George,[77] D. Gerbaudo,[163] A. Gershon,[153] S. Ghasemi,[141] H. Ghazlane,[135b] B. Giacobbe,[20a] S. Giagu,[132a,132b] V. Giangiobbe,[12] P. Giannetti,[124a,124b] B. Gibbard,[25] S. M. Gibson,[77] M. Gignac,[168] M. Gilchriese,[15] T. P. S. Gillam,[28] D. Gillberg,[30] G. Gilles,[34] D. M. Gingrich,[3,e] N. Giokaris,[9] M. P. Giordani,[164a,164c] F. M. Giorgi,[20a] F. M. Giorgi,[16] P. F. Giraud,[136] P. Giromini,[47] D. Giugni,[91a] C. Giuliani,[101] M. Giulini,[58b] B. K. Gjelsten,[119] S. Gkaitatzis,[154] I. Gkialas,[154] E. L. Gkougkousis,[117] L. K. Gladilin,[99] C. Glasman,[82] J. Glatzer,[30] P. C. F. Glaysher,[46] A. Glazov,[42] M. Goblirsch-Kolb,[101] J. R. Goddard,[76] J. Godlewski,[39] S. Goldfarb,[89] T. Golling,[49] D. Golubkov,[130] A. Gomes,[126a,126b,126d] R. Gonçalo,[126a] J. Goncalves Pinto Firmino Da Costa,[136] L. Gonella,[21] S. González de la Hoz,[167] G. Gonzalez Parra,[12] S. Gonzalez-Sevilla,[49] L. Goossens,[30] P. A. Gorbounov,[97] H. A. Gordon,[25] I. Gorelov,[105] B. Gorini,[30] E. Gorini,[73a,73b] A. Gorišek,[75] E. Gornicki,[39] A. T. Goshaw,[45] C. Gössling,[43] M. I. Gostkin,[65] D. Goujdami,[135c] A. G. Goussiou,[138] N. Govender,[145b] E. Gozani,[152] H. M. X. Grabas,[137] L. Graber,[54] I. Grabowska-Bold,[38a] P. O. J. Gradin,[166] P. Grafström,[20a,20b] J. Gramling,[49] E. Gramstad,[119] S. Grancagnolo,[16] V. Gratchev,[123] H. M. Gray,[30] E. Graziani,[134a] Z. D. Greenwood,[79,o] C. Grefe,[21] K. Gregersen,[78] I. M. Gregor,[42] P. Grenier,[143] J. Griffiths,[8] A. A. Grillo,[137] K. Grimm,[72] S. Grinstein,[12,p] Ph. Gris,[34] J.-F. Grivaz,[117] J. P. Grohs,[44] A. Grohsjean,[42] E. Gross,[172] J. Grosse-Knetter,[54] G. C. Grossi,[79] Z. J. Grout,[149] L. Guan,[89] J. Guenther,[128] F. Guescini,[49] D. Guest,[163] O. Gueta,[153] E. Guido,[50a,50b] T. Guillemin,[117] S. Guindon,[2] U. Gul,[53] C. Gumpert,[44] J. Guo,[33e] Y. Guo,[33b,q] S. Gupta,[120] G. Gustavino,[132a,132b] P. Gutierrez,[113] N. G. Gutierrez Ortiz,[78] C. Gutschow,[44] C. Guyot,[136] C. Gwenlan,[120] C. B. Gwilliam,[74] A. Haas,[110] C. Haber,[15] H. K. Hadavand,[8] N. Haddad,[135e] P. Haefner,[21] S. Hageböck,[21] Z. Hajduk,[39] H. Hakobyan,[177] M. Haleem,[42] J. Haley,[114] D. Hall,[120] G. Halladjian,[90] G. D. Hallewell,[85] K. Hamacher,[175] P. Hamal,[115] K. Hamano,[169] A. Hamilton,[145a] G. N. Hamity,[139] P. G. Hamnett,[42] L. Han,[33b] K. Hanagaki,[66,r] K. Hanawa,[155] M. Hance,[137] B. Haney,[122] P. Hanke,[58a] R. Hanna,[136] J. B. Hansen,[36] J. D. Hansen,[36] M. C. Hansen,[21] P. H. Hansen,[36] K. Hara,[160] A. S. Hard,[173] T. Harenberg,[175] F. Hariri,[117] S. Harkusha,[92] R. D. Harrington,[46] P. F. Harrison,[170] F. Hartjes,[107] M. Hasegawa,[67] Y. Hasegawa,[140] A. Hasib,[113] S. Hassani,[136] S. Haug,[17] R. Hauser,[90] L. Hauswald,[44] M. Havranek,[127] C. M. Hawkes,[18] R. J. Hawkings,[30] A. D. Hawkins,[81] T. Hayashi,[160] D. Hayden,[90] C. P. Hays,[120] J. M. Hays,[76] H. S. Hayward,[74] S. J. Haywood,[131] S. J. Head,[18] T. Heck,[83] V. Hedberg,[81] L. Heelan,[8] S. Heim,[122] T. Heim,[175] B. Heinemann,[15] L. Heinrich,[110] J. Hejbal,[127] L. Helary,[22] S. Hellman,[146a,146b] D. Hellmich,[21] C. Helsens,[12] J. Henderson,[120] R. C. W. Henderson,[72] Y. Heng,[173] C. Hengler,[42] S. Henkelmann,[168] A. Henrichs,[176] A. M. Henriques Correia,[30] S. Henrot-Versille,[117] G. H. Herbert,[16] Y. Hernández Jiménez,[167] G. Herten,[48] R. Hertenberger,[100] L. Hervas,[30] G. G. Hesketh,[78] N. P. Hessey,[107] J. W. Hetherly,[40] R. Hickling,[76] E. Higón-Rodriguez,[167] E. Hill,[169] J. C. Hill,[28] K. H. Hiller,[42] S. J. Hillier,[18] I. Hinchliffe,[15] E. Hines,[122] R. R. Hinman,[15] M. Hirose,[157] D. Hirschbuehl,[175] J. Hobbs,[148] N. Hod,[107] M. C. Hodgkinson,[139] P. Hodgson,[139] A. Hoecker,[30] M. R. Hoeferkamp,[105] F. Hoenig,[100] M. Hohlfeld,[83] D. Hohn,[21] T. R. Holmes,[15] M. Homann,[43] T. M. Hong,[125] W. H. Hopkins,[116] Y. Horii,[103] A. J. Horton,[142] J-Y. Hostachy,[55] S. Hou,[151] A. Hoummada,[135a] J. Howard,[120] J. Howarth,[42] M. Hrabovsky,[115] I. Hristova,[16] J. Hrivnac,[117] T. Hryn'ova,[5] A. Hrynevich,[93] C. Hsu,[145c] P. J. Hsu,[151,s] S.-C. Hsu,[138] D. Hu,[35] Q. Hu,[33b] X. Hu,[89] Y. Huang,[42] Z. Hubacek,[128] F. Hubaut,[85] F. Huegging,[21] T. B. Huffman,[120] E. W. Hughes,[35] G. Hughes,[72] M. Huhtinen,[30] T. A. Hülsing,[83] N. Huseynov,[65,c] J. Huston,[90] J. Huth,[57] G. Iacobucci,[49] G. Iakovidis,[25] I. Ibragimov,[141] L. Iconomidou-Fayard,[117] E. Ideal,[176] Z. Idrissi,[135e] P. Iengo,[30] O. Igonkina,[107] T. Iizawa,[171] Y. Ikegami,[66] K. Ikematsu,[141] M. Ikeno,[66] Y. Ilchenko,[31,t] D. Iliadis,[154] N. Ilic,[143] T. Ince,[101] G. Introzzi,[121a,121b] P. Ioannou,[9] M. Iodice,[134a] K. Iordanidou,[35] V. Ippolito,[57] A. Irles Quiles,[167] C. Isaksson,[166] M. Ishino,[68] M. Ishitsuka,[157] R. Ishmukhametov,[111] C. Issever,[120] S. Istin,[19a] J. M. Iturbe Ponce,[84] R. Iuppa,[133a,133b] J. Ivarsson,[81] W. Iwanski,[39] H. Iwasaki,[66] J. M. Izen,[41] V. Izzo,[104a] S. Jabbar,[3] B. Jackson,[122] M. Jackson,[74] P. Jackson,[1] M. R. Jaekel,[30] V. Jain,[2] K. Jakobs,[48] S. Jakobsen,[30] T. Jakoubek,[127] J. Jakubek,[128] D. O. Jamin,[114] D. K. Jana,[79] E. Jansen,[78] R. Jansky,[62] J. Janssen,[21] M. Janus,[54] G. Jarlskog,[81] N. Javadov,[65,c] T. Javůrek,[48] L. Jeanty,[15] J. Jejelava,[51a,u] G.-Y. Jeng,[150] D. Jennens,[88] P. Jenni,[48,v] J. Jentzsch,[43] C. Jeske,[170] S. Jézéquel,[5] H. Ji,[173] J. Jia,[148] Y. Jiang,[33b] S. Jiggins,[78] J. Jimenez Pena,[167] S. Jin,[33a] A. Jinaru,[26b] O. Jinnouchi,[157] M. D. Joergensen,[36] P. Johansson,[139] K. A. Johns,[7] W. J. Johnson,[138] K. Jon-And,[146a,146b] G. Jones,[170] R. W. L. Jones,[72] T. J. Jones,[74] J. Jongmanns,[58a] P. M. Jorge,[126a,126b] K. D. Joshi,[84] J. Jovicevic,[159a] X. Ju,[173] P. Jussel,[62] A. Juste Rozas,[12,p] M. Kaci,[167] A. Kaczmarska,[39] M. Kado,[117] H. Kagan,[111] M. Kagan,[143] S. J. Kahn,[85] E. Kajomovitz,[45] C. W. Kalderon,[120] S. Kama,[40] A. Kamenshchikov,[130] N. Kanaya,[155] S. Kaneti,[28] V. A. Kantserov,[98] J. Kanzaki,[66] B. Kaplan,[110] L. S. Kaplan,[173] A. Kapliy,[31] D. Kar,[145c] K. Karakostas,[10] A. Karamaoun,[3] N. Karastathis,[10,107] M. J. Kareem,[54] E. Karentzos,[10] M. Karnevskiy,[83] S. N. Karpov,[65]

Z. M. Karpova,[65] K. Karthik,[110] V. Kartvelishvili,[72] A. N. Karyukhin,[130] K. Kasahara,[160] L. Kashif,[173] R. D. Kass,[111] A. Kastanas,[14] Y. Kataoka,[155] C. Kato,[155] A. Katre,[49] J. Katzy,[42] K. Kawade,[103] K. Kawagoe,[70] T. Kawamoto,[155] G. Kawamura,[54] S. Kazama,[155] V. F. Kazanin,[109,d] R. Keeler,[169] R. Kehoe,[40] J. S. Keller,[42] J. J. Kempster,[77] H. Keoshkerian,[84] O. Kepka,[127] B. P. Kerševan,[75] S. Kersten,[175] R. A. Keyes,[87] F. Khalil-zada,[11] H. Khandanyan,[146a,146b] A. Khanov,[114] A. G. Kharlamov,[109,d] T. J. Khoo,[28] V. Khovanskiy,[97] E. Khramov,[65] J. Khubua,[51b,w] S. Kido,[67] H. Y. Kim,[8] S. H. Kim,[160] Y. K. Kim,[31] N. Kimura,[154] O. M. Kind,[16] B. T. King,[74] M. King,[167] S. B. King,[168] J. Kirk,[131] A. E. Kiryunin,[101] T. Kishimoto,[67] D. Kisielewska,[38a] F. Kiss,[48] K. Kiuchi,[160] O. Kivernyk,[136] E. Kladiva,[144b] M. H. Klein,[35] M. Klein,[74] U. Klein,[74] K. Kleinknecht,[83] P. Klimek,[146a,146b] A. Klimentov,[25] R. Klingenberg,[43] J. A. Klinger,[139] T. Klioutchnikova,[30] E.-E. Kluge,[58a] P. Kluit,[107] S. Kluth,[101] J. Knapik,[39] E. Kneringer,[62] E. B. F. G. Knoops,[85] A. Knue,[53] A. Kobayashi,[155] D. Kobayashi,[157] T. Kobayashi,[155] M. Kobel,[44] M. Kocian,[143] P. Kodys,[129] T. Koffas,[29] E. Koffeman,[107] L. A. Kogan,[120] S. Kohlmann,[175] Z. Kohout,[128] T. Kohriki,[66] T. Koi,[143] H. Kolanoski,[16] M. Kolb,[58b] I. Koletsou,[5] A. A. Komar,[96,a] Y. Komori,[155] T. Kondo,[66] N. Kondrashova,[42] K. Köneke,[48] A. C. König,[106] T. Kono,[66] R. Konoplich,[110,x] N. Konstantinidis,[78] R. Kopeliansky,[152] S. Koperny,[38a] L. Köpke,[83] A. K. Kopp,[48] K. Korcyl,[39] K. Kordas,[154] A. Korn,[78] A. A. Korol,[109,d] I. Korolkov,[12] E. V. Korolkova,[139] O. Kortner,[101] S. Kortner,[101] T. Kosek,[129] V. V. Kostyukhin,[21] V. M. Kotov,[65] A. Kotwal,[45] A. Kourkoumeli-Charalampidi,[154] C. Kourkoumelis,[9] V. Kouskoura,[25] A. Koutsman,[159a] R. Kowalewski,[169] T. Z. Kowalski,[38a] W. Kozanecki,[136] A. S. Kozhin,[130] V. A. Kramarenko,[99] G. Kramberger,[75] D. Krasnopevtsev,[98] M. W. Krasny,[80] A. Krasznahorkay,[30] J. K. Kraus,[21] A. Kravchenko,[25] S. Kreiss,[110] M. Kretz,[58c] J. Kretzschmar,[74] K. Kreutzfeldt,[52] P. Krieger,[158] K. Krizka,[31] K. Kroeninger,[43] H. Kroha,[101] J. Kroll,[122] J. Kroseberg,[21] J. Krstic,[13] U. Kruchonak,[65] H. Krüger,[21] N. Krumnack,[64] A. Kruse,[173] M. C. Kruse,[45] M. Kruskal,[22] T. Kubota,[88] H. Kucuk,[78] S. Kuday,[4b] S. Kuehn,[48] A. Kugel,[58c] F. Kuger,[174] A. Kuhl,[137] T. Kuhl,[42] V. Kukhtin,[65] R. Kukla,[136] Y. Kulchitsky,[92] S. Kuleshov,[32b] M. Kuna,[132a,132b] T. Kunigo,[68] A. Kupco,[127] H. Kurashige,[67] Y. A. Kurochkin,[92] V. Kus,[127] E. S. Kuwertz,[169] M. Kuze,[157] J. Kvita,[115] T. Kwan,[169] D. Kyriazopoulos,[139] A. La Rosa,[137] J. L. La Rosa Navarro,[24d] L. La Rotonda,[37a,37b] C. Lacasta,[167] F. Lacava,[132a,132b] J. Lacey,[29] H. Lacker,[16] D. Lacour,[80] V. R. Lacuesta,[167] E. Ladygin,[65] R. Lafaye,[5] B. Laforge,[80] T. Lagouri,[176] S. Lai,[54] L. Lambourne,[78] S. Lammers,[61] C. L. Lampen,[7] W. Lampl,[7] E. Lançon,[136] U. Landgraf,[48] M. P. J. Landon,[76] V. S. Lang,[58a] J. C. Lange,[12] A. J. Lankford,[163] F. Lanni,[25] K. Lantzsch,[21] A. Lanza,[121a] S. Laplace,[80] C. Lapoire,[30] J. F. Laporte,[136] T. Lari,[91a] F. Lasagni Manghi,[20a,20b] M. Lassnig,[30] P. Laurelli,[47] W. Lavrijsen,[15] A. T. Law,[137] P. Laycock,[74] T. Lazovich,[57] O. Le Dortz,[80] E. Le Guirriec,[85] E. Le Menedeu,[12] M. LeBlanc,[169] T. LeCompte,[6] F. Ledroit-Guillon,[55] C. A. Lee,[145a] S. C. Lee,[151] L. Lee,[1] G. Lefebvre,[80] M. Lefebvre,[169] F. Legger,[100] C. Leggett,[15] A. Lehan,[74] G. Lehmann Miotto,[30] X. Lei,[7] W. A. Leight,[29] A. Leisos,[154,y] A. G. Leister,[176] M. A. L. Leite,[24d] R. Leitner,[129] D. Lellouch,[172] B. Lemmer,[54] K. J. C. Leney,[78] T. Lenz,[21] B. Lenzi,[30] R. Leone,[7] S. Leone,[124a,124b] C. Leonidopoulos,[46] S. Leontsinis,[10] C. Leroy,[95] C. G. Lester,[28] M. Levchenko,[123] J. Levêque,[5] D. Levin,[89] L. J. Levinson,[172] M. Levy,[18] A. Lewis,[120] A. M. Leyko,[21] M. Leyton,[41] B. Li,[33b,z] H. Li,[148] H. L. Li,[31] L. Li,[45] L. Li,[33e] S. Li,[45] X. Li,[84] Y. Li,[33c,aa] Z. Liang,[137] H. Liao,[34] B. Liberti,[133a] A. Liblong,[158] P. Lichard,[30] K. Lie,[165] J. Liebal,[21] W. Liebig,[14] C. Limbach,[21] A. Limosani,[150] S. C. Lin,[151,bb] T. H. Lin,[83] F. Linde,[107] B. E. Lindquist,[148] J. T. Linnemann,[90] E. Lipeles,[122] A. Lipniacka,[14] M. Lisovyi,[58b] T. M. Liss,[165] D. Lissauer,[25] A. Lister,[168] A. M. Litke,[137] B. Liu,[151,cc] D. Liu,[151] H. Liu,[89] J. Liu,[85] J. B. Liu,[33b] K. Liu,[85] L. Liu,[165] M. Liu,[45] M. Liu,[33b] Y. Liu,[33b] M. Livan,[121a,121b] A. Lleres,[55] J. Llorente Merino,[82] S. L. Lloyd,[76] F. Lo Sterzo,[151] E. Lobodzinska,[42] P. Loch,[7] W. S. Lockman,[137] F. K. Loebinger,[84] A. E. Loevschall-Jensen,[36] K. M. Loew,[23] A. Loginov,[176] T. Lohse,[16] K. Lohwasser,[42] M. Lokajicek,[127] B. A. Long,[22] J. D. Long,[165] R. E. Long,[72] K. A. Looper,[111] L. Lopes,[126a] D. Lopez Mateos,[57] B. Lopez Paredes,[139] I. Lopez Paz,[12] J. Lorenz,[100] N. Lorenzo Martinez,[61] M. Losada,[162] P. J. Lösel,[100] X. Lou,[33a] A. Lounis,[117] J. Love,[6] P. A. Love,[72] H. Lu,[60a] N. Lu,[89] H. J. Lubatti,[138] C. Luci,[132a,132b] A. Lucotte,[55] C. Luedtke,[48] F. Luehring,[61] W. Lukas,[62] L. Luminari,[132a] O. Lundberg,[146a,146b] B. Lund-Jensen,[147] D. Lynn,[25] R. Lysak,[127] E. Lytken,[81] H. Ma,[25] L. L. Ma,[33d] G. Maccarrone,[47] A. Macchiolo,[101] C. M. Macdonald,[139] B. Maček,[75] J. Machado Miguens,[122,126b] D. Macina,[30] D. Madaffari,[85] R. Madar,[34] H. J. Maddocks,[72] W. F. Mader,[44] A. Madsen,[166] J. Maeda,[67] S. Maeland,[14] T. Maeno,[25] A. Maevskiy,[99] E. Magradze,[54] K. Mahboubi,[48] J. Mahlstedt,[107] C. Maiani,[136] C. Maidantchik,[24a] A. A. Maier,[101] T. Maier,[100] A. Maio,[126a,126b,126d] S. Majewski,[116] Y. Makida,[66] N. Makovec,[117] B. Malaescu,[80] Pa. Malecki,[39] V. P. Maleev,[123] F. Malek,[55] U. Mallik,[63] D. Malon,[6] C. Malone,[143] S. Maltezos,[10] V. M. Malyshev,[109] S. Malyukov,[30] J. Mamuzic,[42] G. Mancini,[47] B. Mandelli,[30] L. Mandelli,[91a] I. Mandić,[75] R. Mandrysch,[63] J. Maneira,[126a,126b] A. Manfredini,[101] L. Manhaes de Andrade Filho,[24b] J. Manjarres Ramos,[159b] A. Mann,[100] A. Manousakis-Katsikakis,[9] B. Mansoulie,[136] R. Mantifel,[87] M. Mantoani,[54] L. Mapelli,[30] L. March,[145c] G. Marchiori,[80]

M. Marcisovsky,[127] C. P. Marino,[169] M. Marjanovic,[13] D. E. Marley,[89] F. Marroquim,[24a] S. P. Marsden,[84] Z. Marshall,[15] L. F. Marti,[17] S. Marti-Garcia,[167] B. Martin,[90] T. A. Martin,[170] V. J. Martin,[46] B. Martin dit Latour,[14] M. Martinez,[12,p] S. Martin-Haugh,[131] V. S. Martoiu,[26b] A. C. Martyniuk,[78] M. Marx,[138] F. Marzano,[132a] A. Marzin,[30] L. Masetti,[83] T. Mashimo,[155] R. Mashinistov,[96] J. Masik,[84] A. L. Maslennikov,[109,d] I. Massa,[20a,20b] L. Massa,[20a,20b] P. Mastrandrea,[5] A. Mastroberardino,[37a,37b] T. Masubuchi,[155] P. Mättig,[175] J. Mattmann,[83] J. Maurer,[26b] S. J. Maxfield,[74] D. A. Maximov,[109,d] R. Mazini,[151] S. M. Mazza,[91a,91b] G. Mc Goldrick,[158] S. P. Mc Kee,[89] A. McCarn,[89] R. L. McCarthy,[148] T. G. McCarthy,[29] N. A. McCubbin,[131] K. W. McFarlane,[56,a] J. A. Mcfayden,[78] G. Mchedlidze,[54] S. J. McMahon,[131] R. A. McPherson,[169,l] M. Medinnis,[42] S. Meehan,[145a] S. Mehlhase,[100] A. Mehta,[74] K. Meier,[58a] C. Meineck,[100] B. Meirose,[41] B. R. Mellado Garcia,[145c] F. Meloni,[17] A. Mengarelli,[20a,20b] S. Menke,[101] E. Meoni,[161] K. M. Mercurio,[57] S. Mergelmeyer,[21] P. Mermod,[49] L. Merola,[104a,104b] C. Meroni,[91a] F. S. Merritt,[31] A. Messina,[132a,132b] J. Metcalfe,[25] A. S. Mete,[163] C. Meyer,[83] C. Meyer,[122] J-P. Meyer,[136] J. Meyer,[107] H. Meyer Zu Theenhausen,[58a] R. P. Middleton,[131] S. Miglioranzi,[164a,164c] L. Mijović,[21] G. Mikenberg,[172] M. Mikestikova,[127] M. Mikuž,[75] M. Milesi,[88] A. Milic,[30] D. W. Miller,[31] C. Mills,[46] A. Milov,[172] D. A. Milstead,[146a,146b] A. A. Minaenko,[130] Y. Minami,[155] I. A. Minashvili,[65] A. I. Mincer,[110] B. Mindur,[38a] M. Mineev,[65] Y. Ming,[173] L. M. Mir,[12] K. P. Mistry,[122] T. Mitani,[171] J. Mitrevski,[100] V. A. Mitsou,[167] A. Miucci,[49] P. S. Miyagawa,[139] J. U. Mjörnmark,[81] T. Moa,[146a,146b] K. Mochizuki,[85] S. Mohapatra,[35] W. Mohr,[48] S. Molander,[146a,146b] R. Moles-Valls,[21] R. Monden,[68] K. Mönig,[42] C. Monini,[55] J. Monk,[36] E. Monnier,[85] A. Montalbano,[148] J. Montejo Berlingen,[12] F. Monticelli,[71] S. Monzani,[132a,132b] R. W. Moore,[3] N. Morange,[117] D. Moreno,[162] M. Moreno Llácer,[54] P. Morettini,[50a] D. Mori,[142] T. Mori,[155] M. Morii,[57] M. Morinaga,[155] V. Morisbak,[119] S. Moritz,[83] A. K. Morley,[150] G. Mornacchi,[30] J. D. Morris,[76] S. S. Mortensen,[36] A. Morton,[53] L. Morvaj,[103] M. Mosidze,[51b] J. Moss,[143] K. Motohashi,[157] R. Mount,[143] E. Mountricha,[25] S. V. Mouraviev,[96,a] E. J. W. Moyse,[86] S. Muanza,[85] R. D. Mudd,[18] F. Mueller,[101] J. Mueller,[125] R. S. P. Mueller,[100] T. Mueller,[28] D. Muenstermann,[49] P. Mullen,[53] G. A. Mullier,[17] J. A. Murillo Quijada,[18] W. J. Murray,[170,131] H. Musheghyan,[54] E. Musto,[152] A. G. Myagkov,[130,dd] M. Myska,[128] B. P. Nachman,[143] O. Nackenhorst,[54] J. Nadal,[54] K. Nagai,[120] R. Nagai,[157] Y. Nagai,[85] K. Nagano,[66] A. Nagarkar,[111] Y. Nagasaka,[59] K. Nagata,[160] M. Nagel,[101] E. Nagy,[85] A. M. Nairz,[30] Y. Nakahama,[30] K. Nakamura,[66] T. Nakamura,[155] I. Nakano,[112] H. Namasivayam,[41] R. F. Naranjo Garcia,[42] R. Narayan,[31] D. I. Narrias Villar,[58a] T. Naumann,[42] G. Navarro,[162] R. Nayyar,[7] H. A. Neal,[89] P. Yu. Nechaeva,[96] T. J. Neep,[84] P. D. Nef,[143] A. Negri,[121a,121b] M. Negrini,[20a] S. Nektarijevic,[106] C. Nellist,[117] A. Nelson,[163] S. Nemecek,[127] P. Nemethy,[110] A. A. Nepomuceno,[24a] M. Nessi,[30,ee] M. S. Neubauer,[165] M. Neumann,[175] R. M. Neves,[110] P. Nevski,[25] P. R. Newman,[18] D. H. Nguyen,[6] R. B. Nickerson,[120] R. Nicolaidou,[136] B. Nicquevert,[30] J. Nielsen,[137] N. Nikiforou,[35] A. Nikiforov,[16] V. Nikolaenko,[130,dd] I. Nikolic-Audit,[80] K. Nikolopoulos,[18] J. K. Nilsen,[119] P. Nilsson,[25] Y. Ninomiya,[155] A. Nisati,[132a] R. Nisius,[101] T. Nobe,[155] M. Nomachi,[118] I. Nomidis,[29] T. Nooney,[76] S. Norberg,[113] M. Nordberg,[30] O. Novgorodova,[44] S. Nowak,[101] M. Nozaki,[66] L. Nozka,[115] K. Ntekas,[10] G. Nunes Hanninger,[88] T. Nunnemann,[100] E. Nurse,[78] F. Nuti,[88] B. J. O'Brien,[46] F. O'grady,[7] D. C. O'Neil,[142] V. O'Shea,[53] F. G. Oakham,[29,e] H. Oberlack,[101] T. Obermann,[21] J. Ocariz,[80] A. Ochi,[67] I. Ochoa,[35] J. P. Ochoa-Ricoux,[32a] S. Oda,[70] S. Odaka,[66] H. Ogren,[61] A. Oh,[84] S. H. Oh,[45] C. C. Ohm,[15] H. Ohman,[166] H. Oide,[30] W. Okamura,[118] H. Okawa,[160] Y. Okumura,[31] T. Okuyama,[66] A. Olariu,[26b] S. A. Olivares Pino,[46] D. Oliveira Damazio,[25] A. Olszewski,[39] J. Olszowska,[39] A. Onofre,[126a,126e] K. Onogi,[103] P. U. E. Onyisi,[31,t] C. J. Oram,[159a] M. J. Oreglia,[31] Y. Oren,[153] D. Orestano,[134a,134b] N. Orlando,[154] C. Oropeza Barrera,[53] R. S. Orr,[158] B. Osculati,[50a,50b] R. Ospanov,[84] G. Otero y Garzon,[27] H. Otono,[70] M. Ouchrif,[135d] F. Ould-Saada,[119] A. Ouraou,[136] K. P. Oussoren,[107] Q. Ouyang,[33a] A. Ovcharova,[15] M. Owen,[53] R. E. Owen,[18] V. E. Ozcan,[19a] N. Ozturk,[8] K. Pachal,[142] A. Pacheco Pages,[12] C. Padilla Aranda,[12] M. Pagáčová,[48] S. Pagan Griso,[15] E. Paganis,[139] F. Paige,[25] P. Pais,[86] K. Pajchel,[119] G. Palacino,[159b] S. Palestini,[30] M. Palka,[38b] D. Pallin,[34] A. Palma,[126a,126b] Y. B. Pan,[173] E. St. Panagiotopoulou,[10] C. E. Pandini,[80] J. G. Panduro Vazquez,[77] P. Pani,[146a,146b] S. Panitkin,[25] D. Pantea,[26b] L. Paolozzi,[49] Th. D. Papadopoulou,[10] K. Papageorgiou,[154] A. Paramonov,[6] D. Paredes Hernandez,[154] M. A. Parker,[28] K. A. Parker,[139] F. Parodi,[50a,50b] J. A. Parsons,[35] U. Parzefall,[48] E. Pasqualucci,[132a] S. Passaggio,[50a] F. Pastore,[134a,134b,a] Fr. Pastore,[77] G. Pásztor,[29] S. Pataraia,[175] N. D. Patel,[150] J. R. Pater,[84] T. Pauly,[30] J. Pearce,[169] B. Pearson,[113] L. E. Pedersen,[36] M. Pedersen,[119] S. Pedraza Lopez,[167] R. Pedro,[126a,126b] S. V. Peleganchuk,[109,d] D. Pelikan,[166] O. Penc,[127] C. Peng,[33a] H. Peng,[33b] B. Penning,[31] J. Penwell,[61] D. V. Perepelitsa,[25] E. Perez Codina,[159a] M. T. Pérez García-Estañ,[167] L. Perini,[91a,91b] H. Pernegger,[30] S. Perrella,[104a,104b] R. Peschke,[42] V. D. Peshekhonov,[65] K. Peters,[30] R. F. Y. Peters,[84] B. A. Petersen,[30] T. C. Petersen,[36] E. Petit,[42] A. Petridis,[1] C. Petridou,[154] P. Petroff,[117] E. Petrolo,[132a] F. Petrucci,[134a,134b] N. E. Pettersson,[157] R. Pezoa,[32b] P. W. Phillips,[131] G. Piacquadio,[143] E. Pianori,[170]

A. Picazio,[49] E. Piccaro,[76] M. Piccinini,[20a,20b] M. A. Pickering,[120] R. Piegaia,[27] D. T. Pignotti,[111] J. E. Pilcher,[31] A. D. Pilkington,[84] A. W. J. Pin,[84] J. Pina,[126a,126b,126d] M. Pinamonti,[164a,164c,ff] J. L. Pinfold,[3] A. Pingel,[36] S. Pires,[80] H. Pirumov,[42] M. Pitt,[172] C. Pizio,[91a,91b] L. Plazak,[144a] M.-A. Pleier,[25] V. Pleskot,[129] E. Plotnikova,[65] P. Plucinski,[146a,146b] D. Pluth,[64] R. Poettgen,[146a,146b] L. Poggioli,[117] D. Pohl,[21] G. Polesello,[121a] A. Poley,[42] A. Policicchio,[37a,37b] R. Polifka,[158] A. Polini,[20a] C. S. Pollard,[53] V. Polychronakos,[25] K. Pommès,[30] L. Pontecorvo,[132a] B. G. Pope,[90] G. A. Popeneciu,[26c] D. S. Popovic,[13] A. Poppleton,[30] S. Pospisil,[128] K. Potamianos,[15] I. N. Potrap,[65] C. J. Potter,[149] C. T. Potter,[116] G. Poulard,[30] J. Poveda,[30] V. Pozdnyakov,[65] P. Pralavorio,[85] A. Pranko,[15] S. Prasad,[30] S. Prell,[64] D. Price,[84] L. E. Price,[6] M. Primavera,[73a] S. Prince,[87] M. Proissl,[46] K. Prokofiev,[60c] F. Prokoshin,[32b] E. Protopapadaki,[136] S. Protopopescu,[25] J. Proudfoot,[6] M. Przybycien,[38a] E. Ptacek,[116] D. Puddu,[134a,134b] E. Pueschel,[86] D. Puldon,[148] M. Purohit,[25,gg] P. Puzo,[117] J. Qian,[89] G. Qin,[53] Y. Qin,[84] A. Quadt,[54] D. R. Quarrie,[15] W. B. Quayle,[164a,164b] M. Queitsch-Maitland,[84] D. Quilty,[53] S. Raddum,[119] V. Radeka,[25] V. Radescu,[42] S. K. Radhakrishnan,[148] P. Radloff,[116] P. Rados,[88] F. Ragusa,[91a,91b] G. Rahal,[178] S. Rajagopalan,[25] M. Rammensee,[30] C. Rangel-Smith,[166] F. Rauscher,[100] S. Rave,[83] T. Ravenscroft,[53] M. Raymond,[30] A. L. Read,[119] N. P. Readioff,[74] D. M. Rebuzzi,[121a,121b] A. Redelbach,[174] G. Redlinger,[25] R. Reece,[137] K. Reeves,[41] L. Rehnisch,[16] J. Reichert,[122] H. Reisin,[27] C. Rembser,[30] H. Ren,[33a] A. Renaud,[117] M. Rescigno,[132a] S. Resconi,[91a] O. L. Rezanova,[109,d] P. Reznicek,[129] R. Rezvani,[95] R. Richter,[101] S. Richter,[78] E. Richter-Was,[38b] O. Ricken,[21] M. Ridel,[80] P. Rieck,[16] C. J. Riegel,[175] J. Rieger,[54] O. Rifki,[113] M. Rijssenbeek,[148] A. Rimoldi,[121a,121b] L. Rinaldi,[20a] B. Ristić,[49] E. Ritsch,[30] I. Riu,[12] F. Rizatdinova,[114] E. Rizvi,[76] S. H. Robertson,[87,l] A. Robichaud-Veronneau,[87] D. Robinson,[28] J. E. M. Robinson,[42] A. Robson,[53] C. Roda,[124a,124b] S. Roe,[30] O. Røhne,[119] S. Rolli,[161] A. Romaniouk,[98] M. Romano,[20a,20b] S. M. Romano Saez,[34] E. Romero Adam,[167] N. Rompotis,[138] M. Ronzani,[48] L. Roos,[80] E. Ros,[167] S. Rosati,[132a] K. Rosbach,[48] P. Rose,[137] P. L. Rosendahl,[14] O. Rosenthal,[141] V. Rossetti,[146a,146b] E. Rossi,[104a,104b] L. P. Rossi,[50a] J. H. N. Rosten,[28] R. Rosten,[138] M. Rotaru,[26b] I. Roth,[172] J. Rothberg,[138] D. Rousseau,[117] C. R. Royon,[136] A. Rozanov,[85] Y. Rozen,[152] X. Ruan,[145c] F. Rubbo,[143] I. Rubinskiy,[42] V. I. Rud,[99] C. Rudolph,[44] M. S. Rudolph,[158] F. Rühr,[48] A. Ruiz-Martinez,[30] Z. Rurikova,[48] N. A. Rusakovich,[65] A. Ruschke,[100] H. L. Russell,[138] J. P. Rutherfoord,[7] N. Ruthmann,[30] Y. F. Ryabov,[123] M. Rybar,[165] G. Rybkin,[117] N. C. Ryder,[120] A. Ryzhov,[130] A. F. Saavedra,[150] G. Sabato,[107] S. Sacerdoti,[27] A. Saddique,[3] H. F-W. Sadrozinski,[137] R. Sadykov,[65] F. Safai Tehrani,[132a] P. Saha,[108] M. Sahinsoy,[58a] M. Saimpert,[136] T. Saito,[155] H. Sakamoto,[155] Y. Sakurai,[171] G. Salamanna,[134a,134b] A. Salamon,[133a] J. E. Salazar Loyola,[32b] M. Saleem,[113] D. Salek,[107] P. H. Sales De Bruin,[138] D. Salihagic,[101] A. Salnikov,[143] J. Salt,[167] D. Salvatore,[37a,37b] F. Salvatore,[149] A. Salvucci,[60a] A. Salzburger,[30] D. Sammel,[48] D. Sampsonidis,[154] A. Sanchez,[104a,104b] J. Sánchez,[167] V. Sanchez Martinez,[167] H. Sandaker,[119] R. L. Sandbach,[76] H. G. Sander,[83] M. P. Sanders,[100] M. Sandhoff,[175] C. Sandoval,[162] R. Sandstroem,[101] D. P. C. Sankey,[131] M. Sannino,[50a,50b] A. Sansoni,[47] C. Santoni,[34] R. Santonico,[133a,133b] H. Santos,[126a] I. Santoyo Castillo,[149] K. Sapp,[125] A. Sapronov,[65] J. G. Saraiva,[126a,126d] B. Sarrazin,[21] O. Sasaki,[66] Y. Sasaki,[155] K. Sato,[160] G. Sauvage,[5,a] E. Sauvan,[5] G. Savage,[77] P. Savard,[158,e] C. Sawyer,[131] L. Sawyer,[79,o] J. Saxon,[31] C. Sbarra,[20a] A. Sbrizzi,[20a,20b] T. Scanlon,[78] D. A. Scannicchio,[163] M. Scarcella,[150] V. Scarfone,[37a,37b] J. Schaarschmidt,[172] P. Schacht,[101] D. Schaefer,[30] R. Schaefer,[42] J. Schaeffer,[83] S. Schaepe,[21] S. Schaetzel,[58b] U. Schäfer,[83] A. C. Schaffer,[117] D. Schaile,[100] R. D. Schamberger,[148] V. Scharf,[58a] V. A. Schegelsky,[123] D. Scheirich,[129] M. Schernau,[163] C. Schiavi,[50a,50b] C. Schillo,[48] M. Schioppa,[37a,37b] S. Schlenker,[30] K. Schmieden,[30] C. Schmitt,[83] S. Schmitt,[58b] S. Schmitt,[42] B. Schneider,[159a] Y. J. Schnellbach,[74] U. Schnoor,[44] L. Schoeffel,[136] A. Schoening,[58b] B. D. Schoenrock,[90] E. Schopf,[21] A. L. S. Schorlemmer,[54] M. Schott,[83] D. Schouten,[159a] J. Schovancova,[8] S. Schramm,[49] M. Schreyer,[174] N. Schuh,[83] M. J. Schultens,[21] H.-C. Schultz-Coulon,[58a] H. Schulz,[16] M. Schumacher,[48] B. A. Schumm,[137] Ph. Schune,[136] C. Schwanenberger,[84] A. Schwartzman,[143] T. A. Schwarz,[89] Ph. Schwegler,[101] H. Schweiger,[84] Ph. Schwemling,[136] R. Schwienhorst,[90] J. Schwindling,[136] T. Schwindt,[21] F. G. Sciacca,[17] E. Scifo,[117] G. Sciolla,[23] F. Scuri,[124a,124b] F. Scutti,[21] J. Searcy,[89] G. Sedov,[42] E. Sedykh,[123] P. Seema,[21] S. C. Seidel,[105] A. Seiden,[137] F. Seifert,[128] J. M. Seixas,[24a] G. Sekhniaidze,[104a] K. Sekhon,[89] S. J. Sekula,[40] D. M. Seliverstov,[123,a] N. Semprini-Cesari,[20a,20b] C. Serfon,[30] L. Serin,[117] L. Serkin,[164a,164b] T. Serre,[85] M. Sessa,[134a,134b] R. Seuster,[159a] H. Severini,[113] T. Sfiligoj,[75] F. Sforza,[30] A. Sfyrla,[30] E. Shabalina,[54] M. Shamim,[116] L. Y. Shan,[33a] R. Shang,[165] J. T. Shank,[22] M. Shapiro,[15] P. B. Shatalov,[97] K. Shaw,[164a,164b] S. M. Shaw,[84] A. Shcherbakova,[146a,146b] C. Y. Shehu,[149] P. Sherwood,[78] L. Shi,[151,hh] S. Shimizu,[67] C. O. Shimmin,[163] M. Shimojima,[102] M. Shiyakova,[65] A. Shmeleva,[96] D. Shoaleh Saadi,[95] M. J. Shochet,[31] S. Shojaii,[91a,91b] S. Shrestha,[111] E. Shulga,[98] M. A. Shupe,[7] S. Shushkevich,[42] P. Sicho,[127] P. E. Sidebo,[147] O. Sidiropoulou,[174] D. Sidorov,[114] A. Sidoti,[20a,20b] F. Siegert,[44] Dj. Sijacki,[13] J. Silva,[126a,126d] Y. Silver,[153] S. B. Silverstein,[146a] V. Simak,[128] O. Simard,[5] Lj. Simic,[13] S. Simion,[117] E. Simioni,[83]

B. Simmons,[78] D. Simon,[34] P. Sinervo,[158] N. B. Sinev,[116] M. Sioli,[20a,20b] G. Siragusa,[174] A. N. Sisakyan,[65,a] S. Yu. Sivoklokov,[99] J. Sjölin,[146a,146b] T. B. Sjursen,[14] M. B. Skinner,[72] H. P. Skottowe,[57] P. Skubic,[113] M. Slater,[18] T. Slavicek,[128] M. Slawinska,[107] K. Sliwa,[161] V. Smakhtin,[172] B. H. Smart,[46] L. Smestad,[14] S. Yu. Smirnov,[98] Y. Smirnov,[98] L. N. Smirnova,[99,ii] O. Smirnova,[81] M. N. K. Smith,[35] R. W. Smith,[35] M. Smizanska,[72] K. Smolek,[128] A. A. Snesarev,[96] G. Snidero,[76] S. Snyder,[25] R. Sobie,[169,l] F. Socher,[44] A. Soffer,[153] D. A. Soh,[151,hh] G. Sokhrannyi,[75] C. A. Solans,[30] M. Solar,[128] J. Solc,[128] E. Yu. Soldatov,[98] U. Soldevila,[167] A. A. Solodkov,[130] A. Soloshenko,[65] O. V. Solovyanov,[130] V. Solovyev,[123] P. Sommer,[48] H. Y. Song,[33b,z] N. Soni,[1] A. Sood,[15] A. Sopczak,[128] B. Sopko,[128] V. Sopko,[128] V. Sorin,[12] D. Sosa,[58b] M. Sosebee,[8] C. L. Sotiropoulou,[124a,124b] R. Soualah,[164a,164c] A. M. Soukharev,[109,d] D. South,[42] B. C. Sowden,[77] S. Spagnolo,[73a,73b] M. Spalla,[124a,124b] M. Spangenberg,[170] F. Spanò,[77] W. R. Spearman,[57] D. Sperlich,[16] F. Spettel,[101] R. Spighi,[20a] G. Spigo,[30] L. A. Spiller,[88] M. Spousta,[129] R. D. St. Denis,[53,a] A. Stabile,[91a] S. Staerz,[44] J. Stahlman,[122] R. Stamen,[58a] S. Stamm,[16] E. Stanecka,[39] C. Stanescu,[134a] M. Stanescu-Bellu,[42] M. M. Stanitzki,[42] S. Stapnes,[119] E. A. Starchenko,[130] J. Stark,[55] P. Staroba,[127] P. Starovoitov,[58a] R. Staszewski,[39] P. Steinberg,[25] B. Stelzer,[142] H. J. Stelzer,[30] O. Stelzer-Chilton,[159a] H. Stenzel,[52] G. A. Stewart,[53] J. A. Stillings,[21] M. C. Stockton,[87] M. Stoebe,[87] G. Stoicea,[26b] P. Stolte,[54] S. Stonjek,[101] A. R. Stradling,[8] A. Straessner,[44] M. E. Stramaglia,[17] J. Strandberg,[147] S. Strandberg,[146a,146b] A. Strandlie,[119] E. Strauss,[143] M. Strauss,[113] P. Strizenec,[144b] R. Ströhmer,[174] D. M. Strom,[116] R. Stroynowski,[40] A. Strubig,[106] S. A. Stucci,[17] B. Stugu,[14] N. A. Styles,[42] D. Su,[143] J. Su,[125] R. Subramaniam,[79] A. Succurro,[12] S. Suchek,[58a] Y. Sugaya,[118] M. Suk,[128] V. V. Sulin,[96] S. Sultansoy,[4c] T. Sumida,[68] S. Sun,[57] X. Sun,[33a] J. E. Sundermann,[48] K. Suruliz,[149] G. Susinno,[37a,37b] M. R. Sutton,[149] S. Suzuki,[66] M. Svatos,[127] M. Swiatlowski,[143] I. Sykora,[144a] T. Sykora,[129] D. Ta,[48] C. Taccini,[134a,134b] K. Tackmann,[42] J. Taenzer,[158] A. Taffard,[163] R. Tafirout,[159a] N. Taiblum,[153] H. Takai,[25] R. Takashima,[69] H. Takeda,[67] T. Takeshita,[140] Y. Takubo,[66] M. Talby,[85] A. A. Talyshev,[109,d] J. Y. C. Tam,[174] K. G. Tan,[88] J. Tanaka,[155] R. Tanaka,[117] S. Tanaka,[66] B. B. Tannenwald,[111] N. Tannoury,[21] S. Tapia Araya,[32b] S. Tapprogge,[83] S. Tarem,[152] F. Tarrade,[29] G. F. Tartarelli,[91a] P. Tas,[129] M. Tasevsky,[127] T. Tashiro,[68] E. Tassi,[37a,37b] A. Tavares Delgado,[126a,126b] Y. Tayalati,[135d] F. E. Taylor,[94] G. N. Taylor,[88] P. T. E. Taylor,[88] W. Taylor,[159b] F. A. Teischinger,[30] M. Teixeira Dias Castanheira,[76] P. Teixeira-Dias,[77] K. K. Temming,[48] D. Temple,[142] H. Ten Kate,[30] P. K. Teng,[151] J. J. Teoh,[118] F. Tepel,[175] S. Terada,[66] K. Terashi,[155] J. Terron,[82] S. Terzo,[101] M. Testa,[47] R. J. Teuscher,[158,l] T. Theveneaux-Pelzer,[34] J. P. Thomas,[18] J. Thomas-Wilsker,[77] E. N. Thompson,[35] P. D. Thompson,[18] R. J. Thompson,[84] A. S. Thompson,[53] L. A. Thomsen,[176] E. Thomson,[122] M. Thomson,[28] R. P. Thun,[89,a] M. J. Tibbetts,[15] R. E. Ticse Torres,[85] V. O. Tikhomirov,[96,jj] Yu. A. Tikhonov,[109,d] S. Timoshenko,[98] E. Tiouchichine,[85] P. Tipton,[176] S. Tisserant,[85] K. Todome,[157] T. Todorov,[5,a] S. Todorova-Nova,[129] J. Tojo,[70] S. Tokár,[144a] K. Tokushuku,[66] K. Tollefson,[90] E. Tolley,[57] L. Tomlinson,[84] M. Tomoto,[103] L. Tompkins,[143,kk] K. Toms,[105] E. Torrence,[116] H. Torres,[142] E. Torró Pastor,[138] J. Toth,[85,ll] F. Touchard,[85] D. R. Tovey,[139] T. Trefzger,[174] L. Tremblet,[30] A. Tricoli,[30] I. M. Trigger,[159a] S. Trincaz-Duvoid,[80] M. F. Tripiana,[12] W. Trischuk,[158] B. Trocmé,[55] C. Troncon,[91a] M. Trottier-McDonald,[15] M. Trovatelli,[169] L. Truong,[164a,164c] M. Trzebinski,[39] A. Trzupek,[39] C. Tsarouchas,[30] J. C-L. Tseng,[120] P. V. Tsiareshka,[92] D. Tsionou,[154] G. Tsipolitis,[10] N. Tsirintanis,[9] S. Tsiskaridze,[12] V. Tsiskaridze,[48] E. G. Tskhadadze,[51a] K. M. Tsui,[60a] I. I. Tsukerman,[97] V. Tsulaia,[15] S. Tsuno,[66] D. Tsybychev,[148] A. Tudorache,[26b] V. Tudorache,[26b] A. N. Tuna,[57] S. A. Tupputi,[20a,20b] S. Turchikhin,[99,ii] D. Turecek,[128] R. Turra,[91a,91b] A. J. Turvey,[40] P. M. Tuts,[35] A. Tykhonov,[49] M. Tylmad,[146a,146b] M. Tyndel,[131] I. Ueda,[155] R. Ueno,[29] M. Ughetto,[146a,146b] M. Ugland,[14] F. Ukegawa,[160] G. Unal,[30] A. Undrus,[25] G. Unel,[163] F. C. Ungaro,[48] Y. Unno,[66] C. Unverdorben,[100] J. Urban,[144b] P. Urquijo,[88] P. Urrejola,[83] G. Usai,[8] A. Usanova,[62] L. Vacavant,[85] V. Vacek,[128] B. Vachon,[87] C. Valderanis,[83] N. Valencic,[107] S. Valentinetti,[20a,20b] A. Valero,[167] L. Valery,[12] S. Valkar,[129] S. Vallecorsa,[49] J. A. Valls Ferrer,[167] W. Van Den Wollenberg,[107] P. C. Van Der Deijl,[107] R. van der Geer,[107] H. van der Graaf,[107] N. van Eldik,[152] P. van Gemmeren,[6] J. Van Nieuwkoop,[142] I. van Vulpen,[107] M. C. van Woerden,[30] M. Vanadia,[132a,132b] W. Vandelli,[30] R. Vanguri,[122] A. Vaniachine,[6] F. Vannucci,[80] G. Vardanyan,[177] R. Vari,[132a] E. W. Varnes,[7] T. Varol,[40] D. Varouchas,[80] A. Vartapetian,[8] K. E. Varvell,[150] F. Vazeille,[34] T. Vazquez Schroeder,[87] J. Veatch,[7] L. M. Veloce,[158] F. Veloso,[126a,126c] T. Velz,[21] S. Veneziano,[132a] A. Ventura,[73a,73b] D. Ventura,[86] M. Venturi,[169] N. Venturi,[158] A. Venturini,[23] V. Vercesi,[121a] M. Verducci,[132a,132b] W. Verkerke,[107] J. C. Vermeulen,[107] A. Vest,[44] M. C. Vetterli,[142,e] O. Viazlo,[81] I. Vichou,[165] T. Vickey,[139] O. E. Vickey Boeriu,[139] G. H. A. Viehhauser,[120] S. Viel,[15] R. Vigne,[62] M. Villa,[20a,20b] M. Villaplana Perez,[91a,91b] E. Vilucchi,[47] M. G. Vincter,[29] V. B. Vinogradov,[65] I. Vivarelli,[149] F. Vives Vaque,[3] S. Vlachos,[10] D. Vladoiu,[100] M. Vlasak,[128] M. Vogel,[32a] P. Vokac,[128] G. Volpi,[124a,124b] M. Volpi,[88] H. von der Schmitt,[101] H. von Radziewski,[48] E. von Toerne,[21] V. Vorobel,[129] K. Vorobev,[98] M. Vos,[167] R. Voss,[30] J. H. Vossebeld,[74] N. Vranjes,[13]

M. Vranjes Milosavljevic,[13] V. Vrba,[127] M. Vreeswijk,[107] R. Vuillermet,[30] I. Vukotic,[31] Z. Vykydal,[128] P. Wagner,[21] W. Wagner,[175] H. Wahlberg,[71] S. Wahrmund,[44] J. Wakabayashi,[103] J. Walder,[72] R. Walker,[100] W. Walkowiak,[141] C. Wang,[151] F. Wang,[173] H. Wang,[15] H. Wang,[40] J. Wang,[42] J. Wang,[150] K. Wang,[87] R. Wang,[6] S. M. Wang,[151] T. Wang,[21] T. Wang,[35] X. Wang,[176] C. Wanotayaroj,[116] A. Warburton,[87] C. P. Ward,[28] D. R. Wardrope,[78] A. Washbrook,[46] C. Wasicki,[42] P. M. Watkins,[18] A. T. Watson,[18] I. J. Watson,[150] M. F. Watson,[18] G. Watts,[138] S. Watts,[84] B. M. Waugh,[78] S. Webb,[84] M. S. Weber,[17] S. W. Weber,[174] J. S. Webster,[31] A. R. Weidberg,[120] B. Weinert,[61] J. Weingarten,[54] C. Weiser,[48] H. Weits,[107] P. S. Wells,[30] T. Wenaus,[25] T. Wengler,[30] S. Wenig,[30] N. Wermes,[21] M. Werner,[48] P. Werner,[30] M. Wessels,[58a] J. Wetter,[161] K. Whalen,[116] A. M. Wharton,[72] A. White,[8] M. J. White,[1] R. White,[32b] S. White,[124a,124b] D. Whiteson,[163] F. J. Wickens,[131] W. Wiedenmann,[173] M. Wielers,[131] P. Wienemann,[21] C. Wiglesworth,[36] L. A. M. Wiik-Fuchs,[21] A. Wildauer,[101] H. G. Wilkens,[30] H. H. Williams,[122] S. Williams,[107] C. Willis,[90] S. Willocq,[86] A. Wilson,[89] J. A. Wilson,[18] I. Wingerter-Seez,[5] F. Winklmeier,[116] B. T. Winter,[21] M. Wittgen,[143] J. Wittkowski,[100] S. J. Wollstadt,[83] M. W. Wolter,[39] H. Wolters,[126a,126c] B. K. Wosiek,[39] J. Wotschack,[30] M. J. Woudstra,[84] K. W. Wozniak,[39] M. Wu,[55] M. Wu,[31] S. L. Wu,[173] X. Wu,[49] Y. Wu,[89] T. R. Wyatt,[84] B. M. Wynne,[46] S. Xella,[36] D. Xu,[33a] L. Xu,[25] B. Yabsley,[150] S. Yacoob,[145a] R. Yakabe,[67] M. Yamada,[66] D. Yamaguchi,[157] Y. Yamaguchi,[118] A. Yamamoto,[66] S. Yamamoto,[155] T. Yamanaka,[155] K. Yamauchi,[103] Y. Yamazaki,[67] Z. Yan,[22] H. Yang,[33e] H. Yang,[173] Y. Yang,[151] W-M. Yao,[15] Y. C. Yap,[80] Y. Yasu,[66] E. Yatsenko,[5] K. H. Yau Wong,[21] J. Ye,[40] S. Ye,[25] I. Yeletskikh,[65] A. L. Yen,[57] E. Yildirim,[42] K. Yorita,[171] R. Yoshida,[6] K. Yoshihara,[122] C. Young,[143] C. J. S. Young,[30] S. Youssef,[22] D. R. Yu,[15] J. Yu,[8] J. M. Yu,[89] J. Yu,[114] L. Yuan,[67] S. P. Y. Yuen,[21] A. Yurkewicz,[108] I. Yusuff,[28,mm] B. Zabinski,[39] R. Zaidan,[63] A. M. Zaitsev,[130,dd] J. Zalieckas,[14] A. Zaman,[148] S. Zambito,[57] L. Zanello,[132a,132b] D. Zanzi,[88] C. Zeitnitz,[175] M. Zeman,[128] A. Zemla,[38a] Q. Zeng,[143] K. Zengel,[23] O. Zenin,[130] T. Ženiš,[144a] D. Zerwas,[117] D. Zhang,[89] F. Zhang,[173] G. Zhang,[33b] H. Zhang,[33c] J. Zhang,[6] L. Zhang,[48] R. Zhang,[33b,j] X. Zhang,[33d] Z. Zhang,[117] X. Zhao,[40] Y. Zhao,[33d,117] Z. Zhao,[33b] A. Zhemchugov,[65] J. Zhong,[120] B. Zhou,[89] C. Zhou,[45] L. Zhou,[35] L. Zhou,[40] M. Zhou,[148] N. Zhou,[33f] C. G. Zhu,[33d] H. Zhu,[33a] J. Zhu,[89] Y. Zhu,[33b] X. Zhuang,[33a] K. Zhukov,[96] A. Zibell,[174] D. Zieminska,[61] N. I. Zimine,[65] C. Zimmermann,[83] S. Zimmermann,[48] Z. Zinonos,[54] M. Zinser,[83] M. Ziolkowski,[141] L. Živković,[13] G. Zobernig,[173] A. Zoccoli,[20a,20b] M. zur Nedden,[16] G. Zurzolo,[104a,104b] and L. Zwalinski[30]

(ATLAS Collaboration)

[1]*Department of Physics, University of Adelaide, Adelaide, Australia*
[2]*Physics Department, SUNY Albany, Albany, New York, USA*
[3]*Department of Physics, University of Alberta, Edmonton, Alberta, Canada*
[4a]*Department of Physics, Ankara University, Ankara, Turkey*
[4b]*Istanbul Aydin University, Istanbul, Turkey*
[4c]*Division of Physics, TOBB University of Economics and Technology, Ankara, Turkey*
[5]*LAPP, CNRS/IN2P3 and Université Savoie Mont Blanc, Annecy-le-Vieux, France*
[6]*High Energy Physics Division, Argonne National Laboratory, Argonne, Illinois, USA*
[7]*Department of Physics, University of Arizona, Tucson, Arizona, USA*
[8]*Department of Physics, The University of Texas at Arlington, Arlington, Texas, USA*
[9]*Physics Department, University of Athens, Athens, Greece*
[10]*Physics Department, National Technical University of Athens, Zografou, Greece*
[11]*Institute of Physics, Azerbaijan Academy of Sciences, Baku, Azerbaijan*
[12]*Institut de Física d'Altes Energies and Departament de Física de la Universitat Autònoma de Barcelona, Barcelona, Spain*
[13]*Institute of Physics, University of Belgrade, Belgrade, Serbia*
[14]*Department for Physics and Technology, University of Bergen, Bergen, Norway*
[15]*Physics Division, Lawrence Berkeley National Laboratory and University of California, Berkeley, California, USA*
[16]*Department of Physics, Humboldt University, Berlin, Germany*
[17]*Albert Einstein Center for Fundamental Physics and Laboratory for High Energy Physics, University of Bern, Bern, Switzerland*
[18]*School of Physics and Astronomy, University of Birmingham, Birmingham, United Kingdom*
[19a]*Department of Physics, Bogazici University, Istanbul, Turkey*
[19b]*Department of Physics Engineering, Gaziantep University, Gaziantep, Turkey*
[19c]*Department of Physics, Dogus University, Istanbul, Turkey*
[20a]*INFN Sezione di Bologna, Italy*

[20b]*Dipartimento di Fisica e Astronomia, Università di Bologna, Bologna, Italy*
[21]*Physikalisches Institut, University of Bonn, Bonn, Germany*
[22]*Department of Physics, Boston University, Boston, Massachusetts, USA*
[23]*Department of Physics, Brandeis University, Waltham Massachusetts, USA*
[24a]*Universidade Federal do Rio De Janeiro COPPE/EE/IF, Rio de Janeiro, Brazil*
[24b]*Electrical Circuits Department, Federal University of Juiz de Fora (UFJF), Juiz de Fora, Brazil*
[24c]*Federal University of Sao Joao del Rei (UFSJ), Sao Joao del Rei, Brazil*
[24d]*Instituto de Fisica, Universidade de Sao Paulo, Sao Paulo, Brazil*
[25]*Physics Department, Brookhaven National Laboratory, Upton, New York, USA*
[26a]*Transilvania University of Brasov, Brasov, Romania*
[26b]*National Institute of Physics and Nuclear Engineering, Bucharest, Romania*
[26c]*National Institute for Research and Development of Isotopic and Molecular Technologies, Physics Department, Cluj Napoca, Romania*
[26d]*University Politehnica Bucharest, Bucharest, Romania*
[26e]*West University in Timisoara, Timisoara, Romania*
[27]*Departamento de Física, Universidad de Buenos Aires, Buenos Aires, Argentina*
[28]*Cavendish Laboratory, University of Cambridge, Cambridge, United Kingdom*
[29]*Department of Physics, Carleton University, Ottawa, Ontario, Canada*
[30]*CERN, Geneva, Switzerland*
[31]*Enrico Fermi Institute, University of Chicago, Chicago, Illinois, USA*
[32a]*Departamento de Física, Pontificia Universidad Católica de Chile, Santiago, Chile*
[32b]*Departamento de Física, Universidad Técnica Federico Santa María, Valparaíso, Chile*
[33a]*Institute of High Energy Physics, Chinese Academy of Sciences, Beijing, China*
[33b]*Department of Modern Physics, University of Science and Technology of China, Anhui, China*
[33c]*Department of Physics, Nanjing University, Jiangsu, China*
[33d]*School of Physics, Shandong University, Shandong, China*
[33e]*Department of Physics and Astronomy, Shanghai Key Laboratory for Particle Physics and Cosmology, Shanghai Jiao Tong University, Shanghai, China*
[33f]*Physics Department, Tsinghua University, Beijing 100084, China*
[34]*Laboratoire de Physique Corpusculaire, Clermont Université and Université Blaise Pascal and CNRS/IN2P3, Clermont-Ferrand, France*
[35]*Nevis Laboratory, Columbia University, Irvington, New York, USA*
[36]*Niels Bohr Institute, University of Copenhagen, Kobenhavn, Denmark*
[37a]*INFN Gruppo Collegato di Cosenza, Laboratori Nazionali di Frascati, Italy*
[37b]*Dipartimento di Fisica, Università della Calabria, Rende, Italy*
[38a]*AGH University of Science and Technology, Faculty of Physics and Applied Computer Science, Krakow, Poland*
[38b]*Marian Smoluchowski Institute of Physics, Jagiellonian University, Krakow, Poland*
[39]*Institute of Nuclear Physics, Polish Academy of Sciences, Krakow, Poland*
[40]*Physics Department, Southern Methodist University, Dallas, Texas, USA*
[41]*Physics Department, University of Texas at Dallas, Richardson, Texas, USA*
[42]*DESY, Hamburg and Zeuthen, Germany*
[43]*Institut für Experimentelle Physik IV, Technische Universität Dortmund, Dortmund, Germany*
[44]*Institut für Kern- und Teilchenphysik, Technische Universität Dresden, Dresden, Germany*
[45]*Department of Physics, Duke University, Durham, North Carolina, USA*
[46]*SUPA—School of Physics and Astronomy, University of Edinburgh, Edinburgh, United Kingdom*
[47]*INFN Laboratori Nazionali di Frascati, Frascati, Italy*
[48]*Fakultät für Mathematik und Physik, Albert-Ludwigs-Universität, Freiburg, Germany*
[49]*Section de Physique, Université de Genève, Geneva, Switzerland*
[50a]*INFN Sezione di Genova, Italy*
[50b]*Dipartimento di Fisica, Università di Genova, Genova, Italy*
[51a]*E. Andronikashvili Institute of Physics, Iv. Javakhishvili Tbilisi State University, Tbilisi, Georgia*
[51b]*High Energy Physics Institute, Tbilisi State University, Tbilisi, Georgia*
[52]*II Physikalisches Institut, Justus-Liebig-Universität Giessen, Giessen, Germany*
[53]*SUPA—School of Physics and Astronomy, University of Glasgow, Glasgow, United Kingdom*
[54]*II Physikalisches Institut, Georg-August-Universität, Göttingen, Germany*
[55]*Laboratoire de Physique Subatomique et de Cosmologie, Université Grenoble-Alpes, CNRS/IN2P3, Grenoble, France*
[56]*Department of Physics, Hampton University, Hampton, Virginia, USA*
[57]*Laboratory for Particle Physics and Cosmology, Harvard University, Cambridge, Massachusetts, USA*

[58a]Kirchhoff-Institut für Physik, Ruprecht-Karls-Universität Heidelberg, Heidelberg, Germany
[58b]Physikalisches Institut, Ruprecht-Karls-Universität Heidelberg, Heidelberg, Germany
[58c]ZITI Institut für technische Informatik, Ruprecht-Karls-Universität Heidelberg, Mannheim, Germany
[59]Faculty of Applied Information Science, Hiroshima Institute of Technology, Hiroshima, Japan
[60a]Department of Physics, The Chinese University of Hong Kong, Shatin, N.T., Hong Kong, China
[60b]Department of Physics, The University of Hong Kong, Hong Kong, China
[60c]Department of Physics, The Hong Kong University of Science and Technology, Clear Water Bay, Kowloon, Hong Kong, China
[61]Department of Physics, Indiana University, Bloomington IN, United States of America
[62]Institut für Astro- und Teilchenphysik, Leopold-Franzens-Universität, Innsbruck, Austria
[63]University of Iowa, Iowa City, Iowa, USA
[64]Department of Physics and Astronomy, Iowa State University, Ames, Iowa, USA
[65]Joint Institute for Nuclear Research, JINR Dubna, Dubna, Russia
[66]KEK, High Energy Accelerator Research Organization, Tsukuba, Japan
[67]Graduate School of Science, Kobe University, Kobe, Japan
[68]Faculty of Science, Kyoto University, Kyoto, Japan
[69]Kyoto University of Education, Kyoto, Japan
[70]Department of Physics, Kyushu University, Fukuoka, Japan
[71]Instituto de Física La Plata, Universidad Nacional de La Plata and CONICET, La Plata, Argentina
[72]Physics Department, Lancaster University, Lancaster, United Kingdom
[73a]INFN Sezione di Lecce, Italy
[73b]Dipartimento di Matematica e Fisica, Università del Salento, Lecce, Italy
[74]Oliver Lodge Laboratory, University of Liverpool, Liverpool, United Kingdom
[75]Department of Physics, Jožef Stefan Institute and University of Ljubljana, Ljubljana, Slovenia
[76]School of Physics and Astronomy, Queen Mary University of London, London, United Kingdom
[77]Department of Physics, Royal Holloway University of London, Surrey, United Kingdom
[78]Department of Physics and Astronomy, University College London, London, United Kingdom
[79]Louisiana Tech University, Ruston, Louisiana, USA
[80]Laboratoire de Physique Nucléaire et de Hautes Energies, UPMC and Université Paris-Diderot and CNRS/IN2P3, Paris, France
[81]Fysiska institutionen, Lunds universitet, Lund, Sweden
[82]Departamento de Fisica Teorica C-15, Universidad Autonoma de Madrid, Madrid, Spain
[83]Institut für Physik, Universität Mainz, Mainz, Germany
[84]School of Physics and Astronomy, University of Manchester, Manchester, United Kingdom
[85]CPPM, Aix-Marseille Université and CNRS/IN2P3, Marseille, France
[86]Department of Physics, University of Massachusetts, Amherst, Massachusetts, USA
[87]Department of Physics, McGill University, Montreal, Québec, Canada
[88]School of Physics, University of Melbourne, Victoria, Australia
[89]Department of Physics, The University of Michigan, Ann Arbor, Michigan, USA
[90]Department of Physics and Astronomy, Michigan State University, East Lansing, Michigan, USA
[91a]INFN Sezione di Milano, Italy
[91b]Dipartimento di Fisica, Università di Milano, Milano, Italy
[92]B. I. Stepanov Institute of Physics, National Academy of Sciences of Belarus, Minsk, Republic of Belarus
[93]National Scientific and Educational Centre for Particle and High Energy Physics, Minsk, Republic of Belarus
[94]Department of Physics, Massachusetts Institute of Technology, Cambridge, Massachusetts, USA
[95]Group of Particle Physics, University of Montreal, Montreal, Québec, Canada
[96]P. N. Lebedev Institute of Physics, Academy of Sciences, Moscow, Russia
[97]Institute for Theoretical and Experimental Physics (ITEP), Moscow, Russia
[98]National Research Nuclear University, MEPhI, Moscow, Russia
[99]D. V. Skobeltsyn Institute of Nuclear Physics, M. V. Lomonosov Moscow State University, Moscow, Russia
[100]Fakultät für Physik, Ludwig-Maximilians-Universität München, München, Germany
[101]Max-Planck-Institut für Physik, Werner-Heisenberg-Institut, München, Germany
[102]Nagasaki Institute of Applied Science, Nagasaki, Japan
[103]Graduate School of Science and Kobayashi-Maskawa Institute, Nagoya University, Nagoya, Japan
[104a]INFN Sezione di Napoli, Italy
[104b]Dipartimento di Fisica, Università di Napoli, Napoli, Italy
[105]Department of Physics and Astronomy, University of New Mexico, Albuquerque, New Mexico, USA

[106]*Institute for Mathematics, Astrophysics and Particle Physics, Radboud University Nijmegen/Nikhef, Nijmegen, Netherlands*
[107]*Nikhef National Institute for Subatomic Physics and University of Amsterdam, Amsterdam, Netherlands*
[108]*Department of Physics, Northern Illinois University, DeKalb, Illinois, USA*
[109]*Budker Institute of Nuclear Physics, SB RAS, Novosibirsk, Russia*
[110]*Department of Physics, New York University, New York, New York, USA*
[111]*Ohio State University, Columbus, Ohio, USA*
[112]*Faculty of Science, Okayama University, Okayama, Japan*
[113]*Homer L. Dodge Department of Physics and Astronomy, University of Oklahoma, Norman, Oklahoma, USA*
[114]*Department of Physics, Oklahoma State University, Stillwater, Oklahoma, USA*
[115]*Palacký University, RCPTM, Olomouc, Czech Republic*
[116]*Center for High Energy Physics, University of Oregon, Eugene, Oregon, USA*
[117]*LAL, Université Paris-Sud and CNRS/IN2P3, Orsay, France*
[118]*Graduate School of Science, Osaka University, Osaka, Japan*
[119]*Department of Physics, University of Oslo, Oslo, Norway*
[120]*Department of Physics, Oxford University, Oxford, United Kingdom*
[121a]*INFN Sezione di Pavia, Italy*
[121b]*Dipartimento di Fisica, Università di Pavia, Pavia, Italy*
[122]*Department of Physics, University of Pennsylvania, Philadelphia, Pennsylvania, USA*
[123]*National Research Centre "Kurchatov Institute", B. P. Konstantinov Petersburg Nuclear Physics Institute, St. Petersburg, Russia*
[124a]*INFN Sezione di Pisa, Italy*
[124b]*Dipartimento di Fisica E. Fermi, Università di Pisa, Pisa, Italy*
[125]*Department of Physics and Astronomy, University of Pittsburgh, Pittsburgh, Pennsylvania, USA*
[126a]*Laboratório de Instrumentação e Física Experimental de Partículas—LIP, Lisboa, Portugal*
[126b]*Faculdade de Ciências, Universidade de Lisboa, Lisboa, Portugal*
[126c]*Department of Physics, University of Coimbra, Coimbra, Portugal*
[126d]*Centro de Física Nuclear da Universidade de Lisboa, Lisboa, Portugal*
[126e]*Departamento de Fisica, Universidade do Minho, Braga, Portugal*
[126f]*Departamento de Fisica Teorica y del Cosmos and CAFPE, Universidad de Granada, Granada, Spain*
[126g]*Dep Fisica and CEFITEC of Faculdade de Ciencias e Tecnologia, Universidade Nova de Lisboa, Caparica, Portugal*
[127]*Institute of Physics, Academy of Sciences of the Czech Republic, Praha, Czech Republic*
[128]*Czech Technical University in Prague, Praha, Czech Republic*
[129]*Faculty of Mathematics and Physics, Charles University in Prague, Praha, Czech Republic*
[130]*State Research Center Institute for High Energy Physics (Protvino), NRC KI, Russia*
[131]*Particle Physics Department, Rutherford Appleton Laboratory, Didcot, United Kingdom*
[132a]*INFN Sezione di Roma, Italy*
[132b]*Dipartimento di Fisica, Sapienza Università di Roma, Roma, Italy*
[133a]*INFN Sezione di Roma Tor Vergata, Italy*
[133b]*Dipartimento di Fisica, Università di Roma Tor Vergata, Roma, Italy*
[134a]*INFN Sezione di Roma Tre, Italy*
[134b]*Dipartimento di Matematica e Fisica, Università Roma Tre, Roma, Italy*
[135a]*Faculté des Sciences Ain Chock, Réseau Universitaire de Physique des Hautes Energies—Université Hassan II, Casablanca, Morocco*
[135b]*Centre National de l'Energie des Sciences Techniques Nucleaires, Rabat, Morocco*
[135c]*Faculté des Sciences Semlalia, Université Cadi Ayyad, LPHEA-Marrakech, Morocco*
[135d]*Faculté des Sciences, Université Mohamed Premier and LPTPM, Oujda, Morocco*
[135e]*Faculté des sciences, Université Mohammed V, Rabat, Morocco*
[136]*DSM/IRFU (Institut de Recherches sur les Lois Fondamentales de l'Univers), CEA Saclay (Commissariat à l'Energie Atomique et aux Energies Alternatives), Gif-sur-Yvette, France*
[137]*Santa Cruz Institute for Particle Physics, University of California Santa Cruz, Santa Cruz, California, USA*
[138]*Department of Physics, University of Washington, Seattle, Washington, USA*
[139]*Department of Physics and Astronomy, University of Sheffield, Sheffield, United Kingdom*
[140]*Department of Physics, Shinshu University, Nagano, Japan*
[141]*Fachbereich Physik, Universität Siegen, Siegen, Germany*
[142]*Department of Physics, Simon Fraser University, Burnaby, British Columbia, Canada*
[143]*SLAC National Accelerator Laboratory, Stanford, California, USA*

[144a]*Faculty of Mathematics, Physics & Informatics, Comenius University, Bratislava, Slovak Republic*
[144b]*Department of Subnuclear Physics, Institute of Experimental Physics of the Slovak Academy of Sciences, Kosice, Slovak Republic*
[145a]*Department of Physics, University of Cape Town, Cape Town, South Africa*
[145b]*Department of Physics, University of Johannesburg, Johannesburg, South Africa*
[145c]*School of Physics, University of the Witwatersrand, Johannesburg, South Africa*
[146a]*Department of Physics, Stockholm University, Sweden*
[146b]*The Oskar Klein Centre, Stockholm, Sweden*
[147]*Physics Department, Royal Institute of Technology, Stockholm, Sweden*
[148]*Departments of Physics & Astronomy and Chemistry, Stony Brook University, Stony Brook, New York, USA*
[149]*Department of Physics and Astronomy, University of Sussex, Brighton, United Kingdom*
[150]*School of Physics, University of Sydney, Sydney, Australia*
[151]*Institute of Physics, Academia Sinica, Taipei, Taiwan*
[152]*Department of Physics, Technion: Israel Institute of Technology, Haifa, Israel*
[153]*Raymond and Beverly Sackler School of Physics and Astronomy, Tel Aviv University, Tel Aviv, Israel*
[154]*Department of Physics, Aristotle University of Thessaloniki, Thessaloniki, Greece*
[155]*International Center for Elementary Particle Physics and Department of Physics, The University of Tokyo, Tokyo, Japan*
[156]*Graduate School of Science and Technology, Tokyo Metropolitan University, Tokyo, Japan*
[157]*Department of Physics, Tokyo Institute of Technology, Tokyo, Japan*
[158]*Department of Physics, University of Toronto, Toronto, Ontario, Canada*
[159a]*TRIUMF, Vancouver, British Columbia, Canada*
[159b]*Department of Physics and Astronomy, York University, Toronto, Ontario, Canada*
[160]*Faculty of Pure and Applied Sciences, and Center for Integrated Research in Fundamental Science and Engineering, University of Tsukuba, Tsukuba, Japan*
[161]*Department of Physics and Astronomy, Tufts University, Medford, Massachusetts, USA*
[162]*Centro de Investigaciones, Universidad Antonio Narino, Bogota, Colombia*
[163]*Department of Physics and Astronomy, University of California Irvine, Irvine, California, USA*
[164a]*INFN Gruppo Collegato di Udine, Sezione di Trieste, Udine, Italy*
[164b]*ICTP, Trieste, Italy*
[164c]*Dipartimento di Chimica, Fisica e Ambiente, Università di Udine, Udine, Italy*
[165]*Department of Physics, University of Illinois, Urbana, Illinois, USA*
[166]*Department of Physics and Astronomy, University of Uppsala, Uppsala, Sweden*
[167]*Instituto de Física Corpuscular (IFIC) and Departamento de Física Atómica, Molecular y Nuclear and Departamento de Ingeniería Electrónica and Instituto de Microelectrónica de Barcelona (IMB-CNM), University of Valencia and CSIC, Valencia, Spain*
[168]*Department of Physics, University of British Columbia, Vancouver, British Columbia, Canada*
[169]*Department of Physics and Astronomy, University of Victoria, Victoria, British Columbia, Canada*
[170]*Department of Physics, University of Warwick, Coventry, United Kingdom*
[171]*Waseda University, Tokyo, Japan*
[172]*Department of Particle Physics, The Weizmann Institute of Science, Rehovot, Israel*
[173]*Department of Physics, University of Wisconsin, Madison WI, United States of America*
[174]*Fakultät für Physik und Astronomie, Julius-Maximilians-Universität, Würzburg, Germany*
[175]*Fachbereich C Physik, Bergische Universität Wuppertal, Wuppertal, Germany*
[176]*Department of Physics, Yale University, New Haven, Connecticut, USA*
[177]*Yerevan Physics Institute, Yerevan, Armenia*
[178]*Centre de Calcul de l'Institut National de Physique, Nucléaire et de Physique des Particules (IN2P3), Villeurbanne, France*

[a]Deceased.
[b]Also at Department of Physics, King's College London, London, United Kingdom.
[c]Also at Institute of Physics, Azerbaijan Academy of Sciences, Baku, Azerbaijan.
[d]Also at Novosibirsk State University, Novosibirsk, Russia.
[e]Also at TRIUMF, Vancouver BC, Canada.
[f]Also at Department of Physics, California State University, Fresno CA, United States of America.
[g]Also at Department of Physics, University of Fribourg, Fribourg, Switzerland.
[h]Also at Departamento de Fisica e Astronomia, Faculdade de Ciencias, Universidade do Porto, Portugal.
[i]Also at Tomsk State University, Tomsk, Russia.
[j]Also at CPPM, Aix-Marseille Université and CNRS/IN2P3, Marseille, France.

[k]Also at Universita di Napoli Parthenope, Napoli, Italy.
[l]Also at Institute of Particle Physics (IPP), Canada.
[m]Also at Particle Physics Department, Rutherford Appleton Laboratory, Didcot, United Kingdom.
[n]Also at Department of Physics, St. Petersburg State Polytechnical University, St. Petersburg, Russia.
[o]Also at Louisiana Tech University, Ruston LA, United States of America.
[p]Also at Institucio Catalana de Recerca i Estudis Avancats, ICREA, Barcelona, Spain.
[q]Also at Department of Physics, The University of Michigan, Ann Arbor MI, United States of America.
[r]Also at Graduate School of Science, Osaka University, Osaka, Japan.
[s]Also at Department of Physics, National Tsing Hua University, Taiwan.
[t]Also at Department of Physics, The University of Texas at Austin, Austin TX, United States of America.
[u]Also at Institute of Theoretical Physics, Ilia State University, Tbilisi, Georgia.
[v]Also at CERN, Geneva, Switzerland.
[w]Also at Georgian Technical University (GTU),Tbilisi, Georgia.
[x]Also at Manhattan College, New York NY, United States of America.
[y]Also at Hellenic Open University, Patras, Greece.
[z]Also at Institute of Physics, Academia Sinica, Taipei, Taiwan.
[aa]Also at LAL, Université Paris-Sud and CNRS/IN2P3, Orsay, France.
[bb]Also at Academia Sinica Grid Computing, Institute of Physics, Academia Sinica, Taipei, Taiwan.
[cc]Also at School of Physics, Shandong University, Shandong, China.
[dd]Also at Moscow Institute of Physics and Technology State University, Dolgoprudny, Russia.
[ee]Also at Section de Physique, Université de Genève, Geneva, Switzerland.
[ff]Also at International School for Advanced Studies (SISSA), Trieste, Italy.
[gg]Also at Department of Physics and Astronomy, University of South Carolina, Columbia SC, United States of America.
[hh]Also at School of Physics and Engineering, Sun Yat-sen University, Guangzhou, China.
[ii]Also at Faculty of Physics, M. V. Lomonosov Moscow State University, Moscow, Russia.
[jj]Also at National Research Nuclear University MEPhI, Moscow, Russia.
[kk]Also at Department of Physics, Stanford University, Stanford CA, United States of America.
[ll]Also at Institute for Particle and Nuclear Physics, Wigner Research Centre for Physics, Budapest, Hungary.
[mm]Also at University of Malaya, Department of Physics, Kuala Lumpur, Malaysia.